Supercritical Adsorption of CO_2 and CH_4 on Shales and Other Porous Media

Humera Sultana Ansari

Department of Chemical Engineering

Imperial College London

A thesis submitted in part fulfilment of the requirements for the degree of
Doctor of Philosophy of Imperial College London
and the Diploma of Imperial College London

2021

Statement of Originality

I hereby declare that the work included in this thesis is entirely my own and anything else is appropriately referenced. Some of the work has been published or has been submitted for publication and the relevant references can be found at the start of each chapter.

Copyright Declaration

Abstract

Low natural gas recovery factors from shale reservoirs have stimulated interest in Enhanced Shale Gas Recovery (ESGR) using CO_2 injection. This process seeks to exploit the preferential adsorption of CO_2 in shale's nanometric pores, so as to enhance desorption of CH_4 and to promote geological sequestration of CO_2. To facilitate the design of this process, an integrated experimental and modelling workflow was developed and deployed on shale samples from the Longmaxi (China), Marcellus (USA) and Bowland (UK) formations to achieve the following: (i) high-resolution textural characterisation, (ii) supercritical adsorption measurements with CO_2 and CH_4, and (iii) their description by a novel mathematical model that predicts adsorption in chemically and morphologically heterogeneous materials. The results show that CO_2 adsorbs more than CH_4 at all pressures (2–3 times) and that both adsorption capacities and textural properties are strongly influenced by the shale mineralogy. The model developed in this work is based on the lattice Density Functional Theory and describes adsorption systems featuring both slit and cylindrical pores and accounts for the presence of energetically distinct organic- and clay-rich pore surfaces. The workflow was calibrated on three model adsorbents (mesoporous carbon, microporous activated carbon and micro/mesoporous zeolite) to reveal the distinct pore-filling mechanisms in micro- and meso-pores. The use of these model materials enabled the creation of a predictive modelling approach for the description of shale adsorption data, which only requires knowledge of the shale's composition. An equilibrium-based ESGR proxy reservoir model was also developed and demonstrated that a cyclic CO_2 injection operation, which includes a so-called soaking stage, may be required to achieve sufficient recovery and secure CO_2 storage. The practical workflow presented in this thesis can be used to quantify accurately the Gas-in-Place and CO_2 storage potential of shale reservoirs at subsurface conditions and design an optimal CO_2-ESGR process.

Publications

H. Ansari, L. Joss, M. Trusler, G. Maitland, C. Delle Piane and R. Pini, "Enhanced shale gas recovery: gas sorption controls on recoverable gas and CO_2 storage capacity," *14th Greenhouse Gas Control Technologies Conference Melbourne 21-26 October 2018 (GHGT-14)*, 2019, doi.org/10.2139/ssrn.3365806.

C. Delle Piane, **H. Ansari**, W. Rickard, M. Saunders, J. Mata and D. N. Dewhurst, "Organic hosted porosity in the Wufeng-Longmaxi shale: a combined electron microscopy and neutron scattering approach," *Sixth EAGE Shale Workshop*, 2019, doi.org/10.3997/2214-4609.201900308.

H. Ansari, M. Trusler, G. Maitland, C. Delle Piane and R. Pini, "Characterisation of the Bowland shale porosity using N_2 and CO_2 adsorption," *Sixth EAGE Shale Workshop*, 2019, doi.org/10.3997/2214-4609.201900274.

H. Ansari, L. Joss, J. Hwang, J. P. M. Trusler, G. Maitland and R. Pini, "Supercritical adsorption in micro- and meso-porous carbons and its utilisation for textural characterisation," *Microporous and Mesoporous Materials*, 308, 110537, 2020, doi.org/10.1016/j.micromeso.2020.110537.

H. Ansari, M. Trusler, G. Maitland, C. Delle Piane and R. Pini, "The Gas-in-Place and CO_2 storage capacity of shale reservoirs at subsurface conditions," *Proceedings of the 15th Greenhouse Gas Control Technologies Conference 15-18 March 2021*, 2021, doi.org/10.2139/ssrn.3820831.

R. Pini, **H. Ansari** and J. Hwang, "Measurement and interpretation of unary supercritical gas adsorption isotherms in micro-mesoporous solids," *Adsorption*, 27, p.659-671, 2021, doi.org/10.1007/s10450-021-00313-z.

H. Ansari, E. Rietmann, L. Joss, J. P. M. Trusler, G. Maitland and R. Pini, "A shortcut Pressure Swing Adsorption analogue model to estimate Gas-in-Place and CO_2 storage potential of gas shales,"

Fuel, 301, 121014, 2021, doi.org/10.1016/j.fuel.2021.121014.

L. Ma, A.-L. Fauchille, **H. Ansari**, M. Chandler, P. Ashby, K. Taylor, R. Pini and P. D. Lee, "Linking multi-scale 3D microstructure to potential enhanced natural gas recovery and subsurface CO_2 storage for Bowland shale, UK," *Energy & Environmental Science*, 2021, doi.org/10.1039/D0EE03651J.

T. Tian, J. Hou, **H. Ansari**, Y. Xiong, A. L'Hermitte, D. Danaci, R. Pini and C. Petit, "Mechanically stable structured porous boron nitride with high volumetric adsorption capacity," *Journal of Materials Chemistry A*, 9, p.13366-13373, 2021, doi.org/10.1039/D1TA02001C.

C. Delle Piane, **H. Ansari**, Z. Li, J. Mata, W. Rickard, R. Pini, D. N. Dewhurst and N. Sherwood, "Influence of maceral type on porosity development in the Wufeng-Longmaxi shale: a combined electron microscopy, neutron scattering and physisorption approach," *Submitted for publication*, 2021.

Acknowledgements

I would like to sincerely thank my three PhD supervisors, Prof. Geoffrey Maitland, Prof. J. P. Martin Trusler and Dr Ronny Pini for their unwavering support and invaluable advice. Their constant guidance, mentorship, and words of encouragement made this journey a lot easier.

I am also very grateful to the Marit Mohn Scholarship for funding my PhD at the Department of Chemical Engineering at Imperial College London. Marit is a constant source of inspiration and her advice has always been extremely useful.

A special thank you to CSIRO for also sponsoring this project. In particular, Dr Claudio Delle Piane hosted my research visits in Perth, Australia, and introduced me to a new field of research. I am thankful for his technical expertise and collaborative spirit.

A massive thanks to all my friends and collaborators at Imperial College. This journey would have been nowhere near as enjoyable without you all. Thank you to Anna-Maria Eckel, Nerine Joewondo, Emily Chapman, Takeshi Kurotori, Junyoung Hwang, Caroline Jones, Swapna Rabha, Sayed Alireza Hosseinzadeh Hejazi, Lisa Joss, Rebecca Liyanage, Hassan Azzan, Mihaela Stevar, Lorena Dos Santos de Souza, Geraldine Torin Ollarves, Theodor Videnberg, Yolanda Vincente-Sanchez, Weparn Julian Tay, Ines da Graca, Sultan Al-Habsi, Benaiah Anabaraonye, Chidi Efika, Malyanah Binti Mohd Taib, Ziqing Pan, Kaiqiang Zhang, Nadine Moustafa and Lu Ai. Thank you for the great memories.

I would also like to thank all my wonderful school teachers at Cambridge International School, Dubai, who helped me realise how much I love learning and discovering. I am also very thankful to all the technicians, administrators, maintenance and cleaning staff at Imperial College who made my research possible.

Lastly, this PhD would not have been possible without my parents and my sister. Words are not enough to describe how grateful I am for their support, encouragement, love and kindness. Thank you for believing in me, motivating me and guiding me across the miles.

Contents

List of Figures

List of Tables

List of Abbreviations

AC	Activated Carbon
B_	Bowland shale
BET	Brunauer-Emmett-Teller
CCUS	Carbon Capture, Utilisation and Storage
CPG	Controlled Pore Glass
D-A	Dubinin-Astakhov
DFT	Density Functional Theory
D-R	Dubinin-Radushkevich
ESGR	Enhanced Shale Gas Recovery
GIP	Gas-in-Place
GCMC	Grand Canonical Monte Carlo
LDFT	Lattice Density Functional Theory
LG_	Longmaxi shale
LNG	Liquefied Natural Gas
MC	Mesoporous Carbon
MIP	Mercury Intrusion Porosimetry
ML	Marcellus shale
MP_1	Measuring Point 1
MP_2	Measuring Point 2
MSB	Magnetic Suspension Balance
MZ	Mesoporous Zeolite
NLDFT	Non Local Density Functional Theory
OGIP	Original Gas-in-Place
PSD	Pore Size Distribution
QSDFT	Quenched Solid Density Functional Theory
RAST	Real Adsorbed Solution Theory
SANS	Small-Angle Neutron Scattering
SLD	Simplified Local Density
SSA	Specific Surface Area
TOC	Total Organic Carbon
USANS	Ultra-Small-Angle Neutron Scattering
ZP	Zero Point

List of Symbols

c_{sat}	Saturation factor
C_{t}	Concentration of the bulk phase
δ	Experimental uncertainty
d	Diameter of a lattice site
D_{p,J_k}	Pore diameter
$\varepsilon_{\mathrm{ff}}$	Adsorbate-adsorbate interaction energy
$\varepsilon_{\mathrm{sf}}$	Adsorbate-adsorbent interaction energy
$\overline{\varepsilon}_{\mathrm{sf}}$	Effective adsorbate-adsorbent interaction energy in cylindrical pores
E	Number of experimental points
f	Fugacity
f_i	Partitioning factor for component i
G_{p}	Cumulative amount of gas produced
$G_{\mathrm{t},0}$	OGIP
$\Delta h_0/\Delta\widetilde{h}_0$	Isosteric enthalpy of adsorption at zero loading
H	Henry constant
$H_0/\widetilde{H_0}$	Pre-factors of the van't Hoff equation
J	Number of layers
K	Langmuir equilibrium constant
k_{B}	Boltzmann's constant
$\mathrm{MP}_{1,0}$	MP_1 under vacuum
$\mathrm{MP}_{2,0}$	MP_2 under vacuum
$\mathrm{MP}_{\mathrm{empty}}$	MP with an empty basket
$\mathrm{MP}_{\mathrm{He}}$	MP under Helium
m_{s}	Adsorbent mass
M_{w}	Molecular weight
n^{∞}	Saturation limit in the Langmuir model
n^{a}	Absolute amount adsorbed

n^{ex}	Excess amount adsorbed
$n^{\mathrm{ex}}_{\mathrm{cyl}}$	Excess amount adsorbed for cylindrical pores
$n^{\mathrm{ex}}_{\mathrm{slit}}$	Excess amount adsorbed for slit pores
n^{net}	Net amount adsorbed
$N^{q}_{\mathrm{g,inj}}$	Amount of gas injected per cycle
ϕ	Reservoir porosity
Φ	Value of the objective function
P	Pressure
P_0	Saturation pressure
P_{c}	Critical pressure
P_{L}	Production pressure
P_{o}	Initial reservoir pressure
ρ_{a}	Adsorbed phase density
$\overline{\rho}_{\mathrm{a}}$	Adsorbed phase density of a gas mixture
ρ_{b}	Bulk fluid density
ρ_{c}	Critical density
$\rho_{\mathrm{e},i}$	Mineral density of component i
ρ_j	Density in layer j
ρ_{sc}	Density of the fluid at standard conditions
ρ_{max}	Maximum lattice density
$\rho_{\mathrm{w,s}}$	Bulk density of the reservoir
Q	Total number of gas injection cycles
r_j	Distance from the centre of pore to layer j in a cylindrical pore
R	Universal gas constant
R_{m}	Enhanced Recovery factor
σ	Collision diameter of a gas molecule
S_{g}	Storage factor
θ_{b}	Probability of occupancy in the bulk
θ_{j}	Probability of occupancy of layer j
T	Temperature
T_{c}	Critical temperature
v	Normalised volumetric fraction of TOC
$v_{\mathrm{a}}/V_{\mathrm{a}}$	Volume of the adsorbed phase
V	Volume of the reservoir
V_{met}	Volume of the metal parts
ν_{mic}	Micropore volume

ν_{mes}	Mesopore volume
ν_{tot}	Total pore volume
$\nu_{\mathrm{p},k}$	Pore volume of pore class k
V_{s}	Volume of the solid
V_{sk}	Volume of the sinker
V_0	Sum of the volumes of the solid and metal parts
w_k	Surface area fraction of pore class k
x_i	Fraction of element i in the shale
y_i	Mole fraction of component i in the bulk phase
z^{b}	Bulk coordination number
z_i	Mole fraction of component i in the adsorbed phase
z_j^{s}	Coordination number in the same layer
z^{a}	Coordination number with the adjacent layer
$z_j^{\mathrm{a}+}$	Coordination number with the outer adjacent layer
$z_j^{\mathrm{a}-}$	Coordination number with the inner adjacent layer
Z	Fluid compressibility

Chapter 1

Introduction

Some of the material in this chapter is published in Ansari et al. (2021) [1].

1.1 Shale Gas

Due to the rising global demand for natural gas, the interest in unconventional gas resources, such as gas shales, has recently grown [2]. Progress in production techniques, such as hydraulic fracturing and horizontal drilling, is allowing access to massive reserves of natural gas [3, 4, 5]. In conventional reservoirs, natural gas exists mostly as compressed supercritical fluid in pores and fractures, and its behaviour is described by a suitable equation of state. Shales, on the other hand, have very small pores (nanometric in size), where gas can densify as a result of physical adsorption [6]. While the presence of nano-scale pores enhances storage capacity by retaining gas at liquid-like densities [7], it also introduces severe limitations to mass transfer in terms of low (nano-Darcy) permeability [8]. Production from shale formations starts to decline in less than 3–4 years from initial production and recovery factors from these reservoirs are low, usually ranging from 1–30% [9, 10]. In so-called conventional reservoirs, enhanced recovery methods are routinely used to sustain productivity. By analogy with coal-bed methane recovery [11], reservoir engineering practices can be considered for shale, whereby gas is injected into the formation to sustain a pressure gradient, while reducing the partial pressure of methane and increasing its extraction. When CO_2 is used as the injected gas, it can be retained in the formation by the same mechanisms that led to the accumulation of natural gas, thereby reducing the impact of hydrocarbon production on climate change. Shale plays are usually significant in size, providing a potentially large CO_2 sequestration site [12, 13]. The coupling of gas recovery with CO_2 injection and storage (CO_2-Enhanced Shale Gas Recovery or CO_2-ESGR) also poses many operational benefits, including the utilisation of existing infrastructure to achieve higher recovery rates [14], and the maintenance of reservoir pressure to limit the risk of subsidence [15].

1.2 Geological Sequestration of CO_2 in Shale Reservoirs

Climate change has been attributed to the increase in anthropogenic greenhouse gas emissions. The rise in the atmospheric levels of CO_2 is of particular concern and, as a result, experts agree that to meet the target of limiting the global temperature rise to 2 °C, we need Carbon Capture, Utilisation and Storage (CCUS) [16]. CCUS encompasses the process of capturing carbon from point sources or even directly from air, using CO_2 to create useful products such as chemicals, or transporting the CO_2 to a storage site, where it can be permanently sequestered and monitored in geological formations [17, 2]. The proposed CO_2-ESGR process can be considered a part of CCUS. This is particularly meaningful in the context of shale gas as the CO_2 from fossil fuel combustion accounts for nearly 90% of all energy-related greenhouse gas emissions [18]. Shale gas is seen as a low-carbon transition fuel [19] as natural gas, when burned, produces about half the CO_2 emissions, per unit of energy, as compared to coal [20]. In fact, if the industry is well regulated and fugitive emissions can be minimised, shale gas can have half the life-cycle carbon footprint of coal [21]. The USA has already seen a decrease in their carbon emissions since replacing coal with shale gas [22].

CO_2-ESGR has been considered to have great economic potential - 71 trillion m^3 additional CH_4 recovery, while providing 280 Gt of CO_2 storage [23]. A few modelling studies have evaluated the potential of specific shale plays. Tao and Clarens (2013) estimated that the Marcellus shale (one of the major shale plays in the USA) would be able to store 10.4–18.4 Gt of CO_2 by 2030 based on the CH_4 production rates [14]. Similarly, Edwards et al. (2015), found storage capacities of 7.2–9.6 Gt for the Marcellus shale and 2.1–3.1 Gt for the Barnett shale (another shale in the USA) [24]. Li and Elsworth (2015) showed an enhanced recovery between 2–29% depending on the CO_2 injection strategy [13]. Practical demonstration of *in-situ* CO_2 injections are quite rare however. In a small-scale trial, around 500 tons of CO_2 were injected in a shale reservoir located in the Morgan County, Tennessee (USA) and results showed that, after an initial soaking period, the daily average production rate of hydrocarbons from the well increased compared to data before CO_2 injection [25].

1.3 Research Objectives

There are still questions that remain to be answered about the ESGR process itself. To list a few: How could such an operation be implemented in practice given the low permeability of shale? What would be the optimum pressure to operate such a process? Is there an injection scheme that maximises recovery and storage simultaneously? Answering these questions requires an understanding of the gas adsorption properties of shale at the elevated pressure and temperature conditions typically found in shale formations. CO_2-ESGR is in fact founded upon the principle that CO_2 adsorbs preferentially

within the rock as compared to CH_4 [12, 24]. While experimental studies have confirmed a favourable adsorption selectivity towards CO_2 [26, 27], these measurements are often not performed at subsurface conditions (where both CO_2 and CH_4 are supercritical) and partly because of the relatively low adsorption capacities of shale, results are often very scattered. Supercritical adsorption measurements on shale can be very challenging to interpret due to the inherent heterogeneity of shales. This manifests itself in both shale's pore space, which includes micropores (< 2 nm) and mesopores (2–50 nm), and mineralogy, which includes two adsorbing components (the organic matter and clay minerals) that potentially interact with fluids differently. Furthermore, the adsorption data are usually modelled by adsorption models that are not either suitable at supercritical conditions or are too computationally expensive and cannot be reliably integrated with reservoir models. Moreover, the use of adsorption quantities in volumetric calculations for storage capacity estimation has not yet been addressed properly. A key element in the analysis is the use of the so-called excess amount adsorbed, which is the truly measurable quantity in a high pressure gas adsorption experiment and accounts correctly for the porosity occupied by the supercritical adsorbed phase.

The overall research objectives of this work, designed to address these issues, can be summarised as follows:

1. To quantify experimentally the adsorption behaviour of supercritical CO_2 and CH_4 in both shale rocks and synthetic nanoporous materials at representative subsurface conditions,
2. To identify the main controls on gas adsorption in shale,
3. To model the experimental measurements using suitable adsorption models that are able to describe and predict adsorption in heterogeneous materials,
4. To use the experimental and modelling results to optimise the engineering design of gas recovery from shale reservoirs. This includes the potential for enhanced shale gas production using injected supercritical CO_2 and the capacity to combine this with CO_2 sequestration.

1.4 Outline of the Thesis

One goal of this work is to build on the understanding and methodologies developed by addressing the objectives defined above, to develop a detailed workflow to characterise and systematically investigate any particular shale for its potential for ESGR. In this thesis, the workflow was demonstrated by its application to three typical and contrasting shale plays. The thesis first begins in Chapter 2 with an in-depth look at gas shales in terms of their petrophysical characteristics, such as permeability and pore size distribution, and current research into the design of an ESGR process. Adsorption

theory is presented alongside existing experimental and modelling research into adsorption in shale, and research gaps are identified.

Although the focus of this thesis is on shale, synthetic adsorbents, such as porous carbons and zeolites, are also studied and provide benchmarks for the analysis of adsorption in mesoporous materials. Chapter 3 describes these materials and the selected shales (from the Longmaxi, Marcellus and Bowland shale formations), including their mineralogy. This is followed by a detailed description of the working principle behind two of the main experimental techniques utilised in this work to measure adsorption at low and elevated pressures. The full experimental setup used for the latter, which includes the Magnetic Suspension Balance, and the governing equations of the system are presented, including an explanation of the method for quantifying experimental uncertainties.

Chapter 4 presents the adsorption modelling frameworks considered in this thesis. These include models based on empirical isotherm equations, such as the Langmuir model, and a model based on the lattice Density Functional Theory (lattice DFT). The latter has been formulated to describe adsorption in both slit and cylindrical pores for the purpose of describing supercritical adsorption on a variety of adsorbents. With relevance to shales, a new hybrid formulation of the lattice DFT model involving both slit and cylindrical pores, each with unique surface interaction energies, is also presented.

Material characterisation is an important precursor to the interpretation of supercritical adsorption measurements. Chapter 5 focuses on characterising each adsorbent in this study through a combination of subcritical adsorption using N_2, Ar and CO_2 at cryogenic conditions and supercritical adsorption with CO_2 at near-critical conditions ($T/T_c = 1.01$–1.03). While the former is used to identify the pore size distribution (PSD) up to 100 nm and the surface areas of each material, the latter pinpoints the pore sizes contributing the most to supercritical adsorption. Through the use of synthetic adsorbents, such as porous carbons, and pure clay minerals, correlations of mineralogy with the textural properties of shales are investigated.

The focus of Chapter 6 is the adsorption behaviour of CO_2 and CH_4 in the synthetic adsorbents, which include mesoporous carbon (MC), activated carbon (AC) and mesoporous zeolite (MZ). The results of the supercritical adsorption measurements for these materials at various temperatures are detailed here. Thermodynamic parameters, such as Henry constants and the isosteric enthalpies of adsorption, are also quantified for each adsorbent. The lattice DFT model is then used to describe the experimental data and provide mechanistic insights into the interaction of these fluids with the carbon or zeolite surface.

Chapters 7 and 8 deal with the supercritical adsorption of CO_2 and CH_4 on the Longmaxi, Marcellus and Bowland shales, from an experimental and modelling perspective, respectively. Excess and net

adsorption isotherms are presented in Chapter 7 and insights from these experiments are highlighted. The results for the synthetic adsorbents are also used to create synthetic isotherms based on each shale's composition and compared to the experimental results with shales. In Chapter 8, the hybrid lattice DFT model is tested on the shales considered in this work and the impact of pore geometry on the adsorption behaviour is determined. Both the experimental and modelled isotherms are used to calculate the Gas-in-Place of each shale reservoir.

The outcomes of the previous chapters are essential for the successful design and delivery of an ESGR process. Chapter 9 presents a modelled ESGR cyclic process, based on the Marcellus shale, that involves three stages: CO_2 Injection, Soak and Production. Various isotherm types are tested to evaluate their effect on primary gas recovery, which is then compared to the corresponding ESGR scenario in terms of quantities such as the amount of enhanced CH_4 recovery and of CO_2 stored. This forms the basis of a CO_2-ESGR workflow.

Finally, Chapter 10 summarises the main conclusions of this thesis, provides guidelines for practitioners seeking to design ESGR processes, and suggests avenues for further research to aid the successful deployment of CO_2-ESGR.

Chapter 2

Context, Background and Theory

This chapter illustrates some of the research in the shale gas arena. Some of the areas covered include the current shale gas extraction process, the proposed means of CO_2 injection to improve recovery, the characteristics of shale itself, including its mineralogy and pore structure, and gas storage and gas transport mechanisms. Adsorption theory is presented as well as an overview of experimental adsorption measurements at low and high pressures with shale and modelling approaches commonly utilised for supercritical adsorption. Some of the material in this chapter has been published in Ansari et al. (2018, 2020, 2021) [28, 29, 1].

2.1 Introduction

The shale gas industry has recently seen a boom in production, with forecasts suggesting that natural gas will continue to be used for many years to come. Fracking has opened the doors to vast amounts of shale gas and there has been considerable global interest in exploring this resource even more. In particular, shale gas has revitalised the USA's energy industry [4], allowing the country to export the relatively cheap natural gas as Liquefied Natural Gas (LNG) [30]. However, critics have argued that the 'shale boom' is unsustainable and that strong projections are misleading. Although shale gas wells produce well initially, the rates continuously decline soon after. This leads to the drilling of more wells, which might not produce as strongly even at the start of their production life [30]. In addition, production forecasts, which drive investment, can be based on coarse-grained studies of prominent shale formations, which are not detailed enough to take into account the fact that these formations have small 'sweet spots' [31]. If these projections prove to be incorrect, production companies could face economic repercussions and the wider shale gas industry can potentially suffer.

To better comprehend the necessity for research around shale, it is essential to look at what is at

stake in terms of global shale gas resources and current production trends. Firstly, it is imperative to appreciate the difference between resources and reserves. The former represents the total amount of gas the reservoir holds, i.e. all gas that has potential value. Reserves constitute all gas that is technically recoverable within economic limits. Therefore, reserves are a subset of the total resources [32, 33]. The U.S. EIA estimates that the total global risked shale resources are about 35,800 tcf and the total risked technically recoverable gas is 7,800 tcf [9]. 'Risked' estimates account for uncertainty with regards to the level of geological information and production history for a specific formation [34]. Another aspect that influences natural gas as a commodity is production rates. Currently, only four countries produce shale gas commercially: USA, Canada, China and Argentina [35]. The USA is current leading shale gas production at a rate of approximately 70 bcf/d [36]. The scale of this implies that shale gas is indeed profitable and investment of research into sustaining these levels could be beneficial.

2.2 Shale Gas Extraction

Shale is categorised as an 'unconventional' source of natural gas [37]. The unconventionality refers to the rock itself rather than the natural gas extracted from it, which is mostly comprised of CH_4 [38, 39]. Typically, formations that have a permeability of less than 1 mD are considered as unconventional, as this makes the rock tight and provides resistance to the flow of gas. Economics of the extraction is another factor that can class a formation as unconventional [4]. Extraction from shale formations is more difficult than conventional reservoirs as shale has very low permeability which does not allow gas to naturally flow into a well [8]. To overcome these challenges, current extraction processes use novel techniques such as hydraulic fracturing and horizontal drilling [3].

2.2.1 Fracking

The first stage of shale gas extraction is exploration. Seismic surveys are conducted to create sub-surface 3D images of the formation and, in conjunction with other studies, an appropriate drill site is selected [40]. The required site infrastructure, such as roads and pipelines, are constructed and vertical production wells are drilled to a depth of 2000–3000 m, depending on the characteristics of the formation [3]. The wells might also have horizontal sections further down the well. Horizontal wells increase the wellbore contact with the surrounding rock and this allows for more fractures and better extraction. This technique also causes the hydraulic fracturing energy to be dispersed over a larger area, reducing the possibility of unwarranted fracture growth. In addition, restrictions due to land ownership or access can prevent vertical drilling accomplishing the same level of extraction as

horizontal drilling [41]. Horizontal wells are created when the drill bit (at the front of the well) is deviated to run horizontally (or any other angle) [42]. The well is then lined with steel casing and cement to increase borehole stability and to allow for future well intervention activities [41]. Holes are created through the casing and cement by a perforation gun at fixed locations [40]. Hydraulic fracturing or 'fracking' is then carried out; through this method, the permeability of shale gas formations is essentially increased [43]. Fracking eases the movement of fluids to the wellbore and allows for continuous production [44]. The main goal of the process is to create a network of fractures next to the borehole [32]. Fractures are crucial to the process as they enhance permeability, increase the available specific surface area and expand potential transport channels. It is also important that the formation is well fractured so that the natural fracture system is fully incorporated with the hydraulic fractures [3]. Fractures are created by pumping the fracturing fluid at a rate necessary to increase the pressure downhole, and enough to overcome the pressure gradient of the adjacent rock. The fracturing fluid consists of water (around 90%), chemical additives and sand proppant, which is used to maintain the fracture width once injection has stopped and the pressure is reduced [4]. The composition of the fracturing fluid in multistage fracturing can be varied depending on the conditions in a specific location in the formation [42]. Once fracturing is complete, the fracturing fluid rises to the surface of the well due to the created pressure gradient, along with natural gas [3].

2.2.1.1 Issues with Fracking

Although a lot of progress has been made in shale gas extraction due to fracking, the process comes with certain potential issues. The main concerns are with the fracturing fluid and the potential for groundwater contamination, induced seismicity, fugitive emissions and public perception. The problem with the fracturing fluid arises mainly in relation to its procurement and disposal. Around 40–80% of the fracturing fluid is returned to the well surface [45]. The fluid contains many chemicals that will be harmful to human health and the environment and management of its disposal is vital. Water quality in the surrounding areas might be reduced if there are leaks due to poor well integrity or the waste from the extraction process is not properly disposed of. However, these issues can be designed out if proper waste management programs are maintained and the process is well regulated [45].

There is also some concern that shale gas extraction can be a contributing factor to increased seismicity [8]. The two types of seismicity related to fracking are microseismic events and large seismic events [42]. The former arise due to fracture propagation while hydraulic fracturing and are fairly routine. Large seismic events, which are rare, can occur due to the presence of a pre-stressed fault. In the UK, two seismic tremors (of magnitudes 2.3 ML and 1.5 ML) occurred in Blackpool, in 2011, due to exploratory drilling, which was the cause of massive public concern. As a result of this, a temporary

moratorium on shale gas was placed in the UK [45]. An investigation revealed that the two events were caused by the reactivation of pre-stressed fault. The fault could have been either crossed by the well or been reactivated due to pressure changes induced by hydraulic fracturing [42].

Fugitive emissions are methane emissions that occur invariably during the shale gas extraction process [32]. These can be up to about 2% of the total natural gas extracted from shale [46]. It is imperative these emissions are avoided so that shale gas can still be considered a viable option for the future energy mix. This issue also impacts the public perception of shale gas. Social acceptability is one of the key factors that can unlock new energy sources and encourage massive funding. Local communities are affected by such projects and it is important that public opinions are gauged and acceptance gained before any commitment is made. In a recent study, 1500 people from the UK were asked about shale gas [47]. The results showed that generally, people were unsure and ambivalent about shale gas. Most of the participants were more aware of the risks rather than benefits of shale gas extraction, specifically groundwater contamination and induced seismicity. However, a key result was that when they were given more information, people became more positive, indicating that proper communication is key to positively influencing the public perception of shale gas.

2.2.2 Enhanced Recovery

Although the issues with fracking highlighted in the previous section pose a significant challenge towards the proliferation of shale gas globally, perhaps the biggest barrier is the poor recoveries it normally results in. Within 3–4 years from initial production from a shale reservoir, rates start to decline and recovery factors are usually below 30% [9, 10]. Enhanced techniques can be used to increase extraction and achieve an economically stable production rate [48]. Enhanced extraction has been historically used for oil [24], where it can lead to an increase in recovery by 7–23% [49]. In shale, natural gas (mostly methane) is adsorbed (discussed more in Section 2.5). The underlying principle behind CO_2-ESGR is the preferential adsorption of CO_2 on shale, as compared to CH_4 [12, 24]. This poses several advantages, the primary one being that CO_2 injection will potentially cause more displacement of CH_4, leading to enhanced recovery. Additionally, leakage of CO_2 would be low as it is trapped through adsorption and CH_4 storage has demonstrated that the shale can provide a good seal for the gas. Another benefit is that CO_2 injection will maintain the reservoir pressure [15]. Shale plays are usually large and so they can potentially be substantial CO_2 sequestration sites [12]. The CO_2-ESGR process can be considered analagous to coal-bed methane recovery [50].

Theoretical studies have attempted to quantify the CO_2 storage potential of various shale plays. Two main kinds of models are in existence, namely the dual-porosity model and the triple-porosity model. The dual porosity model divides the system into the fracture and the matrix. The fracture provides

the flow path and the matrix is where the gas is stored and acts a source or sink. In these models, once the CH_4 desorbs from the matrix pores, it will flow immediately into the fractures with an inherently assumed infinite rate of transport. This is a simplification because this transport is actually slow. The triple-porosity model improves upon this and divides the matrix into two distinct porous regions with two different permeabilities [15]. This section will examine existing research in this field.

Utilising historic CH_4 production rates is common approach employed by many studies. Tao and Clarens (2013) used this methodology in their model of the Marcellus Shale. The model predicts that the shale will be able to store 10.4–18.4 Gt of CO_2 between 2013 and 2030. They also make the distinction between adsorbed and free methane. As the well produces, the free gas is immediately released and as the pressure decreases, CH_4 starts desorbing. Their results showed that CO_2 adsorbs more quickly than CH_4 desorbs, which means that the injection wells need to operate for a shorter period of time ($\sim$ 2 years) compared to the production wells ($\sim$ 10 years) [14]. This is a huge benefit in terms of the cost of this process. Similar capacities were were also seen by Edwards et al. (2015). They also incorporated excess adsorption in their model, which accounts for the decrease in the free gas-filled porosity due to the presence of the adsorbed phase. The results showed that the total CO_2 storage capacity is 7200–9600 Mt and 2100–3100 Mt for the Marcellus and Barnett shales, respectively [24].

An element that is often neglected is the multi-component gas transport involved during CO_2-ESGR, which involves the convective flow of gas (both CO_2 and CH_4), diffusive flow in the macropores and fractures (secondary pore structure) and multi-component adsorption and diffusion within the primary pore structure of the shale [51]. These processes are simultaneously occurring but within different time frames and characteristic length scales. Using a triple-porosity, single permeability model, Fathi and Akkutlu (2014) modelled the fluid dynamics between two hydraulic fractures in the shale matrix for the following phases: primary production without injection (10 years), CO_2 injection (5 years), soaking and secondary production (30 years). The results showed that there was a considerable influence of surface diffusion of the adsorbed molecules in the micropores which promotes counter-diffusion and competitive adsorption. This led to a total CH_4 recovery of 85% and a recovery of the injected CO_2 of less than 10%, which shows that the competition between the two gases can be exploited beneficially [51].

CO_2 can be continuously (flooding) or cyclically (huff-n-puff) injected into the shale reservoir. Schepers et al. (2009) observed that for their model of the Devonian Ohio Shale, continuous injection was the best scenario, as without injection, only 3.4% of CH_4 was recovered and with injection, this number rose to 11.2% for an injected amount of 300 tonnes of CO_2 over 1.5 months [52]. CO_2 flooding was also considered optimal by Yu et al. (2014) in their model of the Barnett Shale. The huff-n-puff strategy caused 96% of the injected CO_2 to flow back to the surface and the methane recovery to

decrease [53]. On the other hand, Li and Elsworth (2015) showed that continuous injection resulted in early breakthrough of CO_2, which pulsed injection avoided, although it resulted in more CH_4 recovery [13]. They also evaluated the influence of adsorption on permeability and porosity in their dual-porosity model of the CO_2-ESGR process in the Barnett Shale, which integrated competitive adsorption with sorption-dependent permeability and porosity. Two successive flow stages were seen during both scenarios of continuous and cyclic injection: fracture dominated (first 100 days of production) and matrix dominated flow. During fracture dominated flow, matrix permeability was constant and fracture permeability increased considerably (roughly 33%). During matrix dominated flow, matrix permeability only decreased by roughly 1%, while fracture permeability increased slightly [13]. Xu et al. (2017) demonstrated that both the production pressure and production period are significant factors that influence both the methane recovery as well the CO_2 sequestration capacity. In their triple-porosity, dual permeability model of the Sichuan Basin in China, they observed that with decreasing production pressure, gas production increased but the CO_2 storage capacity also decreased. The latter also reduced with an increase in production time [15].

Although the vast majority of the research on enhanced shale gas recovery is still based in modelling, there has a been a recent small-scale study on physical injection of approximately 500 tons of CO_2 into the Chattanooga shale reservoir in Morgan County, Tennessee. The results showed that there was a significant increase in CH_4 recovery after CO_2 injection compared to the previous baseline. Although the production gas also includes some CO_2, the rate has been decreasing over the months since the test. Gas quality generally improved too with a higher proportion of natural gas liquids. This particular study and the computational works highlighted in this section confirm that CO_2-ESGR has strong potential in achieving the aims of improved natural gas recovery and permanent and secure CO_2 sequestration. However, a better understanding of why certain behaviours are observed, especially in relation to adsorption, could greatly benefit the design of such a process.

2.3 Petrophysical Characteristics of Shale

To design a recovery process, it is imperative to understand the properties of shale. The pore structure and composition of shale heavily impact a variety of factors, such as the Gas-in-Place (GIP), gas flow and the capability to seal and trap the gas [54]. The following sections aim to describe the composition of shales, their pore structure and the effect of these factors on the storage and transport of gas.

2.3.1 Shale Mineralogy

Shale is described as a sedimentary, laminated fine-grained argillaceous mudstone [55]. The dominant grain size is less than 63 µm [56]. It is the most abundant sedimentary rock [57] and is formed from deposits of organic matter, clay minerals, mud and silt [42]. Shale that contains natural gas is mainly comprised of organic material, clay minerals and other minerals such as quartz. Depending on the particular formation and its age, the composition varies. Ross and Bustin (2009) analysed Canadian shales from various locations using a coulometer and an element analyser and the results showed that the TOC content varied between 0.11 wt% and 38 wt% and quartz content was in the range 58–93 wt% [58]. Wu et al. (2017) examined roughly 160 organic-rich shales from China using an X-ray diffractometer and found the TOC to be in the range 0.5–6.67 wt%, quartz content between 9–55 wt%, and clay content in the range 3–45 wt%. They also concluded that in samples with clay content lower than 30 wt%, the quartz content was positively correlated with the TOC content. In samples with clay content exceeding 30 wt%, quartz content remained constant with increasing TOC content [59]. Labani et al. (2013) looked at about 25 Australian shales using X-ray diffraction and observed that the TOC content varied between 0.23 wt% and 3.03 wt%, clay content was between 28 wt% and 56 wt%, and quartz content was between 18.2 wt% and 54 wt%. The measurements are quite widespread, highlighting the fact that shales are very diverse and heterogeneous [60].

As it is important to understand the effect of the shale composition on gas storage and transport, it is useful to look at composition on the basis of volume rather than weight. Zhang et al. (2017) used X-ray diffraction on shales from China and reported a TOC content of 0.7–2.58 wt% or 1.57–5.62 vol% for the same samples [61]. Therefore, although the TOC can be quite low on a weight basis, it can be quite significant when considering the volume of shale. In order to further understand the effect of shale composition on the total GIP, it is important to look at the constituents of shale that contribute to gas storage: the organic matter and clay minerals.

2.3.1.1 Organic Matter

The organic component of shale is kerogen [13], which is the most common type of organic matter found in sedimentary rocks [62]. Kerogen is not a chemical compound but is rather a class of compounds, such as proteins. It does not have a unique chemical formula and indeed, there can be many types of kerogen [63]. The four types are shown in Table 2.1.

Shales often contain Type II [54, 65] or Type III kerogen [65]. The multi-scale pore network in kerogen is crucial as the organic matter is one the key components responsible for gas storage in shale. The pore structure is derived from geological processes such as diagenesis, catagenesis and metagenesis. It

Table 2.1: Types of kerogen [64].

Kerogen type	Potential for hydrocarbon generation	Characteristics
Type I	Mostly oil, little gas (depending on thermal maturity)	Hydrogen-rich, oxygen-poor
Type II	Both oil and gas	Hydrogen-rich, carbon-poor
Type III	Dry gas	Oxygen-rich, hydrogen-poor
Type IV	No potential	Carbon-rich, hydrogen-poor

is impacted by the thermal maturity of the rock [66], which also dictates the hydrocarbon capacity of the rock [65]. Shale is generally considered to be thermally mature [54, 65]. Zhang et al. (2012) conducted CH_4 adsorption studies on shales with different types of kerogen (Type I, II and III). They found that CH_4 adsorption was directly proportional to the TOC content. Kerogen Type III showed higher adsorption capacities, followed by type II and finally type I. In addition, they observed that the higher the thermal maturity of the organic matter, the higher the adsorption capacity [67].

2.3.1.2 Clay Minerals

Clay minerals are another contributing source of gas storage in shale. The most common types that are found in shale include Kaolinite, Montmorillonite and Illite [68]. The combination of clay minerals in a particular formation depends heavily on diagenesis and the depositional environment. These minerals can have varying morphologies and pore structures [69]. Ross and Bustin (2009) reported that Fort Simpson shales have Chlorite, Illite and Kaolinite in equal fractions [58]. Han et al. (2016) stated that Kaolinite and Chlorite content varied in the same shale formation in China due to retraction in seawater during deposition [70]. Dong et al. (2017) detected Illite, some Chlorite and a mixed layer of Illite and Smectite in shales from Canada [56]. This indicates that it is difficult to predict an 'average' shale composition even to the extent of what it comprises of.

Like kerogen, clay minerals have a strong effect on storage capacity. Ross and Bustin (2009) conducted a study on pure clay mineral samples of Illite, Kaolinite, Montmorillonite and Chlorite and saw that on a dry basis, Illite and Montmorillonite have a greater adsorption capacity for CH_4 whilst on a wet basis, adsorption on Kaolinite is larger [58]. Zhang et al. (2013) conducted CH_4 adsorption experiments on clay-rich shales and found that the adsorption capacity was in the following order for the samples with these clays: Montmorillonite > Illite-Smectite mixed layer > Kaolinite > Chlorite > Illite [71]. A similar trend was observed in another study on pure clay minerals [72]. However, extrapolation of studies with pure clay minerals to shales should be done with caution as the compaction of the minerals may be different [69].

2.3.2 Pore Space

Shale has a more complex pore structure than conventional source rocks like limestones and sandstones. It has a multi-scale fabric due to the presence of clay minerals and their microstructure [73]. The fabric affects the rock permeability and porosity, factors which influence gas flow [74]. The subsequent sections examine different properties of shale and their relationship with shale composition.

2.3.2.1 Permeability

Permeability is a measure of pore interconnectivity and the ease of flow of fluids in a rock [39]. As discussed before, permeability is one of the key factors that determines recovery and extraction processes need to be designed to increase permeability in tight reservoirs such as shale. Permeability can further be broken down into fracture permeability and matrix permeability [75]. Fracture permeability dictates production early in the process; however, matrix permeability is the key to long term production [76]. Fracture permeability is created though hydraulic fracturing and matrix permeability needs be high enough such that gas can fill the fractures once extraction commences [77]. Permeability is affected by aspects such as adsorption and desorption, multiphase fluid flow, poro-elastic effects and slip flow [76]. In addition, pore volume and pore throat diameter have a strong influence on matrix permeability [56].

In shale, permeability is typically in the nanodarcies range, which is much lower than conventional sandstones. These low permeabilities can even be challenging to measure [56]. In addition, shale's permeability is often anisotropic (directionally-dependent). Higher permeabilities are measured parallel to laminations whilst lower ones are measured perpendicular to laminations [55]. Permeability anisotropy is caused due to stratigraphic layering, positioning of minerals, orientation of pores and diagenesis [78]. Dong et al. (2017) conducted permeability measurements on shales from Canada and found matrix permeabilities to be between 1.69 nD and 42.81 nD. They also stated that porosity has the strongest effect on permeability and that they have a positive correlation. TOC content also exhibited a positive correlation with permeability [56]. Chalmers et al. (2012) also looked at Canadian shales using a custom pulse-decay permeameter, which used methane as a probing gas. Matrix permeabilities were in the range 0.0007–75 nD. They did not find a correlation between mineralogy and permeability, but they found that samples with so-called 'balanced' pore volumes (equal distribution of micro-, meso- and macro-pore volumes) showed higher permeabilities [79]. Tan et al. (2017) examined fracture permeabilities in Chinese shales, including permeability in fractures that have been opened using proppant. Natural fractures had permeabilities in the order of $\sim$ 100 nD, and showed strong anisotropic behaviour. The difference between vertical and horizontal permeabilities was at least a hundred-fold. The fracture permeability with proppant was much higher (about a hundred to a

thousand times higher than the highest natural fracture permeability) under identical experimental conditions. Proppant size and the amount added also affected this increase, suggesting that hydraulic fracturing with proppant is an effective means of increasing permeability and thus, recovery [78].

2.3.2.2 Porosity

Porosity is the ratio between the void space volume and total volume of the rock, and is where the fluid can be stored [39]. It is a key parameter that affects permeability and, by extension, production and storage. In shale, porosity might exist through intergranular porosity, intragranular porosity and microcracks, in different proportions and sizes [54]. Porosity, specifically microporosity, has been known to develop within kerogen with increasing thermal maturity [55]. Liang et al. (2017) performed experiments on undeformed and deformed Chinese shales to examine the dynamic change in pore structure. Using mercury immersion and helium pycnometry, they found porosity in the range 1.3–7.5%, with the undeformed shale having the highest pore volume and porosity [80]. Zeng et al. (2016) measured porosity between 1% and 7.9% on another set of Chinese shales [81]. Clarkson et al. (2013) measured porosities for American shales using Small-Angle/Ultra-Small-Angle Neutron Scattering (SANS/USANS) and found them to be in the range 3.6–7.9% [82]. Ross and Bustin (2009) utilised mercury intrusion porosimetry to determine porosity for Canadian shales. They found that porosities were affected by clay content in the shale. In general, they ranged from 0.5% to 6%. For clay-rich shales, the average porosity was 5.6% whereas for clay-lean shales, the average porosity was 1% [58]. These results were also supported by the work of Wu et al. (2017), in which the clay-rich Chinese shales had higher porosities than the clay-lean ones, for similar TOC content. Porosity also showed a positive correlation with TOC content in this study [59]. Therefore, it is evident that although shales have low porosities (typically $<\sim 10\%$), this factor can be affected by the mineralogy of the rock.

2.3.2.3 Surface Area

Surface area of pores is an important factor as this directly determines the adsorption capacity of any porous material, such as shale [77]. Pore size and surface area are inversely correlated [55]. IUPAC (International Union of Pure and Applied Chemistry) distinguishes between pores based on the pore diameter. The three classifications are micropores (< 2 nm), mesopores (2–50 nm) and macropores (> 50 nm) [83], with the latter contributing the least to the surface area. Microporosity exists within kerogen due to thermal decomposition and increases with thermal maturity, and surface area increases with micropore volume [55]. Subcritical adsorption (further discussed in Section 2.5.1) is commonly used to measure surface areas of porous solids. Kuila and Prasad (2013) used this method to measure

specific surface areas in the range 0.98–31.57 m^2/g on shales from America, with the micropores contributing an average of 27.5% of the total specific surface area, which was stronger than the equivalent contribution on a volume basis [73]. Zeng et al. (2016) conducted a study on shales from China and found specific surface areas between 3.38 m^2/g and 33.45 m^2/g. They determined that pores that were lower than 10 nm in size (i.e. micropores and small mesopores) impacted the specific surface area the most, whilst pores > 100 nm had negligible influence. In addition, mesopores and macropores made up more than 73% of the total pore volume [81]. Furthermore, Ross and Bustin (2009) observed that microporosity (and surface area, by extension) increased with TOC content for the shales they examined, but this was not the case for organic-lean shales, where microporosity was controlled by the clay minerals. Shales with high TOC content and high clay content showed the highest surface areas and micropore volumes [58], which suggests that both TOC and clay content influence the micropore structure. The surface areas for shales are typically much lower than coals, which have been shown to be in the range 100–400 m^2/g [84, 85], indicating the former's lower adsorption capacity.

2.3.2.4 Pore Size Distribution

Pore size distribution (PSD) is extremely useful in predicting the adsorption behaviour of a porous material. A combination of techniques is used to measure the PSD, which include subcritical gas adsorption and mercury intrusion porosimetry (MIP). It is important to note that both yield different results. The former produces pore sizes relative to the pore body while the latter generates pore sizes relative to the pore throat [73]. The PSD of shales normally include a wide distribution of pore sizes, as demonstrated by various studies [77, 60]. The results from the study by Liang et al. (2017) showed that a significant fraction of the total pore volume of shales was in the range 0.3–2 nm, indicating the presence of micropores [80]. Labani et al. (2013) observed that the PSD of some Australian shales, obtained using gas adsorption, was between 1 nm and 200 nm, and, from MIP, in the range 3–375 nm [60]. As discussed before, the difference could arise due to different pore dimensions being measured by each experimental technique. For American shales, Chalmers et al. (2012) found that with decreasing pore diameter, surface area and pore volume increased, which was especially true in the micropore range [55]. Zeng et al. (2016) reported that, for the shales they studied, micropore volumes increased with TOC and that samples with high TOC content had low macropore volumes [81]. Kuila and Prasad (2013) asserted that the presence of microporosity and small mesopores increased with the dominance of Illite-Smectite-like clays in the shale [73]. Han et al. (2016) showed that the average pore size increased with increasing quartz content of the shale, while increasing clay content resulted in decreasing average pore size and increasing pore volume. The complexity of shale reservoirs arises from the fact that these distributions, pore structures and compositions might be different in other domains due to their inherent heterogeneity [70].

2.3.3 Reservoir Conditions

It is important to study the properties of shale and the behaviour of gases in shale at relevant conditions. Generally, reservoir conditions vary across shale formations. The Barnett shale in the USA has a bottom hole temperature of 79.4 °C and a bottom hole pressure of 262 bar [86]. The reservoir temperature for the Marcellus shale in the USA is between 35 °C and 51 °C, while reservoir pressure is up to 410 bar [40]. The Eagle Ford shale has a reservoir temperature range of 113–177 °C and the reservoir pressure is in the range 434–786 bar [87]. For the Haynesville shale, the reservoir temperature is higher than 149 °C and the reservoir pressure can exceed 689 bar [88]. Essentially, shale reservoirs are at very high temperatures and pressures, conditions at which both CH_4 and CO_2 are supercritical.

2.4 Shale Gas

As with the rock itself, shale gas itself can vary across different reservoirs. To adequately assess the potential of enhanced recovery in shales, it is imperative to have a good understanding of the components of shale gas, such that each constituent's behaviour can be studied. Zhang et al. (2017) sampled shale gas from six wells in the Sichuan basin in China for over three years and found that the samples contained between 90.1–99.3% CH_4, 0.3–0.8% C_2H_6, 0.01–0.03% C_3H_8, 0.02–1.38% CO_2, 0.01–7.15% N_2 and 0.017–0.125% He. Over the three years, the CH_4 fraction showed only small fluctuations [89]. Feng et al. (2016) studied fifteen shale gas samples from the same area and found CH_4 in the range of 97.11–99.45%. The total average C_2H_6 and C_3H_8 content was 0.49%, the average CO_2 content was 0.32% and N_2 was 0.81%. Average wetness was 0.49%, which means that shale gas is fairly dry [90]. Similar trends have also been observed for the Barnett and Marcellus shales, where the bulk of the shale gas is comprised of CH_4, with the residual being other hydrocarbons or CO_2 and N_2 [91]. The non-hydrocarbon fraction is usually small [92].

2.5 Gas Storage in Shale

As shale is a 'tight' rock, with low permeability and nanometric pores, fluids can experience the effects of confinement within the shale pore space. Confinement of fluid within the pores leads to altered phase behaviour and thermophysical properties as compared to the bulk state [93]. In these really small pores, the effect of the pore walls on the fluid molecules becomes important, which leads to this disparate behaviour [94], a fact which is compounded by the similarity in the molecular diameter of both CO_2 and CH_4 and the dominant shale pore sizes [95]. Examples of confinement effects include

variations in the dew point [95, 96], bubble point [97, 95, 98, 99], the two phase envelope and the critical point [97, 95, 100] of fluids in these small pores in relation to their bulk condition. An implication of this is that bulk fluid properties should not be used to predict shale gas behaviour or estimate shale gas resources. Another manifestation of confinement is the way gas is stored in shales, i.e. through adsorption.

Shale gas recovery processes can be suitably designed once the pore structure of the shale is well characterised and the gas storage mechanisms are well understood. There are three main ways in which gas is stored in shales: (1) adsorption on the organic matter and the clay minerals; (2) compression as free gas in pores and fractures; and (3) dissolution in formation fluids (oil and water) [101, 102, 103]. Figure 2.1 shows an illustration of these processes using an SEM photomicrograph [104] and a theoretical representation of the same shale for the purposes of this work.

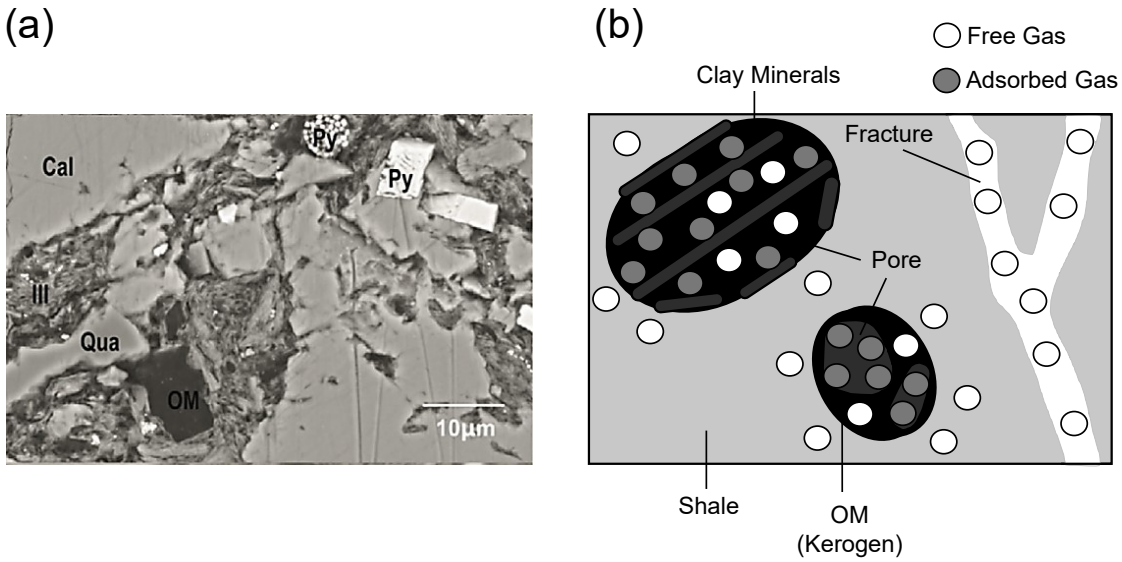

Figure 2.1: (a) SEM photomicrograph of a shale, which is composed of Calcite (Cal), Clay Minerals (Illite (Ill)), Quartz (Qua), Pyrite (Py) and Organic Matter (OM), reproduced from Ma et al. (2016) [104]; (b) Simplified representation of the same shale depicting the two main shale gas storage mechanisms.

Adsorption occurs due to the presence of nanometric pores in shale and is essentially a confinement effect. To accurately quantify the amount of gas stored in shale, the relative proportions of adsorbed, dissolved or free gas needs to be understood. It is estimated that the adsorbed gas contributes between 20% and 85% of the total Gas-in-Place in shale reservoirs [105, 106, 107, 86, 108]. Since these numbers indicate that the adsorbed gas can greatly impact both CH_4 recovery and CO_2 storage, it is crucial to understand adsorption in the context of shales extremely well.

Adsorption is the accumulation of fluid on a solid surface due to interactions between the fluid and the solid, leading to an increase in fluid density near the interface in comparison to the bulk phase [109, 110]. It can be divided into two categories: physical adsorption and chemical adsorption. Physical

adsorption entails weak intermolecular forces, while chemical adsorption results in a chemical bond between the adsorbent (solid surface) and the adsorbate (fluid). In addition, physical adsorption is reversible, fast and non-specific, whereas chemical adsorption is extremely specific, can be irreversible and slow [111]. The former is relevant to shales and will be the focus of this work. Adsorption is an exothermic process and, as a consequence, with an increase in temperature, the adsorbed amount will decrease [112, 113]. The following discussion is comprised of both low pressure and high pressure adsorption. The former is used for the textural characterisation of shales while the latter is more suitable to quantify adsorption capacities at subsurface conditions.

2.5.1 Low Pressure Adsorption

As discussed before, low pressure adsorption is routinely used to characterise porous materials and understand the adsorbent pore space. The specific details of this experimental technique will be discussed in the following chapter. During subcritical gas adsorption, a monolayer first forms on the adsorbent surface, which is followed by multi-layer formation. Capillary condensation then occurs which involves the condensation of gas to a liquid-like phase, at a pressure less than the saturation pressure [114]. This behaviour typically occurs in mesopores [115]. This occurrence is manifested in the form of adsorption hysteresis, whereby the adsorption and desorption curves do not coincide, as they represent the condensation (filling of pores) and evaporation (emptying of pores) of the fluid, respectively. By the very definition, capillary condensation is a phenomenon that occurs at subcritical conditions only.

IUPAC classifies subcritical physical adsorption isotherms into six general types [114]. Microporous adsorbents generally show Type I behaviour, where the filling of micropores relates to the finite saturation limit. Type II isotherms are seen in macroporous adsorbents, or adsorbents with a large distribution of pore sizes. The inflection point is indicative of monolayer completion and the start of the next layer of adsorbate molecules. As the pressure approaches the saturation pressure, condensation of the gas occurs and it becomes bulk liquid. Type III represents adsorbents with a wide PSD and weak attractions between the adsorbate and adsorbent. There is no clear indication of monolayer completion. Type IV isotherms are obtained with mesoporous adsorbents and Type V is characteristic of systems with strong intermolecular attraction effects [111, 110, 114]. The Type VI isotherm is for layer-by-layer adsorption on a uniform non-porous adsorbent surface [110, 114].

2.5.2 High Pressure Adsorption

2.5.2.1 Fundamentals of Supercritical Adsorption

As shale reservoirs are usually at high pressures and temperatures, it is imperative to investigate supercritical adsorption to understand the potential for enhanced shale gas recovery. At these conditions, the general type of isotherms described in the previous section are not adequate, as adsorption does not involve fluid condensation and subsequent hysteresis behaviour [116]. While in subcritical adsorption, there is a clear vapour to liquid transition, at high pressures, a defined phase transition is not present [117]. The isotherms at these conditions show a maxima and density, rather than pressure, should be used to compare adsorption [109]. Although the primary interest for the purpose of evaluating gas storage is the absolute adsorbed amount (n^{a}), experimentally it is difficult to obtain this quantity. At supercritical conditions, particularly at high pressures, the density of the bulk fluid (ρ_{b}) is not negligible compared to the absorbed phase [110]. Therefore, adsorption has to be described as an incremental quantity, implying that there has to be a well-defined reference state [117], as with any thermodynamic property [118]. Two such adsorption definitions exist:

$$\text{Excess adsorption:} \quad n^{\mathrm{ex}} = n^{\mathrm{a}} - \rho_{\mathrm{b}} V_{\mathrm{a}} \tag{2.1a}$$

$$\text{Net adsorption:} \quad n^{\mathrm{net}} = n^{\mathrm{a}} - \rho_{\mathrm{b}}(V_{\mathrm{a}} + V_{\mathrm{s}}) = n^{\mathrm{ex}} - \rho_{\mathrm{b}} V_{\mathrm{s}} \tag{2.1b}$$

Excess adsorption refers to the amount (n^{ex}) that exists within the pores in excess of that which exists in the bulk at a particular temperature and pressure. This excess amount is due to adsorption [109]. The reference state for the excess adsorbed amount is the adsorbent itself and computing n^{ex} requires knowledge of the skeletal volume of the adsorbent, V_{s}. The net adsorbed amount (n^{net}) is the difference between the amount that exists within a vessel with and without the adsorbent [118]. The reference state in this case is the empty vessel. Net adsorption provides a direct indication of the storage enhancement obtained due to adsorption, as a positive net adsorbed amount signifies that adsorption provides a benefit in terms of storage, while negative amounts suggest that more can be stored in the vessel without the adsorbent. Both the adsorbed phase and the adsorbent itself are treated as one and only knowledge of the volume of any experiment-related metal parts is required [117]. It follows that $n^{\mathrm{a}} \geq n^{\mathrm{ex}} \geq n^{\mathrm{net}}$ [119]. However, at low pressures, all three quantities are equal [118].

Conversion to the absolute amount adsorbed in both cases requires knowledge of the volume of the adsorbed phase, V_{a}, or the density of the adsorbed phase, ρ_{a}. In practice, it is quite challenging to

determine the behaviour or magnitude of these quantities as a function of pressure and requires some type of independent measurement. At sufficiently high pressures and after adsorption saturation, both excess and net isotherms should be linear, with their slopes corresponding to V_a or V_a+V_s, respectively, according to Eq. 2.1 [117]. The solid volume, V_s, is usually obtained by using a probing gas such as Helium, with the assumption that it does not adsorb and can access the same pores as the desired adsorbate. A few studies have shown that Helium adsorption might not be negligible [120, 121, 118] and that it possibly accesses more pore volume than an adsorbate with a larger molecular diameter [122]. Pini (2014) argues that adsorbates enter very small pores because they adsorb, and as Helium does not, it will be dissuaded from entering certain small micropores. This factor potentially equalises the pore volume accessed by both Helium and a given adsorbate. The best case scenario is to probe the adsorbent with a probing fluid that is inert but has the same traits as the adsorbate in terms of size [117], but finding such a fluid is extremely challenging.

2.5.2.2 High Pressure Adsorption in Shales

Adsorption capacity in shale is influenced by a variety of factors: kerogen type and maturity, pore structure, pore volume, composition, moisture content and pressure and temperature [103]. Most of these factors have been discussed previously and the focus of the remainder of this section is to summarise the available experimental supercritical adsorption data on shale. Adsorption measurements on shales can be quite challenging due to the fact that they adsorb very little (about 10% of coal's adsorption capacity and about 1% of activated carbon's). This inherently requires experimental measurements to be highly accurate such that the measured adsorption data are useful. It is also difficult to replicate reservoir conditions (i.e. high temperatures and pressures) in the laboratory [123], which means that there is not a lot of shale adsorption data at relevant conditions in the literature. Figure 2.2 shows a compilation of some of the available CO_2 and CH_4 shale adsorption isotherms from various research publications. The measurements are for assorted shales, with varying TOC content, and at different temperatures.

The figure shows that there is a significant amount of variation in the measured excess adsorbed amounts, across studies, particularly for CO_2. The discrepancies exist in terms of capacity but also isotherm shape. There appears to be also very little data above ~ 150 bar for both adsorbates and at high temperatures for CO_2. Reliable adsorption data at reservoir conditions are absolutely essential for evaluating the potential of ESGR adequately. The differences in the isotherms clearly arise from variations in temperature and shale mineralogy but could also depend on experimental techniques or the method used for obtaining the solid volume. For supercritical adsorption, errors in measuring the latter can have huge implications on the measured excess amounts. The lack of reporting of

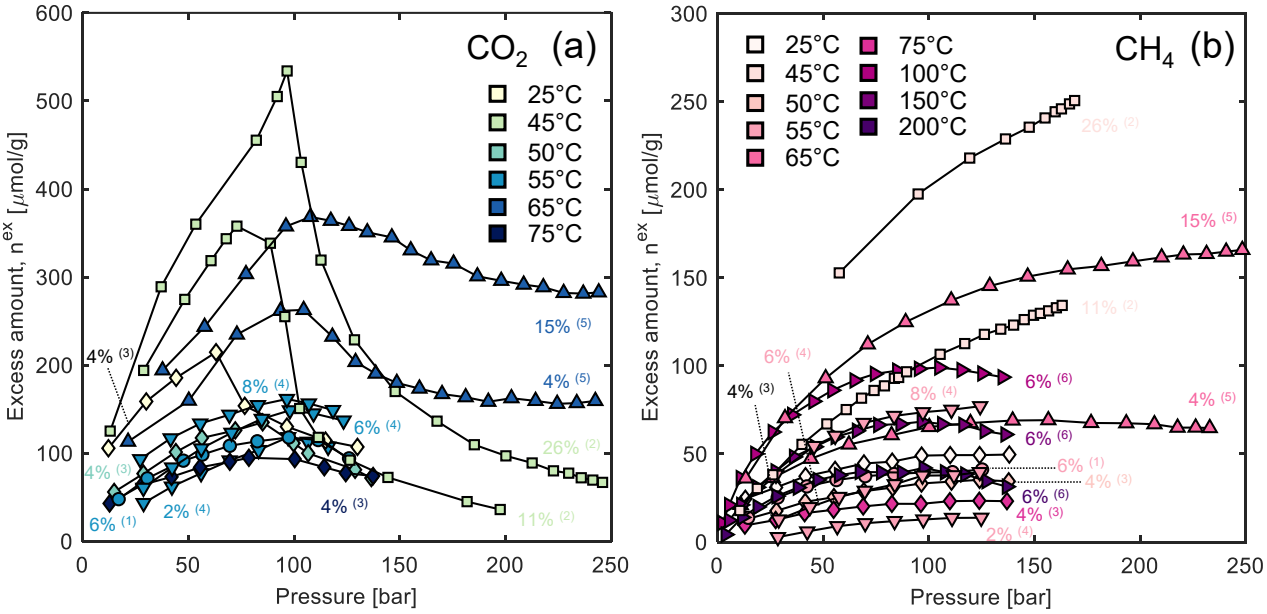

Figure 2.2: (a) CO_2 and (b) CH_4 experimental excess adsorption isotherms from the literature for various shales, with varying TOC content (shown in wt% next to the isotherm), and at different temperatures. Isotherms with the same symbols indicate the same origin of the isotherm (indicated next to the isotherm) and the corresponding references are as follows: (1) Chareonsuppanimit et al. (2012), (2) Weniger et al. (2010), (3) Merey and Sinayuc (2016), (4) Charoensuppanimit et al. (2016), (5) Gasparik et al. (2014), (6) Rexer et al. (2013).

experimental uncertainties by studies also complicates the understanding of the reliability of the measured data. However, researchers in this field have revealed a few insights into adsorption in shales. Chareonsuppanimit et al. (2012) used the volumetric method to measure isotherms on the New Albany Shale and concluded that shale adsorption was as much as 10–30 times lower than that of coal. However, the ratio of CO_2 to CH_4 adsorption was much higher than in coal, a factor which is extremely useful for ESGR [124]. Gasparik et al. (2014) conducted an inter-laboratory study based on two shales from Belgium and Germany and stressed that because of the low sorption capacity of the shales, the measurements have to be quite precise [123]. Weniger et al. (2010) observed that the maximum adsorption capacities increased with the TOC content, but when extrapolated to 0% TOC, the results showed a non-zero intercept for CO_2, suggesting that the other minerals in the rock adsorb as well. CH_4 did not show this behaviour. The CO_2/CH_4 adsorption capacity ratio was in the range 1.4–4.5 [125]. Slightly higher ratios (4–6:1) were measured by Merey and Sinayuc (2016) [27] and Charoensuppanimit et al. (2016) (2.1–8.6), who also observed a positive linear correlation between TOC and adsorption capacity [26]. Rexer et al. (2013) studied a shale from Denmark and obtained a negative linear correlation between the maximum CH_4 excess amount adsorbed and experimental temperature [108].

The effect of moisture content on shale adsorption is relatively less examined. In coal, a decrease in adsorption with increasing moisture content has been observed, until a critical level after which,

adsorption is constant. In shale, it is thought that moisture will act as a gas diluent and hence will result in lower adsorption [103]. Ross and Bustin (2009) demonstrated this on for a few organic-rich shales, in which the moisture-equilibrated shale adsorption capacity was between 50–70% lower than that for the dry shale samples [58]. It has been shown that moisture in shales significantly impacts adsorption capacities in the clay minerals, in particular, due to pore blocking, the occupation of adsorption sites by water, and/or competitive adsorption [58, 69]. Although, the evaluation of the effect of water on shale adsorption is out of the scope of this thesis, it is worth considering this factor in the future.

2.5.2.3 Modelling Supercritical Adsorption

Modelling the adsorption behaviour in shales is an extremely important step towards bridging the gap between the laboratory and the field. Consistency between experimental adsorption measurements at representative conditions and theoretical adsorption models is key to the design and optimisation of adsorption-based processes [126, 127]. However, modelling supercritical adsorption is challenging, as knowledge of the adsorbent's pore space (e.g. PSD) is often required as well as the accurate description of the behaviour of confined fluids [128, 129, 130]. This becomes particularly important for adsorbents that contain large amounts of mesoporosity. However, the use of supercritical data to model adsorption processes is partly hampered by the lack of an unambiguous definition of the volume of the adsorbed phase in mesoporous materials [119], such as shale. This section provides a brief overview of common modelling approaches deployed in the literature for the purpose of describing supercritical adsorption of CO_2 and CH_4 in various adsorbents. Table 2.2 summarises some of these models.

Table 2.2: Models most commonly used to describe supercritical adsorption of CO_2 and CH_4 in the literature.

Model	**Adsorbent**	**Sources**
Langmuir/ Dual-site Langmuir (or similar)	Carbons, Coal, Shale	[131], [132], [133], [134], [135], [136]
BET (or similar)	Shale	[137], [138]
Toth (or similar)	Carbons, Coal	[132], [139]
Pore filling (D-A/ D-R)	Coal, Shale	[140], [141], [142], [143]
Simplified Local Density (SLD)	Carbons, Coal, Shale	[144], [145], [124], [146]
Lattice Density Functional Theory (Lattice DFT)	Carbons, Coal, Shale	[147], [148], [149], [150], [151]
Molecular Simulations	Carbons, Clay Minerals, Kerogen, Shale	[152], [153], [154], [155], [156], [157], [158]

The models utilised for supercritical adsorption vary in their complexity. By far the most commonly used models, particularly for CH_4 adsorption, are simple or empirical models such as Langmuir or BET

type models. Although these models provide benefits in terms of application due to their inherent simplicity, they have been derived based on subcritical adsorption and their extension to high pressures often means that most of their underlying assumptions have to be ignored or that some parameters, such as the saturation pressure in the BET model, lose their physical meaning. As a consequence of their simplicity, they are also often unable to capture the more complex adsorption behaviour of fluids like CO_2 in mesoporous and heterogeneous materials such as shales [159]. In addition, a usual prerequisite to the deployment of these type of models for the description of supercritical adsorption data, is the magnitude and the behaviour of either the volume or the density of the adsorbed phase. In the absence of such information, an assumption usually has to be made [159, 160].

Pore filling models such as Dubinin-Astakhov (D-A) or Dubinin-Radushkevich (D-R) models are based on the Polanyi adsorption potential theory and are usually more suited for microporous adsorbents where micropore filling occurs, rather than mesoporous solids such as shale. Challenges with applying these types of models to supercritical adsorption data have previously been highlighted [160], yet these models are routinely used to describe CH_4 adsorption at elevated pressures in coals and shales.

More complex models such as the Simplified Local Density (SLD) model are more suited for supercritical adsorption as they incorporate adsorbate-adsorbate and adsorbent-adsorbate interactions but this model seems to be limited to slit pores and requires the use of an equation of state. Molecular simulations, such as Grand Canonical Monte Carlo (GCMC) simulations, provide great insight into the adsorption process on a molecular level [161] but are computationally expensive. The Lattice Density Functional Theory (lattice DFT) model incorporates the pore size distribution of the adsorbent to model the adsorption behaviour on a pore-by-pore basis. Although the model possesses reasonable complexity as it can be extended to other pore geometries and comprises of both fluid-fluid and fluid-surface interactions [162], it is still able to benefit from a relatively fast computational speed. As Table 2.2 shows, the lattice DFT model has been applied to a wide range of adsorbents but its application to shale is still in its infancy.

2.5.3 Mesoporous Adsorbents

A particular focus of this thesis is the effect of mesoporosity on supercritical adsorption. To this end, synthetic porous carbons (both micro- and meso-porous) will also be investigated as part of this work. These are also relevant in the context of shales as one of the main adsorbing components within these rocks is carbon-based. This section focuses on both porous carbons and mesoporosity.

Supercritical adsorption in porous carbon materials is integral to several industrial processes. The adsorptive characteristics that qualify the porous carbon material for its intended application depend largely on its textural properties. Activated carbons (AC) draw their versatility from a broad pore-size

distribution, including large amounts of micro-, meso- and macro-porosity [111]. At one end of this spectrum are natural carbonaceous materials (i.e. coal and organic-rich shale), where the environmental 'activation' process has resulted into an even larger variation of pore sizes, from subnano- to micro-metres [163]. At the other end of the spectrum are synthetic porous carbons with an ordered pore structure. These include (i) carbon molecular sieves (CMS), which can be produced with a very narrow distribution of micropores that enables exploiting them for kinetic separations [164], and (ii) mesoporous carbons (MC) that possess a highly-uniform periodic mesoporous structure with well-defined cylindrical pores [165]. Because they can be considered as the building blocks of more complex porous structures, ordered carbons are important reference materials for the textural characterisation of industrial adsorbents by physisorption [166] and for the development of advanced models that describe the phase behaviour of fluids in pores [167]. In this context, a major distinction between micro- and meso-pores is that adsorption in the former is mainly a process of pore-filling [168] and the adsorbed phase volume coincides with the pore volume. On the other hand, a mesopore can accommodate both the adsorbed and bulk phase simultaneously and its diameter is at the length-scale at which condensation transitions under confinement can occur. This gives rise to known features, such as the appearance of subcritical hysteresis loops [167], and affects the criticality of fluids in the pores [169].

Modern methods of Density Functional Theory (DFT) and Monte Carlo simulations are available to obtain accurate pore size distributions of carbonaceous adsorbents over the entire micro- and meso-pore range [127, 170]. To minimize computing demand, the deployment of these numerical approaches is generally limited to pores of simplified geometry (e.g. slits) [130]; an adsorption isotherm is then constructed using the weighted linear combination of isotherms computed for pore classes of varying widths. Such analysis is largely based on the subcritical physisorption of N_2 and/or Ar at their standard boiling point (77 K and 87 K, respectively), because at these conditions the condensation pressure is an explicit function of the pore size. However, there are compelling arguments in favour of extending textural analysis with additional gases and/or thermodynamic conditions, including (i) kinetic restrictions that are inherently present in micropores at cryogenic temperatures [114], (ii) the need to mimic the conditions of the specific industrial application [171], and (iii) the validation of the obtained pore-structural information over a range of conditions, from sub- to super-critical adsorption [128, 172, 130]. As a matter of fact, a more robust approach to PSD analysis could be obtained by a combination of sub- and super-critical adsorption data [173], as the latter also show pore size dependent adsorption behaviour [168, 162, 174]. However, attempts of using measurements at supercritical conditions for the characterisation of porous carbons have been limited to systems that are predominantly microporous [171, 172, 175, 129, 176] and have been so-far only partly successful. We attribute this last observation to (i) the almost exclusive use of slit pores in theoretical adsorption models, and (ii) the lack of supercritical adsorption measurements over the range of conditions required

to characterise the distribution of both micro- *and* meso-pores.

Supercritical adsorption has been studied experimentally, but data on industrially important materials that contain significant levels of mesoporosity remain scattered. Experimental adsorption isotherms on carbon surfaces are largely limited to (micro)porous activated carbons [177, 178, 179, 180, 181, 174, 182, 183], the only exception being the seminal work by Specovious and Findenegg (1980) on graphitised carbon black [168]. Most of the work on ordered mesoporous solids has focused on silicas, including Controlled Pore Glass (CPG) [169, 116], SBA-15 [184, 185], MCM-41 [183] and aerogels [186]. These studies have revealed that supercritical adsorption produces characteristic confinement effects related to the formation of a thick adsorbed layer in mesopores - up to two to five molecular diameters of the adsorbate [168, 174]. The effect can be sustained up to about 10 K above the critical temperature of the adsorbate (T_c) [168] and its strength depends largely on the pore-wall curvature [169, 116]. A practical implication is that the measured excess adsorption isotherms do not exhibit the same features observed on microporous adsorbents, namely an early maximum followed by a linear fall with increasing bulk density [117]. Rather, the maximum of the excess adsorbed amount isotherm is shifted toward higher densities (above 5 mol/L), its value increases markedly with decreasing temperature and the descending part of the isotherm is far from being linear [168]. These attributes suggest that textural properties of the adsorbents can, in principle, be inferred from a supercritical adsorption isotherm. Most importantly, they also indicate that in this endeavour, theoretical approaches are needed where adsorbate-adsorbent *and* adsorbate-adsorbate interactions are explicitly accounted for [169, 162], as opposed to the use of simplified macroscopic adsorption models that are commonly applied to describe supercritical adsorption isotherms [187].

2.6 Gas Transport in Shale

Although the focus of this thesis is on gas adsorption in shales, it is important to have a contextual understanding of the transport mechanisms underpinning gas recovery and storage in these formations. The adsorption process will be limited by how much gas can diffuse into or out of the organic material or clay minerals [188]. Flow in shale reservoirs can be considered a mixture of both Knudsen diffusion and viscous flow, with studies showing that the latter dominates at higher pressures (> 10 bar) [189]. Using the manometric method, Yuan et al. (2014) measured adsorption of CH_4 on shale under equilibrium and kinetic conditions. They concluded that in pores > 5 nm, diffusion was fast (diffusivities of the order $\sim 10^{-9}$ m^2/s) and classified as Fickian (viscous) diffusion, dominated by molecular collisions, and for pores smaller than 5 nm, diffusion was considered slow (diffusivities of the order $\sim 10^{-14}$ m^2/s) and categorised as Knudsen diffusion, dominated by molecule-wall collisions [190]. Other experimental studies have determined even lower diffusivities of CH_4 in shale ($\sim 10^{-20}$ m^2/s) [191, 192], and observed

that these values were up to eight orders of magnitude lower than that for coal [192]. It is evident that improving gas transport in shales is probably crucial to the successful deployment of ESGR. The purpose of this section was to give only a small overview of the gas transport mechanisms in shale. Much more can be said about this challenging topic, and it definitely needs to be explored more.

2.7 Conclusion

Shales are very heterogeneous with complicated mineralogy and pore structure that shows considerable variation across shale plays. Hydraulic fracturing and horizontal drilling have allowed access to shale gas that is trapped within the nanometre-sized pores in the rock but extraction efficiencies can be improved by the injection of CO_2 to enhance the recovery of natural gas and for permanent CO_2 sequestration. The design of such a process mandates a better understanding of the gas storage mechanisms in shales, specifically adsorption, at reservoir conditions. Although there has been some research in this area, more focus needs to be on producing reliable shale adsorption data at elevated pressures and temperatures for both CH_4 and CO_2, such that storage capacities can be accurately quantified. Furthermore, suitable models need to be developed and adopted for the description of this data such that they can be integrated with reservoir models, which themselves also need to account for the adsorbed phase and its significant occupation of the available porosity within the shale.

Chapter 3

Materials and Methods

In this chapter, details of the materials studied and the experimental methodology deployed as part of this thesis are explained. There are two classes of materials examined in this work: synthetic materials and shales. The rationale behind their selection and the background of each shale is described. For the experimental methods, the working principles behind the two main techniques used in this study are outlined. Experimental protocols and data analysis are also fully described. Some of the material in this chapter has been published in Ansari et al. (2020, 2021) [29, 193].

3.1 Materials

As shales are very heterogeneous, interpretation of supercritical adsorption on these materials is not straightforward. To assist in this, three analogue materials were also selected as part of this study. These materials are synthetic and were chosen to represent key elements of the chemical composition of shale or its pore size distribution. The results can aid in the understanding of adsorption in shale. Each analogue material and shale are discussed further in this section.

3.1.1 Synthetic Adsorbents

The adsorption of supercritical gases on porous carbon materials is relevant to many industrial processes. Activated carbons continue to be widely employed for high-pressure gas separations [194] and gas storage applications by adsorption technology [195, 196]. Porous carbonaceous structures are also found in natural environments, where they form the organic matter of sedimentary rocks, such as shale and coal seams [163]. However, the prediction of supercritical adsorption on porous carbons remains a challenging task, requiring knowledge (and use) of the adsorbent's textural parameters (e.g.

geometry and size of the pores), in addition to the accurate description of the physical behaviour of gases under confinement [128, 129, 130]. To address this, we studied two porous carbons in this work as they incorporate different dominant pore sizes: (i) graphitised mesoporous carbon (MC, powder, $45 \pm 5\,\mu m$ particle size, $10 \pm 1\,nm$ average pore diameter), and (ii) microporous Activated Charcoal Norit (AC, RB3, 3 mm rods). These were purchased from Sigma-Aldrich and used as provided.

Synthetic mesoporous adsorbents in general are of considerable interest due to their widespread applications such as catalysis and electrochemical energy storage. They possess a tunable porosity, high specific surface area and a large total pore volume [197]. Mesoporosity can improve the adsorbent's performance at high pressures, in terms of both capacity and selectivity [198]. The use of a mesoporous material also overcomes the diffusional limitations typically associated with microporous materials. This is particularly true for zeolites, which has led to the development of novel hierarchical zeolites, which incorporate both micro- and meso-porosity [199]. To this end, the other major class of materials studied in this work are mesoporous zeolites (MZ, powder). This is a non-commercial hierarchical ZSM-5 zeolite with both micro- (~ 0.54 nm) and meso-pores (~ 15 nm). This material was provided by Mariya Shamzhy from the Czech Academy of Sciences, J. Heyrovský Institute of Physical Chemistry, Czech Republic, and was used as provided. Since it contains a wide distribution of pore sizes, MZ is fairly analogous to shales, and is therefore crucial in understanding the impact of this factor on supercritical adsorption in shales.

The synthetic adsorbents, therefore, represent a wide spectrum of pore sizes, and by extensions, adsorption behaviour. MC is purely mesoporous, AC is mostly microporous and MZ includes both micro- and meso-porosity.

3.1.2 Shales

Three main shale plays were considered in this study: the (i) Bowland shale (UK), (ii) Longmaxi shale (China), and (iii) Marcellus shale (USA). These shales were selected due to their importance in the wider shale gas industry and the fact that there is considerable geological information already known about these plays. The Marcellus shale is the largest shale play in the USA [40] and has about 135 trillion cubic feet of proved reserves [200], while the Longmaxi shale in the Sichuan Basin is one of the key targets in China [201]. In particular, the Fuling area is the largest shale gas producing play in China currently [202]. In the UK, although shale gas exploration is in its infancy, the Bowland shale is considered a prime target for production [203]. The samples used in this study come from the Preese Hall-1 well in the lower Bowland shale formation, a well in the post-mature part of the Marcellus shale in the north east of Pennsylvania, and sections WX-1, WX-5 (in the same well) and WX-7 (in another well) in the Jiaoshiba area (Fuling gas field) and Dingshan area (west of Fuling),

respectively [204, 205, 206].

The complete characterisation of all shale samples considered in this study can be found elsewhere [204, 205, 206] and their composition is shown in Table 3.1. This was obtained using a combination of X-Ray Diffraction (XRD) and other analytical techniques described in the literature where the same samples were used [204, 205, 206]. The shales are composed a variety of clay minerals and have varying degrees of organic content. Table 3.1 also shows two sets of compositions for certain Bowland shales (B2, B6, B8 and B13). The first set (white cells) comes from published work [204] and the second set (grey cells) comes from a repeated set of measurements at University College London (UK), which are currently unpublished. Two discrepancies between these measurements are worth highlighting: (i) the TOC of B6 is much lower, and (ii) the proportion and variety of clay minerals has significantly increased with the second set of measurements. The difference could be the result of shale heterogeneity (i.e. different samples were used), or in the method of analysis. Shale mineralogy is often used in drawing conclusions about the shale play in general but it is often associated with a significant degree of uncertainty in relation to how representative it is of the reservoir. In this work, the composition of shales will be used to aid the understanding of supercritical adsorption in shales but we will assume that there is some flexibility in the composition. The shales also have varying degree of thermal maturity; the Marcellus and Bowland shales have a maximum vitrinite reflectance higher than 4.0% [205] and 1.1% [203], respectively, and the Longmaxi shale samples have an equivalent vitrinite reflectance (as they are vitrinite-free) of 3.3–4.6% [206]. This is also reflected in their visual appearance, whereby the Bowland shales are light grey in colour, while the others are dark grey or almost black.

All of the shales shown in Table 3.1 were considered for low pressure adsorption (Section 3.2.1) but only a few were taken forward for the high pressure adsorption experiments (Section 3.2.2). From the Bowland formation, B6 (organic-rich) and B8 (clay-rich) were the only samples considered as they are polar opposites in composition. For the Longmaxi shale, LG4 was chosen as it also organic-rich and the Marcellus shale (ML) was the final shale studied in the high pressure system. All shale samples were prepared for the study by crushing and sieving to below 100 µm particle size. High pressure experiments with the Marcellus and Longmaxi shales were also conducted on pre-crushed samples, with shale pieces of roughly a few centimetre in size.

3.1.3 Gases

The gases used in this study were procured from BOC, namely CO_2, Ar and He at purities of 99.999% and N_2 at a purity of 99.9992%; for the supercritical adsorption experiments, CO_2 and CH_4 were purchased at a purity of 99.995% and 99.5%, respectively. The critical properties of the

Table 3.1: The mineralogy of all shales in wt%. The references are as follows: Bowland shales - Fauchille et al. (2017) [204] (white cells) and University College London (unpublished, grey cells), Longmaxi shales - Delle Piane et al. (2021) [206], and Marcellus shale - Delle Piane et al. (2018) [205].

	Bowland shale						Longmaxi shale			Marcellus shale
Component	**B1**	**B2**	**B5**	**B6**	**B8**	**B13**	**LG3**	**LG4**	**LG5**	**ML**
Kaolinite	0.0	5.0	6.0	7.0	18.0	5.0	–	–	–	–
		3.3		1.1	2.3	2.1				
Illite/Mica	–	–	–	–	–	–	46.0	18.0	29.0	45.0
		12.2		17.2	19.3	28.8				
Illite/Smectite Mixed Layer	–	–	–	–	–	–	–	–	–	–
		5.0		5.1	Trace	1.5				
Smectite	–	–	–	–	–	–	–	–	–	–
		0.0		0.0	4.0	0.0				
Chlorite	–	–	–	–	–	–	13.0	3.0	8.0	2.0
		–		–	–	–				
Total Clays	0.0	5.0	6.0	7.0	18.0	5.0	59.0	21.0	37.0	47.0
		20.5		23.4	25.5	32.3				
Quartz	58.0	53.0	56.0	71.0	52.0	73.0	31.0	60.0	42.0	29.0
		29.4		46.1	50.2	39.8				
Calcite	15.0	17.0	12.0	6.0	3.0	6.0	0.0	1.0	5.0	6.0
		33.8		7.2	8.6	5.3				
Dolomite/Ankerite	13.0	1.0	6.0	2.0	11.0	0.0	0.0	2.0	2.0	–
		–		Trace	8.6	Trace				
Siderite	–	–	–	–	–	–	–	–	–	–
		0.0		0.0	0.0	3.0				
Marcasite	–	–	–	–	–	–	–	–	–	–
		2.1		0.9	0.6	1.3				
Pyrite	2.0	8.0	6.0	1.0	2.0	1.0	2.0	3.0	3.0	7.0
		10.0		8.4	2.2	9.6				
Muscovite	9.0	5.0	10.0	10.0	5.0	11.0	–	–	–	–
		–		–	–	–				
Albite	3.0	5.0	4.0	3.0	9.0	4.0	8.0	10.0	10.0	11.0
		Trace		Trace	1.2	Trace				
Orthoclase	–	–	–	–	–	–	0.0	3.0	1.0	–
		Trace		1.2	2.1	2.2				
Gypsum	–	–	–	-	–	–	–	–	–	–
		0.0		8.6	0.0	0.0				
Anatase	–	–	–	–	–	–	–	–	–	–
		0.0		0.6	0.0	0.9				
TOC	1.4	4.1	3.2	6.1	1.1	5.6	0.6	7.8	3.1	6.1
		4.2		3.6	0.9	5.4				

pure adsorbates are as follows: $T_c(CO_2)$ = 304.1 K, $P_c(CO_2)$ = 7.37 MPa, $\rho_c(CO_2)$ = 10.62 mol/L [207]; $T_c(CH_4)$ = 190.6 K, $P_c(CH_4)$ = 4.60 MPa, $\rho_c(CH_4)$ = 10.14 mol/L [208].

3.2 Experimental Methods

The two main experimental techniques used in this thesis are low pressure and high pressure adsorption. Low pressure adsorption was conducted for the purpose of characterising all materials in this study and high pressure adsorption was performed to determine adsorption at representative conditions. These methods are discussed in more detail below.

3.2.1 Low Pressure Adsorption

Subcritical adsorption is a common experimental technique used to characterise materials [55]. In this method, the material is exposed to increasing increments of adsorbate pressure up to the saturation pressure, after which, the pressure is incrementally reduced [73]. The amount adsorbed at a certain relative pressure will be influenced by the pore structure [209]. Based on the adsorption isotherms (amount adsorbed vs. relative pressure) and any hysteresis, various analysis techniques can be used to gauge the surface area, pore size distribution, and total pore volume [83].

In this work, low pressure adsorption was primarily measured on the Quantachrome Autosorb iQ (Figure 3.1), in the pressure range 1×10^{-7}–0.1 MPa. The adsorbates used for material characterisation were N_2 (77 K), Ar (87 K) and CO_2 (273 K). For the purpose of quantifying Henry constants and extending the temperature range covered in the high pressure measurements, additional measurements with CO_2 at various temperatures were also conducted. The CryoSync module was used to achieve cryogenic temperatures above 77 K and the CO_2 experiments were conducted using a liquid circulating thermostat (Julabo CORIO CD-200F), which maintained the temperature of a bath containing a mixture of water and ethylene glycol (50 vol%).

These measurements rely on measuring the change in pressure within the measuring cell. A known amount of gas is admitted into the cell, and upon adsorption, the pressure decreases until equilibrium is reached. The amount adsorbed at this equilibrium pressure is related to the difference between the initial amount of gas admitted and the amount of gas required to fill the dead volume of the cell (determined by a calibration experiment with pure Helium prior to the adsorption experiments). With successive dosing (adsorption branch) or removal (desorption branch) of gas volumes, a full adsorption isotherm is constructed [114].

The operating procedure for each experiment was as follows:

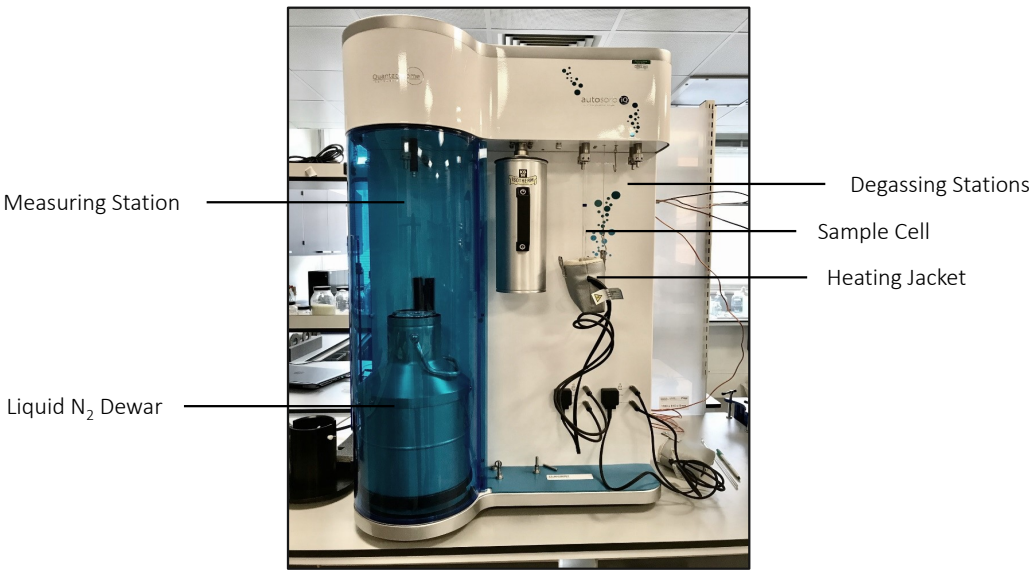

Figure 3.1: The Quantachrome Autosorb iQ used for the low pressure adsorption measurements.

1. Measure the mass of a clean and empty sample cell,
2. Measure the mass of the same sample cell with the sample added,
3. Load the cell in the equipment's external degassing station and specify the degassing protocol (the duration of vacuum and heating at specific temperatures), which is dependent on the material,
4. Once degassing is complete, backfill the cell with N_2 and weigh the sample cell again to obtain the degassed mass of the sample,
5. Load the cell in the measuring station and start the measurement. A measurement with Helium is first conducted to estimate the void volume of the measuring cell, followed by the measurement with the selected adsorbate in both adsorption and desorption mode.

A small subset of low pressure adsorption measurements were also conducted on a similar apparatus, the Micromeritics 3Flex Surface Characterisation Analyzer, which follows a very similar experimental protocol as above, with the addition of in-situ degassing for 3 hours prior to the measurement. The details of all experiments are given in Table 3.2.

The experimental data were interpreted upon application of various models such as the Density Functional Theory (DFT) and Grand Canonical Monte Carlo (GCMC) simulations, available within the instrument software, to obtain the pore size distribution, specific surface area and total pore volume of the adsorbents. The model was selected based on the adsorbate, the surface type (carbon or silica), and the lowest fitting error. These models pose a considerable advantage over classical models; they account for the pore size and shape and consider the adsorbed phase on a molecular

Table 3.2: Details of the low pressure adsorption experiments. [a]Sample regeneration involved the application of vacuum and the specified regeneration protocol.

Material	Instrument	Adsorbate	Mass	Regeneration protocol[a]
MC	Autosorb	CO_2 Ar, N_2	1.05 g 0.15 g	25 °C (10 min), 60 °C (1 h), 90 °C (1 h), 120 °C (16 h)
AC	Autosorb	CO_2 Ar	1.71 g 0.06 g	25 °C (10 min), 60 °C (1 h), 90 °C (1 h), 120 °C (16 h)
MZ	Autosorb	CO_2 Ar, N_2	0.28 g 0.06 g	25 °C (10 min), 100 °C (1 h), 200 °C (1 h), 300 °C (16 h)
B1	3Flex	CO_2 N_2	1.15 g 1.09 g	Ex-situ 120 °C (12 h) + in-situ 120 °C (3 h)
B2	3Flex	CO_2 N_2	1.18 g 1.18 g	Ex-situ 120 °C (12 h) + in-situ 120 °C (3 h)
B5	3Flex	CO_2 N_2	1.09 g 1.10 g	Ex-situ 120 °C (12 h) + in-situ 120 °C (3 h)
B6	Autosorb	Ar CO_2 N_2	0.55 g 1.00 g 1.63 g	25 °C (10 min), 60 °C (1 h), 90 °C (1 h), 120 °C (16 h)
B8	Autosorb	Ar CO_2 N_2	0.62 g 1.42 g 1.23 g	25 °C (10 min), 60 °C (1 h), 90 °C (1 h), 120 °C (16 h)
B13	Autosorb	CO_2 N_2	1.06 g 1.06 g	25 °C (10 min), 60 °C (1 h), 90 °C (1 h), 120 °C (16 h)
LG3	Autosorb	Ar	0.20 g	25 °C (10 min), 60 °C (1 h), 90 °C (1 h), 120 °C (16 h)
LG4	Autosorb	N_2, CO_2 Ar	1.04 g 0.22 g	25 °C (10 min), 60 °C (1 h), 90 °C (1 h), 120 °C (16 h)
LG5	Autosorb	Ar	0.22 g	25 °C (10 min), 60 °C (1 h), 90 °C (1 h), 120 °C (16 h)
ML	Autosorb	N_2, CO_2 Ar	1.03 g 0.18 g	25 °C (10 min), 60 °C (1 h), 90 °C (1 h), 120 °C (16 h)

level [210, 114, 211]. These models have been widely used to interpret data for carbons [212, 213], zeolites [214], and silicas [215]. The models considered in this work are the non local DFT (NLDFT), quenched solid DFT (QSDFT), which additionally accounts for surface heterogeneity and roughness [211], and GCMC simulations.

3.2.2 High Pressure Adsorption

CO_2 and CH_4 adsorption isotherms were measured gravimetrically at various temperatures using a Rubotherm Magnetic Suspension Balance (MSB) in the pressure range 0–300 bar. The MSB provides high-resolution (10 µg) weight measurements from which both the excess adsorbed amount and the bulk density of the adsorbate are extracted [216]. Figure 3.2 shows a schematic of the experimental setup that includes the MSB in addition to various ancillary components, namely (i) the control unit that also houses two pressure transmitters (Model 33X by Keller UK Ltd.) for moderate (< 35 bar) and high pressure measurements (< 700 bar) both at 0.01% full-scale accuracy, (ii) one liquid thermostat (Model 25F by Julabo GmbH) that controls the temperature in the measuring chamber (± 0.01°C), (iii) one syringe-pump (Teledyne ISCO) to achieve and maintain a constant pressure in the measuring chamber beyond cylinder pressure, (iv) a single-stage gas booster (Maximator DLE-75-1) using dry air as an input, and (iv) a rotary vane vacuum pump (Model RZ 2.5, Vacuubrand) for taking measurements below atmospheric pressure and for regenerating the adsorbent. The components of the experimental system are connected with stainless steel tubing and hand valves (SITEC, Sieber Engineering AG). Figure 3.3 shows an external and internal view of the MSB. There were two sample baskets used during the course of this study: (i) the original basket supplied by Rubotherm, and (ii) a new basket made with a lid covered with fine mesh to prevent sample elutriation during the course of the experiments.

The MSB essentially provides weight measurements. It has the capability of separating the microbalance, which provides mass measurements, and the measuring atmosphere using a suspension magnet. This consists of a permanent magnet, a sensor core and decoupling device [217]. The sample to be weighed is connected to the suspension magnet while the microbalance itself is connected to an electromagnet outside the measuring cell [216]. The electromagnet maintains a freely suspended state of the suspension magnet using an electric control unit [217]. A vertical position is maintained in the cell and the mass is transmitted from the measuring cell to the microbalance [218]. This allows the weight measurements to remain uninfluenced by the measuring environment [217].

The MSB provides three distinct weights: (i) Zero Point (ZP), where only the permanent magnet is in a freely suspended state. This point is used for taring and calibration, (ii) Measuring Point 1 (MP_1), where only the sample basket with the adsorbent is lifted, and (iii) Measuring Point 2 (MP_2), where both the sample basket and a titanium sinker (of known mass and volume) are lifted [217].

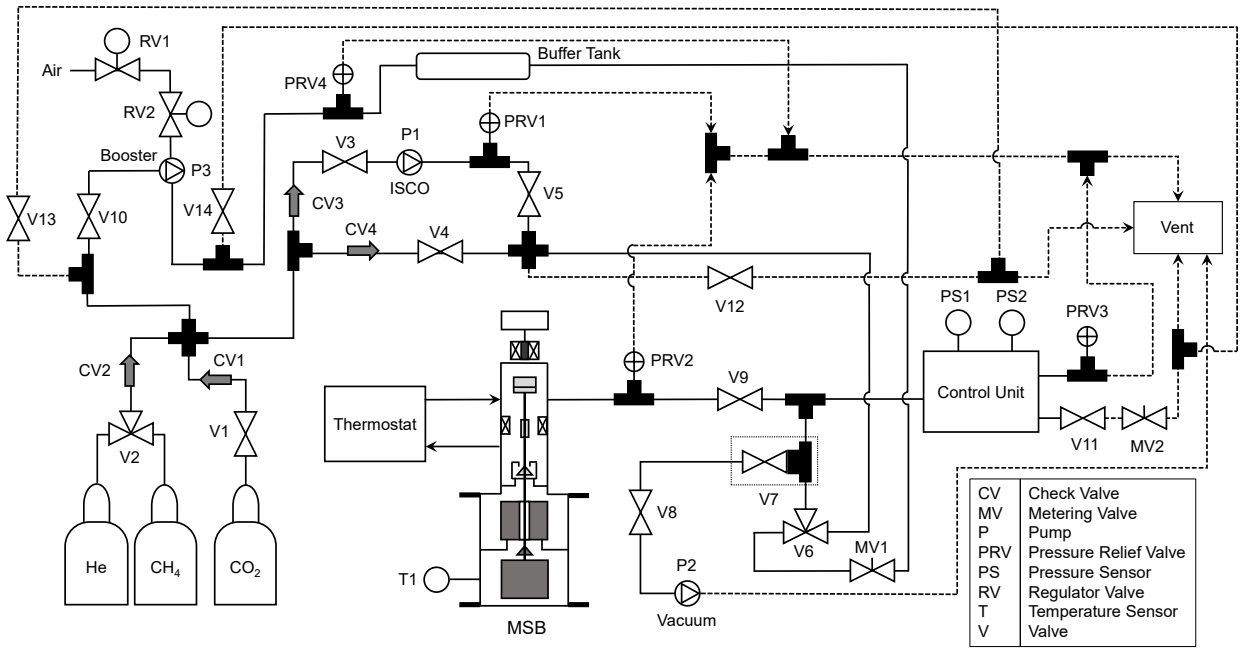

Figure 3.2: The schematic of the experimental setup used to measure high pressure adsorption with CO_2 and CH_4 in a Rubotherm Magnetic Suspension Balance (MSB).

At each pressure point, the MSB software automatically cycles between the Zero Point and the two measuring points MP_1 and MP_2, with a settling time of at least 30 s, 1.5 min and 30 s, respectively. All measurements are logged and, for each pressure and temperature combination, the average of the last five readings was taken as the equilibrium point.

The operating procedure of the high pressure adsorption measurements was as follows:

1. Perform a measurement with an empty basket (adsorbent mass (m_s) = 0) and CO_2 at various pressures (so as to cover a wider range of densities as compared to the same experiment with Helium) and a fixed temperature (60 °C) to obtain $MP_{1,empty}$. The following equation can then be used to estimate the mass (m_{met}) and volume of the lifted metals parts (V_{met}):

$$MP_{1,empty}(\rho_b, T) = m_{met} - \rho_b V_{met} \tag{3.1}$$

   where ρ_b is the density of the bulk fluid obtained by combining weight measurements in the two measuring positions (using a calibrated titanium sinker, see below). This measurement needs to be performed once only. Figure 3.4 shows the results of these measurements for both baskets, where the weighted linear regression approach outlined below was applied for their interpretation. V_{met} and m_{met} were found to be 0.667 g/cm^3 and 5.29 g respectively for the original basket, and 1.42 g/cm^3 and 7.71 g respectively for the current basket.

2. Prepare the system for adsorption measurements. First, load the sample in the sample basket

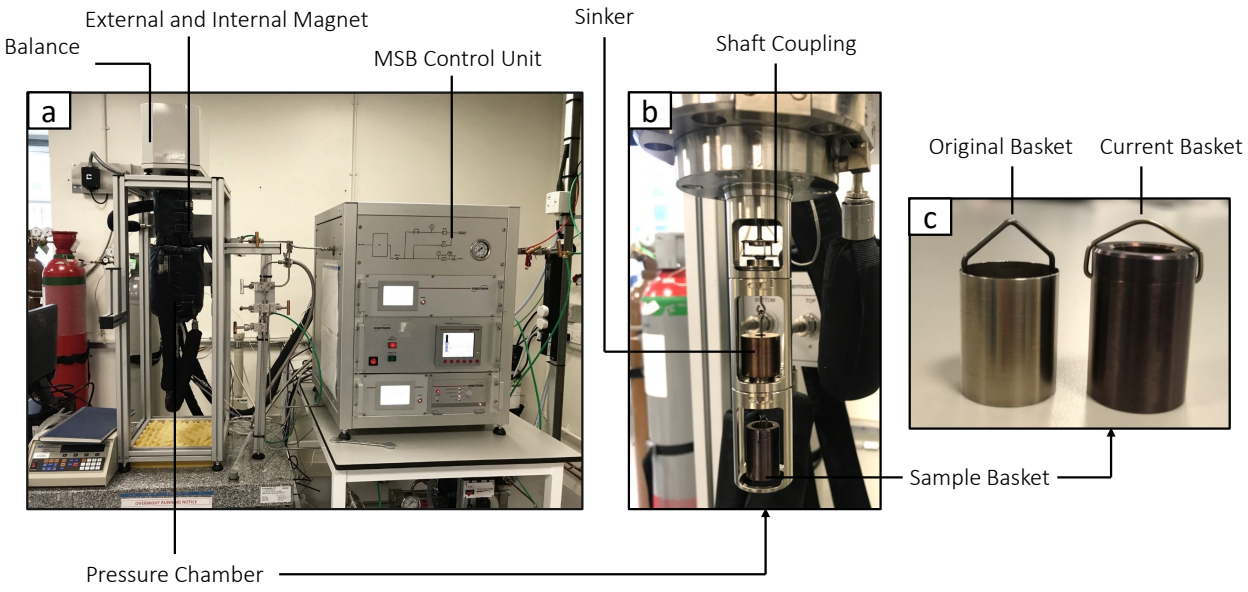

Figure 3.3: The experimental setup used for high pressure adsorption measurements with the (a) Rubotherm Magnetic Suspension Balance (MSB). (b) Cross-section of the pressure chamber showing the sample basket and sinker and (c) close-up of the two sample baskets used in this study.

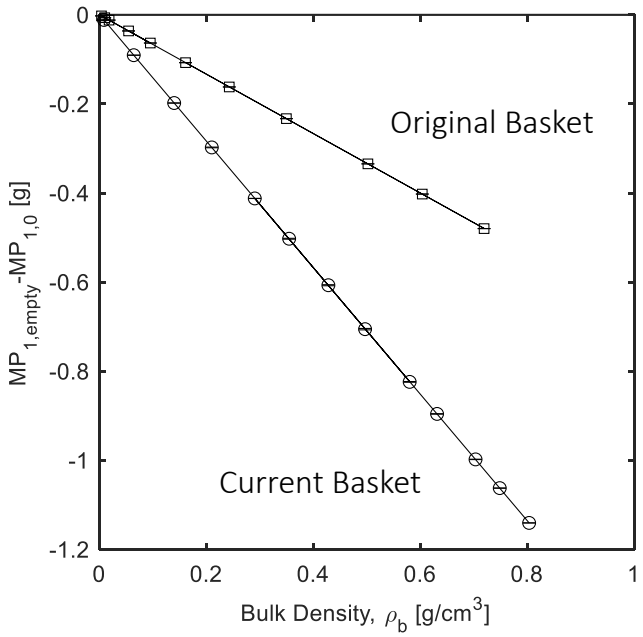

Figure 3.4: Corrected MP_1 [$MP_{1,empty} - MP_{1,0}$] as a function of CO_2 density (experiment conducted at 60 °C and over the pressure range 2-271 bar for the two sample baskets considered in this study). The slope of the regression line corresponds to V_{met}.

and close the pressure chamber. Then, degas the sample for a specified duration under vacuum and at a specific temperature,

3. Cool the system to 80 °C and take a measurement under vacuum in the two measuring positions ($MP_{1,0} = m_s + m_{met}$ and $MP_{2,0} = MP_{1,0} + m_{sk}$), where m_s, m_{met} and m_{sk} are the mass of the adsorbent, the lifted metal parts and the calibrated sinker, respectively,

4. Perform a measurement with Helium at 80 °C and at various pressure points to obtain $MP_{1,He}$ and $MP_{2,He}$. These data were used to estimate the combined skeletal volume of the adsorbent and the lifted metal parts, $V_0 = V_s + V_{met}$, using the following equation:

$$MP_{1,He}(\rho_b, T) = MP_{1,0} - \rho_b V_0 \tag{3.2}$$

   The results of the Helium measurements are described in Chapters 6 (synthetic adsorbents) and 7 (shales),

5. Evacuate the entire system for a specified period of time and purge the lines with the selected adsorbate,

6. Heat the system to the desired isotherm temperature and measure adsorption points by filling the chamber at various pressures and allowing the system to equilibrate for a fixed period of time. The equilibration time for all samples was in the range of 1–2 hours. Overnight measurements were regularly acquired to confirm the absence of significant adsorption (or desorption) beyond the chosen equilibration time. To check for any hysteresis, measurements were typically performed both in adsorption and desorption mode. The majority of the measurements were obtained in desorption mode, however. Repeat this step for isotherms at other temperatures,

7. After the completion of measurements with one adsorbate, repeat steps 3–7 to measure adsorption with the next adsorbate. These adsorption isotherms are presented in Chapters 6 (synthetic adsorbents) and 7 (shales),

8. After the completion of all adsorption measurements, repeat steps 3–5 to obtain a final Helium measurement. This particular step was not carried out with all of the samples.

The above is an idealised operating procedure. In reality, issues such as external power cuts meant that the MSB had to be opened sometimes to reset the coupling. If this happened, the sample was degassed again and the measurements continued from when they had been interrupted. As with low pressure adsorption, the degassing temperature and duration was dependent on the sample. The order in which CO_2 and CH_4 measurements were done was also regularly changed across materials. The specifics of each experiment are shown in Table 3.3. Although supercritical adsorption on AC was not measured in this work, a comprehensive data set of supercritical adsorption isotherms of CH_4 and CO_2 is reported in the literature [180, 219], which we have used in this study to evaluate the general applicability of our experimental and modelling workflow.

The following three equations are used to compute the bulk density of the adsorbate, the excess adsorbed amount and the net adsorbed amount:

Table 3.3: Details of the high pressure adsorption experiments. [a]Sample regeneration involved the application of vacuum and the specified regeneration protocol.

Sample	Mass	Regeneration protocol[a]	Adsorbate sequence	Basket
MC	1.22 g	Heat to 120 °C (7 h)	(i) CO_2 (ii) CH_4	Original
MZ	1.15 g	300 °C (12 h)	(i) CO_2 (ii) CH_4	Current
B6	2.15 g	120 °C (12 h)	(i) CO_2 (ii) CH_4	Original
B8	2.66 g	120 °C (12 h)	(i) CH_4 (ii) CO_2	Current
LG4	1.96 g	120 °C (16 h)	(i) CH_4 (ii) CO_2	Current
ML	1.58 g	120 °C (16 h)	(i) CH_4 (ii) CO_2	Current

$$\rho_{\mathrm{b}} = \frac{(\mathrm{MP}_{2,0} - \mathrm{MP}_{1,0}) - (\mathrm{MP}_2(\rho_{\mathrm{b}}, T) - \mathrm{MP}_1(\rho_{\mathrm{b}}, T))}{V_{\mathrm{sk}}} \tag{3.3a}$$

$$n^{\mathrm{ex}} = \frac{\mathrm{MP}_1(\rho_{\mathrm{b}}, T) - \mathrm{MP}_{1,0} + \rho_{\mathrm{b}} V_0}{M_{\mathrm{w}} m_{\mathrm{s}}} \tag{3.3b}$$

$$n^{\mathrm{net}} = \frac{\mathrm{MP}_1(\rho_{\mathrm{b}}, T) - \mathrm{MP}_{1,0} + \rho_{\mathrm{b}} V_{\mathrm{met}}}{M_{\mathrm{w}} m_{\mathrm{s}}} \tag{3.3c}$$

where M_{w} is the molecular weight of the adsorbate and V_{sk} is the volume of the calibrated titanium sinker. As described below, Eq. 3.3 is used to estimate the uncertainty associated with the measured bulk density and excess amount adsorbed following classic formula of error propagation that include contributions from the observed standard deviation of the measured weights, the sinker volume (4.364± 0.002 cm^3) and the estimated value of V_0. The latter represents the main driver of the uncertainty associated with supercritical adsorption measurements at elevated pressures.

3.2.2.1 Uncertainty Analysis

The uncertainty associated with the high pressure adsorption measurements carried out in this study has been quantified using the general formula of error propagation [220]:

$$\delta_b = \sqrt{\delta_x^2 \left(\frac{\partial q}{\partial x}\right)^2 + \delta_y^2 \left(\frac{\partial q}{\partial y}\right)^2 + \delta_z^2 \left(\frac{\partial q}{\partial z}\right)^2} \tag{3.4}$$

where δ_b is the absolute uncertainty associated with the quantity $b = f(x, y, z)$ and depends on other (measured) quantities (x, y and z) and their corresponding uncertainties (δ_x, δ_y and δ_z). Using this approach, the following definitions for the uncertainty in the measured excess amount adsorbed ($\delta_{n^{\mathrm{ex}}}$) and bulk fluid density ($\delta_{\rho_{\mathrm{b}}}$) are obtained:

$$\delta_{n^{\mathrm{ex}}} = \sqrt{\frac{\delta^2_{\mathrm{MP}_1} + \delta^2_{\mathrm{MP}_{1,0}} + \rho_{\mathrm{b}}^2\delta^2_{V_0} + V_0^2\delta^2_{\rho_{\mathrm{b}}} + (n^{\mathrm{ex}})^2 M_{\mathrm{w}}^2\delta^2_{m_{\mathrm{s}}}}{(M_{\mathrm{w}}m_{\mathrm{s}})^2}} \tag{3.5a}$$

$$\delta_{\rho_{\mathrm{b}}} = \sqrt{\frac{\delta^2_{m_{\mathrm{sk}}} + \delta^2_{m_{\mathrm{sk},0}} + \rho_{\mathrm{b}}^2\delta^2_{V_{\mathrm{sk}}}}{V^2_{\mathrm{sk}}}} \tag{3.5b}$$

where δ_{MP_j} and $\delta_{\mathrm{MP}_{j,0}}$ are the standard deviations in the measured weight at measuring position j ($j = 1, 2$) at a given density (MP_j) and under vacuum ($\mathrm{MP}_{j,0}$), respectively. In our study, δ_{MP_j} and $\delta_{\mathrm{MP}_{j,0}}$ were set to be equal to the resolution of the balance (10 µg), if the estimated value was below this threshold. V_0 is the combined volume of the adsorbent and the lifted metal parts, and m_{s} is the mass of the adsorbent; these quantities (and their uncertainties δ_{V_0} and $\delta_{m_{\mathrm{s}}}$) are obtained from the analysis of Helium gravimetry experiments, as described below. The volume of the titanium sinker and its uncertainty are specified by the supplier's calibration, $V_{\mathrm{sk}} = 4.364 \pm 0.002$ cm^3. The mass of the sinker at a given density, m_{sk}, corresponds to the difference between the weights obtained at the two measuring positions:

$$m_{\mathrm{sk}} = \mathrm{MP}_2 - \mathrm{MP}_1 \tag{3.6a}$$

$$\delta_{m_{\mathrm{sk}}} = \sqrt{\delta^2_{\mathrm{MP}_1} + \delta^2_{\mathrm{MP}_2}} \tag{3.6b}$$

An analogous set of equations can be written for the mass of the sinker under vacuum ($m_{\mathrm{sk},0}$) and its uncertainty ($\delta^2_{m_{\mathrm{sk},0}}$). As anticipated above, V_0 and m_{s} are obtained by a Helium gravimetry, as given by the following relationship:

$$\mathrm{MP}_{1,\mathrm{He}}(\rho_{\mathrm{b}}, T) = \mathrm{MP}_{1,0} - \rho_{\mathrm{b}}V_0 \tag{3.7}$$

where $\mathrm{MP}_{1,0} = m_{\mathrm{s}} + m_{\mathrm{met}}$. m_{s} and V_0 (and their uncertainties) are found by weighted linear regression [220] of the experimental measurements ($\mathrm{MP}_{1,\mathrm{He}}$ and ρ_{b}), as shown below:

$$V_0 = \frac{\sum w \sum w\rho_{\mathrm{b}} \mathrm{MP}_{1,\mathrm{He}}(\rho_{\mathrm{b}}) - \sum w\rho_{\mathrm{b}} \sum w \mathrm{MP}_{1,\mathrm{He}}(\rho_{\mathrm{b}})}{\sum w \sum w\rho_{\mathrm{b}}^2 - \left(\sum w\rho_{\mathrm{b}}\right)^2} \tag{3.8a}$$

$$m_{\mathrm{s}} = \frac{\sum w\rho_{\mathrm{b}}^2 \sum w \mathrm{MP}_{1,\mathrm{He}}(\rho_{\mathrm{b}}) - \sum w\rho_{\mathrm{b}} \sum w\rho_{\mathrm{b}} \mathrm{MP}_{1,\mathrm{He}}(\rho_{\mathrm{b}})}{\sum w \sum w\rho_{\mathrm{b}}^2 - \left(\sum w\rho_{\mathrm{b}}\right)^2} - m_{\mathrm{met}} \tag{3.8b}$$

$$\delta_{V_0} = \sqrt{\frac{\sum w}{\sum w \sum w\rho_{\mathrm{b}}^2 - \left(\sum w\rho_{\mathrm{b}}\right)^2}} \tag{3.8c}$$

$$\delta_{m_{\mathrm{s}}} = \sqrt{\frac{\sum w\rho_{\mathrm{b}}^2}{\sum w \sum w\rho_{\mathrm{b}}^2 - \left(\sum w\rho_{\mathrm{b}}\right)^2} + \delta_{m_{\mathrm{met}}}^2} \tag{3.8d}$$

where $w = 1/\delta_{\mathrm{MP}_{1,He}}$ (the subscript i associated with each experimental point has been omitted for clarity of presentation). The uncertainty values for each adsorbent will be reported in Chapters 6 (synthetic adsorbents) and 7 (shales).

3.3 Summary

Two classes of materials have been studied to investigate the supercritical adsorption of CO_2 and CH_4: synthetic adsorbents and shales. The former comprises of model systems that incorporate different dominant pore sizes and are analagous to various characteristics of shale, and the latter includes shales from the Bowland, Longmaxi and Marcellus shale plays. The experimental methods consist of (i) low pressure adsorption for the characterisation of all adsorbents, and (ii) high pressure adsorption with a Magnetic Suspension Balance that is able to produce reliable adsorption data at elevated pressures and temperatures.

Chapter 4

Modelling of Supercritical Gas Adsorption

A mathematical representation of adsorption equilibria is fundamental to designing industrial adsorption processes. This is equally true for ESGR. This chapter details the equilibrium adsorption models considered for the description of the supercritical adsorption measurements on shales and the synthetic adsorbents. There are two main class of models considered: (i) empirical models and (ii) the lattice Density Functional Theory (DFT) model. Some of the material in this chapter has been published in Ansari et al. (2020) [29].

4.1 Langmuir Model

Empirical models provide a convenient and computationally inexpensive way to deal with many types of materials and adsorption behaviours. In this study, we consider the most commonly used one. The Langmuir model, Eq. 4.1, is often used to depict supercritical adsorption isotherms measured in microporous materials, such as activated carbon [183] and coal [221]:

$$n^{\mathrm{ex}} = \left(\frac{n^{\infty} K f}{1 + K f}\right)\left(1 - \frac{\rho_{\mathrm{b}}}{\rho_{\mathrm{a}}}\right) \tag{4.1}$$

where n^{∞} is the saturation limit (monolayer), K is the Langmuir equilibrium constant and f is the fugacity. The second term on the right-hand side of the equation is the correction required to describe excess adsorption data $\left(n^{\mathrm{ex}} = n^{\mathrm{a}}(1 - \frac{\rho_{\mathrm{b}}}{\rho_{\mathrm{a}}})\right)$, upon assuming a certain behaviour for the density of the adsorbed phase, ρ_{a} [222]. Although the Langmuir model itself has a thermodynamic basis [111], its application to supercritical adsorption data renders it empirical. Because it qualitatively describes

a Type I isotherm, the Langmuir model performs reasonably well on microporous adsorbents by appropriate choice of constant values for n^{∞}, K_{L} and ρ_{a}, although often the main assumptions of the model are relaxed (e.g. n^{∞} is let to be dependent on the temperature [223, 183]). However, its suitability to describe supercritical adsorption on mesoporous materials is questionable, as a major assumption of this model is the use of a constant adsorbed phase density, irrespective of the bulk density and the adsorbent's pore size distribution.

4.2 Lattice DFT Model

The model used in this study belongs to the class of lattice-gas models, also referred to as the lattice Density Functional Theory (lattice DFT) [224, 225]. The theory approximates the adsorbent using a distribution of properly weighted model pores of simple geometries (e.g. slit, channels or cages), whose internal space is discretised, so that fluid molecules form a regular pattern (a lattice). This coarse-graining facilitates considerably the estimation of the density profile within the pore, as opposed to standard implementations of DFT, which are computationally expensive to implement [167]. In addition to incorporating information about the adsorbent geometry, the lattice DFT model considers both adsorbate-adsorbate and adsorbate-adsorbent interactions, thereby enabling the description of a wide spectrum of adsorption isotherms and behaviours [226]. With relevance to this study, the lattice DFT approach has been shown to correctly capture the adsorption of supercritical fluids on both micro- and meso-porous adsorbents, without requiring any assumption of the density of the adsorbed fluid [162, 150, 148, 227]. While in these previous studies the analysis was mostly restricted to either 1D slit or 2D pore channels, shales can be comprised of pores with varying morphologies. To account for this, the model used in this work is a hybrid formulation consisting of both slit and cylindrical pores. Although the lattice DFT model for slit pores at supercritical conditions is fully developed, we develop here the equivalent model for cylindrical pores. We note that cylindrical pores were previously used by Qajar and co-workers [228] to describe N_2 adsorption on shale and coal, but their study was limited to subcritical conditions; we build on these developments by deriving in the following the relevant operating equations for supercritical gas adsorption.

4.2.1 Lattice DFT Model for Cylindrical Pores

We consider a cylindrical pore with a cubic lattice to accommodate fluid molecules, as shown in Figure 4.1. To facilitate the description of the mathematical formulation of the model, we compare the cylindrical pore to a rectangular channel (image on the left-hand side) with the same number of lattice sites (four lattice layers are shown in the example and represented by the dashed lines). In our

treatment, $j = 1$ and $j = J$ represent the central and outer (wall) layer, respectively, and the radius of each layer, r_j, is defined as follows:

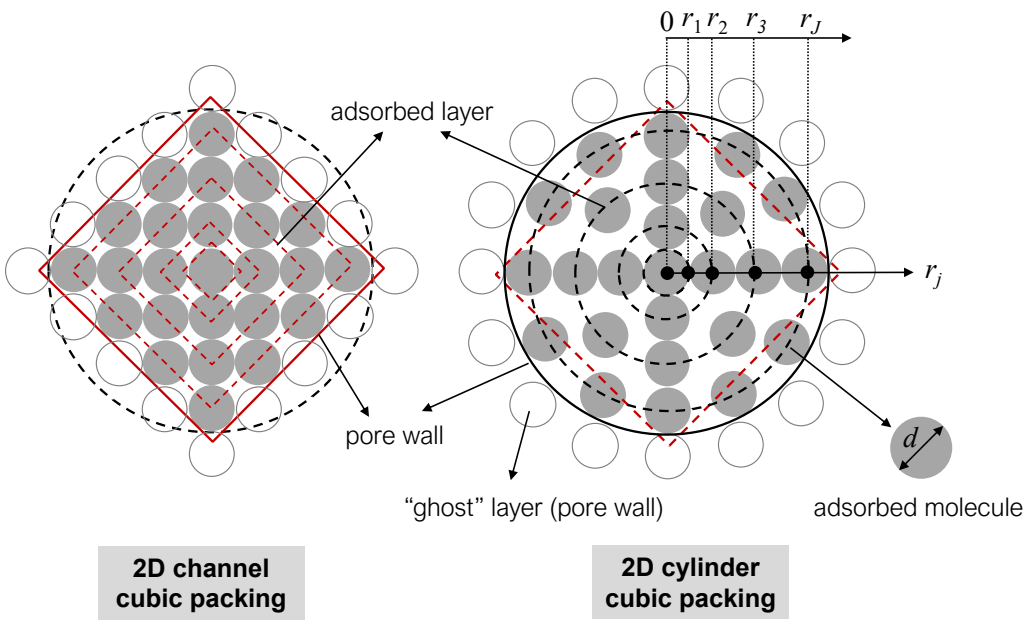

Figure 4.1: Depiction of a cylindrical pore considered in the lattice DFT framework. Circles represent adsorbed molecules with diameter d and lattice layers are denoted by the distance, r_j, from the centre of the pore of diameter $d(2J-1)$, where J is the total number of layers.

$$r_j = \begin{cases} d/2 & \text{for } j = 1 \\ (j-1)d & \text{for } j > 1 \end{cases} \tag{4.2}$$

where d is the diameter of the lattice site, which in our study is taken as the collision diameter of the gas molecule ($\sigma_{CO_2} \approx \sigma_{CH_4} \approx 4$ Å). The pore diameter is therefore readily obtained as, $D_{p,J_k} = d(2J-1)$. With reference to the generic three-dimensional formalism presented by Hocker et al. (2003) [162], the Ono-Kondo lattice equations for a molecule in a cylindrical pore with J lattice layers are:

$$\begin{aligned}
0 &= \varepsilon_{ff}(z_j^{a+}\theta_{j+1} + z_j^{s}\theta_j - z^{b}\theta_b) + k_B T \ln\left[\frac{\theta_j(1-\theta_b)}{\theta_b(1-\theta_j)}\right] \qquad \text{for} \qquad j = 1 \\
0 &= \varepsilon_{ff}(z_j^{a+}\theta_{j+1} + z_j^{a-}\theta_{j-1} + z_j^{s}\theta_j - z^{b}\theta_b) + k_B T \ln\left[\frac{\theta_j(1-\theta_b)}{\theta_b(1-\theta_j)}\right] \qquad \text{for} \qquad 1 < j < J \\
0 &= \varepsilon_{sf} z_j^{a+} + \varepsilon_{ff}(z_j^{a-}\theta_{j-1} + z_j^{s}\theta_j - z^{b}\theta_b) + k_B T \ln\left[\frac{\theta_j(1-\theta_b)}{\theta_b(1-\theta_j)}\right] \qquad \text{for} \qquad j = J
\end{aligned} \tag{4.3}$$

where θ_b is the probability of occupancy in the bulk and θ_j is the probability of having layer j occupied. This probability is interpreted as the degree of occupancy and can be translated into a corresponding density (bulk or adsorbed phase) using a suitable mapping function (see below). The equations also

include k_{B} (the Boltzmann's constant), T (the temperature), $\varepsilon_{\mathrm{ff}}$ (the adsorbate-adsorbate interaction energy) and $\varepsilon_{\mathrm{sf}}$ (the adsorbate-adsorbent interaction energy). In this formulation, these interactions are confined to the nearest neighbouring molecules by using a set of coordination numbers, namely z^{b} (bulk), z_j^{s} (same layer), $z_j^{\mathrm{a}+}$ (outer adjacent layer) and $z_j^{\mathrm{a}-}$ (inner adjacent layer), for which the following general relationship holds:

$$z^{\mathrm{b}} = z_j^{\mathrm{s}} + z_j^{\mathrm{a}+} + z_j^{\mathrm{a}-} \quad \text{for all } j \tag{4.4}$$

For a cubic lattice in a slit pore, $z^{\mathrm{a}+} = z^{\mathrm{a}-} = z^{\mathrm{a}}$ and the coordination numbers do not depend on the position, j, i.e. $z^{\mathrm{b}} = 6$, $z^{\mathrm{s}} = 4$ and $z^{\mathrm{a}} = (z^{\mathrm{b}} - z^{\mathrm{s}})/2 = 1$. In a cylindrical pore, however, the capacity of each layer increases when moving from the centre of the pore to the pore wall; accordingly, the two coordination numbers with the adjacent layers can be expressed as the ratio of the perimeters of the relevant layers:

$$\begin{aligned} z_j^{\mathrm{a}+} &= \frac{r_{j+1}}{r_j} = \frac{j}{j-1} \qquad && \text{for } j > 1 \\ z_j^{\mathrm{a}-} &= \frac{r_{j-1}}{r_j} = \frac{j-2}{j-1} \qquad && \text{for } j > 2 \end{aligned} \tag{4.5}$$

which thus correspond to the ratio of the number of sites between two adjacent layers (note also that $z_j^{\mathrm{a}-} = 1/z_{j-1}^{\mathrm{a}+}$); once these have been computed, the corresponding value for z_j^{s} is found from Eq. 4.4 ($z^{\mathrm{b}} = 6$). The only exception to Eq. 4.5 is for layers 1 and 2, as the former is the only layer where the radius is defined at the edge, rather than the centre of the lattice site. In particular, for $j = 1$, $z_1^{\mathrm{a}+} = 4$ and $z_1^{\mathrm{a}-} = 0$; accordingly, $z_1^{\mathrm{s}} = 2$ to satisfy Eq. 4.4. For $j = 2$, $z_2^{\mathrm{a}+} = 2$ (Eq. 4.5) and $z_2^{\mathrm{a}-} = 1/z_1^{a+} = 1/4$; consequently, $z_1^{\mathrm{s}} = 3.75$ to satisfy Eq. 4.4. For layers $j > 2$, the lateral coordination number, z^{s}, is always 4. It is worth highlighting that the unique features of the cylindrical geometry are also accounted for in the *effective* surface energy term in Eq. 4.3, $\varepsilon_{\mathrm{sf}} z_J^{\mathrm{a}+}$, where $z_J^{\mathrm{a}+}$ refers to the coordination with a "ghost" layer at the wall of the pore. The term accounts for the enhanced adsorbate-adsorbent interaction due to the curvature of the wall relative to a flat surface and introduces a dependency of the strength of such interaction on the size of the pore. Accordingly, when more than one pore-class is considered, the *average* adsorbate-adsorbent interaction is obtained as their weighted average:

$$\overline{\varepsilon}_{\mathrm{sf}} = \sum_{k=1}^{K} w_k \varepsilon_{\mathrm{sf}} z_{J_k}^{\mathrm{a}+} \tag{4.6}$$

where J_k is the number of layers in the pore-class k and w_k is its surface area fraction, obtained

directly from the textural characterisation by physisorption.

4.2.1.1 From Lattice to Physical Units

A mapping function is used to convert the occupancy values obtained from the lattice model to density:

$$\rho = \frac{\rho_{\max}\rho_{\mathrm{c}}\theta}{\rho_{\max}(1-\theta) - \rho_{\mathrm{c}}(1-2\theta)} \tag{4.7}$$

This function satisfies three important physical constraints [162]: (i) for $\theta = 0$, $\rho = 0$; (ii) for $\theta = 1$, $\rho = \rho_{\max}$ (maximum packing density when the lattice is fully occupied); (iii) for $\theta = 0.5$, $\rho = \rho_{\mathrm{c}}$ (critical density of the fluid at half occupancy). Once the density values in each layer are known, the excess adsorbed amount can be computed. To this aim, we consider the three coordinates (r, θ, z), and assume that adsorption in the pore depends only on the radial coordinate, r, i.e. axisymmetry applies ($\partial n^{\mathrm{ex}}/\partial\theta = 0$) and edge effects are negligible ($\partial n^{\mathrm{ex}}/\partial z = 0$). Therefore, for a single cylindrical pore of radius R and length L, the excess adsorption is defined as follows:

$$n_R^{\mathrm{ex}} = \int_0^R (\rho(r) - \rho_{\mathrm{b}})A(r)dr \tag{4.8}$$

where $A(r) = 2\pi rL$ is the (lateral) area in cylindrical coordinates. By further considering that the space in the pore is discretised with lattice sites, Eq. 4.8 can be recasted as follows:

$$\begin{aligned} n_R^{\mathrm{ex}} &= (\rho_1 - \rho_{\mathrm{b}})\pi r_1^2 L + \sum_{j=2}^{J_R}(\rho_j - \rho_{\mathrm{b}})2\pi r_j L d \\ &= \pi d^2 L\Big[\frac{1}{4}(\rho_1 - \rho_b) + 2\sum_{j=2}^{J_R}(\rho_j - \rho_b)(j-1)\Big] \end{aligned} \tag{4.9}$$

where we have used the definitions of the radii of each layer in the pore, r_j, given by Eq. 4.2 and depicted in Figure 4.1 (J_R is the total number of layers in the pore). Accordingly, the volume of the pore can be readily computed as:

$$\nu_{\mathrm{p},R} = L\int_0^R A(r)dr = \pi\frac{d^2}{4}L + 2\pi d^2 L\sum_{j=2}^{J_R}(j-1) \tag{4.10}$$

By combining Eqs. 4.9 and 4.10, the following expression is obtained:

$$n_R^{\mathrm{ex}} = \frac{\nu_{\mathrm{p},R}}{\frac{1}{4} + 2\sum_{j=2}^{J_R}(j-1)} \Big[\frac{1}{4}(\rho_1 - \rho_b) + 2\sum_{j=2}^{J_R}(\rho_j - \rho_b)(j-1)\Big] \tag{4.11}$$

In the lattice framework the pore space of the adsorbent is discretized into a set of pores of specific radius and weight in the discretized distribution. In particular, the latter consists of K types of pores, where every pore (class) k is made of J_k lattice layers. Therefore, each pore class has a specific pore volume, $\nu_{\mathrm{p},k}$, with the physical constraint that the total pore volume of the adsorbent $\nu_{\mathrm{p}}^{\mathrm{tot}} = \sum_{k=1}^{K} \nu_{\mathrm{p},k}$. The total excess adsorption per unit mass of adsorbent is therefore computed as:

$$n^{\mathrm{ex}} = c_{\mathrm{sat}} \sum_{k=1}^{K} \frac{\nu_{\mathrm{p},k}}{\left[\frac{1}{4} + J_k(J_k-1)\right]} \Big[\frac{1}{4}(\rho_1 - \rho_b) + 2\sum_{j=2}^{J_k}(\rho_j - \rho_b)(j-1)\Big] \tag{4.12}$$

where $\sum_{j=2}^{J_k}(j-1) = J_k(J_k-1)/2$, ρ_j is the density in layer j of pore class k, and $c_{\mathrm{sat}} \in [0,1]$ is a saturation capacity factor that is independent of pore size, but depends on the temperature. Note that c_{sat} has been introduced to account for a reduction of the volume occupied by the supercritical adsorbed phase at $\rho = \rho_{\max}$ as compared to a close packing of molecules. The total pore volume occupied by the adsorbed phase at 'saturation' is thus obtained as $c_{\mathrm{sat}}\nu_{\mathrm{p}}^{\mathrm{tot}}$. We note that because the saturation factor is defined based on the pore volume of the adsorbent, it applies to both absolute and excess adsorption.

4.2.2 Lattice DFT Model for Slit Pores

In a slit pore, each layer has the same number of lattice sites and adsorption occurs on a flat surface, as shown by Figure 4.2. This simplifies the lattice DFT formulation, as compared to cylindrical pores.

The equations for the lattice DFT model applied to a slit pore are as follows [227]:

$$\begin{aligned}
0 &= \varepsilon_{\mathrm{sf}} + \varepsilon_{\mathrm{ff}}(z^{\mathrm{a}}\theta_{j+1} + z^{\mathrm{s}}\theta_j - z^{\mathrm{b}}\theta_{\mathrm{b}}) + k_{\mathrm{B}}T\ln\left[\frac{\theta_j(1-\theta_{\mathrm{b}})}{\theta_{\mathrm{b}}(1-\theta_j)}\right] \qquad \text{for} \qquad j = 1 \\
0 &= \varepsilon_{\mathrm{ff}}(z^{\mathrm{a}}\theta_{j+1} + z^{\mathrm{a}}\theta_{j-1} + z^{\mathrm{s}}\theta_j - z^{\mathrm{b}}\theta_{\mathrm{b}}) + k_{\mathrm{B}}T\ln\left[\frac{\theta_j(1-\theta_{\mathrm{b}})}{\theta_{\mathrm{b}}(1-\theta_j)}\right] \qquad \text{for} \qquad 1 < j < J \\
0 &= \varepsilon_{\mathrm{sf}} + \varepsilon_{\mathrm{ff}}(z^{\mathrm{a}}\theta_{j-1} + z^{\mathrm{s}}\theta_j z^{\mathrm{b}}\theta_{\mathrm{b}}) + k_{\mathrm{B}}T\ln\left[\frac{\theta_j(1-\theta_{\mathrm{b}})}{\theta_{\mathrm{b}}(1-\theta_j)}\right] \qquad \text{for} \qquad j = J
\end{aligned} \tag{4.13}$$

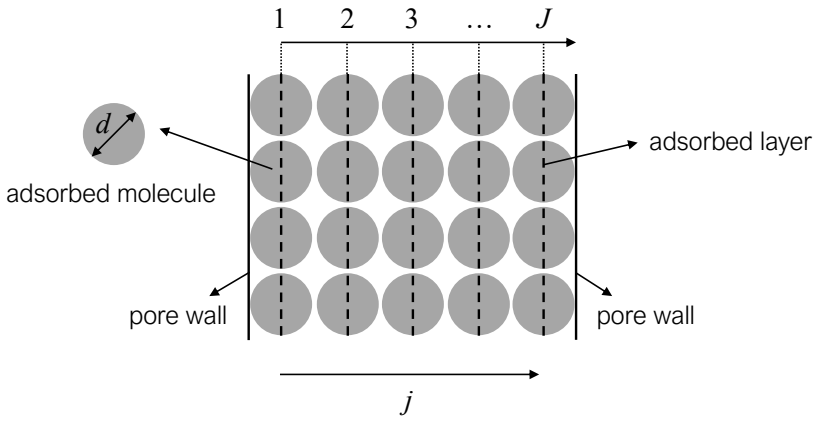

Figure 4.2: Depiction of a slit pore considered in the lattice DFT framework. Circles represent adsorbed molecules with diameter d and the pore width is given by Jd, where J is the total number of layers.

In this formulation, the pore walls are placed at $j = 1$ and $j = J$, and the lattice coordination numbers are $z^{\mathrm{b}} = 6$, $z^{\mathrm{s}} = 4$ and $z^{\mathrm{a}} = 1$ (cubic lattice). The conversion from lattice occupancy (θ) to density (ρ) is achieved with the same mapping function as cylindrical pores (Eq. 4.7), and the excess amount adsorbed is thus obtained as:

$$n^{\mathrm{ex}} = c_{\mathrm{sat}} \sum_{k=1}^{K} \frac{\nu_{\mathrm{p},k}}{J_k} \sum_{j=1}^{J_k} (\rho_j - \rho_{\mathrm{b}}) \tag{4.14}$$

where $\nu_{\mathrm{p},k}$ represents the specific pore volume of pore class k with J_k layers. In a similar manner to the cylindrical pore model, a saturation capacity factor, $c_{\mathrm{sat}} \in [0, 1]$, has been introduced to account for a reduction of the volume occupied by the supercritical adsorbed phase at saturation as compared to a close packing of molecules.

4.2.3 Lattice DFT Model for Hybrid Systems

With relevance to adsorption studies, shales are composed of two different surface chemistries, namely the organic (i.e. kerogen) and inorganic (i.e. clay minerals) components. To address this, there have been approaches that incorporate the dual surface nature of shales through the lattice DFT [151]. Yet, shales tend to have heterogeneity in pore shape as well; clay minerals are usually stacked and layered [229] and form slit pores, while the organic matter can have diverse pore morphology. We present here a novel approach that accounts for heterogeneity in terms of both surface energy and pore shape. In the hybrid lattice DFT model, the shale is divided into two distinct systems: slit pores and cylindrical pores. Each pore type is modelled simultaneously, and all fitted parameters ($\rho_{\max}$ and c_{sat}), bar one, are kept consistent between the two models. The only parameter that varies between the two systems is the surface interaction energy, as we expect the slit ($\varepsilon_{\mathrm{sf}}^{\mathrm{slit}}$) and cylindrical ($\varepsilon_{\mathrm{sf}}^{\mathrm{cyl}}$)

surface energies to be largely associated with the clay minerals and organic matter, respectively. The pore size distribution used within each individual model and the total pore volume allocated to each pore type varies. This will be discussed in the next chapter. The total excess adsorbed amount for the hybrid system is found by the sum of the results from each model:

$$n^{\mathrm{ex}} = n^{\mathrm{ex}}_{\mathrm{slit}} + n^{\mathrm{ex}}_{\mathrm{cyl}} \tag{4.15}$$

where $n^{\mathrm{ex}}_{\mathrm{slit}}$ and $n^{\mathrm{ex}}_{\mathrm{cyl}}$ are the excess adsorbed amounts calculated using the slit and cylindrical lattice DFT models, respectively.

4.2.4 Solution Procedure

The solution to the lattice DFT model is obtained by solving the set of non-linear equations, Eq. 4.3 (cylindrical pore) or Eq. 4.13 (slit pore), for the occupancy θ_j at specified θ_b. The function `lsqnonlin` in MATLAB was used to solve the equations with default parameters of the termination tolerance (1×10^{-6}) and maximum number of iterations (400). The occupancy values are converted to density values using Eq. 4.7, which are in turn used in Eq. 4.12 (cylindrical pore) or Eq. 4.14 (slit pore), and Eq. 4.15 (hybrid system) subsequently if required, to compute the excess amount adsorbed. The following model parameters are specified: (i) a cubic lattice pattern ($z^{\mathrm{b}} = 6$, z^{s}, $z^{\mathrm{a+}}$ and $z^{\mathrm{a+}}$ defined above), (ii) the adsorbate-adsorbate interaction energy, $\varepsilon_{\mathrm{ff}} = -4k_{\mathrm{B}}T_{\mathrm{c}}/z^{\mathrm{b}}$, (iii) the temperature (T), (iv) the measured total specific pore volume of the adsorbent, $\nu_{\mathrm{p}}^{\mathrm{tot}}$, and its discretisation in K representative pore classes. This discretised PSD will be described in Chapter 5. For each adsorbate, the remaining parameters were found by fitting the model to the experimental data, namely (i) the adsorbent-adsorbate interaction energy, $\varepsilon_{\mathrm{sf}}$, and $\varepsilon_{\mathrm{sf}}^{\mathrm{slit}}$ and $\varepsilon_{\mathrm{sf}}^{\mathrm{cyl}}$ for shales (ii) the maximum density in the lattice, ρ_{max} and (iii) the temperature-dependent saturation factor, c_{sat}. The function `fminsearch` in MATLAB was used to minimise the following objective function (specified function and parameter tolerance level of 1×10^{-6}):

$$\Phi = \sum_{t=1}^{T} \sum_{p=1}^{P} \left[n^{\mathrm{ex}}_{\mathrm{exp}}(t,p) - n^{\mathrm{ex}}_{\mathrm{mod}}(t,p) \right]^2 \tag{4.16}$$

where $n^{\mathrm{ex}}_{\mathrm{exp}}$ is the measured experimental point at a specific temperature, t, and density, p, and $n^{\mathrm{ex}}_{\mathrm{mod}}$ is the corresponding amount obtained from the model.

4.3 Henry Constants and Isosteric Enthalpy of Adsorption

Henry constants can provide useful insight into adsorbate selectivity of a material [183] and can also be used for the evaluation of thermodynamic properties. Obtaining Henry constants gravimetrically is fairly challenging as adsorption produces minute weight change at the region of interest, i.e. very low pressures [230]. This section discusses two different approaches to overcome this challenge.

4.3.1 Henry Constants from the Experimental Data

Henry constants were obtained by fitting the experimental excess adsorption isotherms with the Virial equation:

$$\ln(f/n^{\mathrm{ex}}) = \sum_{i=0}^{m} C_i (n^{\mathrm{ex}})^i \tag{4.17}$$

where f is the fugacity and C_i are the Virial coefficients; the temperature-dependent Henry constant is thus obtained as $H = \exp(-C_0)$. For Eq. 4.17 to be valid, only the points measured up to moderate pressures were considered, (i.e. up to ~ 6.1 MPa for CO_2 and ~ 7.0 MPa for CH_4 depending on the temperature); at these conditions, the value of the gas bulk density is less than approximately 10% of the density of the saturated liquid 21.073 mol/L for CO_2 and 26.327 mol/L for CH_4 [231]), and excess and absolute amount adsorbed are effectively equal. For both adsorbents, the first two Virial coefficients were found to be sufficient to describe the data; this was additionally validated by a plot of $\ln(f/n^{\mathrm{ex}})$ vs. n^{ex}, which yields a linear region from which the Henry constant can be extrapolated. The integrated van't Hoff equation is then used to describe the temperature dependence of the Henry constant [111]:

$$H = H_0 \exp\left[-\Delta h_0 / RT\right] \tag{4.18}$$

which enables the graphical estimation of the (experimental) isosteric enthalpy of adsorption at zero coverage, Δh_0, from the so-called van't Hoff plot ($\ln(H)$ vs. $1/T$).

4.3.2 Henry Constants from the Lattice DFT Model

It can be readily shown that the lattice DFT model approaches the limiting behaviour described by Henry's law at low concentrations [227]. Mathematically, for pore class k and for $\theta_{\mathrm{b}} \to 0$, adsorption

is limited to the first layer only in the case of cylindrical pores and also the last layer for slit pores, i.e. $\theta_2, ..., \theta_{J_k-1} = 0$ and $\theta_1, \theta_{J_k} \ll 1$ for both geometries and $\theta_1 = 0$ only for cylindrical pores. The Ono-Kondo lattice equations reduce to:

$$\text{Slit:} \quad \theta_1 = \theta_J = H'_J \theta_\text{b} \tag{4.19a}$$

$$\text{Cylindrical:} \quad \theta_J = H'_J \theta_\text{b} \tag{4.19b}$$

where $H'_J = \exp\left[-\varepsilon_\text{sf}/k_\text{B}T\right]$ (slit model) or $H'_J = \exp\left[-\varepsilon_\text{sf} z_J^{a+}/k_\text{B}T\right]$ (cylindrical model) is the dimensionless Henry constant. The conversion to physical units of density is obtained upon application of the mapping function (Eq. 4.7), which for $\theta \ll 1$ reduces to $\rho = \rho_\text{max}\rho_\text{c}\theta$. Therefore,

$$\text{Slit:} \quad \rho_1 = \rho_{J_k} = H'_J \rho_\text{b} \tag{4.20a}$$

$$\text{Cylindrical:} \quad \rho_{J_k} = H'_J \rho_\text{b} \tag{4.20b}$$

By analogy ($\rho_2, ..., \rho_{J_k-1} = 0$ (both pore geometries) and $\rho_1 = 0$ only for cylindrical pores, and $\rho_\text{b} \to 0$), the expressions for the excess adsorbed amount, Eq. 4.12 and Eq. 4.14, reduce to the following:

$$\text{Slit:} \quad n^\text{ex} = c_\text{sat} \sum_{k=1}^{K} \frac{\nu_{\text{p},k}}{J_k} (\rho_1 + \rho_{J_k}) \tag{4.21a}$$

$$\text{Cylindrical:} \quad n^\text{ex} = c_\text{sat} \sum_{k=1}^{K} \frac{\nu_{\text{p},k}}{\left[\frac{1}{4} + J_k(J_k-1)\right]} \left[2\rho_{J_k}(J_k - 1)\right] \tag{4.21b}$$

Upon combination of Eqs. 4.20 and 4.21, and application of the Ideal Gas Law ($\rho_\text{b} = P/RT$), the following expression is obtained:

$$n^\text{ex} = \widetilde{H} P \tag{4.22}$$

where the Henry constant, $\widetilde{H}$ (in units of mmol/g.bar), is defined as follows:

$$\text{Slit:} \quad \widetilde{H} = \widetilde{H_0} \frac{100}{RT} c_{\text{sat}} \sum_{k=1}^{K} \frac{2\nu_{\text{p},k}}{J_k} \exp\left(\frac{-\varepsilon_{\text{sf}}}{k_{\text{B}}T}\right) \tag{4.23a}$$

$$\text{Cylindrical:} \quad \widetilde{H} = \widetilde{H_0} \frac{100}{RT} c_{\text{sat}} \sum_{k=1}^{K} \frac{2\nu_{\text{p},k}(J_k - 1)}{\left[\frac{1}{4} + J_k(J_k - 1)\right]} \exp\left(\frac{-\varepsilon_{\text{sf}} z_{J_k}^{a+}}{k_{\text{B}}T}\right) \tag{4.23b}$$

where $R = 8.314$ J/mol.K is the gas constant, the temperature T is given in units of Kelvin, and the specific pore volume, $\nu_{\text{p},k}$ is given in units of cm^3/g. We note that a dimensionless constant, $\widetilde{H}_0$, was added to Eq. 4.23 to correct for the lack of a pre-factor in the lattice formulation of Henry's law (Eq. 4.19). Its value can be found by fitting against the experimentally obtained Henry constants. Accordingly, the isosteric enthalpy of adsorption at zero coverage, $\Delta\widetilde{h}_0$, can be obtained upon application of the van't Hoff equation on the computed values of $\widetilde{H}$. We note that $\Delta\widetilde{h}_0$ includes contributions from both the absorbate-adsorbent interaction parameter, ε_{sf}, and the temperature-dependent pore-saturation factor, c_{sat}. Accordingly, linearity on the van't Hoff plot requires that $\ln(c_{\text{sat}}) \sim 1/T$.

4.4 Summary

The two types of models used in this work to describe supercritical gas adsorption are the Langmuir model and the lattice DFT model. While the former is relatively simple to apply, its application at elevated pressures is often restricted to microporous materials since one of its underlying assumptions is that of a constant adsorbed phase density. The lattice DFT model, on the other hand, does not require such an assumption, and incorporates information about the adsorbent's pore size distribution to describe supercritical adsorption of various adsorbates in different types of adsorbents. The lattice DFT model has been extended to cylindrical pores as part of this thesis, and a novel hybrid formulation of the model, that includes both slit and cylindrical pores, has been developed to suitably describe supercritical adsorption on shales. The method for obtaining Henry constants and the isosteric enthalpy of adsorption from both the experimental data and the lattice DFT model has also been outlined.

Chapter 5

Material Characterisation

The study of adsorption in any material for any application requires a robust understanding of the pore structure of the adsorbent. This chapter outlines the results of all material characterisation undertaken as part of this study. The discussion is divided into the characterisation obtained by subcritical and supercritical adsorption. Some of the material in this chapter has been published in Ansari et al. (2019, 2020) [232, 29] and Pini et al. (2021) [233], and is covered in Delle Piane et al. (publication under review) [206].

5.1 Textural Characterisation by Subcritical Adsorption

5.1.1 Synthetic Adsorbents

The three synthetic adsorbents considered in this study, namely activated carbon (AC), mesoporous carbon (MC) and mesoporous zeolite (MZ), have been characterised using subcritical adsorption measurements with three adsorbates, N_2 (77 K), Ar (87 K) and CO_2 (273 K). Figure 5.1 shows the Ar (87 K) isotherm measured on AC. Based on the IUPAC classification [114], the isotherm is of Type I(b) and shows a steep uptake at very low pressures, followed by a gradual approach towards a limiting adsorption value that indicates early completion of (micro)pore filling ($P/P_0 \approx 0.2$). This is confirmed by the presence of a modest Type H4 hysteresis loop at $P/P_0 > 0.4$, which is often observed in micro-mesoporous carbons [114].

The results of the physisorption analysis on MC and MZ are presented in Figure 5.2, which shows CO_2 (273 K), N_2 (77 K) and Ar (87 K) adsorption/desorption isotherms. The characteristic features of the adsorbents are readily visible in Figures 5.2b and 5.2c: adsorption on MC starts with a modest amount of micropore filling at very low pressures ($P/P_0 < 0.01$), indicating the presence of some microporosity.

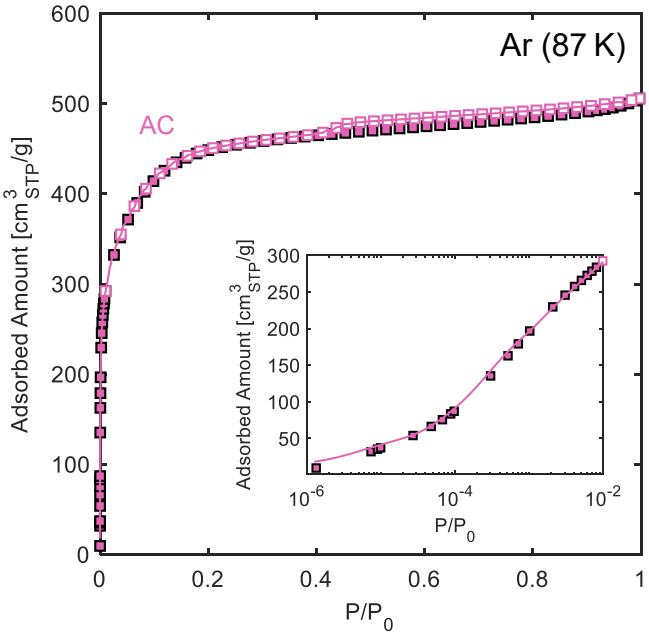

Figure 5.1: Ar (87 K) physisorption isotherm measured in both adsorption (filled symbols) and desorption (empty symbols) mode on activated carbon (AC). STP conditions are defined as 273.15K and 1 atm. P_0 is the saturation pressure at the measurement temperature ($\sim$ 760 torr). Lines show the modelled NLDFT isotherm. Inset shows a closer view of the low pressure region.

It then proceeds with the formation of a monolayer in the mesopores, which is completed at the first inflexion point ($P/P_0 \approx 0.3$); multilayer adsorption ensues and continues until the onset of the second plateau indicating that mesopore filling has concluded ($P/P_0 \approx 0.9$). MZ shows a steeper uptake in the low pressure region but a more gradual increase in adsorption in the mesopore (intermediate pressure) range. MZ's higher microporosity is additionally confirmed by the strength of its CO_2 adsorption shown in Figure 5.2a. The measurements with N_2 and Ar show a qualitatively similar behaviour, but the isotherms of the latter are shifted to larger values of adsorption due to its larger liquid density at saturation ($\rho_{\text{liq}}(\text{Ar}) = 34.91$ mol/L vs. $\rho_{\text{liq}}(\text{N}_2) = 28.84$ mol/L). MC shows Type IV(a) behaviour with hysteresis of Type H1 ($0.56 < P/P_0 < 0.96$), which is characteristic of porous adsorbents with a narrow range of uniform mesopores. MZ also shows Type IV(a) behaviour and has a hysteresis loop of Type H1, but the adsorption branch at $P/P_0 < 0.4$, with Ar in particular, also shows elements of a Type I isotherm. This is indicative of its dual porosity nature. The larger total Ar adsorption of AC (506 $\text{cm}^3_{\text{STP}}/\text{g}$) as compared to MC (376 $\text{cm}^3_{\text{STP}}/\text{g}$) and MZ (360 $\text{cm}^3_{\text{STP}}/\text{g}$) indicates a larger total pore volume.

The experimental adsorption isotherms have been fitted using various NLDFT and GCMC models (details in Table 5.1) to obtain quantitative estimates of pore volumes and their distribution. As shown in Figures 5.1 and 5.2, the models (solid lines) describe accurately the experimental data (desorption branch) on all three adsorbents, with a fitting error below 1% for each gas and adsorbent. The obtained values for the specific surface area (SSA), micro- (ν_{mic}, $D_{\text{p}} < 2$ nm), meso- (ν_{mes}, $D_{\text{p}} = 2 - 50$ nm)

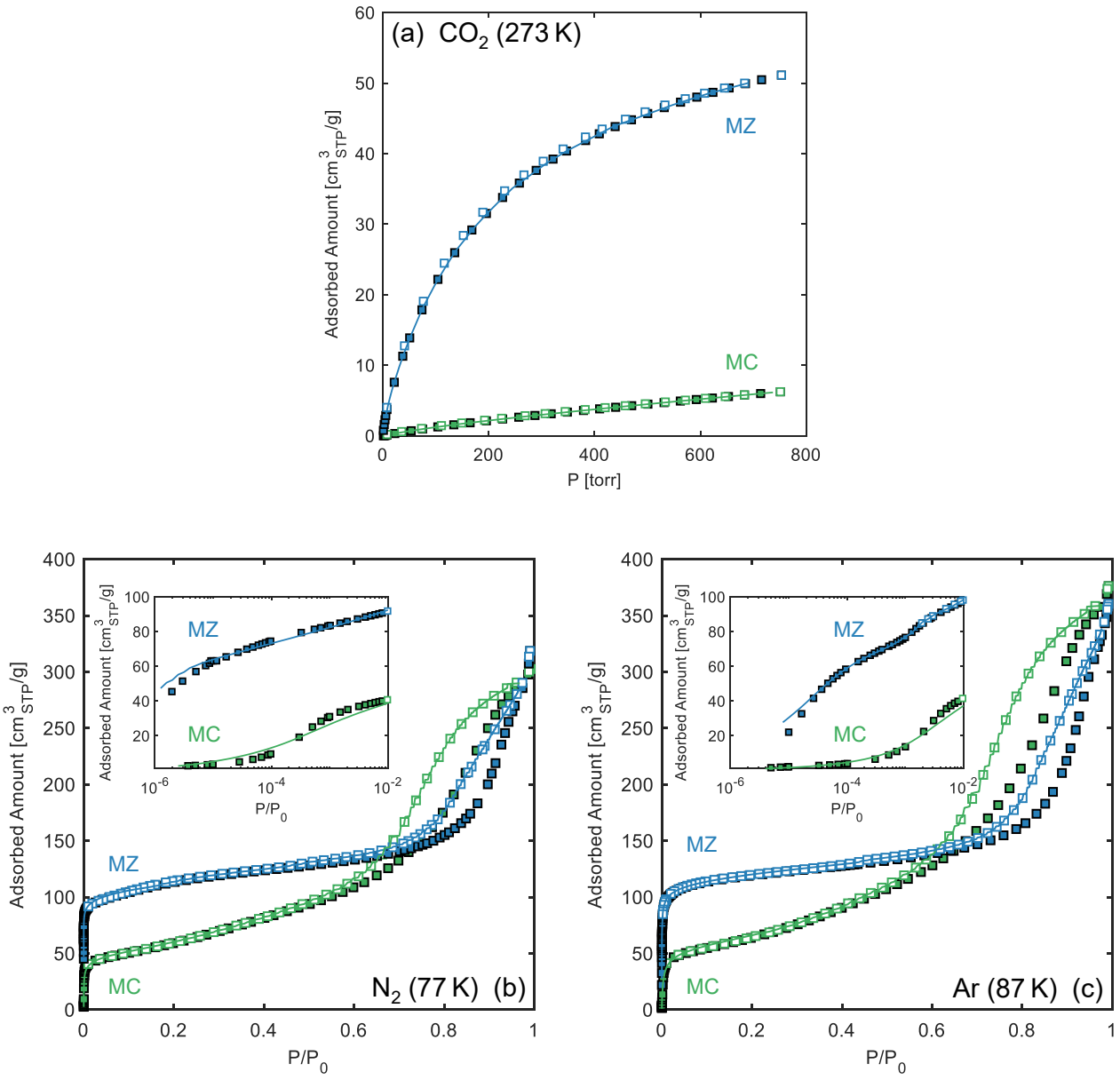

Figure 5.2: (a) CO_2 (273 K), (b) N_2 (77 K) and (c) Ar (87 K) physisorption isotherms measured in both adsorption (filled symbols) and desorption (empty symbols) mode on mesoporous carbon (MC) and mesoporous zeolite (MZ). STP conditions are defined as 273.15K and 1 atm. P_0 is the saturation pressure at the measurement temperature ($\sim$ 760 torr). Lines show the modelled NLDFT or GCMC isotherms. Insets show a closer view of the low pressure region.

and total pore volume ($\nu_{\text{tot}} = \nu_{\text{mic}} + \nu_{\text{mes}} + \nu_{\text{mac}}$) are reported in Table 5.1. It can be seen that the results obtained on MC using Ar and N_2 are in excellent agreement, with deviations on the obtained SSA and ν_{tot} of 0.8% and 2.4%, respectively. Mesopores contribute to more than 98% of the total pore volume and the data also agree with specifications provided by the supplier, i.e. $\nu_{\text{tot}} \approx 0.5$ cm^3/g and SSA $\approx 150 - 250$ m^2/g [234]. The total pore volume of AC is about 40% larger than the value computed for MC and is mostly contained in the micropores ($\sim$ 70 vol.%). Notably, both the total pore volume and specific surface are higher than literature values reported for N_2 physisorption analysis ($\nu_{\text{tot}} = 0.40 - 0.50$ cm^3/g and SSA $= 697 - 1220$ m^2/g) [235, 236, 237, 238]. This observation supports

the common perception that Ar is more suited to the assessment of microporosity as compared to N_2, which is affected by limited diffusion at the conditions of the experiments [114]. Our results on AC Norit RB3 agree reasonably well with properties reported for the AC Norit R1 used in this study for the analysis of supercritical adsorption, namely $\nu_{tot} = 0.605$ cm^3/g [219] and SSA = 1339 m^2/g [180]. MZ also has a slightly higher total pore volume than MC (5% based on Ar) and, similar to AC, there is a significant discrepancy between the N_2 and Ar results (ν_{tot} - 6.3% and SSA - 43%). This also stems from MZ's considerable microporosity of $\sim$ 38 vol.%. The relative mesoporosity within the three synthetic materials is in the order AC < MZ < MC, which also means that the SSA of the two more microporous materials (> 1300 m^2/g) is substantially higher than for MC.

Table 5.1 also shows the results of the GCMC model fitting applied to the CO_2 isotherms shown in Figure 5.2a. The micropore volume obtained corresponds to pores less than $\sim$1.5 nm in size. Although the combination of CO_2 (273 K) and N_2 (77 K) is considered ideal for investigating both micro- and meso-porosity in a material [114], there is some debate about the CO_2 liquid density that occupies the micropores. Typically, the density at the adsorbate's boiling point is assumed, which is reasonable for experiments with adsorbates whose density does not vary significantly beyond the boiling point (like N_2 or Ar). For CO_2, the density can change considerably, and so the choice of the density dictates the micropore volume obtained [117]. Additionally, for solids with polar surfaces, like zeolites, CO_2 is not considered suitable as it is has an even higher quadrupole moment than N_2 which affects the correlation between the micropore filling pressure and pore size [114]. Due to these concerns, we neglect the CO_2 results as a means to estimate micropore volumes for the synthetic materials.

5.1.2 Shales

The physisorption isotherms for the shales used in this study are shown in Figure 5.3. The shales show much lower ($\sim$ 10 times) adsorption than the synthetic materials, indicating their lower total pore volume (Table 5.1). The N_2 and Ar isotherms are all virtually identical in shape (a composite of Type IV and Type II [114]). Adsorption proceeds with some micropore filling, followed by a gradual increase in uptake in the intermediate pressure range, leading to unrestricted monolayer-macropore adsorption as P/P_0 approaches 1. The desorption branch of the shale isotherm also exhibits a sharp closing of the hysteresis loop at $P/P_0 \approx 0.45$. The abrupt drop in adsorption in this range of relative pressure is due to the Tensile Strength Effect and is caused by the breakdown of the hemispherical meniscus during desorption in pores with diameters of less than 4 nm [239, 73]. The hysteresis loop is of Type H3 which is typical of certain clay minerals. The results show that the higher the adsorption, the larger the hysteresis. Generally, the adsorption capacity (and the total pore volume as shown in Table 5.1) is in the following order: Longmaxi > Marcellus > Bowland shales (as clearly shown by

Table 5.1: Textural properties of the synthetic adsorbents and shales considered in this study, obtained upon fitting the specified model kernel (with a fitting error as reported by the instrument software) to the desorption (synthetic adsorbents) or adsorption (shales) branch of the subcritical N_2 (77 K), Ar (87 K) or CO_2 (273 K) adsorption isotherm. Properties reported for the AC Norit R1 used in this study for the analysis of supercritical adsorption isotherms are also given, including SSA [180] and ν_{tot} [219]. [a] denotes measurements taken prior to the high pressure adsorption experiments.

Material	**Adsorbate**	**Model**	**Fitting Error (%)**	**SSA** (m^2/g)	$\nu_{\mathbf{mic}}$ (cm^3/g)	$\nu_{\mathbf{mes}}$ (cm^3/g)	$\nu_{\mathbf{tot}}$ (cm^3/g)
Synthetic Adsorbents							
MC	Ar	NLDFT (carbon, cylindrical)	0.739	218	0.003	0.452	0.456
	N_2	NLDFT (carbon, cylindrical)	0.734	219	0.008	0.437	0.445
	CO_2	NLDFT (carbon, slit)	0.027	–	0.030	–	–
AC (Norit RB3)	Ar	NLDFT (carbon, cylindrical)	0.237	1790	0.461	0.171	0.632
AC (Norit R1)	N_2	–	–	1339	–	–	0.605
MZ	Ar	NLDFT (zeolite, cylindrical)	0.334	1399	0.180	0.270	0.477
	N_2	NLDFT (zeolite, cylindrical)	0.430	976	0.130	0.300	0.449
	CO_2	GCMC (carbon, slit)	0.297	–	0.137	–	–
Shales							
B1	N_2	NLDFT (carbon, slit)	0.405	2.74	0.0003	0.009	0.025
	CO_2	NLDFT (carbon, slit)	0.054	–	0.0009	–	–
B2	N_2	NLDFT (carbon, slit)	0.362	1.69	0.0001	0.008	0.019
	CO_2	NLDFT (carbon, slit)	0.037	–	0.0019	–	–
B5	N_2	NLDFT (carbon, slit)	0.398	2.32	0.0003	0.011	0.021
	CO_2	NLDFT (carbon, slit)	0.041	–	0.0013	–	–
B6	Ar	NLDFT (silica, cylindrical)	0.535	4.10	0.0002	0.011	0.017
	N_2	NLDFT (silica, cylindrical)	0.633	4.06	0.0000	0.015	0.020
	CO_2	NLDFT (carbon, slit)	0.050	–	0.0033	–	–
B8	Ar	NLDFT (silica, cylindrical)	0.748	2.72	0.0000	0.010	0.018
	N_2	NLDFT (silica, cylindrical)	0.718	2.67	0.0000	0.011	0.015
	CO_2	GCMC (carbon, slit)	0.210	–	0.0021	–	–
B13	N_2	NLDFT (silica, cylindrical)	0.840	4.50	0.0000	0.018	0.024
	CO_2	GCMC (carbon, slit)	0.438	–	0.0048	–	–
LG3	Ar	NLDFT (silica, cylindrical)	0.441	17.3	0.0022	0.022	0.033
LG4	Ar[a]	NLDFT (silica, cylindrical)	0.256	69.0	0.0086	0.029	0.043
	Ar	NLDFT (silica, cylindrical)	0.315	67.2	0.0085	0.029	0.048
	N_2	NLDFT (silica, cylindrical)	0.265	42.5	0.0056	0.033	0.043
	CO_2	GCMC (carbon, slit)	0.286	–	0.0098	–	–
LG5	Ar	NLDFT (silica, cylindrical)	0.384	35.5	0.0046	0.023	0.037
ML	Ar[a]	NLDFT (silica, cylindrical)	0.465	12.7	0.0008	0.024	0.036
	Ar	NLDFT (silica, cylindrical)	0.493	8.71	0.0003	0.022	0.032
	N_2[a]	NLDFT (silica, cylindrical)	0.451	11.8	0.0003	0.028	0.035
	CO_2[a]	GCMC (carbon, slit)	0.441	–	0.0074	–	–
	CO_2	GCMC (carbon, slit)	0.561	–	0.0064	–	–

the CO_2 (273 K) measurements in Figure 5.3a). LG4 (organic-rich, more mature shale) is the highest adsorbing shale for all adsorbates while B8 (organic-lean, less mature shale) is the lowest.

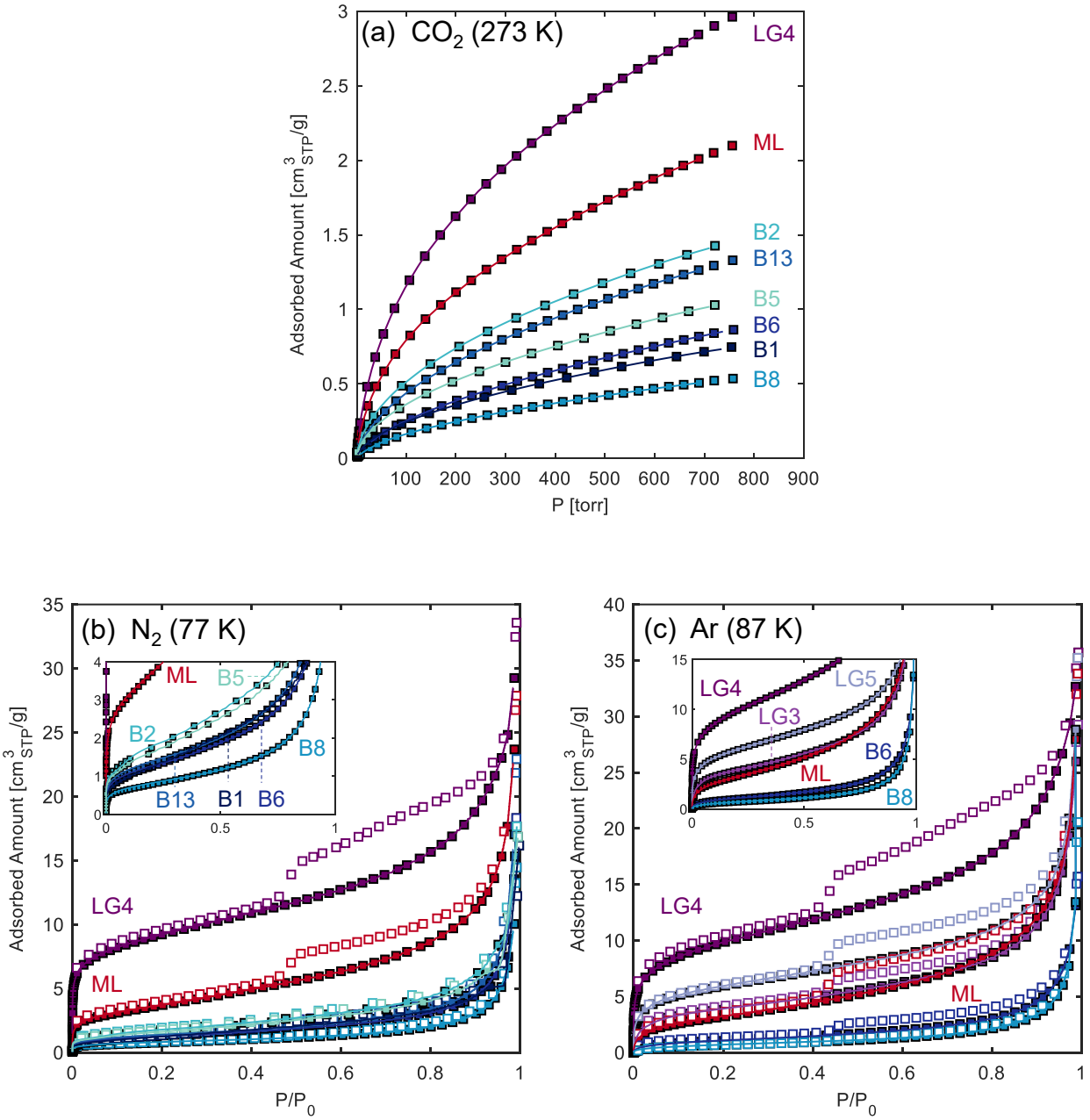

Figure 5.3: (a) CO_2 (273 K), (b) N_2 (77 K) and (c) Ar (87 K) physisorption isotherms measured in both adsorption (filled symbols) and desorption (empty symbols) mode on the Longmaxi (LG3, LG4 and LG5), Marcellus (ML) and Bowland (B1, B2, B5, B6, B8, B13) shales. STP conditions are defined as 273.15K and 1 atm. P_0 is the saturation pressure at the measurement temperature ($\sim$ 760 torr). Lines show the modelled NLDFT or GCMC isotherms. Insets show the adsorption branches in the low adsorption region.

The shale adsorption isotherms have also been interpreted by the application of DFT and GCMC models. These have solely been applied to the adsorption branch as often the Tensile Strength Effect can manifest itself as an artificial peak around 4 nm in the pore size distribution (PSD) if the desorption

branch is used [239]. Although the QSDFT model is more suitable for heterogeneous surfaces such as shale, its application often resulted in higher fitting errors than the NLDFT model. Therefore, the latter was used, and as Figure 5.3 shows, the model (solid lines) results in an excellent description of the N_2 and Ar isotherms. The textural properties of the shales obtained using each probing gas can also be seen in Table 5.1. Notably, the volumes and surface areas acquired are much lower than the synthetic materials. Additionally, these are systematically higher with Ar (4–22% for the total pore volume and 1–8% for the SSA) than with N_2 (with the sole exception of B6). For two shales, LG4 and ML, two sets of measurements can be seen in Table 5.1, before and after the high pressure adsorption experiments. These were conducted to ascertain any residual effects of long-term exposure to supercritical fluids at reservoir conditions on the shale during the high pressure MSB experiments. As these involve a higher sample mass ($>\sim$ 2 g) than the low pressure experiments ($<\sim$ 1 g), it cannot be guaranteed that the exact same aliquot was used for the repeated measurements. Nevertheless, the experiments with Ar post-MSB show that LG4 is fairly unaffected by the supercritical adsorption experiments; the SSA, micro- and meso-pore volume are similar before and after ($< 3\%$ change). The macropore volume is slightly higher after (reflected in the 11% increase in the total pore volume) but as the adsorption isotherms (Figure 5.3) do not reach a plateau at $P/P_0 = 1$, the total pore volume is difficult to estimate anyway [114]. On the other hand, there is a larger deviation in both the Ar and CO_2 measurements taken before and after the high pressure experiments for ML. The largest difference is in the micropore volume (Ar - 61% and CO_2 - 12%), which significantly decreases and this also directly impacts the SSA which shows a 32% decrease post-MSB. These results will be further discussed alongside the results of the supercritical adsorption experiments in Chapter 7.

Table 5.1 shows that the micropore volume for some Bowland shales (B6, B8 and B13), obtained from N_2 or Ar, is zero. For shales, where both adsorption and the available porosity is quite low and diffusional limits exist, the use of CO_2 at 273 K to probe the micropores is warranted. Indeed, the CO_2-modelled isotherms show micropore volumes that are non-zero for these particular shales and are consistently much higher than the obtained micropore volumes from N_2 or Ar for the other shales. The discrepancy could be due to under-equilibration in the N_2 or Ar measurements, which arises because of the low cryogenic temperatures and consequent slow diffusion rates [114]. This has also previously been shown to be true for pure clay minerals [72]. In particular, for narrow micropores, the kinetic restrictions can only be overcome by CO_2, which has a smaller kinetic diameter and has the added advantage of a higher experimental temperature and saturation vapour pressure, which lower the risk of under-equilibrated measurements [114]. Therefore, we can combine the results from CO_2 (microporosity) and either N_2 or Ar (mesoporosity) to obtain the complete pore size distribution of the shale. In this work, this has been done by replacing the distribution (including volume and surface area) $<\sim$ 1.5 nm from N_2 or Ar, with the total distribution from CO_2. Table 5.2 shows the modified

SSA, micropore and total pore volumes for all the shales. The mesopore volume was acquired from the Ar measurements wherever possible and is replicated from Table 5.1.

Table 5.2: Textural properties of the shales considered in this study, obtained upon combining the results of fitting either N_2 (77 K) or Ar (87 K) and CO_2 (273 K) adsorption isotherms with the NLDFT and GCMC models. [a] denotes samples using only pure Ar results.

Shale	**SSA** (m^2/g)	$\nu_{\mathbf{mic}}$ (cm^3/g)	$\nu_{\mathbf{mes}}$ (cm^3/g)	$\nu_{\mathbf{tot}}$ (cm^3/g)
B1	5.51	0.001	0.009	0.025
B2	7.39	0.002	0.008	0.021
B5	6.32	0.002	0.011	0.022
B6	13.2	0.003	0.011	0.020
B8	8.54	0.002	0.010	0.020
B13	18.4	0.005	0.018	0.029
LG3[a]	17.3	0.002	0.022	0.032
LG4	46.0	0.011	0.029	0.050
LG5[a]	35.5	0.005	0.023	0.037
ML	29.4	0.007	0.024	0.042

Table 5.2 shows that the shales do have some microporosity (ranging from 4.6% to 21%), but mesopores dominates their PSDs (34–69%). This is actually quite similar to MZ which has a micro- and meso-porosity of 38% and 57%, respectively. However, the SSA of the shales is almost two order of magnitudes lower than the synthetic materials. Within the shales, the organic-rich mature shales, LG4 and ML, have almost double the total pore volume of the Bowland shales. The relationship between the various textural properties and the composition of shales (TOC or clay content) is illustrated by Figure 5.4. The figure additionally shows linearly-scaled properties (dashed lines) of pure carbon (a combination of MC and AC) and Illite (IMt-2, data from Hwang and Pini (2019) [72]), the dominating clay mineral in this assortment of shales. As the shales have an average mesoporosity of 54%, the carbon component is represented by a weighted average of the textural properties of MC and AC in the ratio 60:40 (MC:AC). As Figure 5.4 shows, most of the properties seem to fall in two distinct groups as a function of shale composition. Therefore, the shales have been segregated into two different categories, thermally mature (Longmaxi and Marcellus shales, in purple) and relatively immature (Bowland shales, in blue) shales. Chapter 3 outlined two separate mineralogies for some of the Bowland shales (Table 3.1). In particular, B6 showed the greatest discrepancy between the measured TOC and and all shales showed an increased amount of clay content in the second study. To draw a comparison between the properties and composition, the Bowland shales have also been divided into two groups: (1) B2, B8 and B13 (light blue points), and (2) B1, B5 and B6 (dark blue points). This is because for Group 1, the TOC is fairly consistent between the two studies. Therefore, an average of the two TOC values has been taken for each of these shales. For Group 2, either no repeated measurement exists (B1 and B5) or there is a considerable difference between the organic content of the two studies (B6). Additionally, the clay content for Group 1 is denoted by the second set of measurements as these are more in line with typical shales (see Chapter 2). Figure 5.4 shows

lines of best fit (solid lines); these are based on Group 1 for the Bowland shales (blue line). The composition of the Group 2 (both TOC and clay content) has then been calculated based on these lines of best fit and an average has been taken between the results of the four correlations shown in Figure 5.4. Based on this analysis, the (new) composition of the Group 2 shales is shown in Table 5.3.

Table 5.3: The composition of certain Bowland shales calculated from correlating shale textural properties and composition of other Bowland shales.

Shale	**TOC**	**Total Clay Content**
B1	1.39	22.5
B5	1.75	22.7
B6	3.30	25.5

The 'new' composition of B6 is actually very similar to the second set of measurements shown in Table 3.1 (TOC - 3.6 wt% and clay content - 23.4 wt%). This is also true for the TOC in B1 (= 1.40 wt% from the first set of measurements in Table 3.1). Furthermore, both B1 and B5 show clay content values that align well with typical shales. The only real change is in the B5 TOC, which was previously reported as 3.2 wt%.

Figure 5.4a indicates that an increase in TOC results in an increase in micropore volume, and there is a fairly good linear correlation between the two quantities. This is particularly true for the thermally mature shales where $R^2 = 0.93$. For these shales, the scaled pure carbon dashed line agrees reasonably well with calculated micropore volumes. In fact, the mature shales have a higher mesopore fraction (58–69%) so if the ratio of MC:AC was modified to reflect this, the agreement could be even better. At low TOC, the shale thermal maturity matters less and the y-intercept of both lines of best fit in Figure 5.4a is almost the same (~ 0.0013 cm^3/g). The relationship between the micropore volume and clay content (Figure 5.4b) is also linear, although the thermally mature shales show a negative correlation ($R^2 = 0.78$), while the Bowland shales show a positive correlation ($R^2 = 0.86$). Illite, the principal clay mineral in the shales, influences the presence of microporosity and small mesopores [73], which is why its scaled micropore volume agrees fairly well with the shales, particularly for the Bowland shales.

Similar trends are observed in both the mesopore volume (Figures 5.4c and 5.4d) and total pore volume (Figures 5.4e and 5.4f). With TOC, the lines of best fit are almost parallel for both groups of shales; the mature shales seem to be offset by a certain pore volume, indicated by the higher intercept on the y-axis. Both groups have stronger correlations with the total pore volume (thermally mature shales - $R^2 = 0.94$ and Bowland shales - $R^2 = 0.59$) than the mesopore volume. At intermediate to higher TOC, the pure carbon dashed line agrees reasonably well with the calculated mesopore or total volumes. This is the inverse of the micropore volume, which means that if the MC:AC ratio was improved to incorporate more mesoporosity, the agreement could be better. At low TOC, it

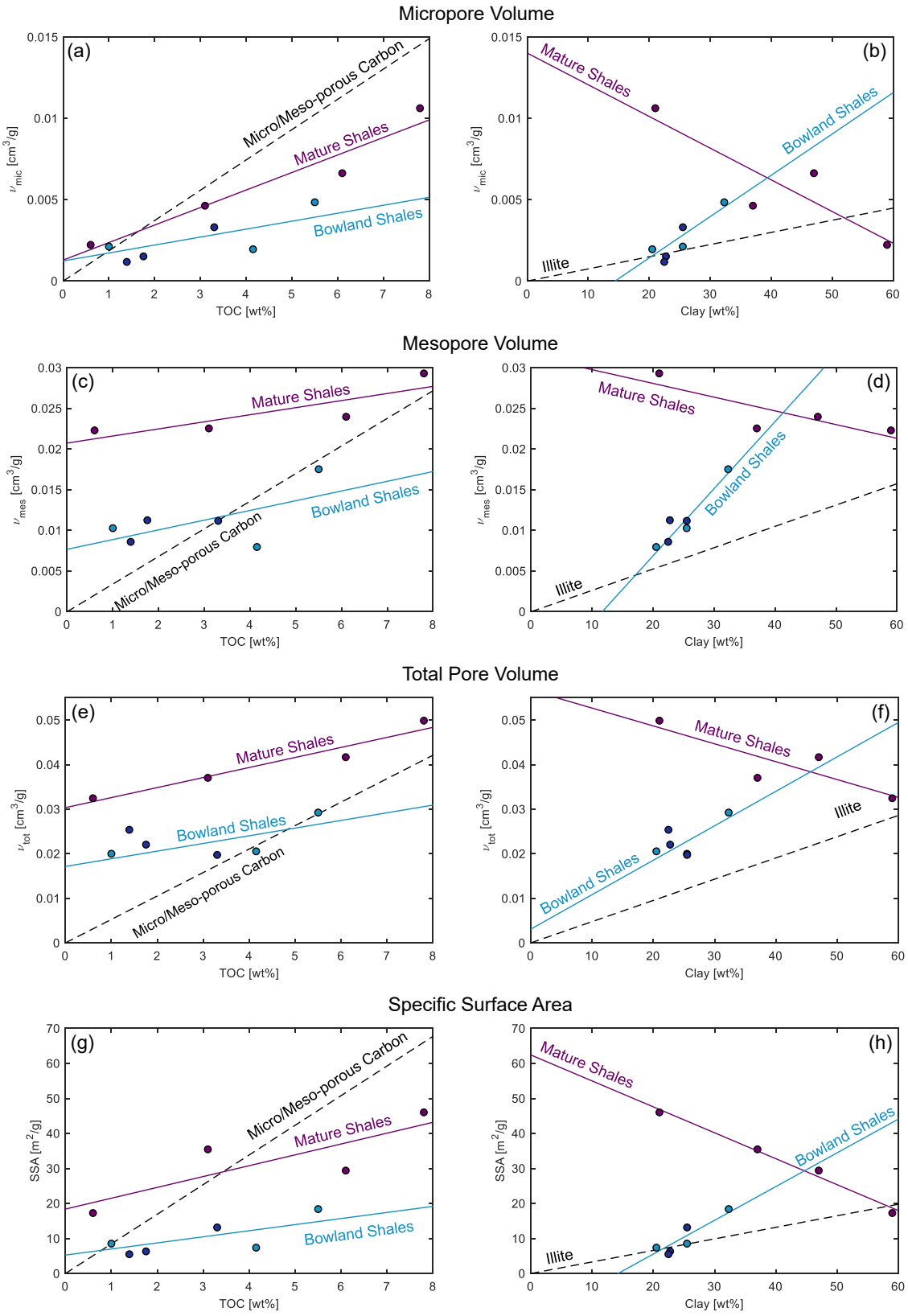

Figure 5.4: Textural properties of shales, including the micropore volume (a, b), mesopore volume (c, d), total pore volume (e, f) and specific surface area (g, h), as a function of TOC or clay content. Points show the properties derived from physisorption, and solid lines denote lines of best fit. Purple refers to the Longmaxi and Marcellus (more thermally mature) shales, while blue refers to the Bowland shales. The light blue points were used to compute the lines of best fit for the Bowland shales, from which, the composition of the dark blue points were derived. Dashed black lines denote the scaled textural properties of MC/AC (60%:40% ratio) or pure Illite [72].

is evident that the mesopore volume (and the total pore volume) originates from other constituents (such as the clay minerals) and not just the organic content, a fact further reinforced by the non-zero intercept of the lines of best fit. The study on adsorption on pure clay minerals helps explain this discrepancy. The Bowland shales specifically show a very strong correlation with clay content for both volumes (mesopore - $R^2 = 0.96$ and total - $R^2 = 0.78$). The darker blue points (with the predicted composition based on all four factors) also agree reasonably well with the line of best fit. The thermally mature shales have a larger distribution of clay content and the (negative) linear correlations with clay content are still quite strong. The Illite line is not as strong a predictor as the pure carbon line and seems to consistently underestimate the pore volume, but compaction can cause some changes in the properties of clays within shales (as compared to pure clay minerals), which might be a reason behind the discrepancy [69].

The specific surface area versus clay content is one of the strongest correlations in this study, particularly for the thermally mature shales where $R^2 = 0.99$ (Figure 5.4h). The pure Illite results (dashed black line) are in a reasonably good agreement with the calculated surface areas for the Bowland shales. The same is also true for the pure carbon dashed line $<\sim 2$ wt% TOC (Figure 5.4g). At higher TOC, the SSA is overestimated due to the incorporation of 40% microporosity in the dashed black line. The trends outlined above and the linear form of these correlations also agree with the literature on various other shales [58, 81].

Generally, the thermally mature shales have stronger correlations between various textural properties and the shale composition. The lowest R^2 value for these shales is 0.68 versus 0.31 for the Bowland shales. The correlations are generally stronger with TOC, proving the importance of the TOC in influencing important shale properties and driving the total adsorption capacity, especially with TOC-rich shales. TOC correlates positively with all properties, irrespective of thermal maturity. On the contrary, the clay content has opposing correlations for the thermally mature (negative correlations) and Bowland (positive correlations) shales. The reasonably good predictions by the pure carbon adsorbents enforces the strength of these materials as suitable analogues for the TOC in shales.

5.2 Textural Characterisation by Supercritical Adsorption

5.2.1 Synthetic Adsorbents

The PSD obtained from the subcritical adsorption data described in the previous section is presented in Figures 5.5a (MC), 5.5b (AC) and 5.5c (MZ). It can be seen that MC possesses a rather narrow

distribution of mesopores centred at about 8.4 nm, while AC is dominated by micropores (<2 nm) and small mesopores (3-5 nm). MZ possesses significant porosity below 1 nm and a distribution of mesoporosity centred at ~ 14 nm.

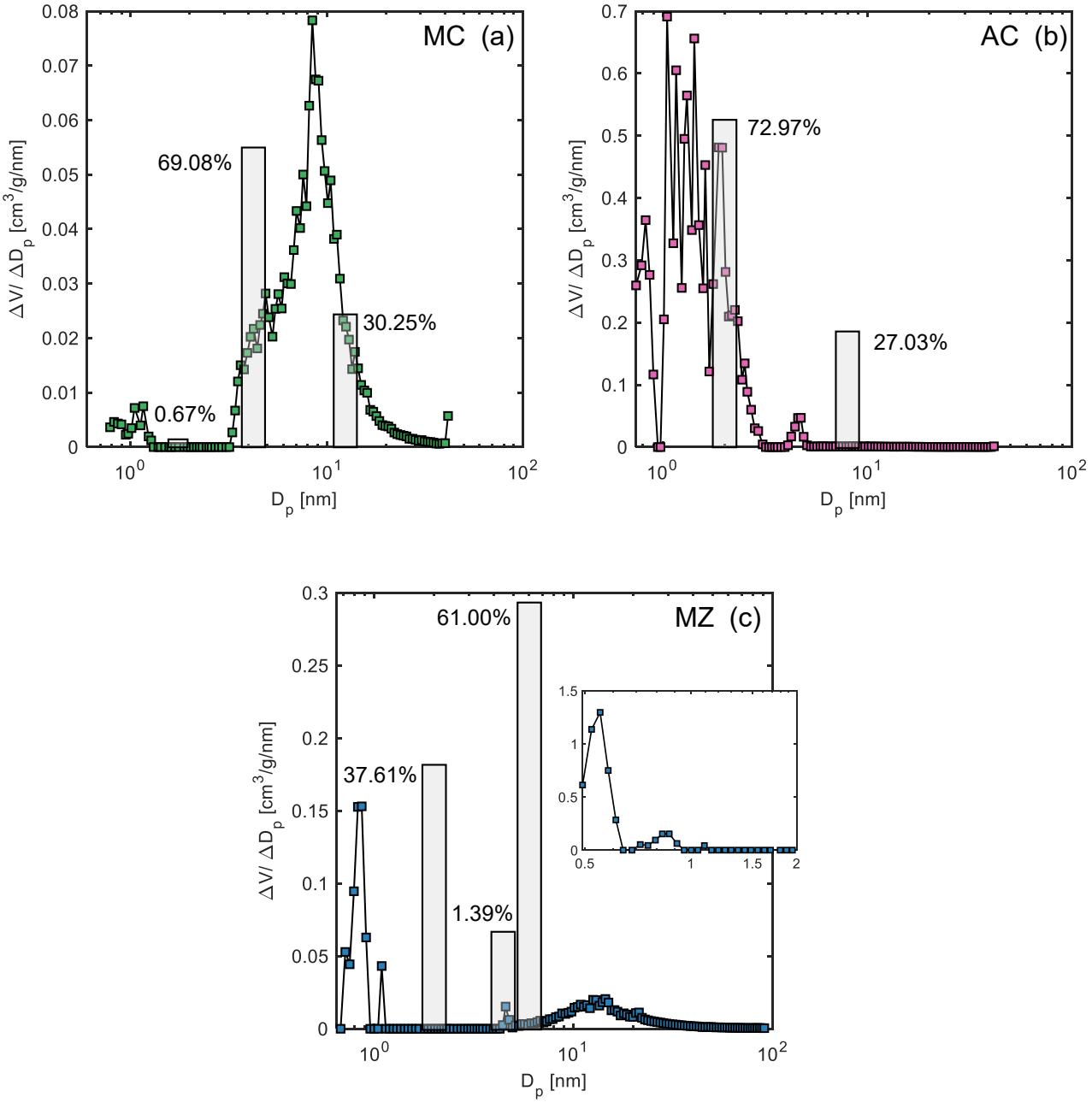

Figure 5.5: The PSD calculated from the desorption branch of the Ar data for (a) mesoporous carbon (MC), (b) activated carbon (AC) and (c) mesoporous zeolite (MZ) using the NLDFT models. The bars represents the discretised PSD obtained from the lattice DFT model; for MC, the selected pore sizes, D_{p}, corresponds to cylindrical pores with $J = 2$ (0.67 vol%), 6 (69.08 vol%) and 15 layers (30.25 vol%). For AC, the selected pore sizes corresponds to cylindrical pores with $J = 3$ (72.97 vol%.) and 11 (27.03 vol%.) layers. For MZ, the cylindrical pore sizes correspond to $J = 3$ (37.61 vol%), 6 (1.39 vol%) and 8 (61.00 vol%) layers. The inset shows the micropore volume for MZ.

The vertical bars plotted alongside the computed PSD in the figure represent the discretised pore size distribution used in the lattice DFT model. To identify the representative pore classes for MC, AC,

and MZ, only the excess adsorption isotherm measured with CO_2 at near-critical conditions (35–40 °C) was considered. To this aim, a fixed number of pore classes were used as additional fitting parameters, while constraining their volume, $\nu_{p,k}$, to the experimentally-obtained PSD (from Ar physisorption at 87 K). In particular, the pore volume allocated to a given pore class k with J_k layers was obtained as the sum of the pore volume in the range $[\nu_{p,k}, \nu_{p,k+1}]$, with the exception of the smallest pore class, for which $\nu_{p,k}$ represents the cumulative specific pore volume up to that pore size. The number of classes, K, was selected by applying the fitting procedure iteratively for increasing number of pore classes until the improvement in the value of the objective function was too minor to warrant an additional parameter. The objective function was minimised using the genetic algorithm (`ga`) available in the MATLAB global optimization toolbox. The population size was 100 times the number of fitted parameters and the number of generations were 100 (although often fewer generations were required to achieve the default tolerance level of 1×10^{-6}). Lower and upper bounds were specified for the fitting parameters and these were progressively narrowed on the basis of the optimal parameters, to achieve a lower value for the objective function Φ. Only integer values were considered for the number of layers, J_k, and a penalty was specified if two classes had the same number of layers. This reduced distribution of pores is used to describe the adsorption of CO_2 at the other temperatures and the full set of CH_4 isotherms.

The model fits to the near-critical CO_2 isotherms for all three adsorbents are shown in Figure 5.6 together with the individual contribution from each pore class to the total excess amount adsorbed. Starting from an initial population of 4 pore classes, the lattice DFT model identified that three (MC, MZ) and two (AC) pore classes are sufficient to accurately describe the supercritical adsorption isotherm over the full range of density values ($0 < \rho/\rho_c < 2.25$, corresponding to pressures up to 25 MPa for MC and MZ and 50 MPa for AC). For MC these classes are associated with pores of size 1.2 nm, 4.4 nm and 11.6 nm, for AC with pores of size 2 nm and 8.4 nm, and MZ with pores of size 2 nm, 4.4 nm and 6 nm. The key observation from Figure 5.6 is that, similar to the physisorption analysis applied to subcritical isotherms, isotherms measured slightly above the critical point of the fluid ($T/T_c = 1.01$–1.03 in this case) also manifest pore size dependent adsorption behaviour, which is reflected in the shape of the isotherms. In particular, the isotherm measured on MC is dominated by the characteristic late filling of mesopores ($J = 5$ and 12) that results in the maximum excess amount adsorbed being attained at a relatively large bulk density ($\rho_b \approx 6$ mol/L). On the contrary, the isotherm measured on AC is dominated by the early filling of micropores ($J = 3$) and only partly by the filling of the mesopores ($J = 10$), and the maximum excess amount adsorbed is observed at a much lower bulk density ($\rho_b \approx 3$ mol/L). MZ shows a much broader peak reflecting its dual-porosity nature; micropore filling ($J = 3$), followed by the filling of small mesopores ($J = 6$ and 8) leads to the maximum excess amount being achieved at $\rho_b \approx 5$ mol/L (between the equivalent densities of MC

and AC).

Moreover, beyond its maximum point, the isotherm measured on MC is concave, while the one measured on AC is more linear and reminiscent of the behaviour observed with microporous adsorbents [117]. MZ incorporates both these features. This behaviour can be traced back to the definition of the excess adsorbed amount ($n^{\mathrm{ex}} = n^{\mathrm{a}} - \rho_{\mathrm{b}} V^{\mathrm{a}}$), which implies a linear dependency with bulk density upon attainment of adsorption saturation (complete micropore filling, with n^{a} and V^{a} approaching a constant value). This sensitivity at (slightly) supercritical conditions of the adsorption behaviour to the characteristic pore structure of the material offers a powerful complementary tool for the textural characterisation of porous materials, enabling the identification of those pore classes that provide the strongest contribution to supercritical adsorption.

5.2.2 Shales

The pore size distributions of the four shales considered for the high pressure experiments (LG4, ML, B6 and B8) are shown in Figure 5.7. It is evident that the shales incorporate a diverse range of pore sizes, which is quite different to the synthetic materials (Figure 5.5). The distribution is multi-modal below 2 nm, but is fairly unimodal in the mesopore range. In fact, the peak around 4–6 nm is present for all shales, albeit with disparate peak sizes. This peak can partly be explained by Illite, the dominant clay mineral in these shales. The PSD of Illite (IMt-2 from the Clay Minerals Society), using both CO_2 and Ar, is replicated from Hwang and Pini (2019) [72] and is shown in Figure 5.8b. Illite also possess the same unimodal mesopore distribution centred around a peak at 4–6 nm (the same pore sizes) as the shales. The micropore peaks at 0.6 nm and 0.8 nm are also commonly retained by all shales and Illite, but the peak at ~ 2 nm is only held by the thermally mature shales and IMt-2. Above 50 nm (not shown in the figure), the size distribution is almost identical for all five materials. The shale that most closely resembles Illite's volume distribution (including peak locations and size) is the Marcellus shale (ML), which is the most clay-rich (47 wt%) in this particular collection of shales. Both have a very similar total pore volume ($\nu_{\mathrm{tot}} = 0.048$ cm^3/g and 0.042 cm^3/g for Illite and ML, respectively) and proportions of micro- (16–17%) and meso-porosity (55–57%). At almost all pore sizes, the pore volume is in the following order: LG4 > ML > B6 > B8. This is also the decreasing order of TOC in each shale.

The textural properties of shales obtained from subcritical adsorption were interpreted with the aid of the synthetic adsorbents and pure clay minerals (Section 5.1.2). This analysis demonstrated that combinations of analogue materials such as pure carbons and clays are able to capture the compositional dependence of the textural properties of shales to a reasonable degree. As the number of developed shale plays continues to grow in the world, it is important that future work incorporates

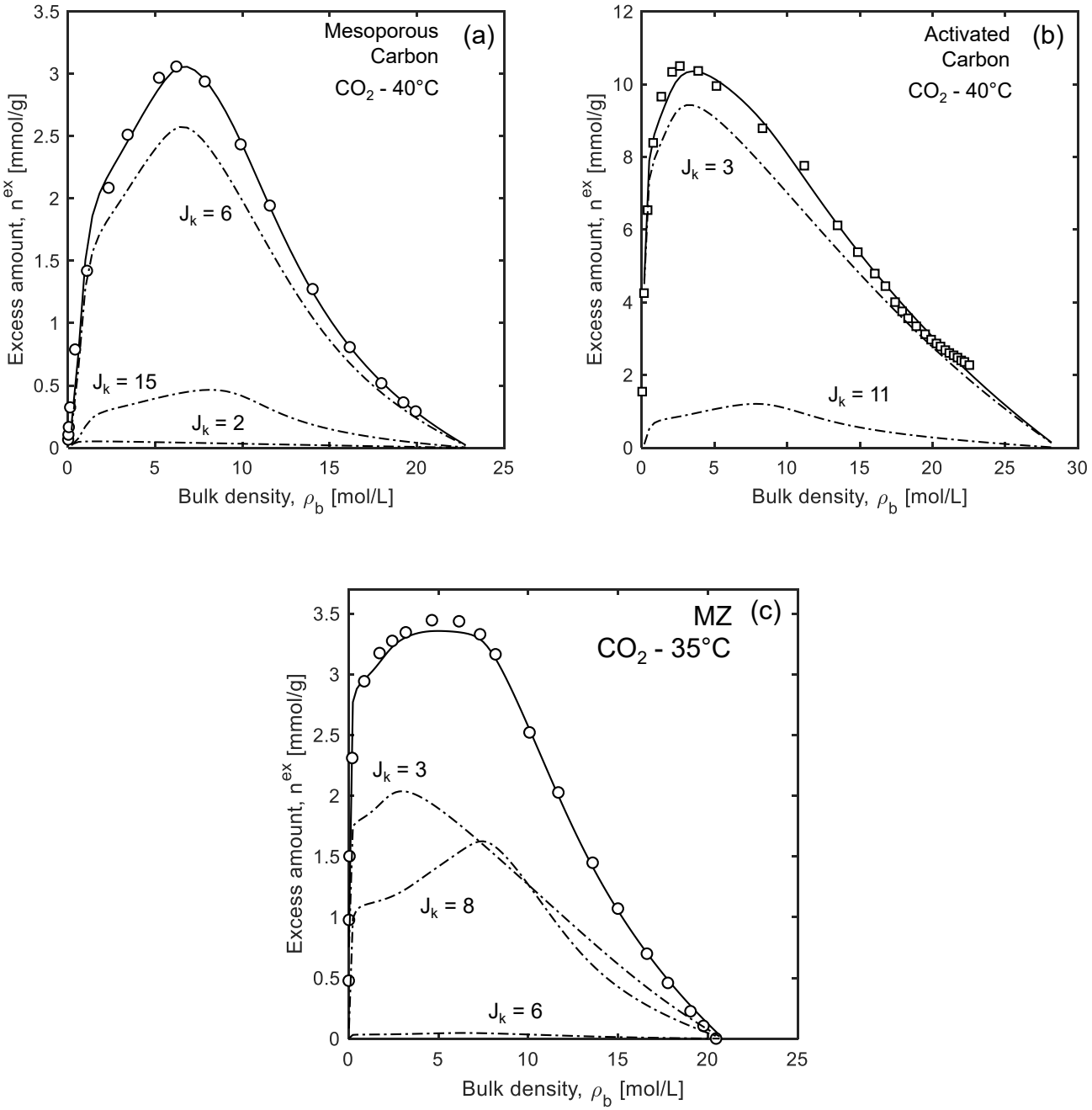

Figure 5.6: Near-critical CO_2 adsorption isotherms for (a) mesoporous carbon (at 40 °C, data measured in this study), (b) activated carbon (at 40 °C, data by Ustinov et al. (2002) [219]) and (c) mesoporous zeolite (at 35 °C, data measured in this study). Symbols represent experimental data, while the solid lines denote optimum fits from the lattice DFT model. The dot-dashed lines are isotherms computed for each pore class k and are labelled in terms of the number of lattice layers J_k.

the use of these analogues and minimises the necessity of lengthy adsorption experiments with each and every shale. To this end, the discretised PSD for the shales was therefore not obtained by implementing the workflow utilised by the synthetic materials, namely by modelling the near-critical CO_2 isotherm. Instead, the synthetic adsorbents and pure clay minerals were used for this purpose. The same workflow as the synthetic adsorbents was applied to a near-critical CO_2 isotherm (50 °C, where $T/T_c = 1.06$) on Illite (data from Hwang and Pini (2019) [72]), as shown in Figure 5.8. Like

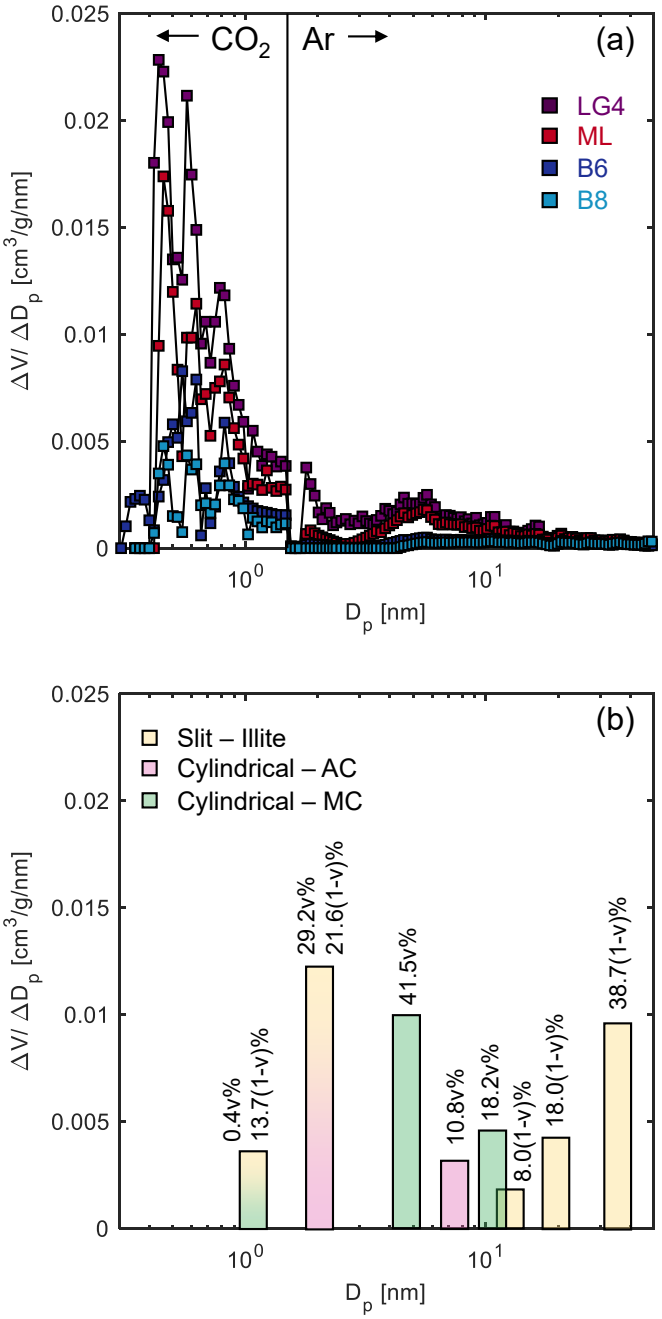

Figure 5.7: (a) The PSD (up to 50 nm) calculated from the Ar (87 K) and CO_2 (273 K) adsorption data using the NLDFT and GCMC models for all shales considered in the high pressure adsorption experiments. (b) The discretised PSD used in the lattice DFT model for the shales. The bars represents a combination of the discretised PSD obtained from the lattice DFT model applied to MC (green bars), AC (pink bars) and Illite (yellow bars). The selected pore sizes, D_{p}, with a slit pore geometry are 1.2 nm, 2 nm, 12.4 nm, 18.8 nm and 36.4 nm and the pore sizes with a cylindrical pore shape are 1.2 nm, 2 nm, 4.4 nm, 7.6 nm and 11.6 nm. The volume assigned to each bar is also based on the same pure adsorbents but is scaled using a scaling factor (v) which is the volume fraction of TOC in each shale. The MC and AC volumes have been combined in the ratio 60:40.

MZ, Illite's maximum excess adsorbed amount occurs at around $\rho_{\mathrm{b}} \approx 5$ mol/L. The isotherm shows a steep uptake at lower densities and emulates MC in its concave non-linear descent at higher pressures. The lattice DFT fit is based on hexagonal packing ($z^{\mathrm{b}} = 12$, $z^{\mathrm{s}} = 6$ and $z^{\mathrm{a}} = 3$) of CO_2 molecules

in slit pores. The Illite pore classes represent slit pores of size 1.6 nm, 2 nm, 12.4 nm, 19.2 nm and 36.4 nm.

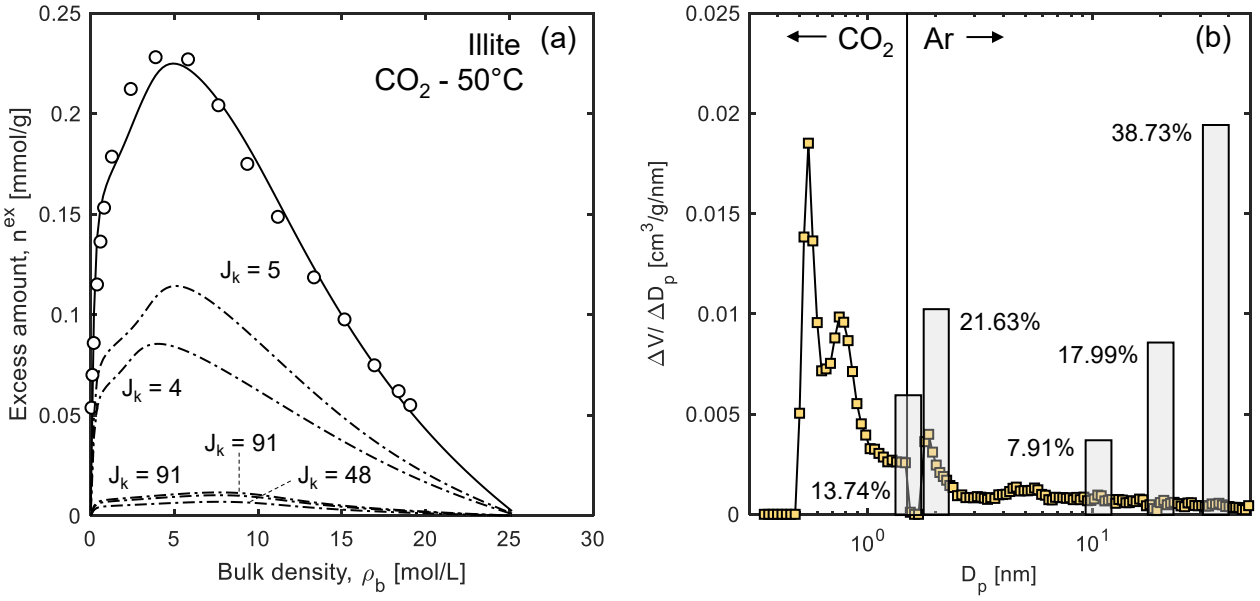

Figure 5.8: (a) CO_2 adsorption isotherm at 50 °C for Illite (IMt-2, data by Hwang and Pini (2019) [72]). Symbols represent experimental data, while the solid lines denote optimum fits from the lattice DFT model. The dot-dashed lines are isotherms computed for each pore class k and are labelled in terms of the number of lattice layers J_k, (b) The PSD (up to 50 nm) calculated from the Ar (87 K) and CO_2 (273 K) data using the NLDFT and GCMC models [72]. The bars represents the discretised PSD obtained from the lattice DFT model; the selected pore sizes, D_{p}, corresponds to slit pores with $J = 4$ (13.74 vol%), 5 (21.63 vol%), 31 (7.91 vol%), 48 (17.99 vol%) and 91 layers (38.73 vol%).

As discussed above, the pore size distribution of shales obtained from the subcritical adsorption experiments includes both micropores and mesopores. This distribution should exist in both the TOC and clay minerals, components which have two different surface chemistries. Therefore, to obtain the discretised PSD to use in the hybrid lattice DFT model for shales, the representative pore classes determined for MC and AC (cylindrical pores) and pure Illite (slit pores) were combined in proportions based on the shale composition to mimic the shale pore space; Figure 5.7b shows vertical bars representing these classes. As various combinations of slit and cylindrical pores in the lattice DFT model are considered in this thesis, some of the slit pore sizes ($D_{\mathrm{p},J} = Jd$) that were identified by the lattice DFT model for Illite, such as 1.6 nm and 19.2 nm, had to be modified so that a cylindrical pore ($D_{\mathrm{p},J} = d(2J-1)$) of the same size would result in the number of layers, J, being an integer; for these classes, the pore size has been decreased by 0.4 nm. Therefore, the reduced PSD for the shales includes cylindrical pores of size $D_{\mathrm{p},J} = [1.2, 2, 4.4, 7.6, 11.6]$ nm (pink and green bars in Figure 5.7b) and slit pores of size $D_{\mathrm{p},J} = [1.2, 2, 12.4, 18.8, 36.4]$ nm (yellow bars in Figure 5.7b). The volume assigned to each pore class is also based on the discretised PSDs from the two porous carbons and Illite but the volume has been scaled based on the composition of each shale. The scaling factor used, v, is the normalised volumetric fraction of the TOC in each shale. Furthermore, the volume allocated

to the cylindrical pores is based on MC:AC in the ratio 60:40. The pore volume represented by each pore class is labelled adjacent to the bar in Figure 5.7b. The two dual-coloured bars, denoting the two micropore classes of $D_p = 1.2$ nm and 2 nm, signify the representation of these two pore classes by both slit and cylindrical pores. As this discretised PSD is based on analogue materials that are representative of the shale pore space, it should be useful for analysis of any shale, even outside this study, as it avoids a heavy experimental burden and relies purely on the shale mineralogy. As with the synthetic adsorbents, this reduced distribution was used to model both CO_2 and CH_4 supercritical adsorption isotherms at various temperatures for the shales considered in this work.

5.3 Conclusion

A combined experimental and modelling approach for textural characterisation, using gas adsorption data acquired at subcritical and supercritical conditions, was applied to three synthetic adsorbents (two porous carbons, MC and AC, and mesoporous zeolite, MZ) and shales, in this chapter. While robust experimental protocols and theoretical frameworks exist for extracting textural information from the adsorption of N_2 and Ar at their standard boiling point, attempts of using supercritical data have so far been only partly successful, because of the following two reasons. First, the weaker sensitivity of supercritical adsorption on the geometry and size of pores requires the measurements to be conducted at sufficiently large pressures and at temperatures that are relatively close (10 K in this study) to the critical temperature of the adsorptive. Second, the simulation of supercritical adsorption has almost exclusively been done for micro- and meso-slit pores, thereby neglecting the topological characteristics of many porous structures.

To this end, the lattice Density Functional Theory (DFT) model was used to identify characteristic sizes upon calibration against outcomes from textural analysis by Ar (87 K) adsorption. Both the experimental and modelling results highlight the effects of each adsorbent's pore size distribution on supercritical adsorption and we contend that the model's predictive capability can be integral to the characterisation of other adsorbents at supercritical conditions. Moreover, by extending the characterisation effort over a wider range of conditions, the combination of sub- and super-critical adsorption data increases the robustness of the analysis, in addition to mimicking more closely the conditions of many industrial applications of adsorption.

The subcritical adsorption measurements with shale revealed the dependency of textural properties, such as micropore volume and specific surface area, on the composition of shale. In addition, the obtained PSDs showed that the shale pore space is represented by a wide distribution of pore sizes that includes both micropores and mesopores. The results from the characterisation workflow applied

to the model sorbents (MC and AC) and a pure clay mineral (Illite, IMt-2) were used to develop the discretised PSD for use in the hybrid lattice DFT model to describe supercritical adsorption in shale. The only additional information required to use this PSD is the normalised volume fraction of the TOC in each shale.

Chapter 6

Supercritical Gas Adsorption in Synthetic Adsorbents

This chapter presents the results of the high pressure adsorption measurements and modelling on the synthetic adsorbents, mesoporous carbon (MC), activated carbon (AC) and mesoporous zeolite (MZ). The discussion commences with the description of the experimental results, which is followed by the the lattice DFT modelling of these measurements. Henry constants and the isoteric heat of adsorption are then quantified using both approaches. Finally, the effect of the pore geometry on the adsorption modelling results is ascertained and the lattice DFT is compared to the Langmuir model. Some of the material in this chapter has been published in Ansari et al. (2020) [29] and Pini et al. (2021) [233].

6.1 Supercritical Adsorption Measurements

6.1.1 Excess Adsorption

Unary excess adsorption isotherms measured with CO_2 and CH_4 on MC at temperatures of 40 °C, 60 °C and 80 °C are shown in Figure 6.1a as a function of bulk density. In Figure 6.1b, the corresponding bulk density values measured *in situ* are plotted alongside data reported by NIST (shown as solid lines); an excellent agreement is observed between the two data sets with an average residual sum of squares of 0.4141 $(\text{mol/L})^2$ (CO_2) and 0.0008 $(\text{mol/L})^2$ (CH_4). The results from Helium gravimetry, which are used to estimate V_0, are reported later in this chapter. CO_2 adsorbs up to three times more than CH_4 on MC, as a result of the higher-order electric multipole moment of the former that leads to a stronger affinity to the carbon surface [240]. Additionally, we note that the experiments have been carried out at a temperature that is relatively close to the critical temperature of CO_2; this

further suggests that in the adsorbed state, CO_2 will have a higher isothermal compressibility than CH_4 leading to a potentially higher selectivity [241]. For both adsorptives, the excess amount adsorbed increases monotonically with density before reaching a maximum value and gradually decreasing with increasing density. For CO_2, the excess amount adsorbed approaches zero at the highest pressure of the experiment, indicating that at these conditions the average density values of the bulk and adsorbed fluid are almost identical and the two phases are indistinguishable. The CH_4 isotherms show less of this effect, as such high bulk densities are never achieved at the maximum pressure in our experiment (25 MPa). As expected, the excess amount adsorbed decreases with increasing temperature, due to the exothermic nature of adsorption. Also, a change in temperature has a larger effect on the adsorption of CO_2 as compared to CH_4, due to the relative proximity of the experimental temperature to the critical temperature of the adsorptive. This condition has a strong effect on the adsorbed phase density within the pores in relation to the bulk fluid density [169, 116]. The manifestation of this behaviour can be readily seen in the smoothening of the characteristic peak in the CO_2 isotherms when moving from 40 °C ($T/T_c = 1.03$) to 80 °C ($T/T_c = 1.16$); farther from T_c the peak is no longer visible, as indicated by the CH_4 isotherms ($T/T_c > 1.65$) that show fairly broad maxima. As it will be discussed in Section 6.2, this behaviour is typical of mesoporous materials, for which the excess isotherm shows Type II behaviour (when plotted as a function of pressure) at near-critical conditions, before falling abruptly towards higher densities due to the marked increase in the bulk fluid density [168].

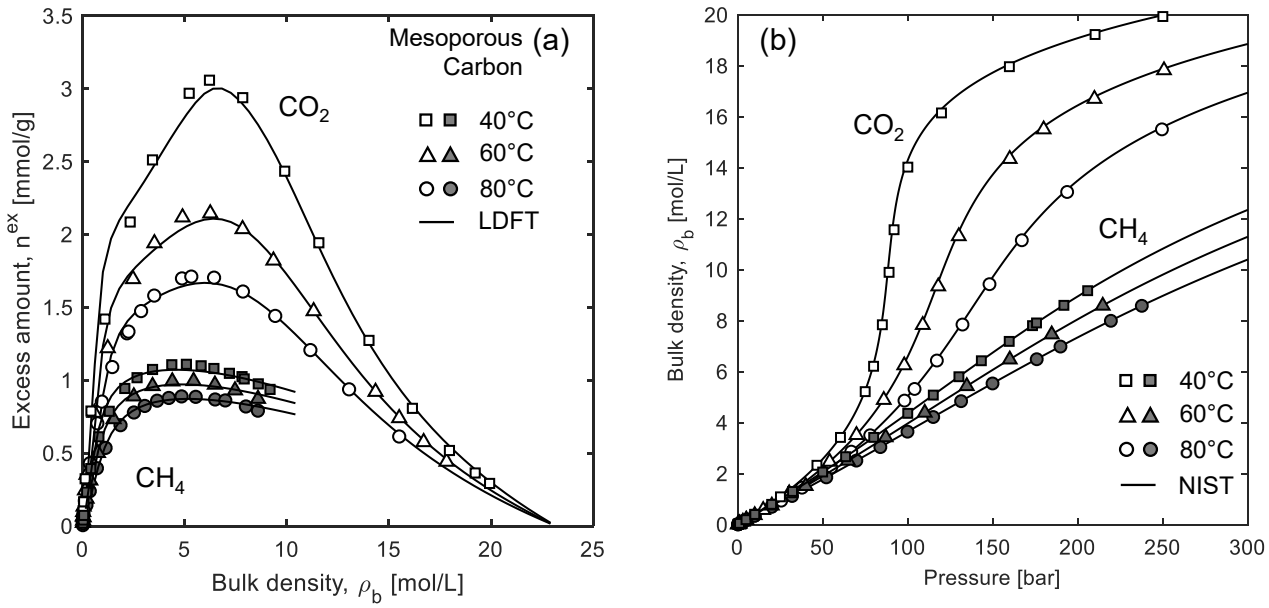

Figure 6.1: (a) Unary excess adsorption isotherms measured with CO_2 (empty symbols) and CH_4 (filled symbols) on mesoporous carbon (MC) plotted as a function of the bulk density at 40 °C, 60 °C and 80 °C. $V_0 = 1.392 \pm 0.001$ cm^3 and $V_{\text{met}} = 0.667$ cm^3. Solid lines denote optimum fits from the lattice DFT model (parameter values reported in Table 6.2). (b) The corresponding bulk density measurements plotted as a function of the measured pressure and their comparison with data reported by NIST (solid lines) [242]. Experimental uncertainties are not shown as they are smaller than the size of the symbols but are tabulated along with the experimental data in Tables A.1 and A.2.

It is highly instructive to compare the results on MC with those obtained with another carbonaceous porous material with a different PSD. To this aim, we use the literature CO_2 and CH_4 excess adsorption isotherms measured on AC Norit over a similar range of temperatures (25–70 °C), but wider range of pressures (up to 50 MPa) (Figure 6.2). The isotherms differ in many aspects from those obtained on MC: (i) they reach considerably higher excess amounts adsorbed (3 to 5 times), (ii) they are initially much steeper, reaching maximum values at $\rho_b \approx 3$ mol/L, and (iii) beyond the maximum point, they fall almost linearly with bulk density. These features can be attributed to the PSD of the material, which is largely dominated by micropores; as discussed in Chapter 5, micropores become readily filled with adsorbed phase at very low bulk densities and their volume largely determines the (constant) volume of the adsorbed phase [117].

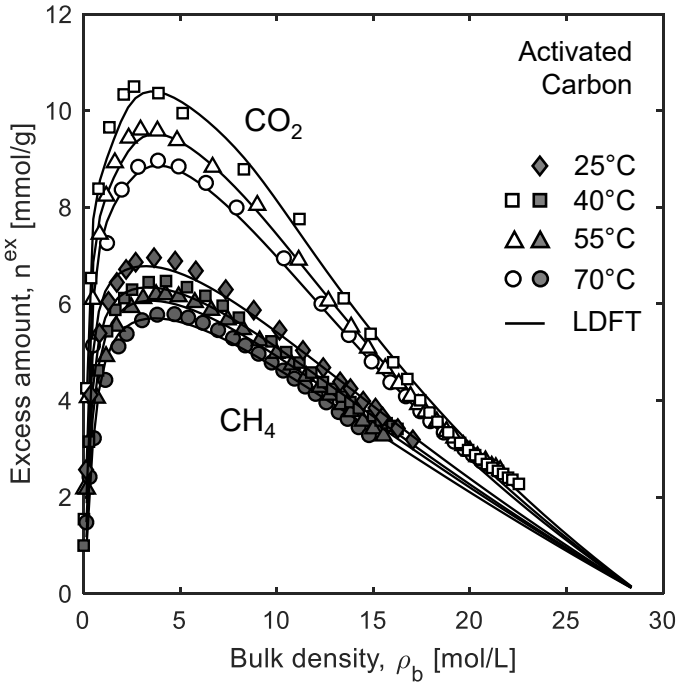

Figure 6.2: Unary excess adsorption isotherms measured with CO_2 (empty symbols) and CH_4 (filled symbols) on activated carbon Norit (AC) plotted as a function of the bulk density at 25 °C, 40 °C, 55 °C and 70 °C. Details of the experimental data set are reported elsewhere [180, 219]. Solid lines denote optimum fits from the lattice DFT model developed in this study (parameter values reported in Table 6.2).

The pore size distribution of MZ features the characteristic elements of MC's (mesoporosity) and AC's (microporosity) PSDs. This is clearly reflected in the shape of the supercritical CO_2 and CH_4 excess adsorption isotherms measured on MZ, which are shown in Figure 6.3a. The CO_2 isotherms initially show a sharp rise (like AC), followed by a broader isotherm peak than MC's and a subsequent non-linear decrease in excess adsorption as the bulk density increases. The MZ and AC CH_4 isotherms are quite similar. This is likely because $T >> T_c$ for CH_4 and, therefore, pore size effects are less pronounced and micropores dominate the adsorption process. Comparable CO_2 adsorption capacities

are observed for MZ and MC; this is linked to the similarity in their total pore volume (0.477 cm^3/g vs. 0.456 cm^3/g, respectively). With increasing mesoporosity, the maximum of the lowest-temperature CO_2 isotherm shifts to higher densities; for MZ the peak is located at ∼5 mol/L, which is higher than AC's (at ∼3 mol/L) and lower than MC's (at ∼6 mol/L) maxima. Figure 6.3b shows that the measured density values correspond very well to the data from NIST; the average residual sum of squares is 1.8129 $(mol/L)^2$ (CO_2) and 0.0004 $(mol/L)^2$ (CH_4). The CO_2 excess isotherms are almost zero at ρ_b =20 mol/L, and thus, the adsorbed and the bulk phases are almost identical here.

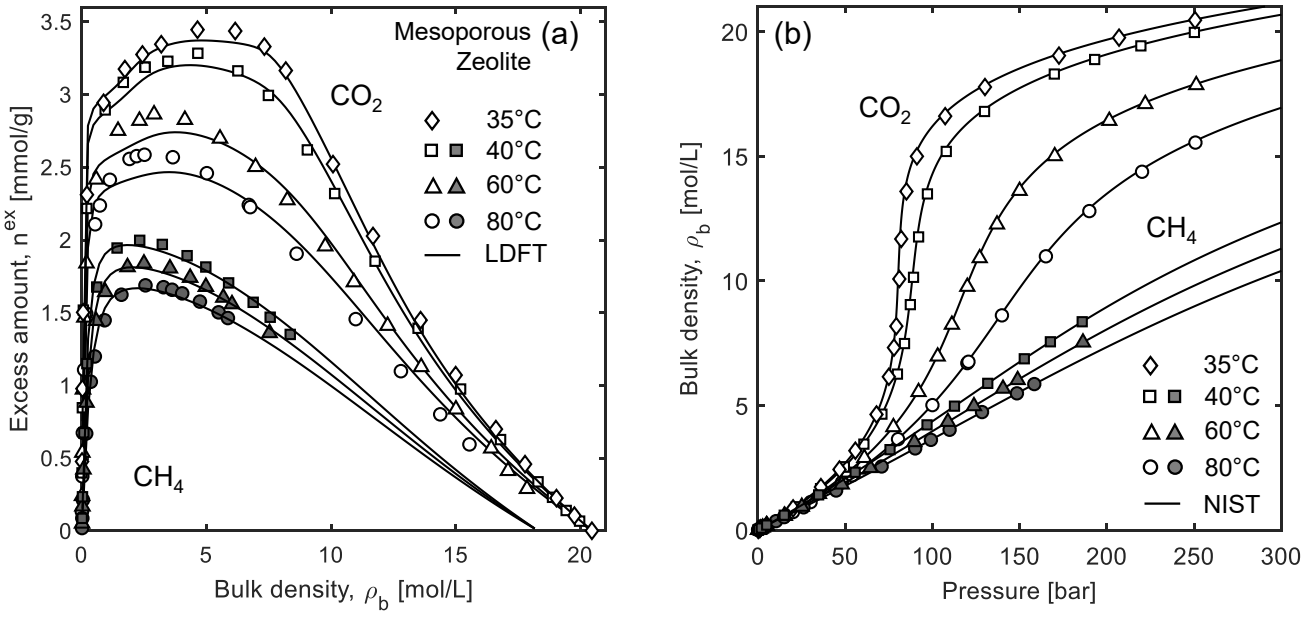

Figure 6.3: (a) Unary excess adsorption isotherms measured with CO_2 (empty symbols) and CH_4 (filled symbols) on mesoporous zeolite (MZ) plotted as a function of the bulk density at 35 °C, 40 °C, 60 °C and 80 °C. V_0 ranges from 1.858 ± 0.002 cm^3 to 1.873 ± 0.003 cm^3, and $V_{met} = 1.419$ cm^3. Solid lines denote optimum fits from the lattice DFT model (parameter values reported in Table 6.2). (b) The corresponding bulk density measurements plotted as a function of the measured pressure and their comparison with data reported by NIST (solid lines) [242]. Experimental uncertainties are not shown as they are smaller than the size of the symbols but are tabulated along with the experimental data in Tables A.3 and A.4.

6.1.2 Helium Gravimetry

Excess adsorption isotherms necessitate the measurement of the solid volume (V_s) through experiments like Helium gravimetry. Figure 6.4 shows these results for both MC and MZ in the form of the corrected weight versus the Helium bulk density. Through weighted linear regression on this data (as described in Chapter 4), we obtain V_0 (the sum of the volume of the metal parts and the solid) and m_s (mass of the adsorbent). As the figure shows, the MC experiments comprised of one Helium run prior to the CO_2 measurements. MZ, on the other hand, had four: (i) Run 1 - prior to the CO_2 measurements, (ii) Run 2 - after one CO_2 isotherm (80 °C) and a further three points on the 60 °C isotherm, (iii) Run 3 - after all CO_2 measurements and prior to the CH_4 measurements, and (iv) Run 4 - at the end of all

experiments. Each run was preceded by a full regeneration of the adsorbent as detailed in Chapter 5. Ideally, all the He isotherms should collapse such that the obtained V_0 and m_s, and by extension, the skeletal density, ρ_{sk}, are fairly constant. During the course of the MZ experiments, there was periodic loss of some fine particles from the sample, which is one of the reasons the MZ He runs are not entirely parallel. While the difference might appear fairly minor, the impact on the excess adsorbed amount, particularly at higher densities, can be quite significant. In fact, this represents the main driver of the uncertainty associated with supercritical adsorption measurements at elevated pressures (as the uncertainty in the excess adsorbed amount scales with $(\rho_b \sigma_{V_0})/(M_w m_s)$, as shown in Chapter 3). An increase of just 1% in V_0, for example, would cause the excess adsorbed amount in MZ's 35 °C CO_2 isotherm to increase by 22% near the peak and by 331% at 251 bar. Table 6.1 describes the main parameters used to calculated the adsorbed amount for both adsorbents. To overcome the variability in MZ's Helium results, an average of the skeletal density (ρ_{sk}) from Run 1 and Run 2 was taken for the CO_2 measurements, and from Runs 3 and 4 for the CH_4 points, as the skeletal density should remain constant. To obtain the respective solid volume and V_0, the mass from each He run was used; this was further verified by the vacuum point taken just before the Helium measurement. The only exception to this was Run 3, where an extra regeneration after the Helium run meant that another vacuum point was taken and a more recent adsorbent mass could be obtained. Table 6.1 shows both the original values of each parameter (white cells) and the values taken based on the average of the skeletal density (grey cells). Therefore, the newly calculated values for Run 1 were used for the 80 °C CO_2 isotherm and for the three 60 °C CO_2 points, Run 2 was used for the remainder of the CO_2 isotherms and Run 3 was used for all CH_4 isotherms. This discussion highlights the importance of repeating He runs multiple times throughout the course of supercritical adsorption experiments to confirm any loss of sample mass or reduce the uncertainty in the measured solid volume. For the data reported in this chapter, the uncertainty on n^{ex} was found to range between 0.47 - 21 µmol/g and 2.1 - 12 µmol/g (MC) and 1.3 - 68 µmol/g and 1.9 - 33 µmol/g (MZ) for CO_2 and CH_4, respectively. These estimates are in line with those reported in the literature for measurements carried out on porous materials using Magnetic Suspension Balances [117, 243].

6.1.3 Net Adsorption

Net adsorption isotherms avoid issues associated with measuring the skeleton volume of the adsorbent using Helium. It can be considered void of any assumptions and only requires knowledge of the volume of the metal parts inside the measuring chamber. The net experimental adsorption data (Figure 6.5) show an initial increase in n^{net}, followed by a maximum after which, the isotherms become negative for the majority of the density range for both gases. Negative values in this quantity are expected when the gain in storage capacity produced by gas adsorption no longer compensates for the loss

Table 6.1: The key parameters and their uncertainties utilised in the calculations of the excess or net adsorbed amount for mesoporous carbon (MC) and mesoporous zeolite (MZ). Where no uncertainty is shown, the uncertainty is below 0.001. For MZ, each Helium run shows two sets of values: white cells represent the raw values obtained through weighted linear regression and the grey cells represent values taken forward for the calculation of the adsorbed amounts.

Adsorbent	m_{met} [g]	V_{met} [cm^3]	V_{sk} [cm^3]	He Run	m_{s} [g]	V_{s} [cm^3]	ρ_{sk} [g/cm^3]
MC	5.285	0.667	4.364 ± 0.002	1	1.224	0.725 ± 0.001	1.688 ± 0.003
MZ	7.705	1.420	4.364 ± 0.002	1	1.149	0.466 ± 0.005	2.469 ± 0.027
					1.149	0.453 ± 0.003	2.535 ± 0.015
				2	1.144	0.440 ± 0.002	2.601 ± 0.011
					1.144	0.451 ± 0.003	2.535 ± 0.015
				3	1.142	0.396 ± 0.002	2.885 ± 0.018
					1.141	0.439 ± 0.002	2.599 ± 0.014
				4	1.141	0.493 ± 0.005	2.313 ± 0.021
					1.141	0.439 ± 0.002	2.599 ± 0.014

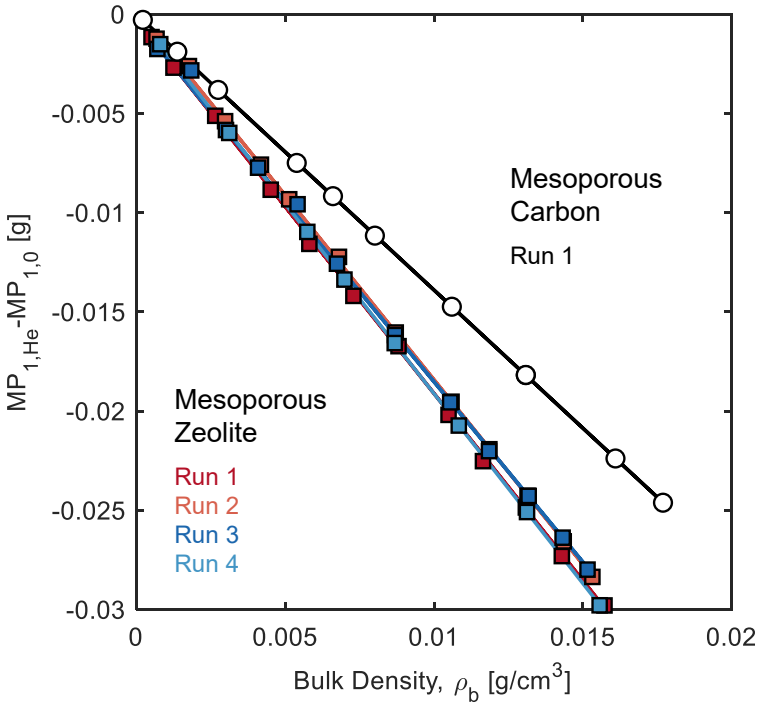

Figure 6.4: Corrected MP_1 [$MP_{1,He} - MP_{1,0}$] as a function of Helium density (experiments conducted at 80 °C and over the pressure range 2-140 bar) for mesoporous carbon (MC) and mesoporous zeolite (MZ). The slope of the regression line corresponds to V_0. MC experiments only had one He measurement (Run 1) while MZ had four (Runs 1-4).

in storage volume introduced by the presence of the solid material itself. This point is reached at higher bulk densities for CO_2 as compared to CH_4 and at lower experimental temperatures. The slope of the descending part of the isotherm, after $n^{net} = 0$, differs between the three adsorbents, just like the excess adsorption isotherms. The PSD of each solid dictates whether the slope is linear (AC - microporous), non-linear (MC - mesoporous) or a combination of the two (MZ - micro- and meso-porous). Additionally, both MZ and AC show a fairly steep uptake just before their respective peaks, which are much sharper than that of MC's isotherms. The transition into negative net adsorbed amounts in the 40 °C CO_2 isotherm occurs in the following order: MC (5 mol/L) < MZ (8 mol/L) < AC (13 mol/L). Therefore, an adsorbent's microporosity benefits adsorption as a gas storage mechanism, as $n^{net} > 0$ over a larger pressure range. Similarly, the size of the peak is directly influenced by the PSD, whereby AC has the largest (9 mmol/g), followed by MZ (3 mmol/g) and MC (0.8 mmol/g).

The slope of a net adsorption isotherm at high densities corresponds to the sum of the adsorbed phase volume and the skeletal volume of the adsorbent ($V_s + V_a$). Based on the skeletal volume obtained from the Helium measurement (shown as dotted lines in Figure 6.5), one can theoretically obtain an adsorbed volume (constant and bulk density-independent) at these conditions (assuming saturation is reached). This is not the case for excess adsorption isotherms (where the slope corresponds to just V_a) as the isotherms have a varying slope, particularly for mesoporous adsorbents. Performing this analysis on the 40 °C CO_2 net isotherm, and restricting the lower bound of the bulk density

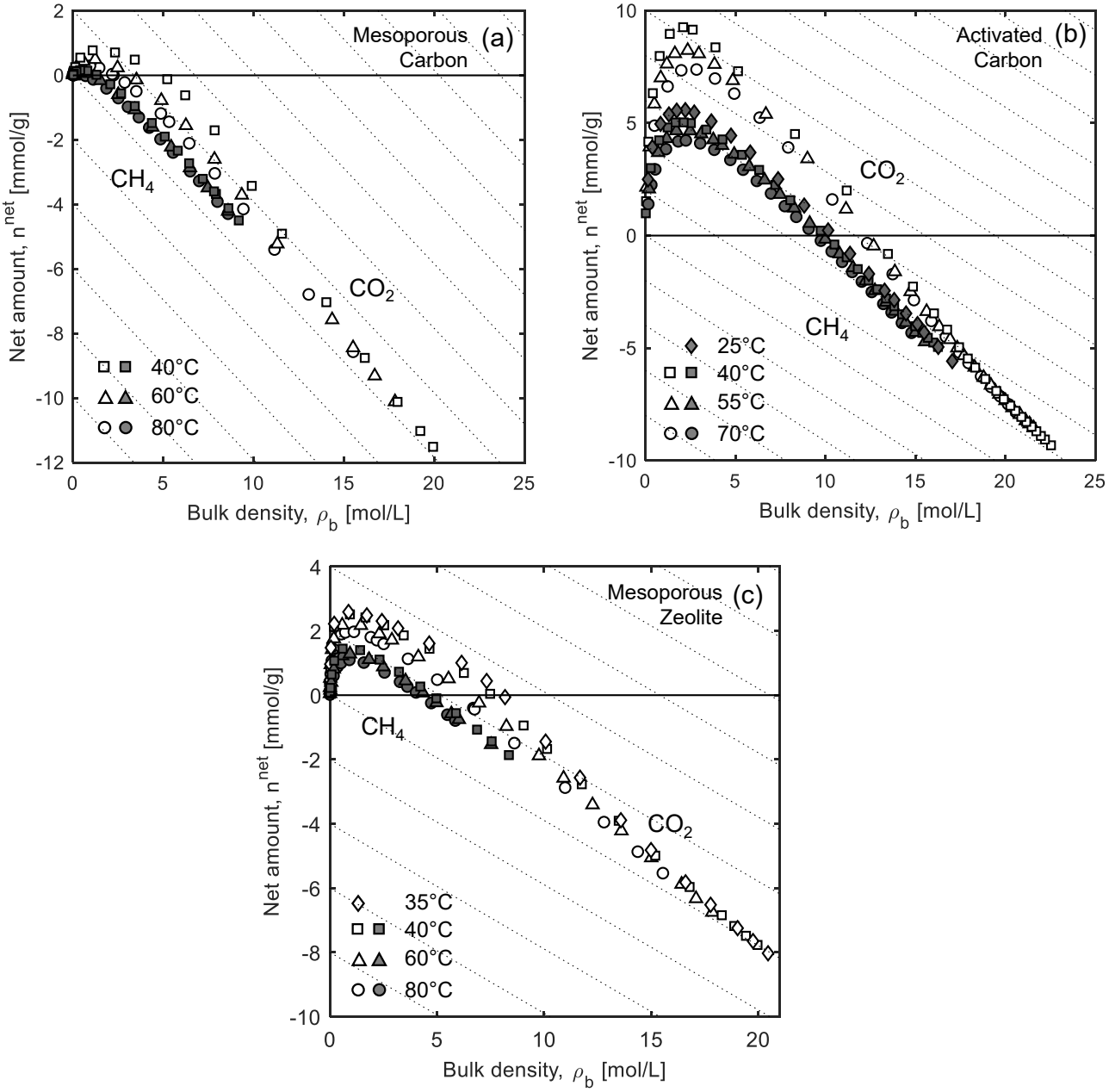

Figure 6.5: Unary net adsorption isotherms measured with CO_2 (empty symbols) and CH_4 (filled symbols) on (a) mesoporous carbon (MC), (b) activated carbon (AC), and (c) mesoporous zeolite (MZ), plotted as a function of the bulk density at various temperatures. Experimental uncertainties are not shown as they are smaller than the size of the symbols but are tabulated along with the experimental data in Tables A.1 and A.2 (MC) and Tables A.3 and A.4 (MZ). Dotted lines have a slope of V_s/m_s.

to 15 mol/L, the V_a/m_s for all adsorbents is as follows: MC (0.14 cm^3/g) < MZ (0.19 cm^3/g <) AC (0.37 cm^3/g). These correspond to 30% (MC), 40% (MZ) and 59% (AC) of the respective total pore volume of each adsorbent. Interestingly, these proportions correspond reasonably well with the microporosity fraction in MZ and AC. The validity of this approach is definitely more appropriate for microporous materials, where the adsorbents experience micropore filling and the adsorbed phase is primarily found in the micropores. This is visible in Figure 6.5b, where the linear region extends

to bulk density values below 15 mol/L. For mesoporous materials, like MC and MZ, this approach is more questionable as mesopores would probably not be fully saturated at these conditions and the adsorbed phase would be more distributed amongst pores of varying sizes [233].

6.2 Lattice DFT Modelling of Supercritical Adsorption

Also shown in Figure 6.1 are the results obtained upon fitting the lattice DFT model to the excess adsorption data on MC. The model provides an accurate description of the adsorption isotherms for both gases at all temperatures and over the entire range of bulk densities. The value of the objective function (normalised by the number of experimental points, E) is $\Phi/E = 0.0096$ (mmol/g)^2 (for CO_2) and 0.0011 (mmol/g)^2 (for CH_4), and is reported in Table 6.2 together with both input and fitted model parameters. For both gases, the value of the temperature-independent adsorbate-adsorbent interaction parameter, ε_{sf}, is significantly lower than the corresponding average value, $\overline{\varepsilon}_{sf}$, that accounts for both the curvature of the pore-wall and the size of the pore. Interestingly, estimates obtained for CH_4 are systematically higher than those for CO_2, despite the fact that the former shows smaller adsorbed amounts. As anticipated before, supercritical adsorption in mesoporous materials cannot be ascribed solely to the strength of the surface-fluid interaction, because of the possibility of multi-layer adsorption at (slightly) supercritical conditions [168]. This condition is therefore also strongly controlled by the fluid-fluid interaction parameter, ε_{ff}, whose value for CO_2 is (significantly) larger than for CH_4 (see Table 6.2).

It can be seen that also in the case of AC (Figure 6.2), the model provides a good description of the experimental data ($\Phi/E = 0.1092$ and 0.0521 (mmol/g)^2 for CO_2 and CH_4, respectively), even though the isotherms are fairly different to MC. AC also shows a much higher $\overline{\varepsilon}_{sf}$ compared to ε_{sf} (44% increase vs. 24% increase for MC). Again, this is due to its high microporosity, which contributes considerably to the surface area fraction incorporated in the calculation of $\overline{\varepsilon}_{sf}$. MZ's modelled CO_2 isotherms, the 35 °C ($T/T_c = 1.01$) one in particular, almost mimic the subcritical N_2 or Ar isotherms. They are characterised by a distinct region of micropore filling, illustrated by the almost vertical uptake and the concave shape for the near-critical isotherms at $\rho_b \approx 1$ mol/L. The model is successful at capturing the adsorption in this dual-structured adsorbent (Figure 6.3) such that $\Phi/E = 0.0171$ (mmol/g)^2 (CO_2) and 0.0026 (mmol/g)^2 (CH_4). The surface interaction energy parameters for MZ are much higher than the carbonaceous adsorbents; $\overline{\varepsilon}_{sf}$ is more than double that of MC. This represents a clear distinction between the carbon and zeolite surface and illustrates that adsorption depends on the size, shape and type of surface of the pore. The average value ($\overline{\varepsilon}_{sf}$) is 48% higher than the fitted ε_{sf}, which again can be contributed to the high fraction of microporosity in MZ's PSD.

Table 6.2: Input and fitted parameters of the cylindrical lattice DFT model applied to the description of experimental excess adsorption isotherms measured on mesoporous carbon (MC), activated carbon (AC) and mesoporous zeolite (MZ). The value of the objective function, Eq. 4.20 (normalised by the number of experimental points, E) is also given.

	Mesoporous carbon		Activated carbon		Mesoporous zeolite	
Parameter	CO_2	CH_4	CO_2	CH_4	CO_2	CH_4
	Input Parameters					
ε_{ff}/k_B [K]	−202.75	−127.04	−202.75	−127.04	−202.75	−127.04
σ [nm]	0.40	0.38	0.40	0.38	0.40	0.38
	Fitted Parameters					
ε_{sf}/k_B [K]	−605.16	−714.33	−724.87	−712.36	−1104.61	−900.88
$\overline{\varepsilon}_{sf}/k_B$ [K]	−749.26	−884.42	−1046.74	−1028.67	−1636.00	−1334.27
ρ_{max} [mol/L]	23.18	31.97	28.86	28.89	20.48	18.31
	Saturation Factor, c_{sat}					
25 °C	–	–	–	0.81	–	–
35 °C	–	–	–	–	0.77	–
40 °C	0.83	0.34	1.00	0.78	0.74	0.63
55 °C	–	–	0.96	0.77	–	–
60 °C	0.70	0.32	–	–	0.67	0.60
70 °C	–	–	0.93	0.74	–	–
80 °C	0.62	0.30	–	–	0.63	0.57
Φ/E [mmol/g]^2	0.0096	0.0011	0.1092	0.0521	0.0171	0.0026

The lattice DFT also enables the estimation of ρ_{max}, the maximum density in the saturated lattice that would theoretically occur once the bulk fluid density is equal to the adsorbed phase density (i.e. when n^{ex} is equal to 0). For AC, the values predicted for both fluids are very similar, with all excess adsorption isotherms converging towards an estimate of 28.9 mol/L. This result is consistent with the interpretation of the pore space with a lattice of sites of equal size (reflecting a similar collision diameter of both CO_2 and CH_4 molecules). For MC, the obtained values are 23.2 mol/L (CO_2) and 32.0 mol/L (CH_4). We note that the value for CH_4 may be overestimated as a result of the limited range of bulk density covered in the experiment with MC ($\rho_b \approx 9$ mol/L, as opposed to $\rho_b \approx 18$ mol/L for the measurements on AC). Most importantly, these estimates of ρ_{max} are systematically larger than the liquid density values at the boiling point of the adsorptive (21.1 mol/L for CO_2 at 273 K and 3.47 MPa; 26.3 mol/L for CH_4 at 111.7 K and 101.35 kPa [231]). Moreover, the larger value observed for CO_2 on AC as compared to MC may be the result of a denser packing of molecules in a micropore, as compared to a mesopore. With MZ, on the other hand, both values are lower than the porous carbons. MZ's CO_2 experimental data incorporate measurements where $n^{ex} \approx 0$, so the corresponding ρ_{max} is an accurate representation of the density in the pores at these conditions. This is also fairly close to the liquid density of CO_2 previously mentioned. Similar to MC, the CH_4 data for MZ is significantly further away from this point, and therefore, its ρ_{max} may be underestimated.

It appears that the presence of mesopores lowers $\rho_{\max}$, as the fluid is less 'confined' in these pores and the adsorbed phase has a density that is closer to the liquid density values. The ability of the lattice DFT model to reveal such insights on the behaviour of the adsorbed phase, makes it a useful model to understand supercritical adsorption in porous materials.

6.3 Henry Constants and Adsorption Energetics

Estimates of the Henry constants were obtained by describing the experimental data on both carbons with the Virial equation (Eq. 4.21). The corresponding Virial plots are presented in Figure 6.6 for (a) MC, (b) AC and (c) MZ, where the points that have been used to obtain the Henry constant from a linear extrapolation to zero loading are clearly visible. The advantage of this approach is highlighted in the figure; the linear region occurs at pressures well beyond the limit of Henry's law [111], which allows for a simple way to calculate the Henry constants from the available measurements. The obtained Henry constants are plotted in Figure 6.7 (and tabulated in Table 6.3) as a function of the reciprocal temperature and show very good fits to a linear regression (solid lines), as expected from the van't Hoff equation (Eq. 4.22). We note that for this analysis we have also considered CO_2 adsorption isotherms measured on MC and MZ using the volumetric apparatus at 0 °C, 10 °C and 25 °C (shown in the inset of Figure 6.6a and 6.6c; raw data is available in the appendices) and additional literature data on AC Norit R1 Extra [244] (shown in Figure 6.7). For both adsorptives, values of the Henry constants obtained for AC are about 24 times higher than estimates on MC (at equivalent temperatures), confirming the stronger affinity of the gases to the microporous AC as compared to MC. Nevertheless, a similar selectivity towards CO_2 (estimated from the ratio of the Henry constants) is observed: 1.78 ± 0.17 for MC and 1.69 ± 0.21 for AC. These values are relatively low and indicate a similar affinity of CO_2 and CH_4 to the carbon surface for both materials. The zeolite surface, on the other hand, shows a much greater selectivity (6.64 ± 0.50 towards CO_2). This difference is also evident in Figure 6.7 where there is a much larger gap between the CO_2 and CH_4 linear fits as compared to the carbons. The Henry constants for CO_2 on MZ are the highest in this study; they are roughly 48 and 2 times higher than MC and AC, respectively, on average. Conversely, the MZ CH_4 Henry constants are about 9 times higher than MC's but are about half that of AC's.

The parameters obtained upon fitting the van't Hoff equation to the Henry constants are reported in Table 6.3 and include the isosteric enthalpy of adsorption, Δh_0 (Virial equation fitted to experimental data) and $\Delta \widetilde{h}_0$ (lattice DFT), and the associated pre-factors (H_0 and $\widetilde{H}_0$). The isosteric heat estimated from the experiments is similar for both carbons and both adsorptives ($\Delta h_0 \approx -20$ kJ/mol), but is systematically larger than the value predicted by the lattice DFT model ($\Delta \widetilde{h}_0 \approx -14$ kJ/mol). This discrepancy may be the result of a lack of experimental points at sufficiently low pressures to constrain

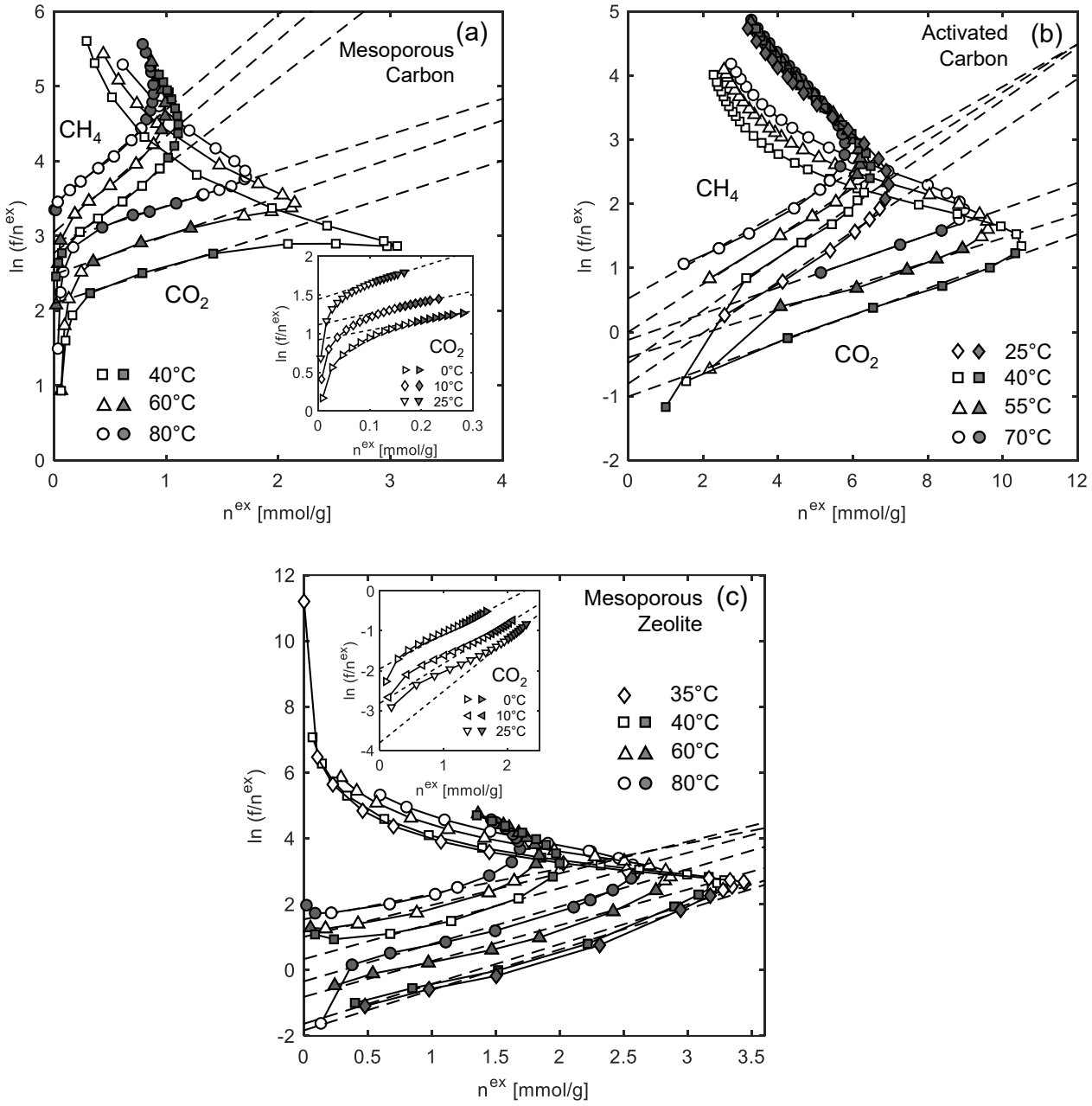

Figure 6.6: The Virial plot [ln(f/n^{ex}) vs. n^{ex}] for (a) MC, (b) AC and (c) MZ. Inset shows subcritical CO_2 data. All experimental points are connected with solid lines. For CO_2, filled points represent the experimental data that were considered part of the linear region, and empty points are the residual experimental data. For the CH_4, empty points are the Virial region points and filled points are the remainder of the experimental data. The dashed lines are the linear fits at all experimental temperatures.

the fitting of model. Nevertheless, these estimates are larger than the latent heat of vapourisation of the two gases (i.e. $\Delta h_{\text{vap}} = -10.3$ kJ/mol for CO_2 at 273.15 K and $\Delta h_{\text{vap}} = -8.2$ kJ/mol for CH_4 at 112 K [231]), in agreement with the expectation that for physisorption, $\Delta h_0/\Delta h_{\text{vap}} < 1.5-2$ [245]. This is also the case for the estimated isosteric heat for MZ from the lattice DFT model ($\Delta\widetilde{h}_0 \approx -18$ kJ/mol) but the experimental heat of adsorption is significantly higher ($\Delta h_0 \approx -31$ kJ/mol). Even so, this is in line with previous estimates of the isosteric enthalpy of adsorption on other zeolites, such as 13X

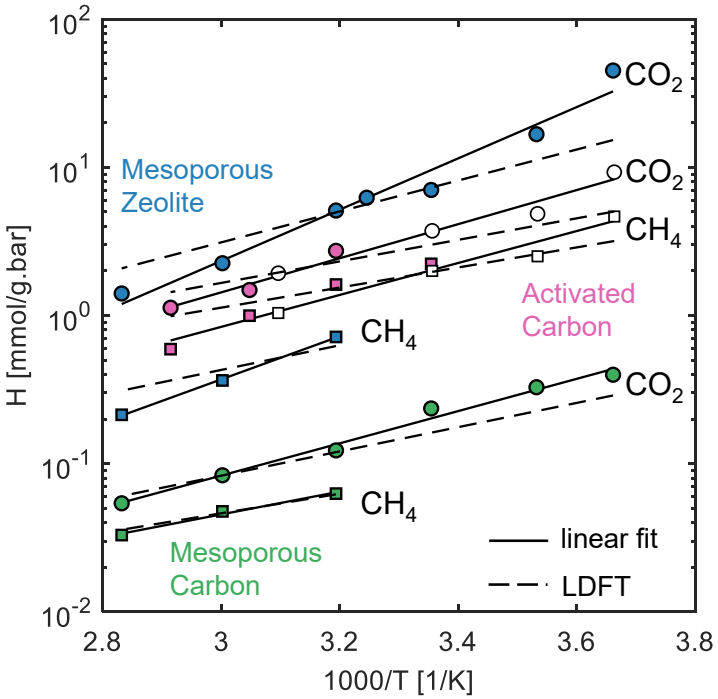

Figure 6.7: Henry constants as a function of the reciprocal temperature for CO_2 and CH_4 on all three synthetic adsorbents. Data on MC and MZ have been obtained in this study. For AC, the filled symbols refer to the analysis carried out on the excess adsorption isotherms reported in [180, 219], while the empty symbols are data reported by Himeno et al. (2005) [244] on a similar AC. Solid lines denote linear fits to the experimental data, while the dashed lines represent prediction from the fitted cylindrical lattice DFT model.

[246], NaX and ZSM-5 zeolites [247].

6.4 Effect of Pore Geometry on Supercritical Adsorption

One of the key features of the lattice DFT model for describing supercritical adsorption is the explicit incorporation of the textural properties of the adsorbent, including the size distribution and geometry of pores. The benefits of this are evident in the ability of this modelling approach to correctly capture the uptake of supercritical fluids on a variety of adsorbents with distinct PSD, such as the microporous and mesoporous materials considered in this study. The latter represents a particularly challenging material, because of the peculiar phase behaviour of fluids within pores of diameters in the order of 10 nm, where interactions between the solid and the fluid are as important as those between the fluid molecules themselves. Once calibrated against experimental data, the lattice DFT model can provide additional insights on the behaviour of the adsorbed phase within the pores, including pore size dependent adsorption behaviour and filling capacities, as discussed in the following section.

Table 6.3: The Henry constants (from high pressure, HP, and low pressure, LP, adsorption experiments), average selectivity and parameters of the integrated van't Hoff equation (Eq. 4.18), including the isosteric heat of adsorption, Δh_0 (Virial equation) and $\Delta\widetilde{h}_0$ (lattice DFT), and the corresponding pre-factors (H_0 and $\widetilde{H_0}$), for all three synthetic adsorbents. The Henry constants are also shown in Figure 6.7.

Parameter		Mesoporous carbon		Activated carbon		Mesoporous zeolite	
		CO_2	CH_4	CO_2	CH_4	CO_2	CH_4
H (mmol/g/bar) – HP	25 °C	–	–	–	2.232	–	–
	35 °C	–	–	–	–	6.241	–
	40 °C	0.123	0.063	2.733	1.618	5.113	0.717
	55 °C	–	–	1.486	0.998	–	–
	60 °C	0.083	0.048	–	–	2.254	0.364
	70 °C	–	–	1.129	0.593	–	–
	80 °C	0.054	0.033	–	–	1.408	0.214
H (mmol/g/bar) – LP	0 °C	0.398	–	–	–	45.065	–
	10 °C	0.328	–	–	–	16.748	–
	25 °C	0.236	–	–	–	7.040	–
Selectivity		1.78 ± 0.17		1.69 ± 0.21		6.64 ± 0.50	
	Virial equation						
H_0 (µmol/g/bar)		0.0451	0.222	0.505	0.489	0.0150	0.0160
Δh_0 (kJ/mol)		−20.8	−14.8	−22.0	−20.6	−33.1	−27.9
	lattice DFT						
$\widetilde{H_0}$ (-)		2.78	2.28	6.04	5.46	6.42	2.42
$\Delta\widetilde{h}_0$ (kJ/mol)		−15.3	−12.4	−13.6	−12.7	−19.6	−15.6

6.4.1 Saturation Factors

Figure 6.8a shows the pore saturation factors obtained for MC, AC and MZ as a function of the inverse reduced temperature (T_c/T). The saturation factor is an indicator of the occupancy of the total pore space by the supercritical adsorbed phase at saturation and accounts for the inefficient packing of molecules, which may depend on both the temperature and the effective size of the adsorbate molecules. Several observations can be made here; first, for a given adsorbent, CO_2 and CH_4 outline a common linear trend, suggesting that temperature is the main driver in controlling the pore filling behaviour. The fact that the saturation factor increases upon approaching the critical temperature of the fluid further indicates that near-complete saturation of the pore space may be achieved at near-critical conditions, in agreement with early observations of critical adsorption on graphitised carbon black [248]. Second, saturation factors obtained on MC (c_{sat} = 0.3–0.8) are systematically lower than those on AC (c_{sat} = 0.7–1) at equivalent reduced temperature. c_{sat} on MZ lie somewhere in between the two carbons (c_{sat} = 0.6–0.8). In fact, the CO_2 saturation factors are very similar for both mesoporous

materials. This result confirms observations from textural analysis in that micropores tend to be readily filled with an adsorbed phase, with a relatively weak dependence on the temperature. On the contrary, complete filling of mesopores can be reached only near the critical temperature of the fluid ($T_c/T > 0.95$). These observations provide additional indications of pore size dependent adsorption behaviour and of the importance of using adsorption models that can account for it.

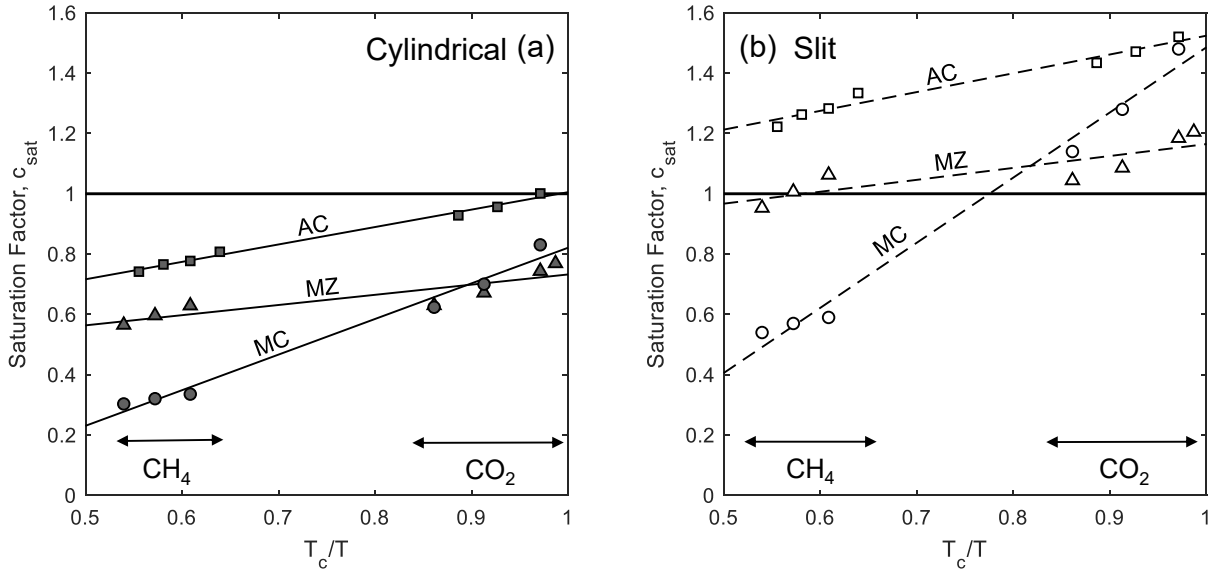

Figure 6.8: The pore saturation factor, c_{sat}, as a function of T_c/T for mesoporous carbon (circles), activated carbon (squares) and mesoporous zeolite (triangles) obtained with the lattice DFT model that uses (a) cylindrical and (b) slit pores. Linear fits for both pore geometries and and all materials are also shown. Note that the relevant plot for calculating Henry constants, namely $\ln(c_{\text{sat}})$ vs. T_c/T, is shown in the appendices.

Figure 6.8b shows the saturation factors obtained when a one-dimensional slit is used to describe the geometry of the pores in the lattice DFT model. The fitted and input model parameters are reported in the appendices. For the calculations, the lattice configuration (cubic) and discretised PSD (shown in Chapter 5) were the same as those used for the cylindrical pore model. We note that the selected (physical) pore sizes ($D_{\text{p},J}$) differ in terms of the number of layers considered in the given geometry, as $D_{\text{p},J} = d(2J-1)$ for a cylinder and $D_{\text{p},J} = Jd$ for a slit. Accordingly, for MC $J = [2, 6, 15]$ (cylinder) and $J = [3, 11, 29]$ (slit), for AC $J = [3, 11]$ (cylinder) and $J = [5, 21]$ (slit) and for MZ $J = [3, 6, 8]$ (cylinder) and $J = [5, 11, 15]$ (slit). As it can be seen in Figure 6.8b, for all materials the majority of the obtained values are larger than one, indicating (i) that the slit geometry requires a larger pore volume and (ii) that the latter is greater than the total pore volume available - a physical limit - to achieve amounts adsorbed that are equivalent to the cylindrical model. As discussed below, the reason for this can be traced back to the effective interaction between the adsorbate and the adsorbent that is described by the lattice coordination number at the wall ($z_J^{\text{a}+}$ for a cylinder and z^{a} for a slit). The cylindrical lattice allows for this coordination number to be larger ($z_J^{\text{a}+} > z^{\text{a}} = 1$) and to depend on

the size of the pore (z_J^{a+} increases with decreasing J), features that are key for accurately describing supercritical adsorption in porous adsorbents.

6.4.2 Surface Interaction Energy

Figure 6.9 shows the (a) CO_2 and (b) CH_4 effective surface interaction parameter ($\varepsilon_{sf} z_J^{a+}/k_B$) as a function of the number of layers J for the cylindrical and slit lattice DFT model for the three synthetic materials. For the cylindrical pore model $|\varepsilon_{sf} z_J^{a+}/k_B|$ decreases strongly (becomes less negative) with increasing pore size, while for the slit pore model its value is constant ($z_J^{a+} = z^a = 1$) and does not depend on the number of layers (shown in the plots by the dashed horizontal lines). Most significantly, for a given adsorptive the two porous carbons outline a common curve, thus supporting the robustness of the proposed approach in capturing surface-fluid interactions correctly, irrespective of the PSD. In fact, the latter manifests itself through the *average* effective interaction energy, $\overline{\varepsilon}_{sf}/k_B$, which accounts for the contribution of each pore class to the surface area of the porous carbon. Not surprisingly, the estimated values (computed with Eq. 4.10 and shown as horizontal solid lines) are larger (more negative) for AC as compared to MC, as a result of a larger amount of microporosity. MZ's values are even more negative, on account of the stronger interactions between the adsorbates and the zeolite surface. Interestingly, these average values are comparable to those obtained with the slit model (ε_{sf}/k_B), a result that may be a mere coincidence, given that the latter produces unphysical values for the pore saturations factors ($c_{sat} > 1$). As anticipated before, the use of a cylindrical lattice does not only provide for a better representation of the true geometry of the pores in these materials, but also leads to estimated pore filling capacities that are physically more meaningful.

6.5 The use (and misuse) of the Langmuir model

A comparison is presented in Figure 6.10 between the application of the lattice DFT (solid lines) and the Langmuir adsorption model (dashed lines) to describe experimental adsorption data obtained on (a) MC, (b) AC and (c) MZ at 40 °C. To utilise the Langmuir model, we have assumed a constant adsorbed phase density and set its value to be the same as ρ_{max} in the lattice DFT model (see Table 6.2), while fitting the parameters n^∞ and K_L (values reported in the caption of the figure). It can be seen that the Langmuir model clearly fails at describing the CO_2 isotherms measured on the three adsorbents. The discrepancy is larger for MC and MZ as compared to AC, as a result of the larger contribution of mesoporosity that gives rise to pore confinement effects and to those isotherm shape features that are characteristic of mesoporous materials, i.e a late maximum and the non-linear behaviour at large densities. On the contrary, both models perform equally well on the data obtained

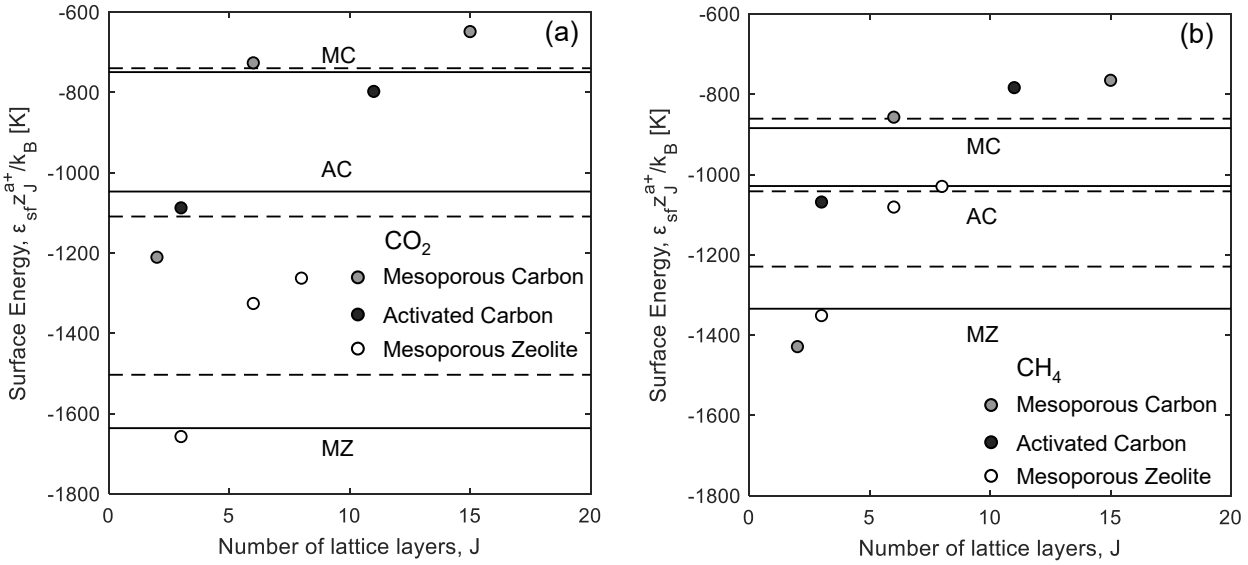

Figure 6.9: (a) CO_2 and (b) CH_4 effective surface interaction parameter ($\varepsilon_{\mathrm{sf}} z_J^{\mathrm{a}+}/k_{\mathrm{B}}$) as a function of the number of layers J for the cylindrical and slit lattice DFT model for all three synthetic adsorbents. Symbols represent estimates for the pore classes used to describe the three adsorbents using the cylindrical lattice DFT model, while the horizontal lines represent average values for the cylindrical ($\overline{\varepsilon}_{\mathrm{sf}}/k_{\mathrm{B}}$ - solid) and slit pore model ($\overline{\varepsilon}_{\mathrm{sf}}/k_{\mathrm{B}} = \varepsilon_{\mathrm{sf}}/k_{\mathrm{B}}$ - dashed).

using CH_4 on all adsorbents, with only slight differences appearing at large bulk densities (ρ_{b} >10 mol/L). Well above the critical temperature or when microporosity dominates, the assumption of a constant adsorbed phase density is likely more justified and the excess adsorption isotherm beyond the maximum becomes more linear. The use of the Langmuir model (and many other Type I adsorption models [187]) requires explicit information on the behaviour of the adsorbed phase density (or volume). The most commonly adopted approaches assume a constant value for this parameter, although this is very likely to be dependent on both the bulk density and PSD of the material [222]. Unless this information is obtained from an independent measurement, the application of such models to describe supercritical adsorption on mesoporous materials is inherently flawed.

6.6 Conclusion

In this chapter, we have presented an integrated experimental and modelling approach to study the adsorption of CO_2 and CH_4 on three important synthetic adsorbents, namely two porous carbons (microporous activated carbon and mesoporous carbon) and a mesoporous zeolite. Unary adsorption isotherms of CO_2 and CH_4 up to 25 MPa at 35 °C, 40 °C, 60 °C and 80 °C have been measured. The characteristic features of each adsorbent's pore size distribution are clearly visible in the excess adsorption isotherms, particularly with CO_2 at near-critical conditions ($T/T_{\mathrm{c}} = 1.01$–1.03). The effect of microporosity is evident in the isotherms through the steep uptake at low pressures, followed by a relatively early maximum and linear descent at high densities (as shown by AC), while mesoporosity

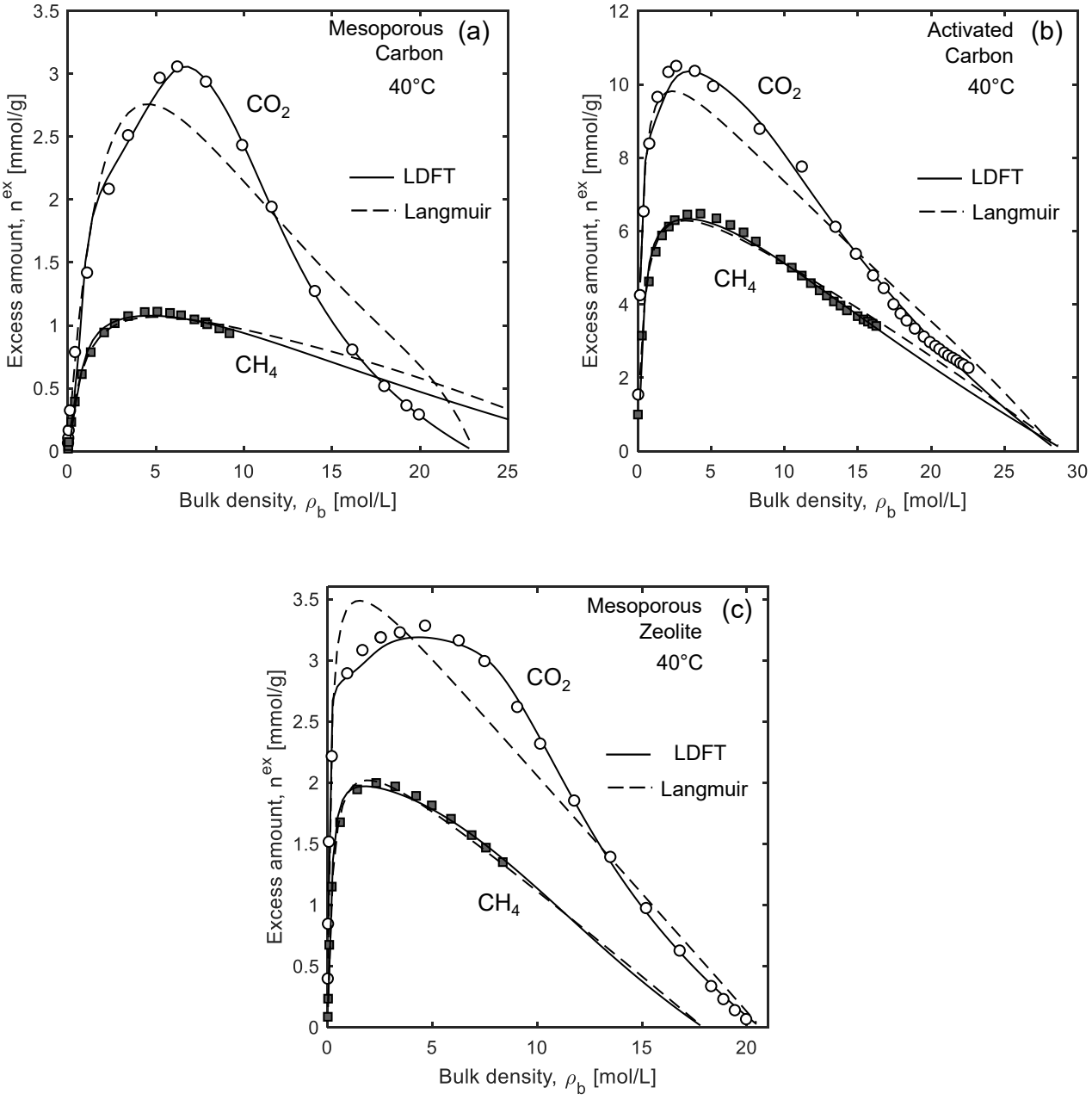

Figure 6.10: A comparison between the description of CO_2 and CH_4 supercritical adsorption obtained upon application of the lattice DFT (solid lines) and Langmuir model (dashed lines) on experimental data measured on (a) mesoporous carbon, (b) activated carbon and (c) mesoporous zeolite at 40 °C. The Langmuir parameters [n^{∞} (mmol/g), K_{L} (1/bar)] are: MC - [24.50, 0.0033] (CO_2) and [1.66, 0.033] (CH_4); AC - [12.75, 0.14] (CO_2) and [8.32, 0.082] (CH_4); MZ - [4.25, 0.27] (CO_2) and [2.61, 0.15] (CH_4).

is represented by an isotherm maximum that is achieved at a higher bulk density and a non-linear descent at high pressures (as indicated by MC). The CO_2 isotherms for MZ show both these elements as this sorbent incorporates both micro- and meso-porosity. The supercritical adsorption isotherms were described by the lattice Density Functional Theory (DFT) model with cylindrical pores. The model revealed additional insights about the interaction between the two adsorbates and the carbon and zeolite surfaces. A comparison between the lattice DFT model and the Langmuir model showed

that the former is more successful at describing supercritical adsorption as it can capture pore size dependent adsorption behaviour.

Chapter 7

Supercritical Gas Adsorption Measurements in Shales

The focus of this chapter is on the analysis of the high pressure adsorption measurements of CO_2 and CH_4 on four shales, namely the Longmaxi (LG4), Marcellus (ML), and Bowland (B6 and B8) shales. The experimental excess and net adsorption isotherms are presented for each shale and the adsorption thermodynamics are investigated. The experimental results are interpreted with the aid of a scaling analysis, which involves the synthetic adsorbents examined in the previous chapter. The Gas-in-Place is then derived from the experimental data for each shale play. Some of the material in this chapter has been published in Ansari et al. (2018, 2021) [28, 193] and Ma et al. (2021) [249].

7.1 Supercritical Adsorption Measurements

This section describes the results of the supercritical adsorption measurement on all shales. As described in Chapter 3, all adsorption measurements for each shale with the MSB include a full in-situ regeneration at 120 °C prior to any experiments, followed by a Helium measurement at 80 °C. After applying vacuum to the entire system, the sample is exposed to either CO_2 or CH_4 at various pressures and temperatures, with an equilibration time of at least 90 minutes. Typically, between gases, a full regeneration was accompanied by another Helium measurement. For all gases, points were taken in both adsorption mode (increasing the pressure in the MSB) and desorption mode (depressurising the MSB).

7.1.1 Helium Gravimetry

The results of the Helium measurements are shown in Figure 7.1 and Table 7.1. For each shale, multiple Helium runs were conducted to ascertain the solid's skeletal volume but also to see if the shale underwent any change due to the presence of supercritical fluids. In some cases, the measurements were interrupted for some external reason, and there was a minor loss of material as the basket was emptied and re-filled; this is the case for Runs 1 for the LG4 and ML shales. In all other cases, after each He run, there is consistently a slight increase in adsorbent mass, m_s (represented by the y-intercept in Figure 7.1). The increase usually occurs after exposure to CO_2 rather than CH_4, as indicated by the results of the Runs with an asterisk in Table 7.1. The same phenomenon was indicated by the vacuum points accompanying each He measurement. Nevertheless, a fairly consistent skeletal density is obtained for each shale, with a maximum deviation of less than 1.5%, indicating the robustness of these measurements. Indeed, all the shales have a very similar ρ_{sk} of approximately 2.6–2.7 g/cm^3. Note that for B6, an average of the skeletal densities of Runs 2 and 3 were taken as the overall skeletal density for each run, as the number of points in each Run was fairly low, and by using the obtained m_s, a corresponding V_s was calculated. The used values are shown in grey cells in Table 7.1.

7.1.2 Net Adsorption

The main contributing factor to the experimental uncertainties associated with adsorption measurements via the MSB, particularly at high densities, is the uncertainty in the measured solid volume (V_s), obtained via Helium measurements. Net adsorption does not require knowledge of this quantity, and therefore, the experimental error associated with these points is negligible. Figure 7.2 shows the net adsorption isotherms at 10 °C, 40 °C and 80 °C for the LG4, ML, B6 and B8 shales. Although the shape of the net isotherms is qualitatively similar to the synthetic adsorbents, here, the net amount is positive for a narrow range of bulk density for both CO_2 and CH_4. The transition into negative values for the 40 °C CO_2 isotherm occurs in the following order: B8 (0.10 mol/L) < B6 (0.15 mol/L) < ML (0.35 mol/L) < LG4 (0.60 mol/L). The maximum net adsorbed amount is also in the same sequence. This is a reflection of the adsorption capacity and the TOC content of each shale. The insets in Figure 7.2 shows that the transition is affected by both the adsorbate and the temperature; for CO_2 and at lower temperatures, negative values start occurring at larger bulk densities. For CH_4, the bulk density range in which positive n^{net} values occur is always smaller than with CO_2, due to the lower adsorption of methane. The net isotherms are mostly linear across the pressure range, especially for CH_4 and the Bowland shales. The slopes of the isotherms at high pressure ($= (V_s + V_a)/m_s$) are only slightly higher than that of the dotted lines, which correspond to negative V_s/m_s. This illustrates the modest contribution of adsorption to gas storage in these shales. The slopes for the 40 °C CO_2

Table 7.1: The key parameters and their uncertainties utilised in the calculations of the excess or net adsorbed amount for the LG4, ML, B6 and B8 shales. Where no uncertainty is shown, the uncertainty is below 0.001. For B6, the Helium Runs 2 and 3 show two sets of values: white cells represent the raw values obtained through weighted linear regression and the grey cells represent values taken forward for the calculation of the adsorbed amounts. * denotes Runs straight after the CO_2 measurement.

Shale	m_{met} [g]	V_{met} [cm^3]	V_{sk} [cm^3]	He Run	m_s [g]	V_s [cm^3]	ρ_{sk} [g/cm^3]
LG4	7.705	1.420	4.364 ± 0.002	1	1.969	0.764 ± 0.001	2.578 ± 0.002
				2	1.959	0.762 ± 0.001	2.572 ± 0.004
				3	1.959	0.762 ± 0.001	2.570 ± 0.005
				4*	1.960	0.752 ± 0.001	2.608 ± 0.004
ML	7.705	1.420	4.364 ± 0.002	1	1.580	0.371 ± 0.001	2.694 ± 0.004
				2	1.577	0.372 ± 0.001	2.690 ± 0.006
				3	1.577	0.371 ± 0.001	2.699 ± 0.006
				4	1.577	0.371 ± 0.001	2.695 ± 0.005
				5*	1.578	0.370 ± 0.001	2.704 ± 0.006
B6	5.285	0.667	4.364 ± 0.002	1	2.154	0.376 ± 0.001	2.662 ± 0.004
				2*	2.155	0.376 ± 0.002	2.660 ± 0.005
					2.155	0.376 ± 0.001	2.663 ± 0.004
				3	2.155	0.375 ± 0.002	2.665 ± 0.006
					2.155	0.376 ± 0.001	2.663 ± 0.004
B8	7.705	1.420	4.364 ± 0.002	1	2.654	0.370 ± 0.001	2.703 ± 0.004
				2	2.655	0.371 ± 0.001	2.693 ± 0.004
				3*	2.655	0.370 ± 0.002	2.703 ± 0.006

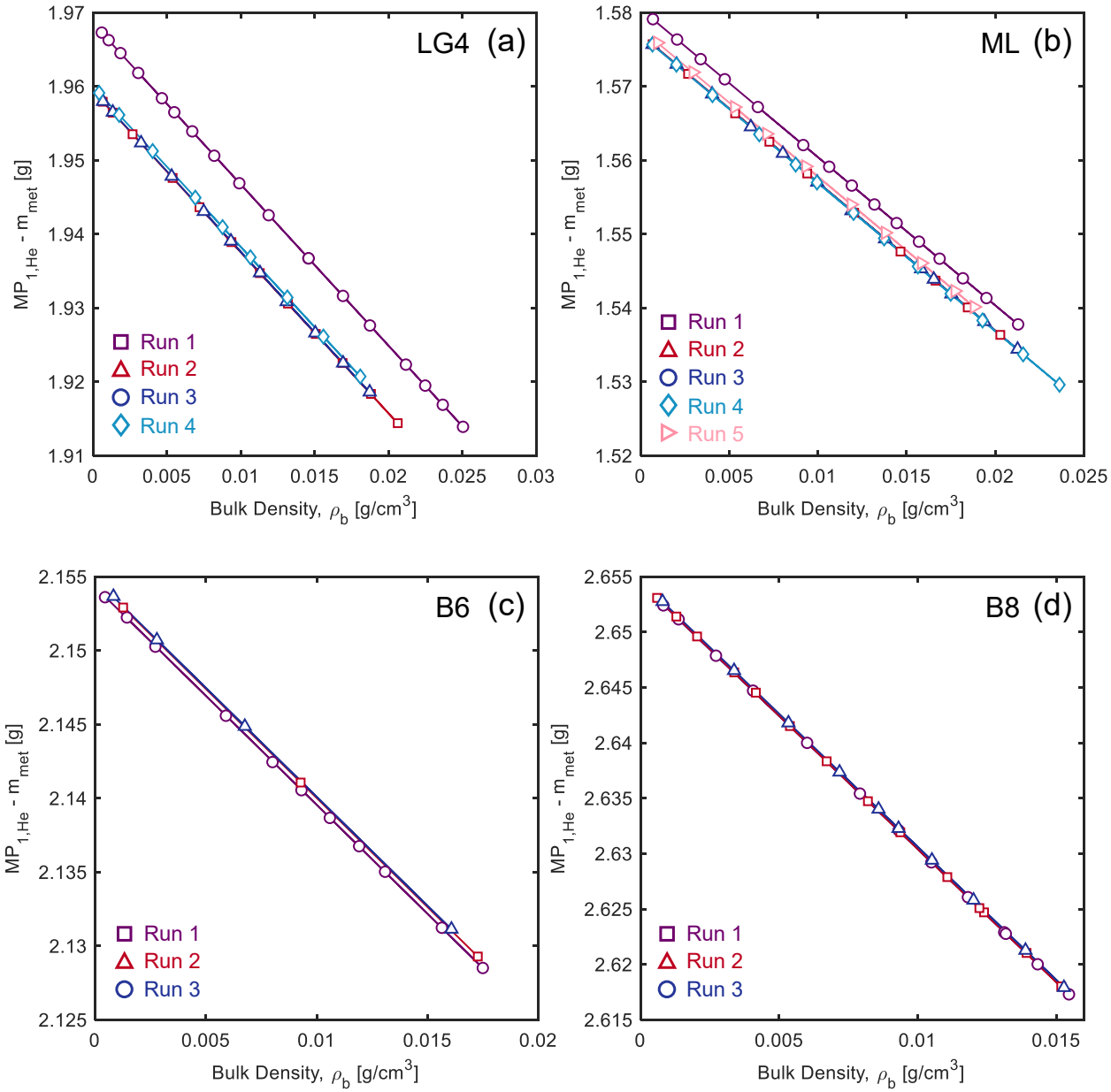

Figure 7.1: Corrected MP_1 [$MP_{1,He} - m_{met}$] as a function of Helium density (experiments conducted at 80 °C and over the pressure range 3-198 bar) for (a) LG4, (b) ML, (c) B6 and (d) B8 for various runs.

isotherm above 15 mol/L correspond to a V_a/m_s of 0.011±0.002 cm^3/g (LG4), 0.009±0.002 cm^3/g (ML), 0.006±0.001 cm^3/g (B6) and 0.0010±0.0005 cm^3/g (B8). The adsorbed phase is larger for the TOC-rich shales (ML and LG4) as the total available pore volume is also bigger. The uncertainties in these values correspond directly with the error in the net measurements (which is minuscule) and the solid volume. The calculated adsorbed phase volumes are 23% (LG4), 22% (ML), 31% (B6) and 5% (B8) of the each shale's respective ν_{tot}. These values are almost the same or slightly higher than the micropore fraction in each shale. As highlighted in the previous chapter, this type of graphical approach is more suited towards micropore-dominated materials as mesoporosity in an adsorbent would cause the adsorbed phase to be distributed amongst pores of varying sizes, some of which will

never be fully saturated.

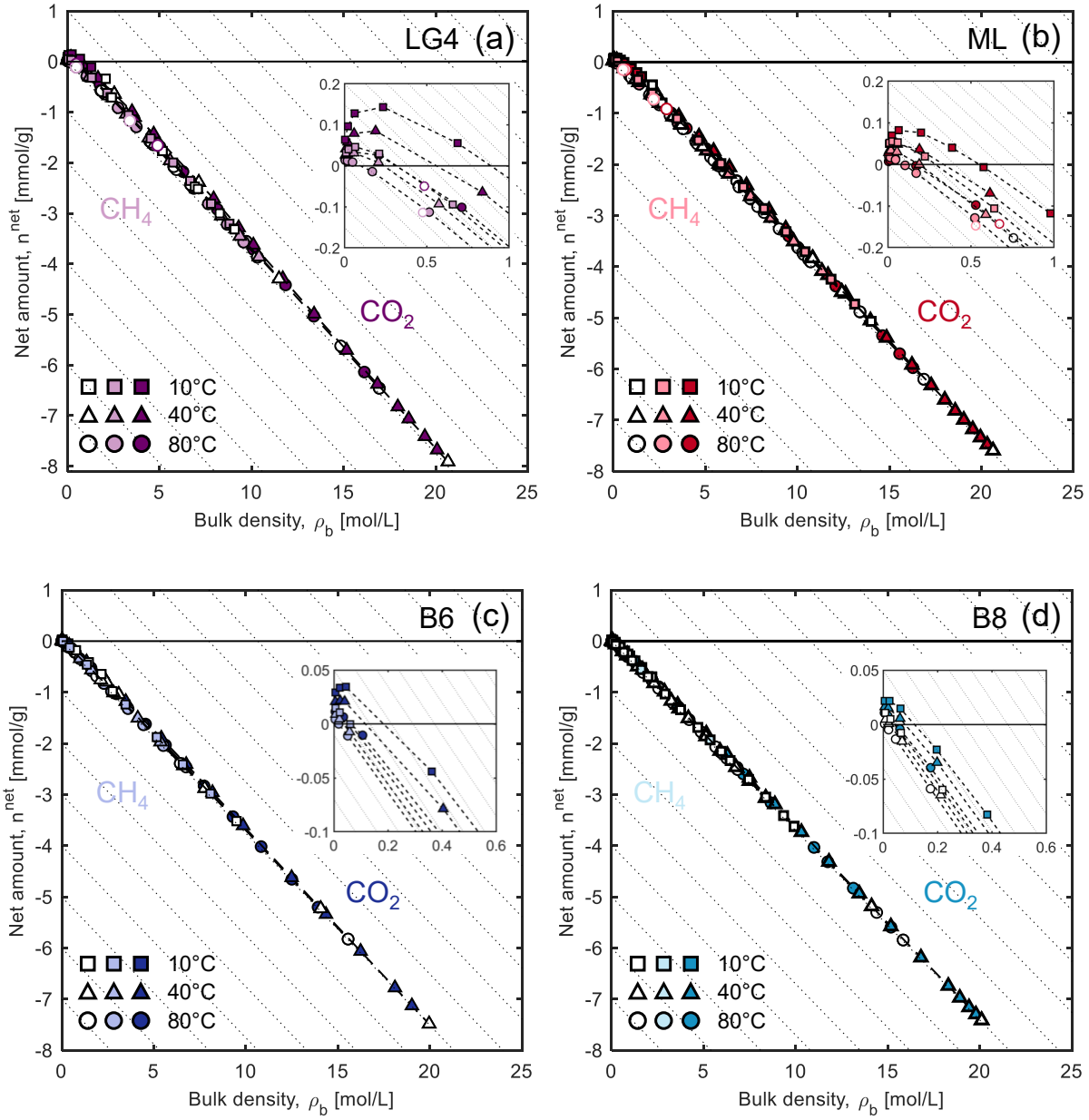

Figure 7.2: Unary net adsorption isotherms measured with CO_2 and CH_4 on (a) LG4, (b) ML, (c) B6 and (d) B8, plotted as a function of the bulk density at 10 °C, 40 °C and 80 °C. Dotted lines have a slope of V_s/m_s. Empty symbols denote data taken in adsorption mode and filled symbols represent data taken in desorption mode. Symbols with a black outline represent data on the powdered sample, while those with a coloured outline, only relevant to the LG4 and ML shales, represent data on the chip sample. Dashed lines connecting the symbols are to guide the eye only. Experimental uncertainties are not shown as they are smaller than the size of the symbols but are tabulated along with the experimental data in Tables B.1 and B.2 (LG4), Tables B.3 and B.4 (ML), Tables B.5 and B.6 (B6) and Tables B.7 and B.8 (B8).

7.1.3 Excess Adsorption

Pure component CO_2 and CH_4 excess adsorption isotherms at 10 °C, 40 °C and 80 °C on the LG4, ML, B6 and B8 shales are shown in Figure 7.3 (I and II). The corresponding in-situ bulk density measurements are shown in the appendices, which are in excellent agreement with the data reported by NIST, with an average residual sum of squares in the range 0.37–0.71 $(mol/L)^2$ (CO_2) and 0.001–0.004 $(mol/L)^2$ (CH_4), across the four shales. Figure 7.3 also shows error bars associated with each experimental point; these have been calculated using the error propagation procedure described in Chapter 3. All experimental data are tabulated in the appendices. CO_2 consistently adsorbs higher than CH_4 for all the shales at all three temperatures. The excess adsorption isotherms have the same qualitative behaviour as the synthetic mesoporous adsorbents; adsorption initially increases monotonically up until 5–7 mol/L, after which, excess adsorption decreases non-linearly with increasing bulk fluid density. With CO_2, excess adsorption approaches $n^{ex} = 0$ at very high densities. At these conditions, the adsorbed phase is virtually identical to the bulk phase. Although the CH_4 excess isotherms also show a maximum, the lack of data at sufficiently high pressure means that this behaviour is never attained with this adsorbate. For B8, the CO_2 excess adsorption seems to level off at a finite value at high pressures, indicating other mechanisms might be at play. Possible explanations could be gas uptake into the shale structure, including fractures or macroporosity (this shale possesses the largest fraction of macroporosity at 40% of its ν_{tot}), rather than adsorption on the surface, or the shale matrix might be changing in some way. Further experimental work and analysis are required to determine the cause of this particular behaviour.

Most of the effects of supercritical adsorption observed with the synthetic adsorbents can also be identified with the shales: (i) as temperature increases, adsorption decreases, (ii) the change in temperature has more of an effect on CO_2 due to the proximity of the experimental temperatures to the adsorbate's critical point, unlike CH_4, and (iii) the isotherm peaks become more narrow and the descending part of the excess isotherms is non-linear at experimental temperatures closer to the critical point of CO_2, which is typical of mesoporous materials as explained in the previous chapter. The uncertainty in the measured excess amount generally increases with an increase in the bulk density as indicated by the error bars in Figure 7.3 (I and II) and suggested by Eq. 3.5a. While in the previous chapter, the error bars were not visible as the experimental uncertainties were smaller than the size of the symbols, the uncertainty is proportionally larger for shales, due to their lower level of adsorption. However, these uncertainty values are still relatively small, which speaks to the high quality of the experimental procedure and measurements.

Comparing the adsorption between the shales, it is evident that the more organic-rich and thermally mature shales (LG4 and ML) adsorb more than twice the amount of gas compared with the Bowland

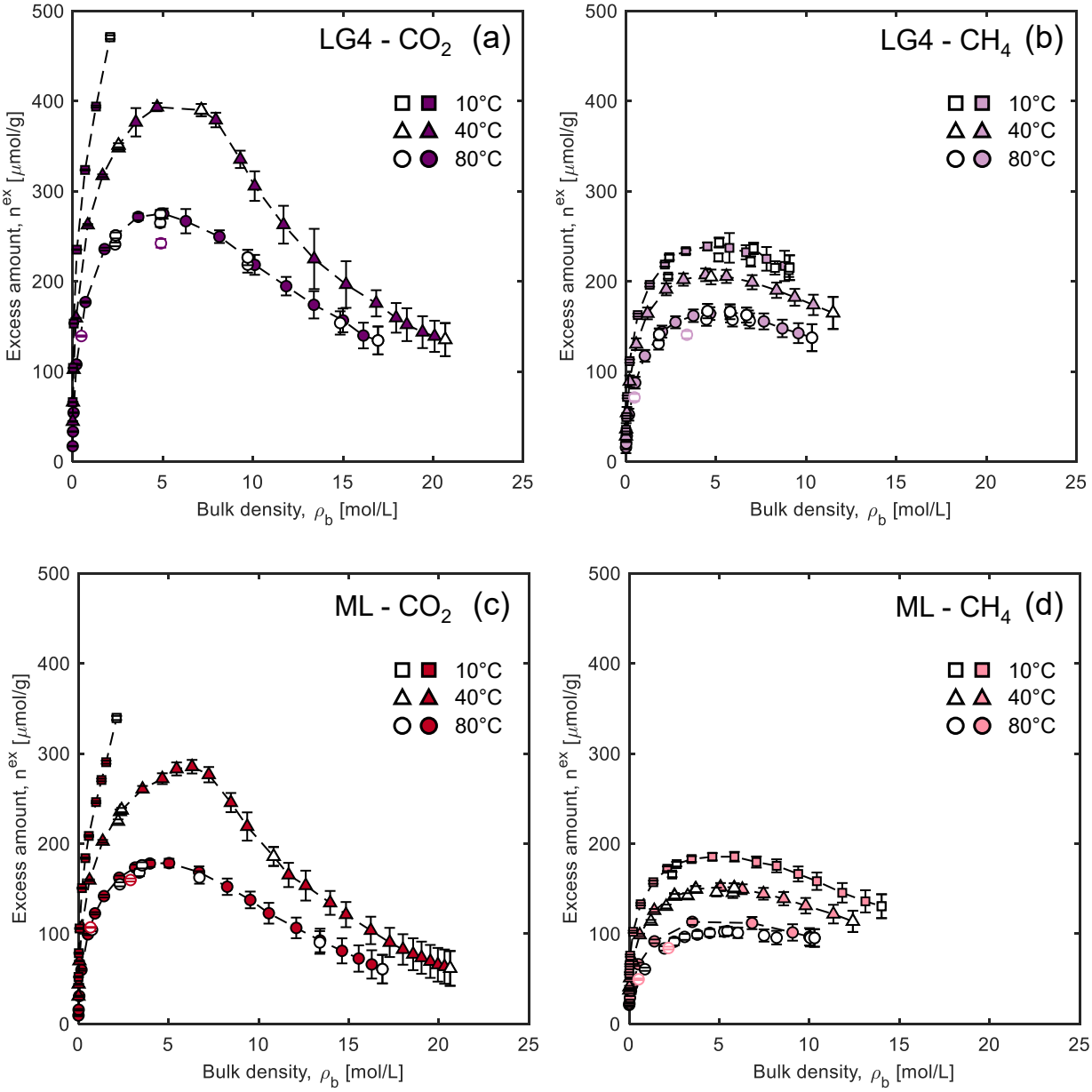

Figure 7.3: I – Unary excess adsorption isotherms measured with CO_2 and CH_4 on (a, b) LG4 and (c, d) ML, plotted as a function of the bulk density at 10 °C, 40 °C and 80 °C. Empty symbols denote data taken in adsorption mode and filled symbols represent data taken in desorption mode. Symbols with a black outline represent data on the powdered sample, while those with a coloured outline represent data on the chip sample. Dashed lines connecting the symbols are to guide the eye only.

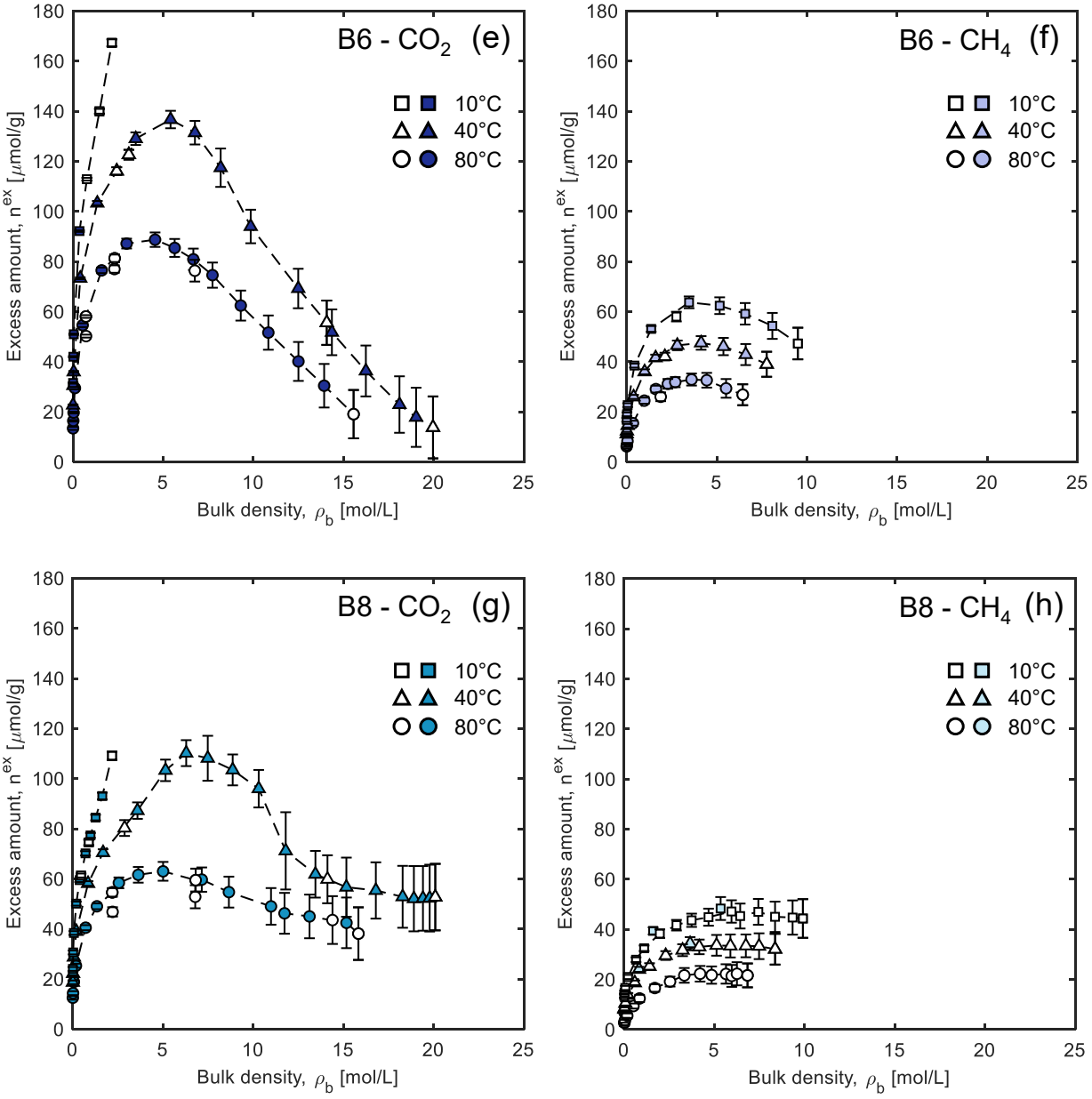

Figure 7.3: II – Unary excess adsorption isotherms measured with CO_2 and CH_4 on (e, f) B6 and (g, h) B8, plotted as a function of the bulk density at 10 °C, 40 °C and 80 °C. Empty symbols denote data taken in adsorption mode and filled symbols represent data taken in desorption mode. Dashed lines connecting the symbols are to guide the eye only.

shales. The ratio of the isotherm peaks of CO_2 versus CH_4 is higher for the Bowland shales, however, at ∼3 times, than the more thermally mature shales, LG4 and ML (at ∼2 times). For the latter, the ratio of the excess adsorption between LG4 and ML is very close to the ratio of TOC within the sample (∼1.3). Within the Bowland shales, the higher TOC of B6 (at 3.3 wt%) means that it has a slightly elevated level of excess adsorption as compared to B8 (TOC = 1.0 wt%). This result is especially useful as both B6 and B8 have an equivalent amount of clay minerals (25.5 wt%). Adsorption capacities of these shales correspond relatively well with other shales that have a similar TOC content [125, 124, 108, 123, 26, 27].

The application of the same rigorous experimental protocol and analysis procedure to a variety of shales enables the understanding of some of the effects of supercritical adsorption of CO_2 and CH_4 on these sorbents. Both Figures 7.2 and 7.3 show experimental points taken by increasing pressure in the MSB (adsorption mode, empty points) and by depressurising the MSB to the desired point (desorption mode, filled points). There were two sets of points usually taken in adsorption mode: (a) on the way to the initial pressurising of the MSB to the maximum experimental pressure of 250–300 bar, and (b) repeat of points (a) after the completion of the full isotherm in the desorption mode. The points from step (a) are clearly evident in the excess isotherms in the form of some empty symbols usually lying just below the connected points at each temperature. The points at these pressures were repeated after the shale had been exposed to the maximum pressure and a full isotherm was complete, as part of step (b), and they correspond very well with the connected isotherm and adsorption is increased relative to the points from step (a). This is repeatedly the case for all shales and both gases. We conclude that perhaps the shale requires some sort of 'activation' before the pores can be fully accessed and gas can be adsorbed. Another possibility is that there is a change in the accessible porosity once the rock is exposed to high pressure gas. The expansion of some small pores at very high bulk density could explain this enhanced adsorption capacity.

Figures 7.3a and 7.3b also show points with a coloured outline. Before the LG4 and ML shales were crushed into powder, MSB experiments with CO_2 and CH_4 were performed using large shale chips (about 2 cm in width) at two different pressures each, with each measurement lasting for at least one day. The primary purpose of these experiments was to ascertain how long equilibrium could take under geological conditions but these measurements can also indicate whether it is exposure to supercritical fluids or the duration of exposure that causes the change in adsorption capacity. The results as a function of time are shown in the appendices. Full equilibrium was established very quickly (in just under an hour) for both gases and samples at two different pressures, indicating that the chosen equilibration time of at least 90 minutes for each adsorption point with the powders is more than sufficient. These results align very well with adsorption points (a) rather than the isotherm obtained after reaching 300 bar, suggesting it is, in fact, the high pressure and not the duration which affects

the so-called 'relaxation' of the shale.

Another interesting observation is the fact that almost all isotherms do not fully close, i.e., they do not reach $n^{ex} = 0$ as pressure is lowered to almost 0 bar. This result is in agreement with the Helium measurements (Section 7.1.1), whereby the adsorbent mass periodically increases. It is clear that either the shale permanently retains some of the adsorbed phase or it undergoes some change which causes this increase in adsorbent mass and skeletal density, as even regenerating the sample under vacuum and at a high temperature does not reverse this condition. Therefore, even when the pressure of the gas is lowered to almost zero, the isotherm approaches a non-zero value for the excess adsorbed amount. A further manifestation of this effect is that repeating experimental points on a higher temperature isotherm after exposing the shale to adsorption at a lower temperature (i.e. moving in the direction of decreasing excess adsorbed amounts) meant that inconsistent results would be obtained, even if the points were repeated after a full degassing procedure. Using the same vacuum point and Helium measurement for both the CO_2 and CH_4 measurements results in either very high and or very low excess adsorbed amounts for one of the adsorbates. This is why it is imperative to repeat both measurements periodically during the course of the supercritical adsorption measurements. Even though the change in both the adsorbate mass and the solid volume might appear minor, just a 1% change in V_0 is enough to induce a shift of more than 50 μmol/g in the excess adsorption isotherms. This is obviously more of a concern for lower-adsorbing shales such as the Bowland shales, and this uncertainty is reflected in the error bars for these samples being proportionally larger.

Changes in shale after exposure to supercritical CO_2 have been documented in the literature. Decreases in microporosity [250, 251, 252], dissolution of certain components such as the organic matter, clay minerals, calcite and carbonates [253, 254, 250, 251, 252], and reduced adsorption capacities of CH_4 and CO_2 [252] are all effects that have been attributed to long-term exposure and interaction of supercritical CO_2 with shale. A similar effect on the ML shale was shown in Chapter 5 via subcritical Ar and CO_2 measurements performed before and after the high pressure experiments; the shale showed a decreased microporosity fraction and specific surface area after the MSB experiments. Clearly the shale undergoes some sort of a transformation as a result of the interaction with supercritical fluids, but to understand the precise mechanisms involved and rigorously evaluate the implications of these on enhanced shale gas recovery, further analyses that are out of the scope of this thesis are required.

7.2 Henry Constants and Adsorption Energetics

This section presents the Henry constants and the isosteric enthalpies of adsorption derived from the high pressure and low pressure adsorption experiments on each shale. These quantities were estimated

by the application of the Virial equation (Eq. 4.21) to the supercritical adsorption data and subcritical CO_2 measurements, which can be found in the appendices. The resultant Virial plots can be seen in Figure 7.4, where a linear region at each temperature is clearly visible. Note that for B6 and B8, adsorption data that were at a bulk density slightly higher than 10% of the liquid density (maximum of 13%) of both adsorbates had to be considered, due to limited data at a lower density. The dashed lines indicate the extrapolation to zero loading to obtain the Henry constants, which are shown in Figure 7.5 (and tabulated in Table 7.2) as a function of the reciprocal temperature. Linear relationships between the Henry constants and the inverse of temperature are observed, in accordance with the the van't Hoff equation (Eq. 4.22) and as demonstrated by the linear fits shown in the figure. There is excellent agreement between the Henry constants obtained from both the MSB and the volumetric apparatus, indicating the suitability of the Virial approach for this purpose. All shales have Henry constants that are higher for CO_2 than CH_4. For both adsorbates, the Henry constants on the TOC-rich shales are up to an order of magnitude higher than the Bowland shales. The CO_2 Henry constants for LG4 are roughly 1.5 times that of ML, but the CH_4 ones are almost equivalent. Within the Bowland shales, the CO_2 Henry constants differ by the same ratio of 1.5 but the CH_4 ones are almost three times higher for B6 as compared to B8. The LG4 and ML shales exhibit a lower selectivity (2.53 ± 0.04 and 1.52 ± 0.35, respectively) towards CO_2 as compared to the Bowland shales (2.86 ± 0.63 for B6 and 5.99 ± 1.40 for B8). These values are higher than those observed with the pure carbon adsorbents shown in the previous chapter suggesting that the clay minerals also contribute towards the enhancement of this selectivity in shales. Indeed, this selectivity has been shown to be much higher (> 5) for pure clay minerals such as Illite [72].

The parameters of the integrated van't Hoff equation applied to the Henry constants can be seen in Table 7.2, including the isosteric enthalpy of adsorption at zero loading. This quantity generally becomes less negative with decreasing TOC content of the shale, with the highest heat of adsorption for the LG4 shale (-24 kJ/mol). The weaker the adsorption capacity, the lower the heat. For the TOC-rich shales, the estimates are similar to the enthalpy of adsorption for the porous carbons described in the previous chapter. They are also similar to other shales reported in the literature [108, 255, 256, 257], but are considerably more negative than the value reported for pure clay minerals (-12 kJ/mol) [72]. This implies that the intensity of interaction between these adsorbates and the shale is similar to pure carbons but that shale's lower adsorption capacity is due to the available pore volume and its distribution. The heat of adsorption for CO_2 is always higher than that for CH_4, signifying shale's preference for the former. These estimates are also greater than the latent heat of vapourisation of the two adsorbates ($\Delta h_{\text{vap}} = -10.3$ kJ/mol for CO_2 at 273.15 K and $\Delta h_{\text{vap}} = -8.2$ kJ/mol for CH_4 at 112 K [231]), and towards the higher end of the expectation that for physisorption, $\Delta h_0 / \Delta h_{\text{vap}} < 1.5 - 2$ [245].

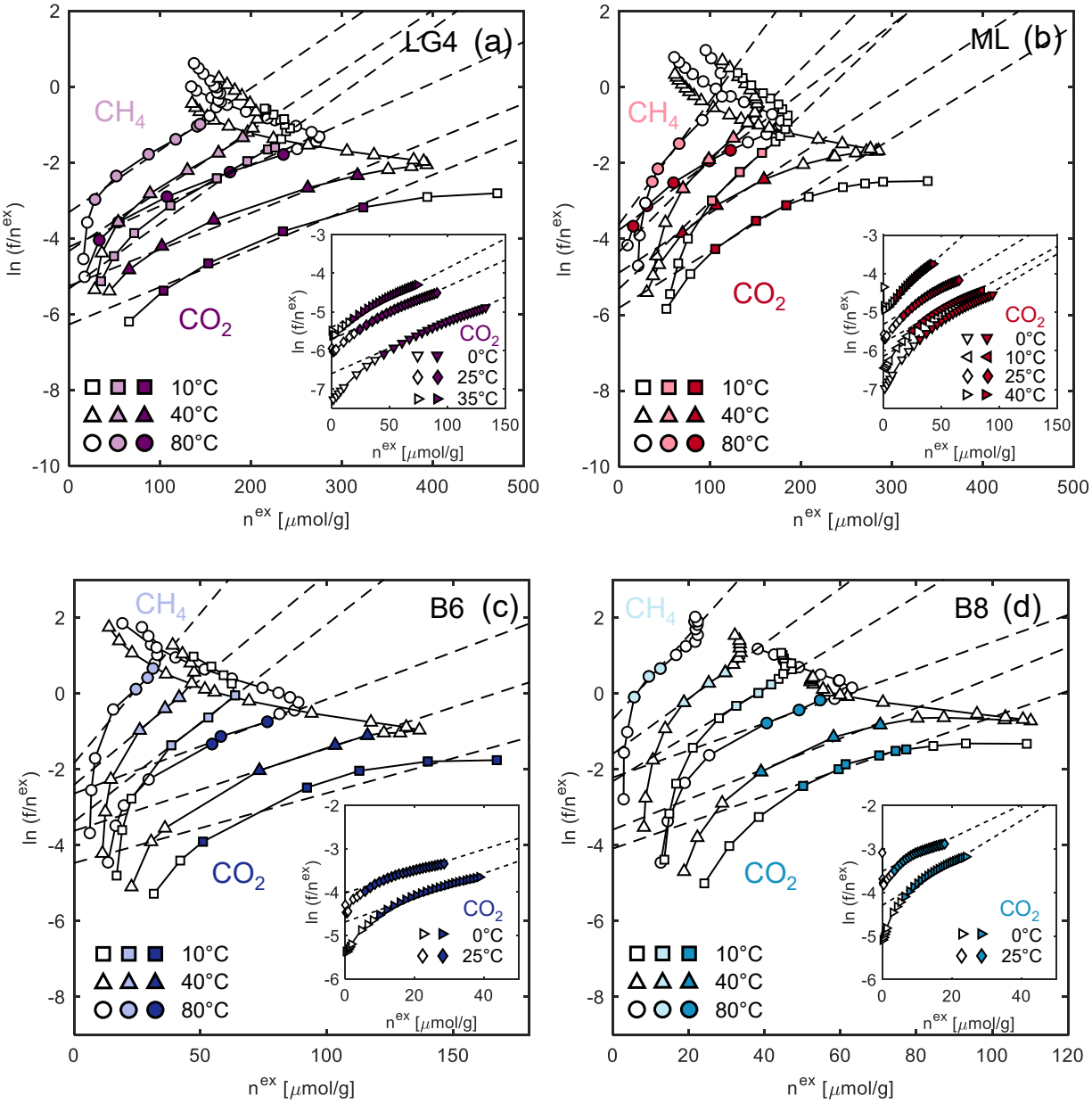

Figure 7.4: The Virial plot [ln(f/n^{ex}) vs. n^{ex}] for (a) LG4, (b) ML, (c) B6 and (d) B8. Insets show the subcritical CO_2 data. All experimental points are connected with solid lines. Filled points represent the experimental data that were considered part of the linear region, and empty points are the residual experimental data. The dashed lines are the linear fits at all experimental temperatures.

7.3 Shale Controls on Gas Adsorption

As the interpretation of supercritical adsorption measurements can be quite challenging, especially with relatively low-adsorbing materials such as shales, it is of significant interest to understand the underlying mechanisms and controlling variables at these conditions so that some steps can be taken towards predicting the behaviour of other shales. This section presents attempts at identifying these very controls on gas adsorption in shales.

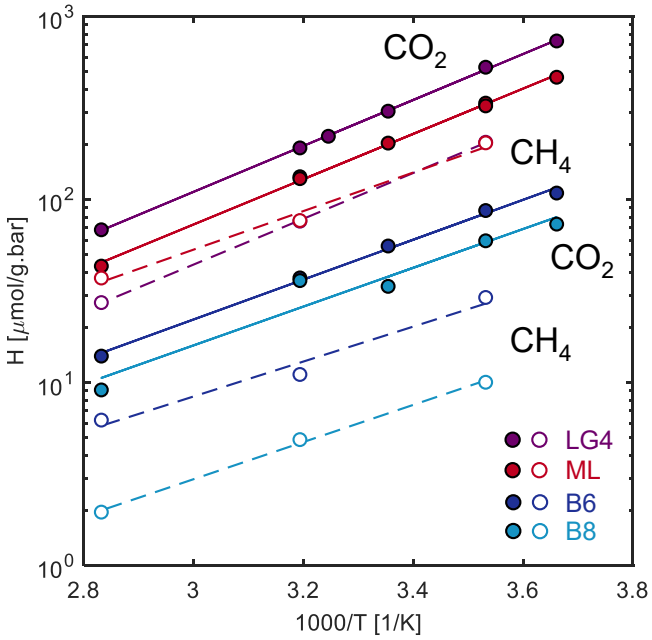

Figure 7.5: Henry constants as a function of the reciprocal temperature for CO_2 and CH_4 on all shales. Lines denote linear fits to the experimental data.

Table 7.2: The Henry constants (from high pressure, HP, and low pressure, LP, adsorption experiments), average selectivity and parameters of the integrated van't Hoff equation (Eq. 4.18), including the isosteric enthalpy of adsorption, Δh_0 and the corresponding pre-factors (H_0), for all four shales. The Henry constants are also shown in Figure 7.5.

		LG4		ML		B6		B8	
Parameter		CO_2	CH_4	CO_2	CH_4	CO_2	CH_4	CO_2	CH_4
	10 °C	528.5	205.6	336.4	204.1	87.1	29.2	59.5	10.0
H (µmol/g/bar) – HP	40 °C	191.5	76.2	133.3	76.8	37.3	11.1	36.1	4.9
	80 °C	68.4	27.4	43.3	37.3	14.0	6.2	9.1	2.0
	0 °C	735.4	–	465.9	–	108.5	–	73.4	–
	10 °C	–	–	324.9	–	–	–	–	–
H (µmol/g/bar) – LP	25 °C	304.0	–	203.5	–	55.7	–	33.6	–
	35 °C	221.8	–	–	–	–	–	–	–
	40 °C	–	–	130.1	–	–	–	–	–
Selectivity		2.53 ± 0.04		1.52 ± 0.35		2.86 ± 0.63		5.99 ± 1.40	
H_0 (µmol/g/bar)		19.0	7.79	14.2	37.0	11.9	11.5	10.6	2.68
Δh_0 (kJ/mol)		−24.0	−24.0	−23.7	−20.2	−20.9	−18.3	−20.3	−19.4

7.3.1 Maximum Excess Adsorbed Amount

Figure 7.6 shows the maximum excess adsorbed amount versus (a) temperature for CH_4, (b) TOC and (c) total pore volume of each shale for both adsorbates. Figure 7.6a shows a linear ($R^2 > 0.98$) negative correlation between the maximum excess adsorbed amount of CH_4 on all four shales versus

temperature. Interestingly, the slopes of the LG4 and ML shales are very similar to each other and more negative than the slopes of the Bowland shales, which are also similar to each other. This result will be extremely useful in predicting adsorption capacities at other temperatures for each shale. The maximum adsorption capacity is dependent not only on the temperature but also on the TOC as shown in Figure 7.6b, which presents a strong positive correlation ($R^2 > 0.96$) between the two. Note that the linear fits are solely based on the LG4, ML and B8 shales; the B6 TOC has been derived as the average of the TOC values obtained from each individual fit (with the knowledge of the maximum excess adsorbed amounts of B6 from Figure 7.3). The results show that B6 TOC should be around 2 wt% which is fairly close to its predicted value (∼3 wt%) from the low pressure adsorption measurements described in Chapter 5. The non-zero y-intercepts of the lines suggest that the adsorption capacity also originates from adsorption on the clay minerals. At the same temperature, the CO_2 lines are steeper than CH_4, indicating that the TOC has a stronger influence on the strength of adsorption of the former. For an incremental rise of 1% in the TOC at 40 °C, n^{ex} rises by 40 µmol/g and 25 µmol/g for CO_2 and CH_4, respectively. Figure 7.6c shows that the maximum excess adsorbed amount also has a positive linear correlation with the total pore volume of each shale, although this correlation is slightly weaker ($R^2 > 0.95$) than the one with TOC, indicating that the latter has a strong control on supercritical adsorption within these rocks. The change in pore volume has a stronger effect on CO_2 than CH_4 (analagous to the relationship with TOC). Collectively, these results are essential in enabling the prediction of adsorption on various shales, with varying compositions and textural properties.

7.3.2 Scaling Analysis

Figure 7.7a shows the results of scaling the isotherms of each shale by the ratio of the maximum excess adsorption of ML (the reference shale) to that for each of the other shales at 40 °C. There is almost a universal curve in the case of both CO_2 and CH_4 at this temperature, with significant differences occurring only at high bulk densities. For CO_2, the shape of each shale's isotherm is virtually identical near the peak. B8 has a lower uptake just before this peak as it has the lowest percentage of microporosity of 10% and has a peak that is shifted to higher bulk densities. This shale also has the lowest TOC of around 1 wt%, which could account for its isotherm being something of an outlier in terms of shape. All four CO_2 isotherms behave differently at $\rho_b >\sim 15$ mol/L, which could be due to a combination of reasons such as clay content (which is in the order B6 = B8 < LG4 < ML) or varying fractions of meso- and macro-porosity in each shale. The CH_4 isotherms are all reasonably congruent as the shape of the isotherms is fairly regular and show less of an effect of varying textural properties, due to the isotherm temperature being much further away from the adsorbate's critical temperature, unlike CO_2. The fact that the scaling factor of the ratio of isotherm peaks applies across

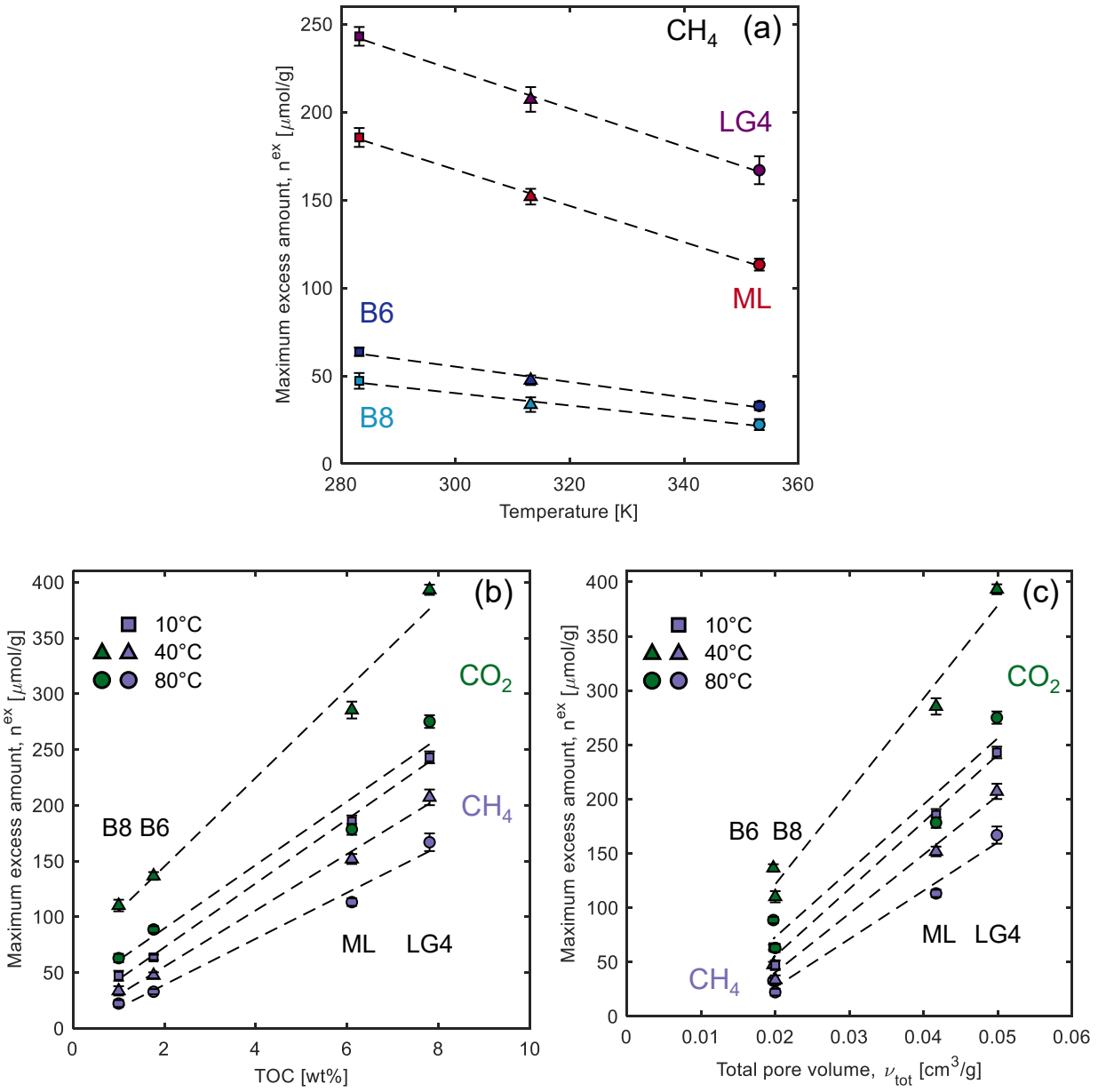

Figure 7.6: (a) CH_4 maximum excess adsorbed amount as a function of experimental temperature for all the shales. Lines denote linear fits to the experimental data, CO_2 and CH_4 maximum excess adsorbed amount as a function of the (b) TOC and (c) total pore volume of each shale at various temperatures. Dashed lines fits denote linear fits to the experimental data. In (b), these linear fits are solely based on LG4, ML and B8 and the TOC of B6 has been calculated based on the average TOC values obtained from each individual fit using the maximum excess adsorbed amounts for B6.

the density range for CH_4 is quite remarkable. The excess adsorption order at high densities is the same as that of CO_2, indicating that it is probably the same factor which determines this behaviour for both gases.

The relationship between the scaling factors used to obtain Figure 7.7a and the TOC and the total pore volume are shown in Figures 7.7b and 7.7c, respectively. There is again a very strong (negative) linear correlation between the scaling factors and these two parameters, where $R^2 > 0.97$ (TOC) and

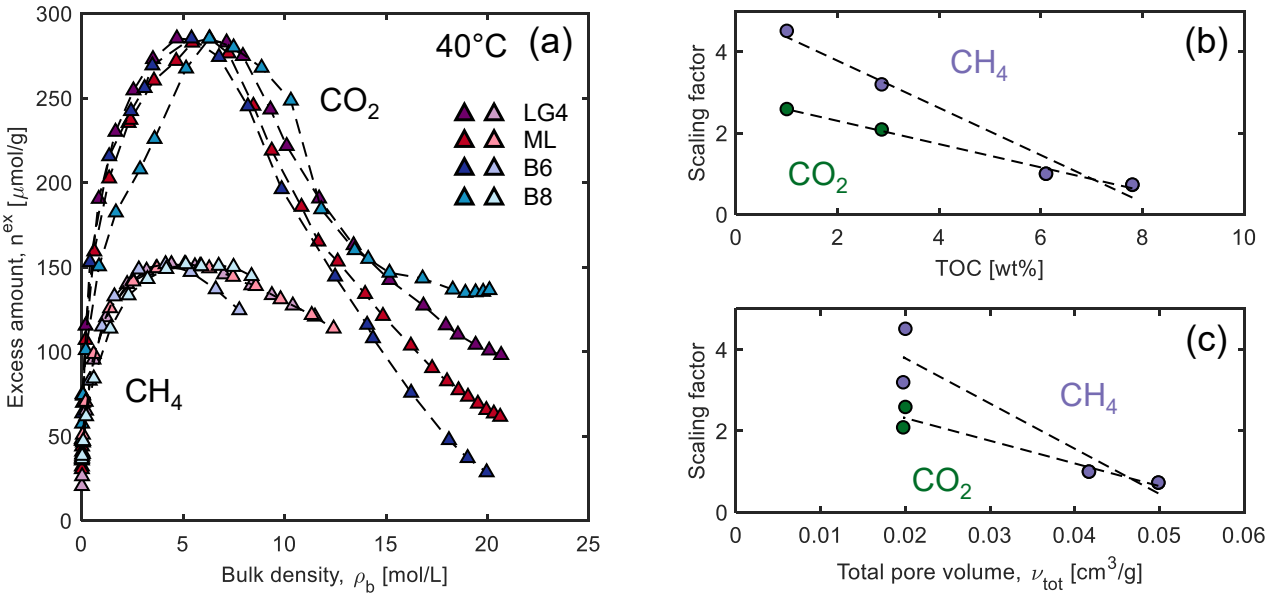

Figure 7.7: (a) Scaled CO_2 and CH_4 excess adsorption isotherms at 40 °C for the LG4, ML, B6 and B8 shales. The isotherms of each shale have been multiplied by the ratio of the maximum excess adsorbed amount of the ML shale and the respective shale itself, for each adsorbate. The scaling factors versus the (b) TOC and (c) total pore volume of each shale. Dashed lines fits denote linear fits to the experimental data. In (b), these linear fits are solely based on LG4, ML and B8 and the TOC of B6 has been calculated based on the average of the results from each linear fit.

0.89 (ν_{tot}). As before, the B6 TOC (= 2.9 wt%) has been calculated based on the linear fits which include the remaining shales; this value is very close to that reported in Chapters 3 and 5. CH_4 requires larger scaling factors for the Bowland shales as compared to CO_2, whereas for LG4, the factors for both adsorbates are almost equal at 0.73. In addition, the lower the TOC and the pore volume, the larger the scaling factor required to superimpose the isotherms onto the reference (ML) isotherms. It is evident from this analysis also that TOC is the stronger control parameter for gas adsorption.

7.3.3 Synthetic Adsorption Isotherms

The synthetic adsorbents studied in the previous chapter and pure clay minerals provide an opportunity to evaluate the independent effect of the constituents of shale on its adsorption behaviour. Figure 7.8 shows synthetic isotherms obtained by combining (summing) the lattice DFT modelled isotherms on mesoporous carbon (MC) and activated carbon (AC) (results shown in Chapter 6), as a representative of the TOC, and Illite (results based on parameters from Hwang and Pini (2019) [72]), as a representative for the clay minerals. This analysis is purely predictive and uses only the shale composition to individually scale the modelled isotherms of the pure carbon(s) and Illite. Comparing these results to the CO_2 and CH_4 shale isotherms at 40 °C shows that combining the synthetic adsorbents in this way is an excellent approach for reproducing the adsorption in these heterogeneous rocks. Particularly for the TOC-rich shales, both CO_2 and CH_4 are well-predicted. Note that with LG4, the carbon

component is represented by an AC:MC ratio of 1:4, which was required to prevent under-prediction of the shale isotherm caused by only using MC. LG4 is the most thermally mature shale, therefore its interaction with the adsorbates should be elevated as compared to the other shales. In fact, the ratio used is very close to the actual fraction of microporosity (22%) in this particular shale and as AC represents a more microporous carbon that has a higher interaction energy with these adsorbates (as described in the previous chapter), the integration of AC in this way is justified.

The figure also shows the individual contributions of the scaled pure carbon(s) and Illite isotherms. For LG4, ML and B6, the carbon component has a stronger influence on the adsorption capacity and isotherm shape, while for B8 (which is relatively organic-lean at 1 wt%), Illite has a larger presence. Both are clearly required as the adsorption capacity at $\rho_b < 5$ mol/L is better represented by Illite and around the excess adsorption isotherm maximum, the carbon component is necessary to describe the shape of the shale isotherm. The shape of both the pure isotherms is fairly distinct, with the MC isotherm having a fairly narrow peak and Illite showing a larger early uptake and flatter peak. The MC/AC isotherm in Figure 7.8a combines both of these effects. The benefit of this approach to estimate the adsorption of complex adsorbents such as shales cannot be underestimated as the high pressure adsorption experiments are very involved and time-consuming. The analysis in this section shows that by using these synthetic adsorbents, a reliable representative shale adsorption isotherm can be ascertained purely through the knowledge of a given shale's composition.

7.4 Gas-in-Place from Adsorption Measurements

Adsorption measurements serve as a useful means to understand the shale pore space as well the behaviour of fluids in these pores. Obtaining experimental adsorption isotherms is also the critical first step in quantifying gas storage potential in shale. Accurate resource estimates are integral and are an important precursor to proper economic analysis of the reservoir. The Gas-in-Place (GIP) can be calculated using a simple material balance approach. The total GIP (G_{tot}) depends on the two main storage mechanisms in shale, namely adsorption (G_{ads}) and gas compression (free gas, G_{free}):

$$G_{tot} = G_{free} + G_{ads} \tag{7.1}$$

The free gas component clearly depends on the accessible porosity and the bulk fluid density. Although adsorption is a strong contributor to the total GIP, classical methods tend to neglect the volume of the adsorbed fluid, which effectively reduces the available pore space for the free gas. This problem is

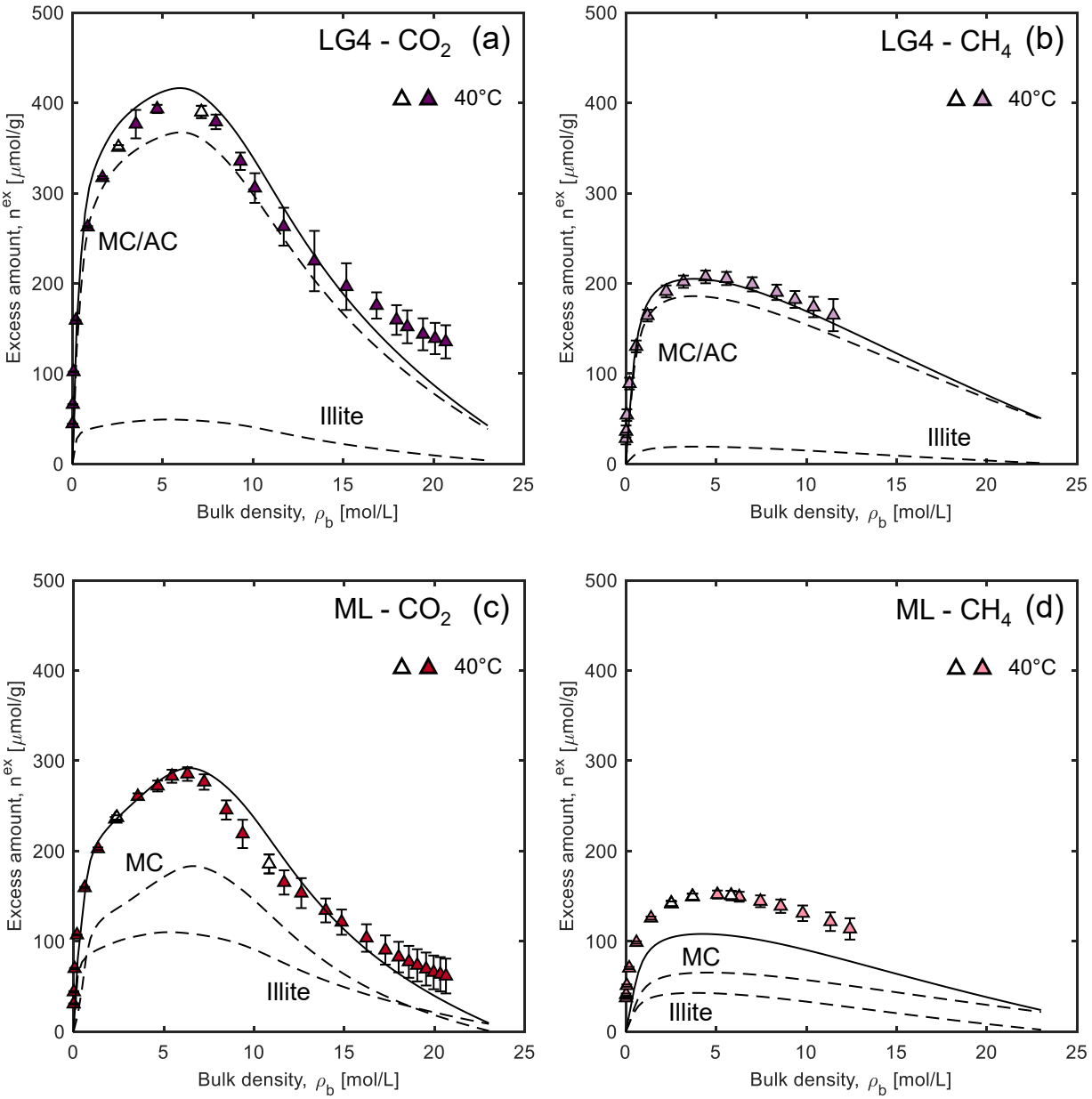

Figure 7.8: I – Excess CO_2 and CH_4 adsorption isotherms for (a, b) LG4, (c, d) ML at 40 °C (empty symbols denote data taken in adsorption mode and filled symbols represent data taken in desorption mode) and synthetic isotherms (solid lines) comprising of summed scaled MC, AC and Illite lattice DFT modelled isotherms at the same temperature. The scaling factors used for the modelled isotherms are based on each shale's TOC and clay content. Dashed lines show the individual contribution from the pure carbon(s) and Illite.

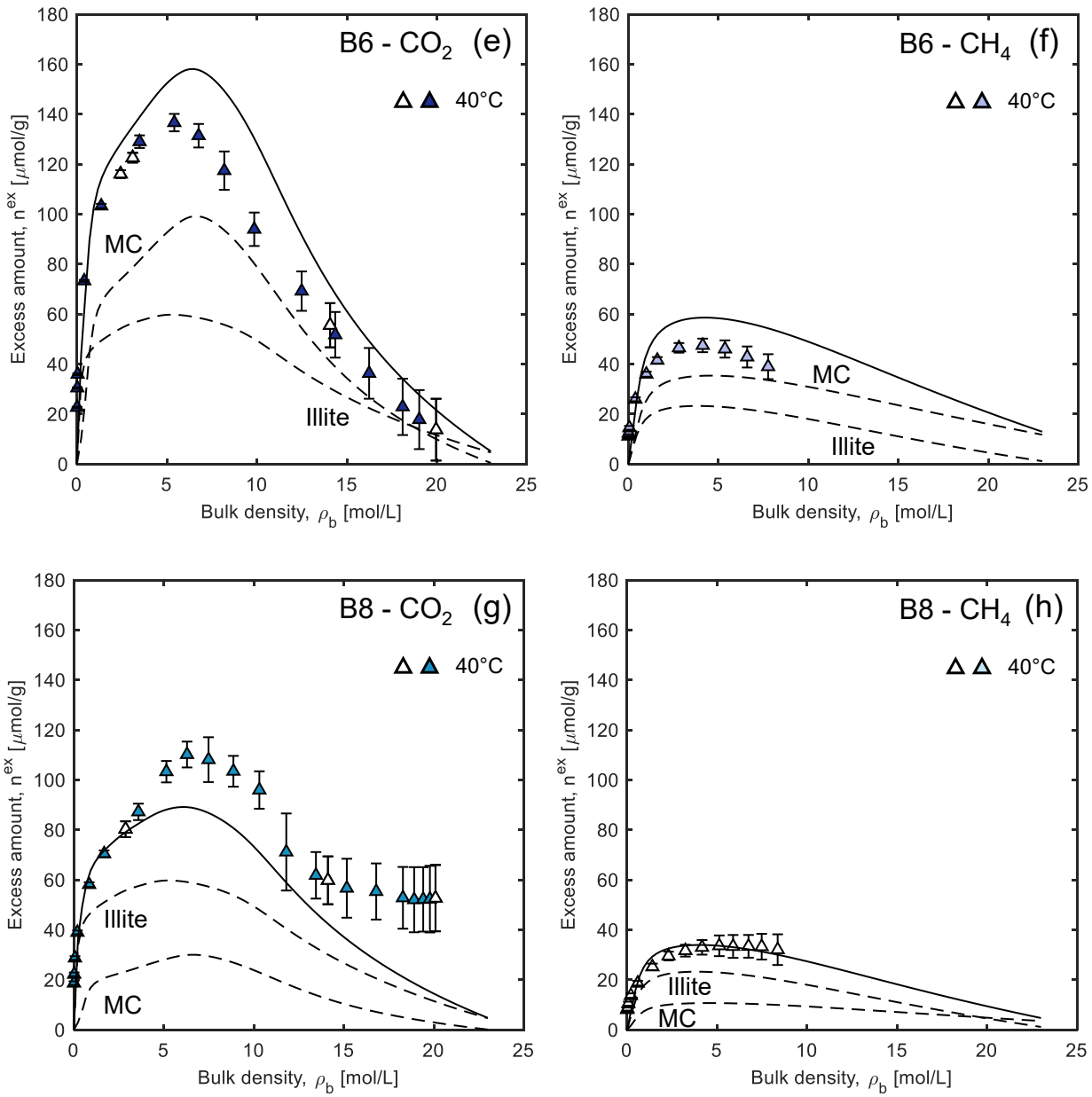

Figure 7.8: II – Excess CO_2 and CH_4 adsorption isotherms for (e, f) B6 (g, h) B8 at 40 °C (empty symbols denote data taken in adsorption mode and filled symbols represent data taken in desorption mode) and synthetic isotherms (solid lines) comprising of summed scaled MC, AC and Illite lattice DFT modelled isotherms at the same temperature. The scaling factors used for the modelled isotherms are based on each shale's TOC and clay content. Dashed lines show the individual contribution from the pure carbon(s) and Illite.

resolved when excess adsorbed quantities are used [7]:

$$G_{\text{tot}} = \frac{1}{\rho_{\text{sc}}}\left(\rho_{\text{b}}\phi - \left(\rho_{\text{b}}V_{\text{a}} + n^{\text{a}}\right)\left((1-\phi)\rho_{\text{sk}}\right)\right) = \frac{1}{\rho_{\text{sc}}}\left(\rho_{\text{b}}\phi + n^{\text{ex}}(1-\phi)\rho_{\text{sk}}\right) \tag{7.2}$$

Here, the free gas component of the total GIP is a function of the total porosity (ϕ), which is the total pore space available for the gas to occupy, and the bulk density of the fluid, ρ_{b} (mol/m^3). The contribution of adsorption to the total GIP comes from the absolute amount adsorbed, n^{a} (mol/g), and its volume, V_{a} (m^3/g). The excess adsorption term, n^{ex} (mol/g), encompasses both these quantities. The adsorption terms are multiplied by the bulk density of the shale ($= (1-\phi)\rho_{\text{sk}}$), a term which includes the skeletal density of the shale, ρ_{sk} (g/m^3). The sum of the two components is scaled by the density of the fluid at standard conditions, ρ_{sc} ($= 44.135$ mol/m^3 for CH_4 [231]), so that G_{tot} is in the units of $\text{m}^3_{\text{STP}}/\text{m}^3$. G_{free} is therefore the free gas that would exist at the same pressure and temperature conditions in a (conventional) reservoir with the same porosity, without any adsorption. It is not the actual free gas found in the shale reservoir, which has an adsorbed-phase that occupies a certain pore volume. Similarly, G_{ads} is the excess amount that exists in the pores due to adsorption and not the absolute amount adsorbed in the pores. The experimental results in this chapter are interpreted using these definitions. We are also interested in the ratio $G_{\text{ads}}/G_{\text{tot}}$, which provides insight into the contribution of adsorption to the total GIP. Additionally, the ratio $G_{\text{tot}}/G_{\text{free}}$ enables a clear comparison between an unconventional and conventional reservoir.

Figure 7.9 shows the CH_4 GIP (cumulative G_{tot}) as a function of P/Z ($= \rho_{\text{b}}RT$, where R and T are the universal gas constant and temperature, respectively), for all four shales. The results are based on a temperature of 80 °C and an assumed porosity of 5%, which is well within the common porosity range found in shale reservoirs [82]. The excess adsorption measurements described in Section 7.1.3 have been used directly in Eq. 7.2 to obtain the points shown in the figure. The plot also shows solid lines that represent G_{free} only, or a so-called volumetric reservoir. The total amount of gas in each shale reservoir (the original GIP or OGIP) can be found at $P/Z = 0$; this is a function of initial reservoir pressure, as the higher this pressure, the higher the bulk density. Therefore, to facilitate an even comparison, two datasets are presented in Figure 7.9: case (i) where the experimental data are restricted to below 200 bar of pressure, and case (ii) where all the excess adsorption data have been used (shown as the inset in Figure 7.9). For case (i), it is evident in the figure that the G_{free} lines for three of the shales are congruent (here, the maximum pressure of the experimental data and thus the initial reservoir pressure is ∼186 bar) and the line for B6 is slightly lower as the initial pressure is 175 bar. In case (ii), the initial pressure of the LG4 and ML reservoirs is higher at ∼297 bar.

Looking at the case where the initial reservoir pressure is consistent across the shales, the OGIP is in the following order: LG4 (16.6 $\text{m}^3_{\text{STP}}/\text{m}^3$) > ML (14.2 $\text{m}^3_{\text{STP}}/\text{m}^3$) > B8 (9.0 $\text{m}^3_{\text{STP}}/\text{m}^3$) > B6

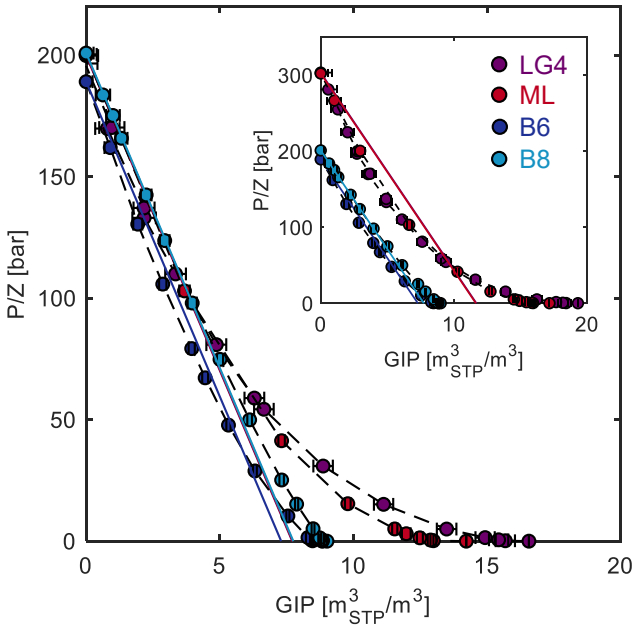

Figure 7.9: Gas-in-Place as a function of P/Z at a temperature of 80 °C and initial reservoir pressure of about 186 bar (LG4, ML, B8) and 175 bar (B6). Inset shows the GIP using the maximum experimental pressure point for each shale. Solid lines represent the volumetric free gas and the points denote the GIP calculated from the excess adsorption data. Dashed lines connecting the symbols are to guide the eye only.

(8.8 m^3_{STP}/m^3). If we account for the maximum experimental pressure, the OGIP for the LG4 and ML shales is 19.3 m^3_{STP}/m^3 and 17.2 m^3_{STP}/m^3, respectively. The sequence is essentially reflective of each shale's adsorption capacity as the OGIP for B6 would in fact be higher than B8 if the initial reservoir pressure was equal. If adsorption was neglected and the GIP calculations only account for the volumetric free gas, the OGIP would reduce significantly. This is particularly true for the organic-rich shales, where the true OGIP is more than double the volumetric reservoir's GIP. For the Bowland shales this difference is up to 17%. The figure also shows that using excess adsorbed quantities can actually lead to a lower GIP at certain pressures compared to a volumetric reservoir. This is due to the shape of the excess adsorption isotherm and the fact that adsorption significantly impacts the porosity available to the bulk phase. The implications of this on shale gas recovery will be discussed in more detail in Chapter 9.

Figure 7.10a shows the ratio of the total GIP and the volumetric free gas GIP as a function of P/Z for all samples. This ratio represents the extra storage obtained due to the adsorption and provides a direct comparison between an unconventional reservoir and a volumetric reservoir, where gas storage is achieved only by gas compression in the pore space. The figure shows that this ratio is always larger than one for all four shales. In particular, a reservoir with adsorption can store more than twice the amount of gas as compared to a conventional reservoir for the majority of the pressure range for the TOC-rich shales LG4 and ML. At low pressures, the ratio increases to > 100 for these two shales.

This is due to the direct link between the strength of each shale's adsorption capacity and the GIP. These results clearly indicate that for the purposes of carbon storage, shale reservoirs pose a clear advantage. Figure 7.10b shows the ratio of excess adsorbed gas and the total GIP as a function of P/Z for all the shales. The plot shows that the contribution of the excess adsorbed gas to the total GIP increases as the reservoir produces (pressure is lowered). Two reasons exist for this behaviour: (i) the characteristic shape of the excess adsorption isotherm, which is steep at low pressures due to the adsorbed phase having liquid-like density, as compared to the behaviour of the bulk density with pressure, (ii) as pressure increases, the bulk density approaches that of the adsorbed phase and so the excess adsorbed amount decreases, diminishing the impact of G_{ads} on the total GIP. Based on this analysis, it is clear that the reservoir will need to be depressurized to low pressures to fully extract the adsorbed methane. At high pressures, at least 50% of the GIP could be achieved by simple compression in the pore space and the gain introduced by adsorption is limited. This might erroneously lead to the conclusion that in shales that have very high reservoir pressures, adsorption is negligible. On the contrary, the adsorbed phase volume and the absolute amount adsorbed are still significant at these pressures even though excess adsorbed quantities might not be. At such high pressures, as the bulk fluid density approaches the adsorbed phase density, the two phases (free and adsorbed) become indistinguishable and therefore equivalent from the point of view of a mass balance. The ratio is consistently higher for the TOC-rich shales as compared to the Bowland shales at the same pressure. At around 185 bar, the contribution of adsorption is much stronger for the LG4 and ML shales at ∼50%, compared to the Bowland shales (∼15%).

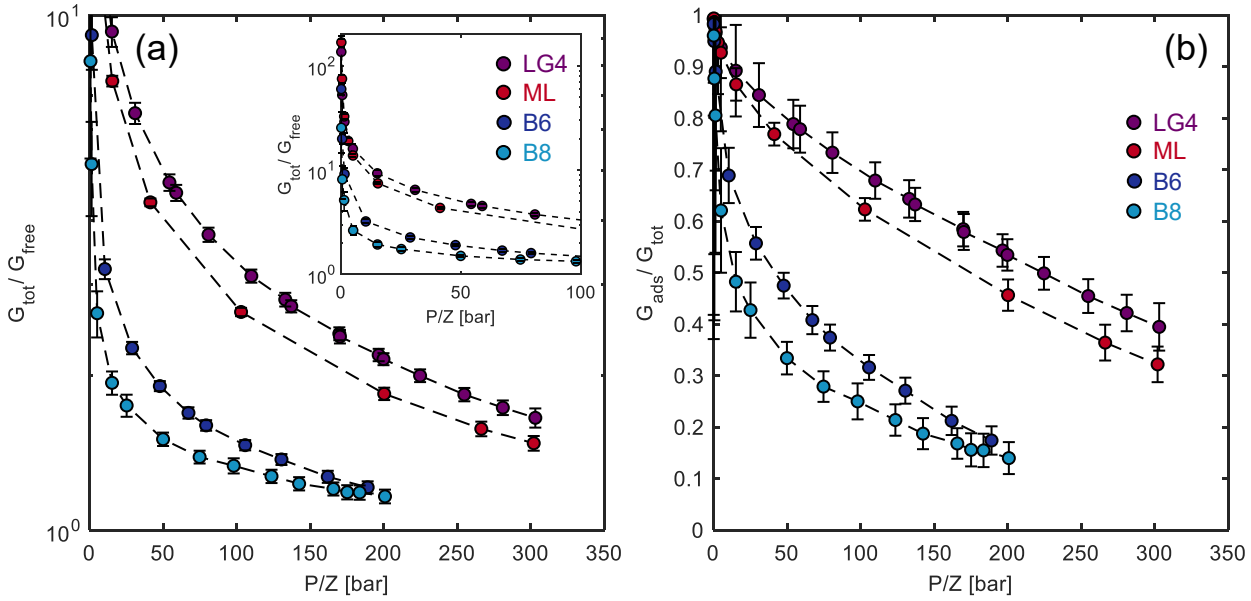

Figure 7.10: (a) The ratio of the GIP of an unconventional and conventional reservoir with the same porosity at 80 °C, as a function of P/Z. Inset shows data up to 100 bar for clarity. (b) The ratio of the excess adsorbed amount and the GIP for each shale as a function of P/Z. Dashed lines connecting the symbols are to guide the eye only.

7.5 Conclusion

High pressure and temperature adsorption isotherms have been measured gravimetrically on shales from three important shale plays: the Longmaxi, Marcellus and Bowland shales. The results show that the TOC is a strong influence on adsorption capacity of both CO_2 and CH_4. Experimental observations showed that some fluid remains permanently locked in the pores and is difficult to remove, which bodes well for secure storage of CO_2 in shale reservoirs. Important thermodynamic parameters such as the Henry constants and the enthalpy of adsorption at zero loading were calculated by applying the Virial model to the shale adsorption isotherms up to moderate pressures. The dominant controls on gas adsorption in shales were obtained by comparing the maximum excess adsorbed amount and temperature, the TOC and the total pore volume of each shale. The results show that the TOC has stronger control on gas adsorption in shales. A fully predictive modelling approach incorporating the use of the lattice DFT modelling results for the pure carbons and Illite clay showed great promise in capturing the adsorption capacity of each shale by requiring only its composition as an input. The experimental measurements have also been used to compute the total Gas-in-Place as well as the individual contribution from the volumetric free gas and the adsorbed gas. Adsorption greatly benefits the shale reservoir in terms of storage capacity, and this benefit is largest for the higher adsorbing LG4 and ML shales.

Chapter 8

Modelling Supercritical Gas Adsorption in Shales

This chapter discusses the modelling approach used to describe supercritical adsorption of CO_2 and CH_4 in samples from three shale plays: the Longmaxi (LG4), Marcellus (ML) and Bowland (B6) shales. The lattice DFT model has been deployed for this purpose and these results are first presented in comparison to the experimental measurements. This is followed by the quantification of thermodynamic parameters, such as Henry constants, and operational factors, such as the Gas-in-Place (GIP), directly from the modelling outputs. Through the lattice DFT, key insights into the adsorption behaviour of shales are obtained and examined to ascertain the effect of pore geometry and mineralogy. Finally, the modelling results are contrasted with the use of the widely adopted Langmuir model.

8.1 Lattice DFT Modelling of Supercritical Adsorption in Shales

The hybrid formulation of the lattice DFT detailed in Chapter 4 was utilised to describe the supercritical gas adsorption experimental measurements on LG4, ML and B6 presented in the previous chapter. B8 is not considered in this chapter, as it is apparent that factors other than pure adsorption affect the isotherms (as discussed in Chapter 7). The hybrid lattice DFT includes both slit and cylindrical pores; the proportion of each type of pore is based on each shale's normalised volumetric fraction of clays (slit pores) and TOC (cylindrical pores). The reduced pore size distribution allocated to each pore type is based on its counterpart obtained by applying the workflow described in Chapter 4 to the near-critical CO_2 isotherms of synthetic carbons (MC and AC) and pure Illite (IMt-2). For the cylindrical fraction, the pore sizes used to describe MC and AC are both included, but the pore volume assigned to each carbon is in the ratio 60:40, as a reflection of the average mesoporosity in these shales. The calculation

of the volumetric fractions of the clay minerals (slit pores) and TOC (cylindrical pores) is detailed in the appendices; the clay fraction amounts to 60% for the LG4 shale and 70% for the ML and B6 shales, with the residue being the TOC. The slit pores are of size $D_{\mathrm{p},J} = [1.2, 2, 12.4, 18.8, 36.4]$ nm which are described by pores with $J = [3, 5, 31, 47, 91]$ layers within the lattice DFT model. The cylindrical pores are of size $D_{\mathrm{p},J} = [1.2, 2, 4.4, 7.6, 11.6]$ nm which correspond to pores with $J = [2, 3, 6, 10, 15]$ layers. The volume allocated to each pore class is shown in Figure 5.6. Attempts at describing supercritical CH_4 adsorption on shale using a dual-site model exist, such as the use of two interaction energies for slit pores [151, 258] or for micro- and meso-pores [151], or the dual-site Langmuir model [135]. However, to our knowledge this is the first attempt at describing both CO_2 and CH_4 supercritical isotherms with two pore geometries, each with their own surface interaction energy.

Figure 8.1 shows the results of applying the hybrid lattice DFT model developed in this work to the measured excess adsorption data of each shale. The figure shows that the model provides an excellent description of both the CO_2 and CH_4 experimental measurements at various temperatures and over the entire bulk density range, fitting essentially within experimental uncertainties. This is also reflected by the low value of the objective function (normalised by the number of experimental points for each shale, $\Phi/E \approx 0.0001$ $(\mathrm{mmol/g})^2$), as shown in Table 8.1, which also reports all the input and fitted model parameters. To model adsorption on shale, $\rho_{\max}$ was considered independent of the adsorbate. As CO_2 and CH_4 have almost the same molecular size (of 0.4 nm), the maximum density within the saturated lattice should be essentially the same when $n^{\mathrm{ex}} = 0$. For LG4 and ML, $\rho_{\max}$ was fitted to both the CO_2 and CH_4 data while for B6, only the CO_2 measurements were considered for this purpose, as the CH_4 data reach comparatively low maximum bulk densities. The predicted values of $\rho_{\max}$ are higher than the liquid density at each adsorbate's boiling point (21.1 mol/L for CO_2 at 273 K and 3.47 MPa; 26.3 mol/L for CH_4 at 111.7 K and 101.35 kPa [231]). LG4 shows the largest value of $\rho_{\max}$ which could be indicative of a higher packing density within it pores, as it possesses the largest proportion of microporosity. Indeed, this value is reasonably close to the results obtained upon applying the cylindrical lattice DFT model to the microporous AC ($\rho_{\max} = 29$ mol/L, Chapter 6). The increasing presence of pores > 2 nm from LG4 to ML and B6 causes $\rho_{\max}$ to decrease and approach values closer to the liquid density of the adsorbate.

The hybrid lattice DFT also provides insights into the adsorbent-adsorbate interaction energy for both slit ($\varepsilon_{\mathrm{sf,slit}}$) and cylindrical ($\varepsilon_{\mathrm{sf,cyl}}$) pores. The average interaction parameter for the cylindrical pores ($\overline{\varepsilon}_{\mathrm{sf}}$), which accounts for the curvature of the pore wall, is systematically higher (more negative) than $\varepsilon_{\mathrm{sf,cyl}}$ for both adsorbates ($\overline{\varepsilon}_{\mathrm{sf}}/k_{\mathrm{B}} \approx -700$ to -500 K), but is still considerably lower than the interaction energy in the slit pores ($\varepsilon_{\mathrm{sf,slit}}/k_{\mathrm{B}} \approx -1700$ to -1500 K). The reason for this may be the larger size of the slit mesopores; as all shales have a higher proportion of slit pores, a larger surface interaction energy is required to capture the adsorption measurements accurately. The values

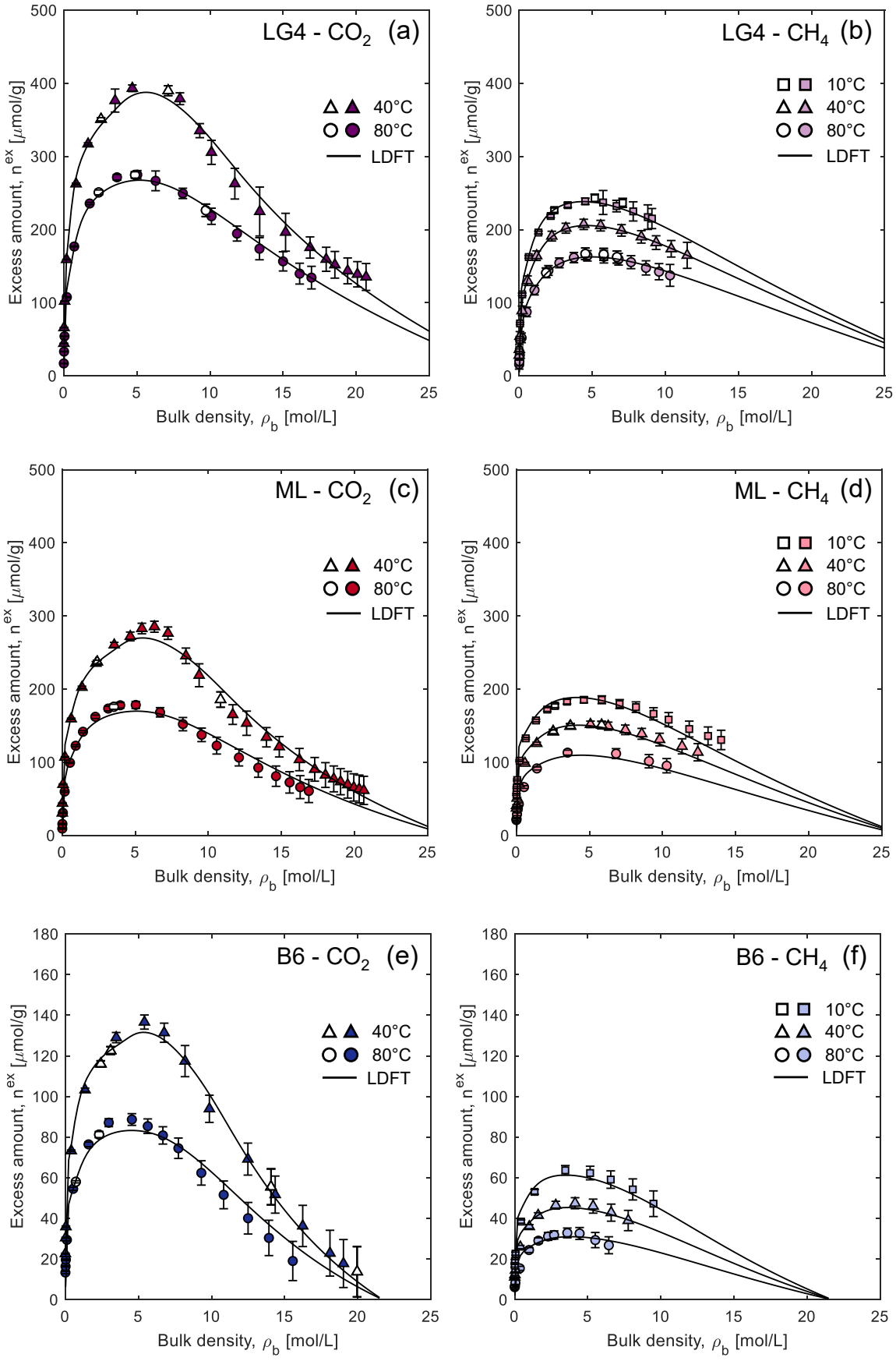

Figure 8.1: Unary excess adsorption isotherms measured with CO_2 and CH_4 on (a, b) LG4, (c, d) ML and (e, f) B6, plotted as a function of the bulk density at 10 °C, 40 °C and 80 °C. Empty symbols denote data taken in adsorption mode and filled symbols represent data taken in desorption mode. Solid lines denote optimum fits from the lattice DFT model (parameter values reported in Table 8.1).

Table 8.1: Input and fitted parameters of the hybrid lattice DFT model applied to the description of experimental excess adsorption isotherms measured on the three shales. The value of the objective function, Eq. 4.20 (normalised by the number of experimental points, E) is also given.

	LG4		ML		B6	
Parameter	CO_2	CH_4	CO_2	CH_4	CO_2	CH_4
	Input Parameters					
ε_{ff}/k_B [K]	−202.75	−127.04	−202.75	−127.04	−202.75	−127.04
σ [nm]	0.40	0.38	0.40	0.38	0.40	0.38
	Fitted Parameters					
$\varepsilon_{sf,slit}/k_B$ [K]	−1711.17	−1549.97	−1449.35	−1616.18	−1669.16	−1617.56
$\varepsilon_{sf,cyl}/k_B$ [K]	−553.06	−442.79	−468.00	−380.71	−499.00	−421.13
$\overline{\varepsilon}_{sf}/k_B$ [K]	−730.65	−584.97	−618.28	−502.96	−659.24	−556.36
ρ_{max} [mol/L]	30.81		26.57		21.72	
	Saturation Factor, c_{sat}					
10 °C	–	0.70	–	0.83	–	0.68
40 °C	0.82	0.65	0.86	0.71	1.10	0.54
80 °C	0.68	0.57	0.65	0.56	0.82	0.40
Φ/E [mmol/g]^2	0.0000991		0.000138		0.0000293	

of $\varepsilon_{sf,slit}/k_B$ for the shales are also higher than those observed for pure clay minerals such as Illite (≈ -1300 to -1000 K) [72]. Conversely, the $\overline{\varepsilon}_{sf}/k_B$ values for shales are relatively similar to those for mesoporous carbon (≈ -700 to -900 K), shown in Chapter 6. The CO_2 interaction energy is generally higher than CH_4 indicating the strength of the former's interaction with the shale surface. For ML, however, the reverse is true for the slit pores, despite the lower adsorption of CH_4 by this shale. As indicated in Chapter 6, supercritical adsorption can lead to multi-layer adsorption which means that the lateral interactions, represented by the fluid-fluid interaction parameter, ε_{ff}, are also important, and as Table 8.1 shows, this interaction is higher for CO_2. The results on all shales show that $|\varepsilon_{sf}| > |\varepsilon_{ff}|$, indicating that the interaction between either of the adsorbates and the shale surface (in a slit or cylindrical pore) is larger than the lateral interactions between the fluid molecules. The ability of the hybrid lattice DFT model to provide these insights and to effectively decouple the interactions of the clay minerals and the organic component of shales with the adsorbates makes it an extremely useful tool to understand adsorption in shale.

8.2 Henry Constants and Adsorption Energetics

The lattice DFT model enables the calculation of Henry constants and the isosteric heat of adsorption at zero loading through the application of the integrated van't Hoff equation (Eq. 4.18). The Henry constants are computed based on the surface interaction energies and the saturation factors detailed in Table 8.1. As there are two ε_{sf} values for each adsorbate per shale, the Henry constants were first

calculated for the slit and cylindrical pores independently and then combined by taking a weighted averaged based on the same volumetric fraction of clay minerals and TOC in each shale that was used to obtain the lattice DFT fits shown in the previous section. Figure 8.2 shows these results in comparison to the Henry constants obtained by applying the Virial model to the experimental data (as described in the previous chapter) and Table 8.2 shows the parameters of the integrated van't Hoff equation applied to the Henry constants obtained from the hybrid lattice DFT model.

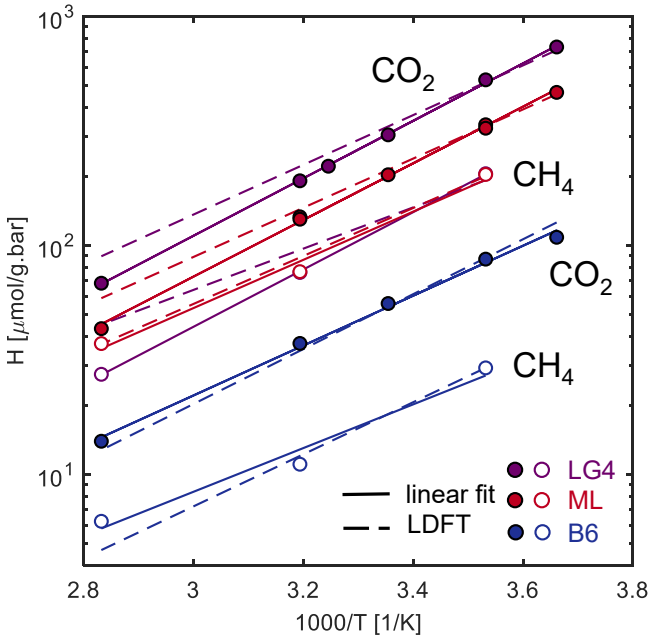

Figure 8.2: Henry constants as a function of the reciprocal temperature for CO_2 and CH_4 on the three shales. Solid lines denote linear fits to the experimental data, while the dashed lines represent prediction from the fitted hybrid lattice DFT model.

Table 8.2: Parameters of the integrated van't Hoff equation (Eq. 4.18), including the isosteric heat of adsorption, $\Delta\widetilde{h}_0$, and the corresponding pre-factors, $\widetilde{H_0}$, for the three shales, derived from the hybrid lattice DFT model. The associated Henry constants are shown in Figure 8.2.

	LG4		ML		B6	
Parameter	CO_2	CH_4	CO_2	CH_4	CO_2	CH_4
$\widetilde{H_0}$ (-)	9.32	7.09	19.9	7.34	4.24	2.73
$\Delta\widetilde{h}_0$ (kJ/mol)	-20.3	-16.9	-20.1	-19.6	-22.5	-21.3

The Henry constants derived from the lattice DFT model are in reasonable agreement with the ones obtained by the Virial model (shown by the symbols in Figure 8.2), particularly for the Bowland shale. The predicted value of the isosteric heat of adsorption for all the shales ($\Delta\widetilde{h}_0 \approx -20$ kJ/mol) is just slightly lower than the average experimental value of $\Delta h_0 \approx -21$ kJ/mol. As described in previous chapters, these estimates are also greater than the latent heat of vapourisation of each gas. Similar to the experimental results, the heat of adsorption for CO_2 is larger than CH_4, confirming shale's preferential selectivity towards the former.

8.3 Effect of Pore Geometry on Supercritical Adsorption in Shale

The lattice DFT model enables the understanding of fluid behaviour on a layer-by-layer basis in pores of various sizes and reveals details about the adsorbed phase itself. This is particularly helpful for hybrid systems, such as shales, where multiple pore morphologies exist. Figure 8.3 shows the adsorbed phase density, ρ_j, of CO_2 at 40 °C as a function of each layer in the pores of two micropores (1.2 nm and 2 nm) and a mesopore ($\sim$ 12 nm) at three different bulk densities (1 mol/L, 10 mol/L, 20 mol/L), for both slit and cylindrical pores in the ML shale.

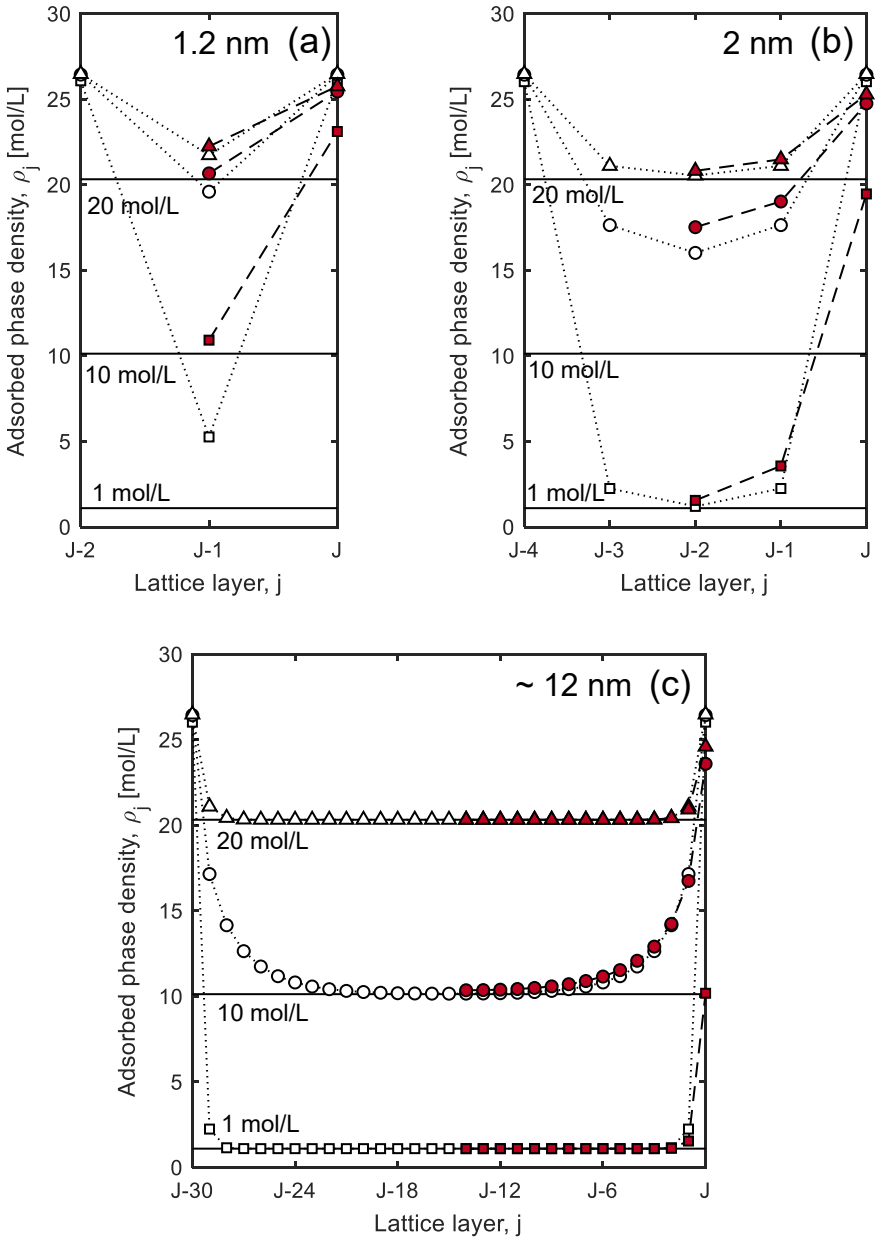

Figure 8.3: The lattice CO_2 adsorbed phase density profiles at 40 °C (T/T_c = 1.03) in slit and cylindrical pores of size (a) 1.2 nm, (b) 2 nm and (c) $\sim$ 12 nm (slit - 12.4 nm and cylindrical - 11.6 nm) corresponding to bulk densities of 1 mol/L, 10 mol/L and 20 mol/L, in the ML shale. Empty and filled symbols indicate slit and cylindrical pores, respectively.

Slit (empty symbols) pores and cylindrical (filled symbols) pores should be interpreted slightly differently; the two faces of a slit pore are denoted by the boundaries in Figures 8.3a–c and the centre of each pore represents the core of the pore, while for a cylindrical pore, the pore wall is represented by the boundary on the right side only and the fluid behaviour is mirrored in all directions. Although the surface interaction energy of slit and cylindrical pores remain constant, the behaviour of CO_2 is quite different in a micropore versus a mesopore. In the larger pores (Figure 8.3c), at a bulk density of 1 mol/L, the fluid density remains at the bulk value up to 1 or 2 layers from the pore wall, where fluid densification occurs. On the other hand, when $\rho_b = 10$ mol/L, fluid densification is experienced across the cylindrical pore and for at least ~ 10 layers adjacent to the slit pore wall, indicating the presence of multi-layer adsorption. When $\rho_b = 20$ mol/L, the bulk fluid density is already so high that the fluid behaviour reverts to the case when the bulk density was only 1 mol/L. In the slit mesopore, the density at the pore wall, $\rho_{j=31}$, is consistently equal to ~ 26 mol/L for all bulk densities, which is very close to the value of ρ_{max} ($= 26.6$ mol/L) for the ML shale. The cylindrical mesopore shows similar values at $\rho_b > 10$ mol/L even with a much lower surface interaction energy than the slit pore.

Figures 8.3a and 8.3b show that micropores experience significant density enhancement in all layers except the central most layer for both slit and cylindrical pores. Note that although both figures show the adsorption behaviour for the same physical pore size ($D_{p,J}$), the number of layers is different for each pore geometry (slit – $D_{p,J} = Jd$ and cylindrical – $D_{p,J} = d(2J-1)$, where d is the molecular diameter). The close proximity of the pore walls means that $\rho_j > \rho_b$ for the 1.2 nm pore for both pore geometries at all three bulk densities. The same is also true for the 2 nm pore at a bulk density of 10 mol/L and above. Multi-layer adsorption for CO_2 in shale nanopores has also been seen in GCMC simulations [259, 260]. Temperature is an additional factor; at 40 °C, $T/T_c = 1.03$ and it has been shown previously that at these near-critical conditions, the attractive potential caused by the pore walls propagates through to the centre of the pore [162]. If the adsorbed phase density is considered to be the average density of the two most adjacent layers to the pore wall, then this is equal to 23 mol/L for the 1.2 nm pore and 22 mol/L for the 2 nm pore at $\rho_b = 10$ mol/L. These values are consistent between both pore geometries. For the mesopore, the same bulk density would correspond to an adsorbed phase density of 22 mol/L (slit) and 20 mol/L (cylindrical). These values are very close or even higher than the liquid density of CO_2 at its boiling point (21.1 mol/L [231]), indicating the enhanced densification experienced by shale pores during supercritical adsorption. GCMC simulations have shown a CO_2 adsorbed phase density in the same range [261]. This analysis reveals that modelling shale adsorption requires the use of multiple pore sizes and both geometries to account for the distinct behaviour in different types of pores.

8.3.1 Surface Interaction Energy

The surface interaction energy has a strong effect on the modelled lattice DFT isotherms. Figure 8.4 shows as symbols the surface interaction energies obtained upon fitting the entire experimental dataset, including both CO_2 and CH_4 at all temperatures, with various models: (i) single surface model (analagous to the model used for the synthetic adsorbents) with either slit, cylindrical or a hybrid model where the interaction energy of a slit and cylindrical pore is the same (these points lie on the identity line shown in the figure), (ii) dual surface model, where both surfaces are in slit pores, cylindrical pores or in either type (this is the hybrid model considered in this work). The results show that for the single surface model, the slit interaction energy is the most negative, followed by the hybrid and then the cylindrical model. This makes sense because the hybrid system combines both pore morphologies. These models results in a larger objective function value than the dual surface models in which the cylindrical/cylindrical model always shows the less negative surface interaction energies for both surfaces. The hybrid model shows a slight increase in $|\varepsilon_{\mathrm{sf,slit}}|$ compared to the dual surface, one pore type model (slit/slit) but the hybrid $|\varepsilon_{\mathrm{sf,cyl}}|$ corresponds reasonably well with the average of the two interaction energies from the cylindrical/cylindrical model. In some cases, the dual surface, one pore type model actually provides a very marginal improvement in the overall fit, which could be due to the heterogeneity present in these rocks in the form of multiple pore morphologies existing in both the clay minerals and organic material.

Figure 8.4 is also a contour map showing the dependence of the objective function (per experimental point, Φ/E), derived from fitting the dual surface hybrid model, on the surface interaction energies of the slit and cylindrical pores for the case of the 40 °C CO_2 isotherm for each shale. The other parameters ($\rho_{\max}$ and c_{sat}) were kept constant at the values shown in Table 8.1. The figure shows that absolute slit surface interaction energies larger than $\sim$ 1500 K yield a large fitting error for all shales, irrespective of the cylindrical surface interaction energy. The same is also true for very low ($>\sim -300$ K) or very high ($<\sim -2000$ K) absolute cylindrical surface interaction energies. In fact, the model outlines two clear regions where the objective function is at a local minimum: where (i) -1000 K $< \varepsilon_{\mathrm{sf,cyl}}/k_{\mathrm{B}} < -400$ K and -1500 K $< \varepsilon_{\mathrm{sf,slit}}/k_{\mathrm{B}} < -800$ K, and (ii) -2000 K $< \varepsilon_{\mathrm{sf,cyl}}/k_{\mathrm{B}} < -1100$ K and -700 K $< \varepsilon_{\mathrm{sf,slit}}/k_{\mathrm{B}} < -300$ K. These optimal solutions indicate that the ratio of interaction energies within the two pore geometries should be roughly 3 but either one could be the higher one. This could potentially be due to the reduced PSD allocated to each type of pore. Although both geometries have the exact same sizes of micropoes (albeit at different volume percentages), the cylindrical PSD has smaller mesopores ($D_{\mathrm{p},J} < 12$ nm) while the mesopores above 12 nm are all slits. To accurately describe the adsorption on each shale, the model needs to compensate for the lower amount of adsorption in these large slit mesopores by increasing the interaction potential between

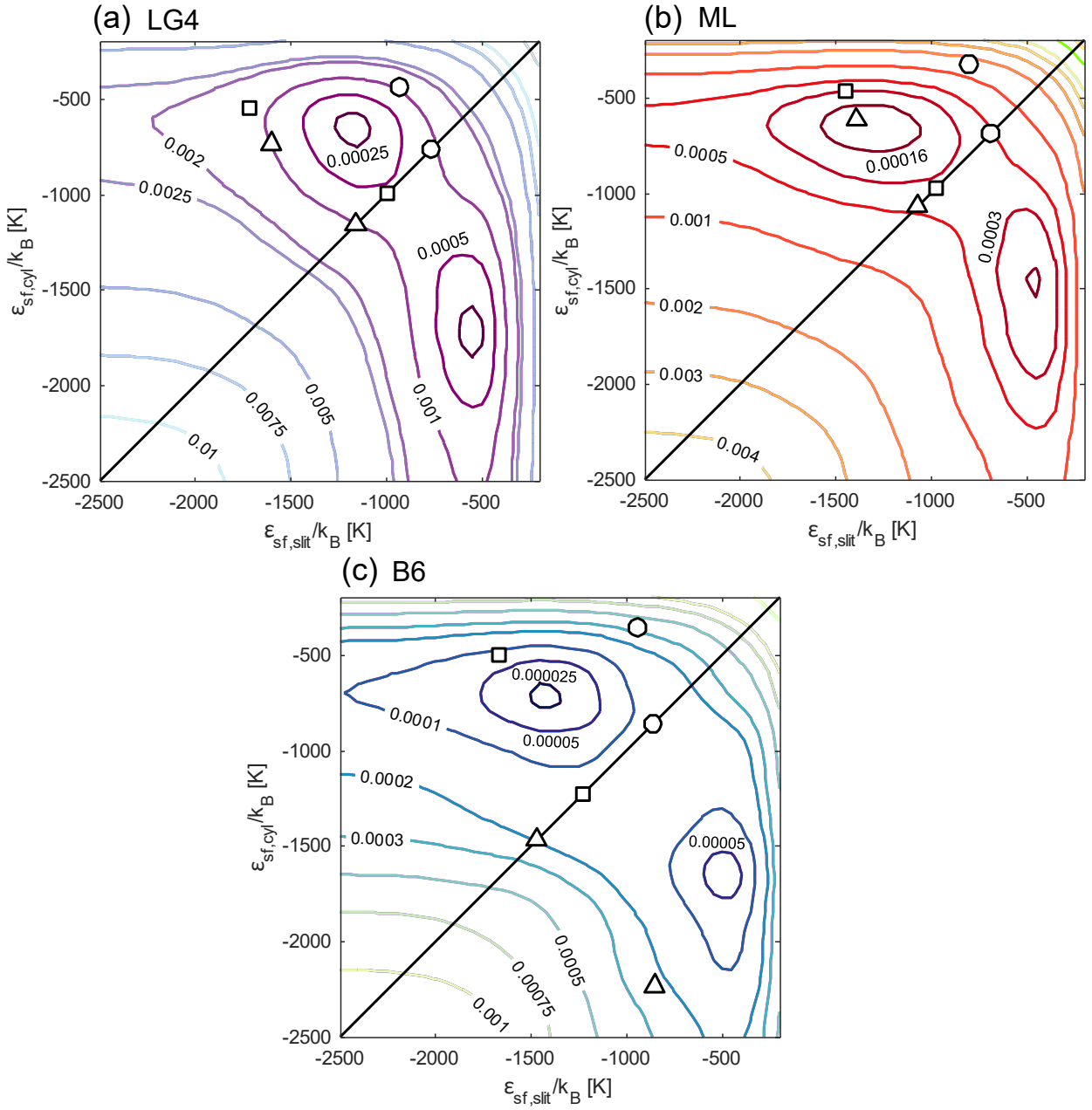

Figure 8.4: Contours indicating the value of the objective function (Eq. 4.20) per experimental point, obtained by varying the cylindrical and slit pore interaction energies for the 40 °C CO_2 isotherm for the (a) LG4, (b) ML and (c) B6 shales. The remainder of the model parameters were fixed as the values in Table 8.1. Points indicate the surface interaction energies obtained by fitting the entire experimental dataset with either the single surface model or the dual surface model for slit (triangle), cylindrical (circle) or hybrid systems (square). The identity line is shown in black.

the slit surface and CO_2, especially as the adsorption on slit pores accounts for the majority of the adsorption in these shales due to the volume fractions used. Conversely, the cylindrical interaction energy could also be higher than the slit energy as the volume percentage in the slit micro- and meso-pores is up to 2–3 times more than the cylindrical pores; so again, the model needs to compensate for this by increasing the interaction in the cylindrical pores and reducing it in the slits. Having equal energies, which would take both of these factors into account, would result in still reasonable values of the objective function, as shown in the figure, but the first factor is clearly the dominant one as the

optimal solutions mostly lie in the region where $|\varepsilon_{sf,slit}| > |\varepsilon_{sf,cyl}|$.

8.3.2 Saturation Factors

The pore saturation factor, c_{sat}, is also affected by pore geometry as shown in Figure 8.5. Here, c_{sat} is reported as a function of the inverse reduced temperature (T_c/T) and the results are shown for the dual surface model, where either slit and cylindrical pores exist with two different surface interaction energies or, as in the hybrid model, both pore types exist with a different ε_{sf} each. In all cases, it is evident that as temperature increases beyond the critical temperature, the adsorbed phase does not occupy the entirety of the available pore space. At temperature close to the adsorbate's critical point however, the saturation factor approaches unity. The results also show that the saturation factors for CH_4 and CO_2 increase linearly with T_c/T. For LG4 and B6, the linearity is strongest, with $R^2 > 0.74$ for the hybrid models. ML shows a larger deviation from this trend as, even though LG4 and ML show very similar CO_2 saturation factors, the ML CH_4 c_{sat} values are much higher than LG4 at the lower temperatures. B6 shows that, for CO_2 at 40 °C, c_{sat} is greater than 1, which would normally be considered unphysical. However, the saturation factor is the ratio of the adsorbed phase volume and the total pore volume, which is obtained from the analysis of the textural properties shown in Chapter 5. These measurements were conducted on a smaller aliquot of the sample in the MSB, so it is possible that the pore volume obtained for B6 is underestimated. This reinforces the experimental challenges associated with heterogeneous adsorbents, such as shale, and sometimes the interpretation of results, given the experimental uncertainties.

The trends for the saturation factors also show some similarities to the behaviour of the surface interaction energy in relation to the pore geometry. The hybrid model yields c_{sat} values that are somewhere in between those from the slit/slit and cylindrical/cylindrical models for both gases and at all temperatures. The slit/slit c_{sat} are always the largest at a fixed temperature and the cylindrical/cylindrical ones are always the lowest. A similar result was observed in Chapter 6, where the slit geometry required a larger pore volume to capture the adsorption on the porous carbons. The effective adsorbate-adsorbent interaction in the cylindrical lattice is dependent on the coordination number at the pore wall, z_J^{a+}, which increases as the pore size decreases, as opposed to a fixed coordination number, z^a (= 1), for slit pores. The stronger interaction in cylindrical pores could explain why a lower adsorbed volume is required to describe the equivalent adsorption on shale, as compared to slit pores, for the same pore sizes.

In Figures 8.5a–c, a coloured straight line is also visible. This represents the MC, AC and Illite saturation factors combined using the volumetric proportions in each shale (the same fractions as the slit/cylindrical pore ratio in the hybrid model). B6 is reasonably well predicted by the combination

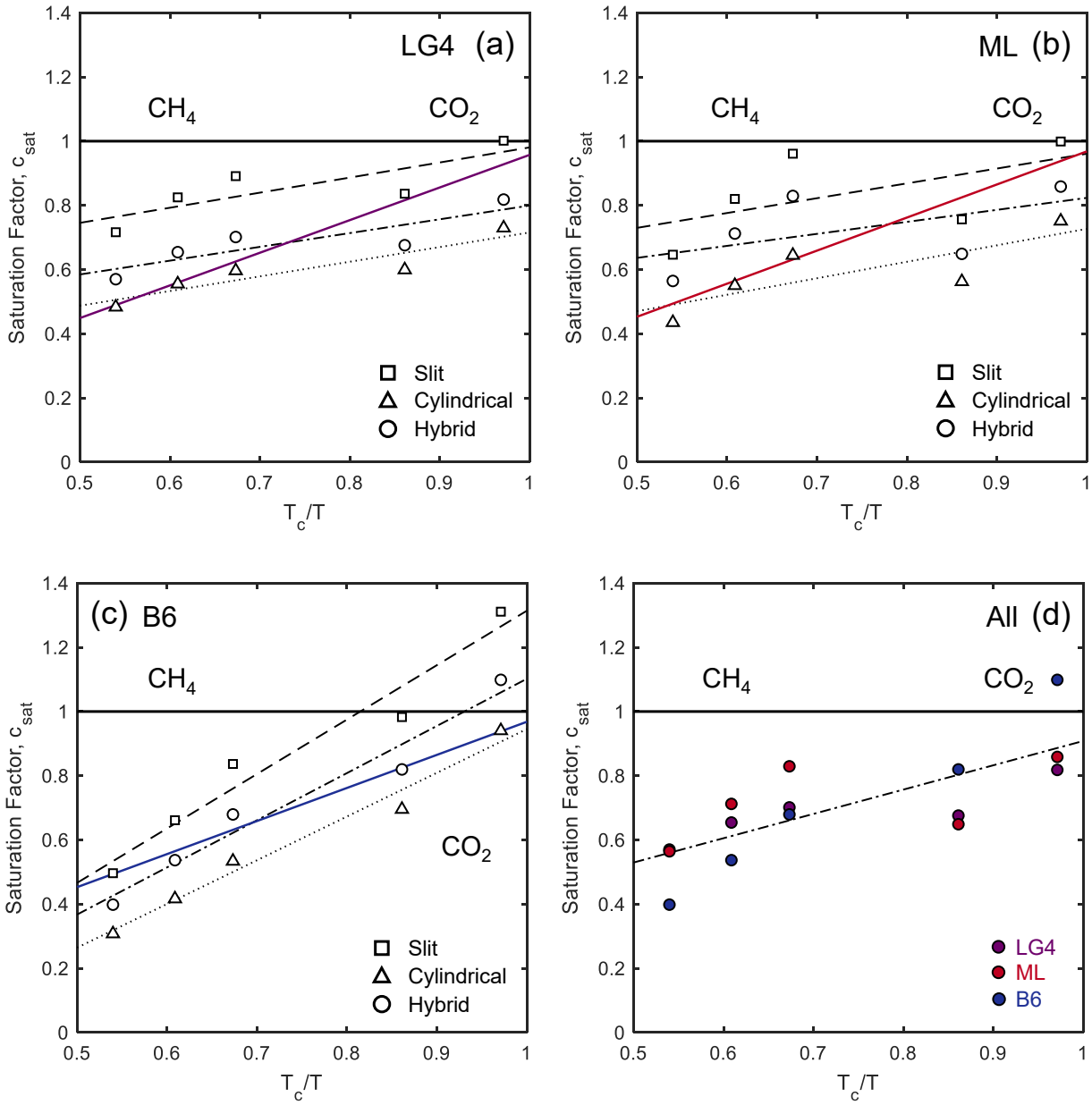

Figure 8.5: The pore saturation factor, c_{sat}, as a function of T_c/T for (a) LG4, (b) ML, (c) B6 and (d) all shales together, obtained with the dual surface lattice DFT model that uses slit (squares), cylindrical (triangles) and both type (hybrid, circles) of pores. Linear fits for all models are also shown. Coloured solid lines indicate the saturation factors obtained upon combining the MC, AC (60:40 ratio) saturation factors, shown in Chapter 6, and pure Illite saturation factors [72] in the volumetric proportions within each shale. (d) shows a linear fit based on the saturation factors from the hybrid model of all the shales.

of the model sorbents, while for LG4 and ML, the CH_4 and CO_2 predictions align well with the cylindrical/cylindrical and slit/slit model, respectively. Both MC and Illite have an excess adsorption of CO_2/CH_4 ratio of around 3, which is the same for B6, but is higher than the ratio of 2 for the more organic-rich shales. As the adsorbed volume should directly correspond with adsorption capacity, this explains why the coloured lines are steeper than any of the black lines in Figures 8.5a and 8.5b. Nevertheless, the saturation factors from the model adsorbents provide a practical way through which

supercritical adsorption in shales could be predicted.

Figure 8.5d shows the hybrid model saturation factors for all three shales together. As discussed above, the LG4 and ML shales have very similar CO_2 factors but the B6 ones are much higher. On the contrary, the B6 CH_4 c_{sat} values are the lowest at the same temperatures. Because the surface interaction energies and the maximum lattice density are not consistent between the three shales, it is difficult to draw strong conclusions from just one parameter and this variation is also reflected in the relative weakness in the linear relationship denoted by the straight line in the figure ($R^2 = 0.57$). Whereas for pure clay minerals [72] and porous carbons (Chapter 6), a strong linear relationship exists between c_{sat} and T_c/T, the same is not as true for this particular assortment of shales. Interestingly, the strength of the linear correlation improves to $R^2 = 0.72$ if only LG4 and B6 were considered. These two shales have very similar clay content (=20–25 wt%), which suggests that a grouping of multiple shales based on mineralogy might prove to be a useful approach.

8.4 Langmuir vs. the Lattice DFT Model for Shales

Figure 8.6 shows a comparison between the lattice DFT model (solid lines) and the Langmuir model (dashed lines) applied to the CO_2 and CH_4 isotherms at 40 °C for all shales. The latter has been used with the assumption of a constant adsorbed phase density which is equal to ρ_{max} from Table 8.1. All other model parameters are reported in the figure caption. Although the Langmuir model is able to describe the adsorption behaviour of CH_4 well, it is not as successful for CO_2. As discussed before, the mesoporosity of the shales manifests itself in the isotherm shape closer to the critical point of the adsorbate, which is the case for CO_2 at 40 °C. The non-linearity of the descending part of the isotherm is completely missed by the Langmuir model. It is, however, described well by the lattice DFT model, which incorporates information about the shale's PSD and does not require any input about the adsorbed phase. The assumption of a constant density of the adsorbed phase, used with the Langmuir model, is unlikely to be true, in particular for CO_2 at these conditions. The use of such simple models always requires knowledge of the behaviour of the adsorbed phase, which is likely to depend on the pressure as well as the adsorbent itself, and this makes it extremely challenging for these models to accurately describe supercritical adsorption in mesoporous materials such as shales.

8.5 Gas-in-Place from Adsorption Modelling

In the previous chapter, the Gas-in-Place (GIP) of each shale was calculated based on the experimental excess adsorption data by correctly accounting for the reduced porosity available to the free gas due

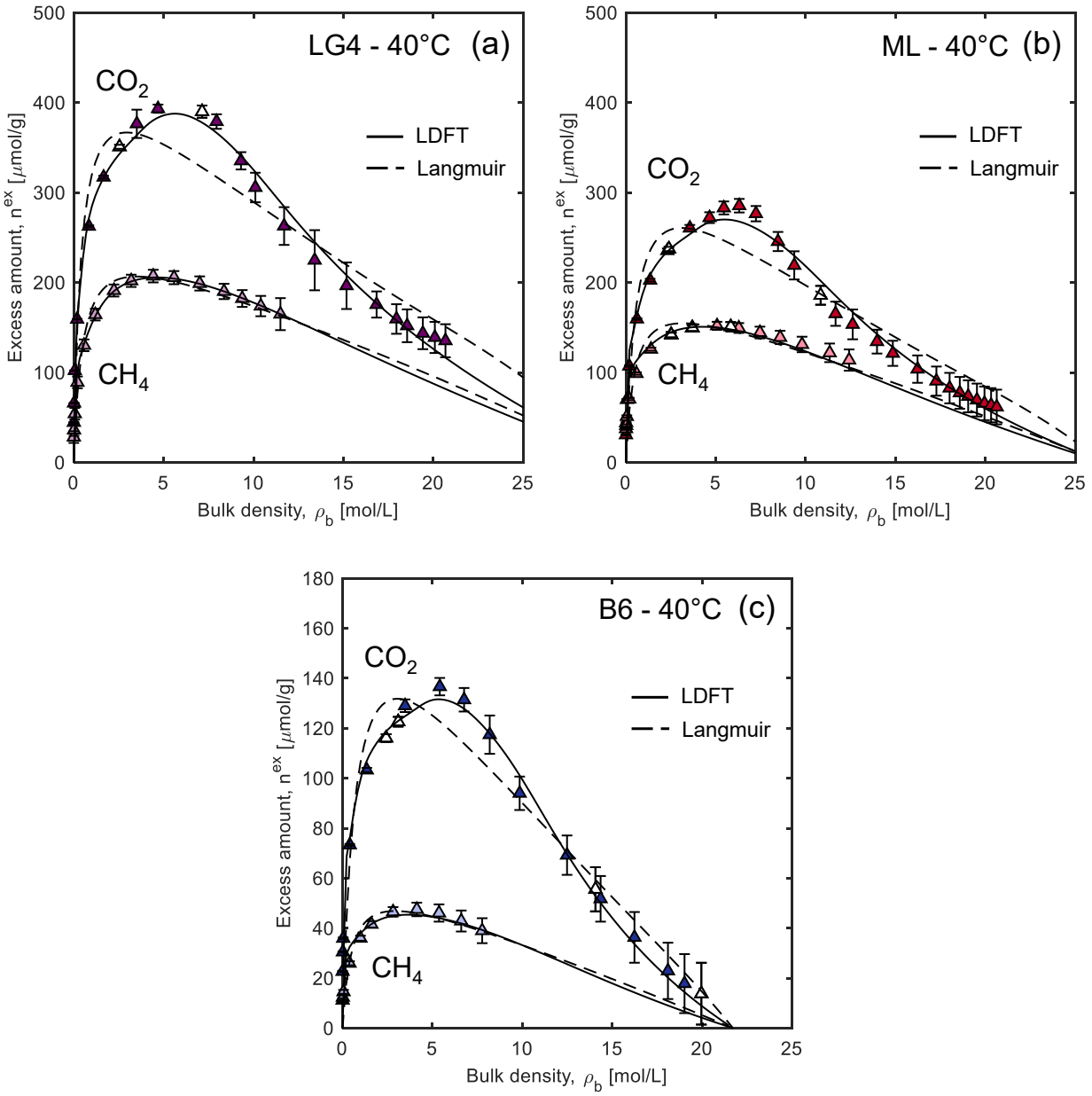

Figure 8.6: A comparison between the description of CO_2 and CH_4 supercritical adsorption obtained upon application of the lattice DFT (solid lines) and Langmuir model (dashed lines) on experimental data measured on (a) LG4, (b) ML and (c) B6 at 40 °C (empty symbols denote data taken in adsorption mode and filled symbols represent data taken in desorption mode). The Langmuir parameters [n^{∞} (µmol/g), K_{L} (1/bar)] are: LG4 - [522.6, 0.081] (CO_2) and [276.9, 0.073] (CH_4); ML - [416.5, 0.056] (CO_2) and [209.9, 0.076] (CH_4); B6 - [238.2, 0.042] (CO_2) and [66.51, 0.070] (CH_4).

to the adsorbed volume (Eq. 7.2). Figure 8.7 presents the same calculation using the modelled lattice DFT isotherms at 80 °C.

The advantage of using these modelled isotherms is the fact that the same initial reservoir pressure can be imposed such that the volumetric free gas (shown by the straight line in the figure) is consistent between all three shale plays. This enables a direct comparison between the impact of adsorption on the recoverable gas from each shale. Note that all other factors, such as a reservoir porosity of 5%,

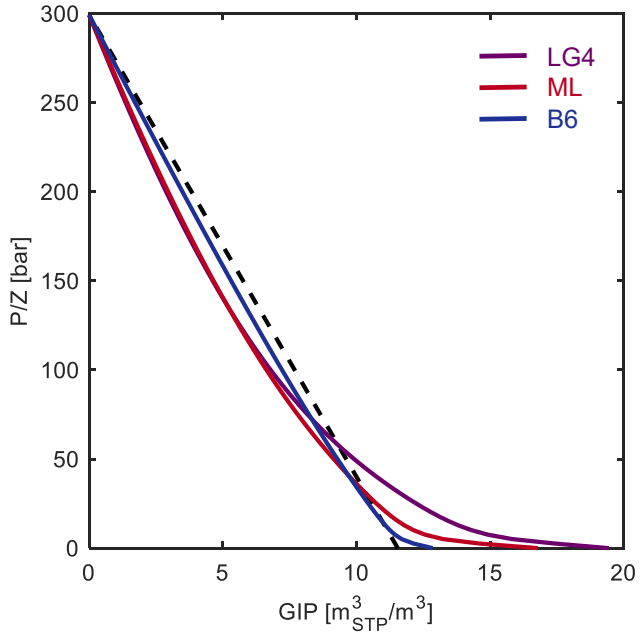

Figure 8.7: Gas-in-Place as a function of P/Z at a temperature of 80 °C obtained via the modelled lattice DFT adsorption isotherms. The dashed line represents the volumetric free gas and the solid lines denote the GIP calculated from the modelled excess adsorption data.

are kept constant as the values from Chapter 7. The figure shows that the total amount of gas in each reservoir, or the original Gas-in-Place (OGIP) obtained at $P/Z = 0$, is in the following order: LG4 (19.4 m^3_{STP}/m^3) > ML (16.8 m^3_{STP}/m^3) > B6 (12.8 m^3_{STP}/m^3). The OGIP values for the organic-rich shales are remarkably close to their experimental counterparts (19.3 m^3_{STP}/m^3 and 17.2 m^3_{STP}/m^3, respectively), showing that the lattice DFT model developed here is extremely useful even beyond scientific interest, as it can effectively capture operational parameters like the Gas-in-Place. B6 shows a greater OGIP here (8.8 m^3_{STP}/m^3 from the experimental measurements) because the chosen reservoir pressure is much higher than the maximum pressure available in the experimental dataset. This is another benefit of using the modelled isotherms as they can be extended to any given pressure that the reservoir might experience. The same trends as the previous chapter are also visible in this figure: (i) the OGIP is strongly dependent on the adsorption capacity, with the higher adsorbing shales showing larger volumes of CH_4 stored, and (ii) depending on the reservoir production pressure, the actual amount of gas produced might even be lower than the so-called volumetric reservoir due to the significant occupation of the total porosity by the adsorbed phase, which is reflected in the excess adsorption quantity. This difference would be the largest for the shales where adsorption is the greatest, i.e. the LG4 and ML shales. As discussed before, it is imperative that these calculations are performed rigorously to avoid flawed predictions about a reservoir's economic potential.

8.6 Conclusion

CO_2 and CH_4 supercritical adsorption isotherms at various temperatures for three important shale plays have been modelled using the novel hybrid lattice DFT model, which combines both slit and cylindrical pores. The model has been used almost independent of requiring much detailed characterisation of the shale itself, with only the need for the shale mineralogy for the purpose of dividing the pore space into the two pore geometries. This makes the model an extremely robust and powerful tool for the description of the adsorption behaviour in these very heterogeneous and diverse geosorbents. The results show that the hybrid model is successful in modelling the excess adsorption isotherms of different types of shales. The additional complexity of the hybrid lattice DFT model, which includes its dual surface nature as well as the diverse range of pore sizes (10 pore classes) required to describe adsorption in shale, makes the isotherm-fitting procedure more computationally expensive compared to a single surface model. However, the model fits experimental isotherms within experimental uncertainties and the results show that this approach provides additional insights into the interaction between the shale surface and each adsorbate, as well as the occupancy of the available porosity by the adsorbed phase. Pore-specific adsorption behaviour can also be revealed by the model, which is invaluable for these mesoporous sorbents and additionally for near-critical fluids such as CO_2. The use of this model also enables the calculation of Henry constants and the isosteric enthalpy of adsorption, which agree extremely well with estimates obtained from experimental measurements. The Gas-in-Place for each shale was also computed, which shows that the model can serve as a practical and efficient means of quantifying the OGIP for shale plays. Additionally, the model developed in this work can be coupled with pore network models to simultaneously provide a detailed description of the adsorption and mass transport processes in the complex pore space of shales.

Chapter 9

A Shortcut Pressure Swing Adsorption Analogue Model for the Description of ESGR in Shale Reservoirs

In this chapter, we develop and deploy a simplified mathematical model that exploits the concept of Pressure Swing Adsorption (PSA), as used in industrial gas separations, to describe an ESGR operation that involves three stages: Injection, Soak and Production. The model framework is built entirely on material balances and uses quantities that can be directly accessed experimentally, so as to correctly account for the pore space occupancy in shale. We evaluate CO_2 and N_2 as injection gases and identify a number of operational constraints and strategies. The material in this chapter is published in Ansari et al. (2021) [1].

9.1 Gas-in-Place

The Gas-in-Place (GIP) is a metric that dictates a reservoir's suitability for production and the design of an optimum production strategy must rely on the knowledge of how GIP varies as a function of reservoir pressure. As discussed in Chapters 7 and 8, common approaches to estimate GIP for shales do account for the mass of adsorbed gas, but they neglect its volume by assuming that the total rock's porosity continues to be available to the free gas [262, 263, 264]. It has been reported that this assumption can lead to an overestimation of the actual GIP by approximately 10–25% [263]. The reliability of this exercise is further compromised by the fact that the distinct dependency of gas bulk density and adsorption capacity on pressure is not accounted for. As anticipated below and described in Section 9.2, the use of excess adsorption in GIP calculations circumvents the problem by correctly

accounting for the usable porosity, while avoiding unnecessary assumptions on the properties of the adsorbed phase and their dependency on the pressure. We note that these complications are largely due to the fact that shale is mostly mesoporous, implying that adsorbed and free gas occupy the same pore space. Filling this pore space with compressed gas and additionally accounting for adsorption leads to double counting. This is in contrast with another natural adsorbent, coal, which is largely microporous and enables the 'simpler' allocation of the adsorbed and free gas phases between the micro- and macro-porous space, respectively.

At the typical shale reservoir conditions, both CH_4 and CO_2 are supercritical. Because of the absence of a vapour-liquid transition, adsorption measurements of supercritical gases are interpreted using excess quantities (as detailed in previous chapters). While the excess adsorbed amount is the measured property experimentally, the practitioner often chooses to convert it to an absolute adsorbed amount for the purpose of process modelling. This conversion requires an assumption on the density (or volume) of the adsorbed phase. For a pure gas, the conversion is given by the following expression:

$$n^{\mathrm{ex}} = n^{\mathrm{a}} - \rho_{\mathrm{b}} v_{\mathrm{a}} = n^{\mathrm{a}} \left(1 - \frac{\rho_{\mathrm{b}}}{\rho_{\mathrm{a}}}\right) \tag{9.1}$$

where n^{ex} and n^{a} are the excess and absolute amount adsorbed, respectively, ρ_{b} is the bulk density of the gas, v_{a} is the volume of the adsorbed phase and $\rho_{\mathrm{a}} = n^{\mathrm{a}}/v_{\mathrm{a}}$ is the density of the adsorbed phase. Figure 9.1 shows (a) excess CH_4 adsorption isotherms and (b) their absolute counterparts, obtained upon assuming a liquid-like adsorbed phase with a density $\rho_{\mathrm{a}} = 22.3$ mol/L. For the sake of generality, four common adsorption isotherm models are considered in the figure (equations provided in the appendices), which prompt the following remarks. First, the absolute amount adsorbed always increases with pressure, while the excess can feature a non-monotonic behaviour (e.g. Langmuir isotherm). The latter does not indicate a decrease in adsorption, but rather a decrease of its contribution to the total amount of gas stored in the porous rock. Secondly, $n^{\mathrm{ex}} \leq n^{\mathrm{a}}$ over the entire pressure range, with the relative difference between the two quantities that increases with increasing pressure ($n^{\mathrm{ex}} \approx n^{\mathrm{a}}$ at $P < 4$–5 MPa). It becomes apparent from these initial considerations that the use of absolute instead of excess quantities in material balance calculations will produce different results, if the volume occupied by the adsorbed phase is not accounted for.

In this study, we will also consider an enhanced recovery operation, in which a gas is injected into the formation to displace natural gas, thereby creating a binary gas mixture. In this case, absolute and excess adsorption are related as follows [183]:

$$n_i^{\mathrm{ex}} = n_i^{\mathrm{a}} \left(1 - \frac{y_i C_{\mathrm{t}}}{z_i \overline{\rho}_{\mathrm{a}}}\right) \tag{9.2}$$

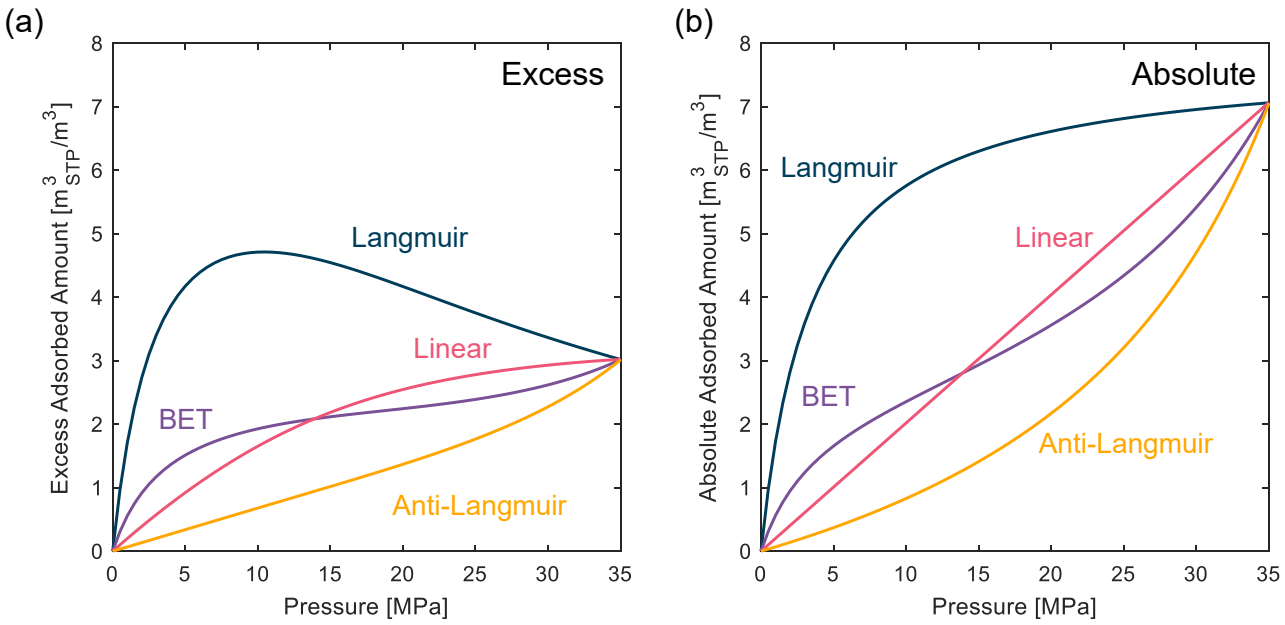

Figure 9.1: CH_4 (a) excess and (b) absolute adsorption isotherms as a function of pressure, as predicted using four adsorption isotherm models, namely the Langmuir, Anti-Langmuir, BET and Linear model. The equations and parameters of each model are provided in the appendices.

where C_t is the total concentration of the bulk phase, $\overline{\rho}_\mathrm{a}$ is the adsorbed phase density of the gas mixture, y_i is the mole fraction of component i in the bulk phase and z_i ($z_i = n_i^\mathrm{a} / \sum_i n_i^\mathrm{a}$) is the mole fraction of component i in the adsorbed phase. The density of the adsorbed phase, $\overline{\rho}_\mathrm{a}$, can be estimated by assuming ideal mixing [181]:

$$\overline{\rho}_\mathrm{a} = \left(\sum_i \frac{z_i}{\rho_{i,\mathrm{a}}} \right)^{-1} \tag{9.3}$$

The volume of the adsorbed phase is then calculated as follows:

$$\overline{v}_\mathrm{a} = \frac{n_i^\mathrm{a}}{z_i \overline{\rho}_\mathrm{a}} \tag{9.4}$$

The amount of component i adsorbed, n_i^a, from the multicomponent gas mixture can be predicted by various means, including thermodynamic approaches (e.g. the Real Adsorbed Solution Theory, RAST) or an appropriate extension of the single-component adsorption isotherm model, such as the extended Langmuir model. The availability of closed-form expressions to predict mixed-gas adsorption equilibria is often used as the argument for choosing the latter option in process optimisation calculations, such as those used to describe cyclic adsorption processes [265].

9.2 Shortcut Pressure Swing Adsorption Analogue model

The proposed model concept is inspired from industrial gas adsorption separations, in which a porous adsorber undergoes cyclically a pressurisation ('adsorption') and de-pressurisation ('desorption') step. Proxy models that assume uniform conditions throughout the system have been shown to provide a useful means to rationalise the results arising from the analysis of such a cyclic operation, while simplifying considerably the mathematical formulation of the problem [266]. Subsurface reservoirs have also been described by tank models as shown by Dake (1983) [267]. We will follow a similar approach in this study to evaluate the exploitation of a shale reservoir that is accessed by wells from which gas is injected and withdrawn. The process is thus reminiscent of a 'huff-n-puff' operation [268, 269, 270], but is extended here to a situation where multiple injection-recovery cycles are carried out, so as to elucidate potential trade-offs between incremental recovery, produced gas quality and gas storage. In our conceptualisation, the following assumptions apply:

- The system is well-mixed, and there are no pressure, concentration or temperature gradients in the system;
- Shale properties, such as porosity and adsorption parameters, are constant throughout the reservoir;
- Formation water is considered to be immobile and is not accounted for in the reservoir porosity;
- The system is isothermal;
- Natural gas is represented by pure methane, CH_4.

The cyclic operation has three distinct stages (Figure 9.2): Injection (I) − where gas is introduced in the reservoir, Soak (S) − where adsorption equilibrium is reached between the fluid and solid phases, and Production (R) − where either CH_4 or a mixture of CH_4 and the injected gas are produced. In the latter case, the two components are separated, and as the process continues, the gas is then re-injected into the reservoir in the following Injection stage. The assumption of a well-mixed reservoir presents a deviation from the expected behaviour in the shale reservoir. There, the finite spacing between natural and artificial fractures will limit the achievable rate of mass transfer, meaning that the well would need to be shut in for a sufficiently long time in order to reach adsorption equilibrium during the Soak stage. In fact, mass transfer rates have a major impact on the achievable gas quality and recovery. In the following, we outline the mathematical formulation of the model, including the performance indicators for the gas recovery/storage operation.

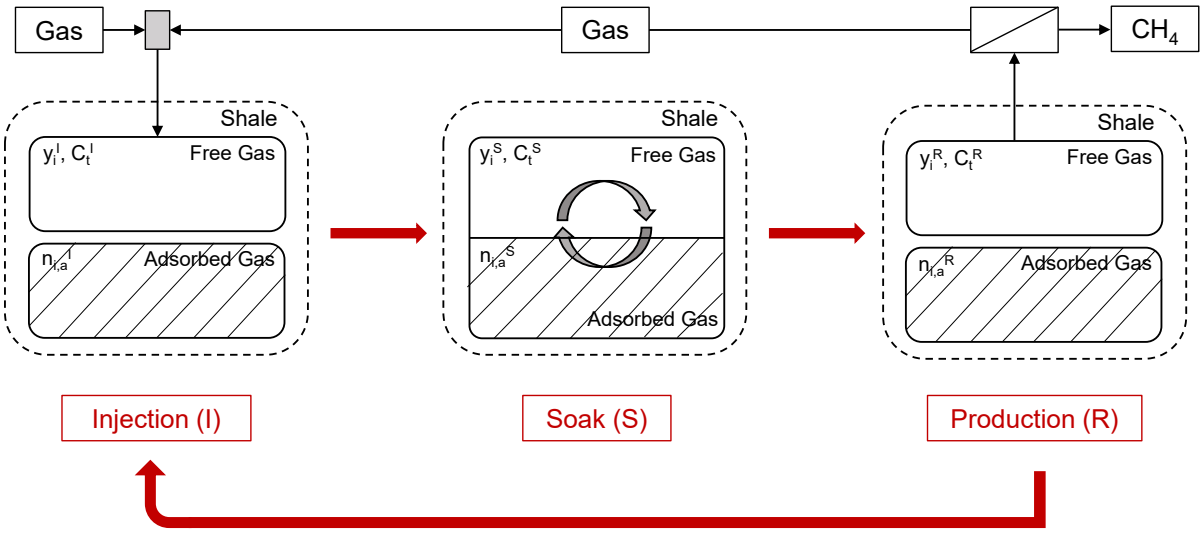

Figure 9.2: Schematic of the cyclic shale production and storage model.

9.2.1 Mathematical Model

The total amount of component i (in moles) in the reservoir at a given stage is $N_{i,\mathrm{t}}$, which includes contributions from the free gas, FG, ($N_{i,\mathrm{f}}$) and the adsorbed phase, AG, ($N_{i,\mathrm{a}}$):

$$N_{i,\mathrm{t}} = N_{i,\mathrm{f}} + N_{i,\mathrm{a}} \tag{9.5}$$

where,

$$N_{i,\mathrm{f}} = V y_i C_{\mathrm{t}} (\phi - \rho_{\mathrm{w,s}} v_{\mathrm{a}}) \tag{9.6}$$

$$N_{i,\mathrm{a}} = V \rho_{\mathrm{w,s}} n_{i,\mathrm{a}} \tag{9.7}$$

In Eqs. 9.6 and 9.7, y_i is the bulk gas phase mole fraction of component i, ϕ is the total reservoir porosity, C_{t} is the total concentration of the bulk phase (in mol/m^3), V is the volume of the reservoir (in m^3), $\rho_{\mathrm{w,s}}$ is the bulk density of the reservoir (in kg/m^3), v_{a} is the specific volume of the adsorbed phase (in m^3/kg) and $n_i^{\mathrm{a}} = f(y_i, P, T)$, is the absolute amount adsorbed per unit mass of shale (in mol/kg). The second term in Eq. 9.6 accounts for the volume occupied by the adsorbed phase and therefore, for the reduction in porosity available to the free gas. By using the definitions introduced in Section 9.1, Eq. 9.5 can be recast as:

$$N_{i,\mathrm{t}} = V(\phi y_i C_{\mathrm{t}} + \rho_{\mathrm{w,s}} n_i^{\mathrm{ex}}) \tag{9.8}$$

The recoverable amount of component i in the reservoir, $G_{i,\mathrm{t}}$, is more conveniently expressed using units of standard volume ($\mathrm{m}^3_{\mathrm{STP}}/\mathrm{m}^3$):

$$G_{i,\mathrm{t}} = \frac{1}{\rho_{\mathrm{sc}}}\left(\phi y_i C_{\mathrm{t}} + \rho_{\mathrm{w,s}} n_i^{\mathrm{ex}}\right) \tag{9.9}$$

where ρ_{sc} is the density of the fluid at standard conditions (1 atm and 0 °C). Eq. 9.9 predicts the amount of recoverable gas purely based on the achieved production pressure. Therefore, it neglects reductions in the recoverable volume that may be caused by practical limitations and/or other physical processes, which are commonly accounted for by means of so-called efficiency factors [271]. We also note that the conventional method of calculating the GIP uses n_i^{a} instead of n_i^{ex} in Eq. 9.9, thereby overestimating the porosity accessed by the free gas. We will compare both methodologies in this chapter.

Traditionally, material balance calculations for primary recovery operations (no injection, single-component gas) use a graphical approach, where the recoverable volume of gas (corresponding to the GIP) is plotted as a function of P/Z (Z is the fluid compressibility) [272]. Mathematically:

$$\mathrm{GIP} = G_{\mathrm{t}} = \frac{1}{\rho_{\mathrm{sc}}}\left(\frac{\phi}{RT}\frac{P}{Z} + \rho_{\mathrm{w,s}} n^{\mathrm{ex}}\right) \tag{9.10}$$

where R is the universal gas constant and T is the reservoir temperature. The amount of gas produced at a given reservoir pressure, P, is thus estimated as:

$$G_{\mathrm{p}} = G_{\mathrm{t},0} - \mathrm{GIP} \tag{9.11}$$

where $G_{\mathrm{t},0}$ is the original GIP (OGIP). For a so-called volumetric reservoir (no adsorption), the OGIP can be readily estimated from production data by extrapolation to $P/Z = 0$, because Eq. 9.11 represents a straight-line. In the presence of adsorption, the production data deviate from linearity [272]; because the strength of the deviation ultimately depends on the amount of gas desorbed, the accurate description of experimental adsorption data is key to obtain reliable estimates of the GIP during primary production.

For enhanced recovery by gas injection, we consider a cyclic operation, where each cycle starts with the Injection stage, followed by the Soak and Production stages (Figure 9.2). We note that the free and adsorbed gas phases are in equilibrium only in the Soak stage, meaning that only the free gas participates in the Injection and Production stages. This choice is motivated by the very low permeability of the unfractured rock matrix. The governing equations for each stage in a generic cycle q are described in the following sections. We refer to CH_4 with the subscript 'm' and the injected

gas with subscript 'g'. The operation starts by depressurising the reservoir from the initial reservoir pressure, P_{o}, to the production pressure, P_{L}, after which the cyclic operation commences.

9.2.1.1 Injection Stage

At the start of the cycle (initial state 'R'), the reservoir is not under equilibrium, as it is straight after the initial depressurisation or a Production stage. A fixed amount, $N^{q}_{\mathrm{g,inj}}$, of pure gas (CO_2 or N_2) is injected into the reservoir (final state 'I'). The gas is only injected into the free phase (subscript 'f'), and the adsorbed phase (subscript 'a') remains unchanged. Only the amount of the injected component changes in the FG, while the amount of methane remains constant:

$$N^{\mathrm{I},q}_{i,\mathrm{a}} = N^{\mathrm{R},q-1}_{i,\mathrm{a}} \tag{9.12a}$$

$$N^{\mathrm{I},q}_{\mathrm{m,f}} = N^{\mathrm{R},q-1}_{\mathrm{m,f}} \tag{9.12b}$$

$$N^{\mathrm{I},q}_{\mathrm{g,f}} = N^{\mathrm{R},q-1}_{\mathrm{g,f}} + N^{q}_{\mathrm{g,inj}} \tag{9.12c}$$

where q refers to the injection cycle. The composition, pressure and total concentration of the bulk phase is then given by:

$$y^{\mathrm{I},q}_{i} = N^{\mathrm{I},q}_{i,\mathrm{f}} / N^{\mathrm{I},q}_{\mathrm{t,f}} \tag{9.13a}$$

$$C^{\mathrm{I},q}_{\mathrm{t}} = \frac{\rho_{\mathrm{w,s}} N^{\mathrm{I},q}_{\mathrm{t,f}}}{\phi - \rho_{\mathrm{w,s}} \overline{v}^{\mathrm{R},q-1}_{\mathrm{a}}} \tag{9.13b}$$

$$P^{\mathrm{I},q} = P(y^{\mathrm{I},q}_{i}, C^{\mathrm{I},q}_{\mathrm{t}}, T) \tag{9.13c}$$

where Eq. 9.13c denotes an equation-of-state. Eqs. 9.12 and 9.13 are only valid for $q > 1$. When $q = 1$, the reservoir comprises only of pure CH_4 and the following equations apply:

$$N^{\mathrm{I},1}_{\mathrm{m,a}} = N^{0}_{\mathrm{m,a}} \tag{9.14a}$$

$$N^{\mathrm{I},1}_{\mathrm{g,a}} = 0 \tag{9.14b}$$

$$N^{\mathrm{I},1}_{\mathrm{m,f}} = V C_{\mathrm{t}}|_{P_{\mathrm{L}}} (\phi - \rho_{\mathrm{w,s}} v^{0}_{\mathrm{a}}) \tag{9.14c}$$

$$N^{\mathrm{I},1}_{\mathrm{g,f}} = N^{1}_{\mathrm{g,inj}} \tag{9.14d}$$

where the superscript '0' refers to the initial reservoir conditions.

9.2.1.2 Soak Stage

After injection, a Soak stage (state 'S') is carried out to let the reservoir gases reach adsorption equilibrium. The following set of equations that describes the total and component mass conservation has to be solved simultaneously:

$$N_{\mathrm{m,a}}^{\mathrm{S},q} + N_{\mathrm{g,a}}^{\mathrm{S},q} + N_{\mathrm{m,f}}^{\mathrm{S},q} + N_{\mathrm{g,f}}^{\mathrm{S},q} = N_{\mathrm{m,a}}^{\mathrm{I},q} + N_{\mathrm{g,a}}^{\mathrm{I},q} + N_{\mathrm{m,f}}^{\mathrm{I},q} + N_{\mathrm{g,f}}^{\mathrm{I},q} \tag{9.15a}$$

$$N_{\mathrm{g,a}}^{\mathrm{S},q} + N_{\mathrm{g,f}}^{\mathrm{S},q} = N_{\mathrm{g,a}}^{\mathrm{I},q} + N_{\mathrm{g,f}}^{\mathrm{I},q} \tag{9.15b}$$

where,

$$N_{i,\mathrm{a}}^{\mathrm{S},q} = V\rho_{\mathrm{w,s}} n_{i,\mathrm{a}}(y_i^{\mathrm{S},q}, C_{\mathrm{t}}^{\mathrm{S},q}) \tag{9.16a}$$

$$N_{i,\mathrm{f}}^{\mathrm{S},q} = V y_i^{\mathrm{S},q} C_{\mathrm{t}}^{\mathrm{S},q}(\phi - \rho_{\mathrm{w,s}} v_{\mathrm{a}}^{\mathrm{S},q}) \tag{9.16b}$$

The two unknowns are the equilibrium bulk phase composition ($y_i^{\mathrm{S},q}$) and the total concentration of the bulk phase ($C_{\mathrm{t}}^{\mathrm{S},q}$). The pressure at the end of the Soak stage is calculated using an equation-of-state:

$$P^{\mathrm{S},q} = P(y_i^{\mathrm{S},q}, C_{\mathrm{t}}^{\mathrm{S},q}, T) \tag{9.17}$$

9.2.1.3 Production Stage

At the start of the Production stage, the reservoir is at equilibrium at a given pressure, $P^{\mathrm{S},q}$, and bulk composition, $y_i^{\mathrm{S},q}$. Gas production is carried out by reducing the reservoir pressure to the specified level, P_{L}. This process is not at equilibrium; while gas is withdrawn from the free bulk phase, the adsorbed phase remains unaffected. The following equations describe the amount of FG and AG at the end of this stage (final state 'R'):

$$N_{i,\mathrm{a}}^{\mathrm{R},q} = N_{i,\mathrm{a}}^{\mathrm{S},q} \tag{9.18a}$$

$$N_{i,\mathrm{f}}^{\mathrm{R},q} = V y_i^{\mathrm{S},q} C_{\mathrm{t}}^{\mathrm{R},q}|_{P_{\mathrm{L}}}(\phi - \rho_{\mathrm{w,s}} \overline{v}_{\mathrm{a}}^{\mathrm{S},q}) \tag{9.18b}$$

$$N_{i,\mathrm{prod}}^{q} = N_{i,\mathrm{f}}^{\mathrm{S},q} - N_{i,\mathrm{f}}^{\mathrm{R},q} \tag{9.18c}$$

Eq. 9.18c is used to compute the amount of component i that is produced. For the first depressurisation, prior to the first Injection stage, the amount of methane gas produced is $N^0_{\mathrm{m,prod}} = V(C_{\mathrm{t}}|_{P_{\mathrm{o}}} - C_{\mathrm{t}}|_{P_{\mathrm{L}}})(\phi - \rho_{\mathrm{w,s}} v^0_{\mathrm{a}})$. After the final Production stage, the reservoir is abandoned; there is a final Soak stage, where the reservoir re-equilibrates.

9.2.1.4 Solution Procedure

The cyclic operation of the reservoir starts and ends at state 'R', passing through the 'I' and 'S' stages. The design variables are P_{L}, $N^q_{\mathrm{g,inj}}$ and the total number of injections, Q. It is worth noting that while the absolute adsorbed amount remains constant during the Injection and Production stages, the excess adsorbed amount may vary, because it depends on the amount of gas in the free bulk phase. The mathematical model was implemented in MATLAB R2020a and the set of nonlinear equations (Eqs. 9.15 and 9.16) was solved using `lsqnonlin` with a tolerance of $1\text{x}10^{-9}$ and the default of 400 iterations. A NIST REFPROP [242] MATLAB wrapper was used for the equation-of-state for each fluid and/or their mixtures.

9.2.2 Model Parameters

In this work, we use the physical properties of the Marcellus shale to demonstrate the applicability of the shortcut PSA analogue model as it is relatively well characterised. Reservoir properties and operational parameters are reported in Table 9.1. Either pure CO_2 or N_2 is injected to displace the resident gas, which is initially pure methane. Five injection cycles are conducted by introducing a constant volume of gas at each injection stage, corresponding to approximately 100 times the pore volume of the reservoir. In the model, excess adsorption isotherms are generated from the corresponding absolute quantity by assuming a constant adsorbed phase density. For each fluid, the latter takes the value of the density of the saturated liquid at 35 MPa (Table 9.2); this reflects common pore densities found in the literature for shale reservoirs [125, 124].

Table 9.1: Model parameters, including reservoir properties and operational parameters.

Parameter	Value	Source
Initial Reservoir Pressure, P_{o}	35 MPa	[40], [273], [138]
Reservoir Temperature, T	55 °C	[40], [273], [138]
Reservoir Porosity, ϕ	8%	[274]
Reservoir Bulk Density, $\rho_{\mathrm{w,s}}$	2,550 kg/m^3	[275]
Production Pressure, P_{L}	10 MPa	–
Number of Cycles, Q	5	–
Gas Injected per Cycle, $N^q_{\mathrm{g,inj}}/V$	357 mol/m^3	–

The model is solved by providing the constitutive equation for a given adsorption isotherm model,

Table 9.2: The adsorbed phase density (ρ_a) and density at standard conditions (ρ_{sc}) for each fluid in this work. [a] Liquid density at 35 MPa and 190 K (CH_4), 303 K (CO_2) and 124 K (N_2).

Gas	CH_4	CO_2	N_2	Source
ρ_a (mol/m^3)[a]	22,342	21,996	25,821	[231]
ρ_{sc} (mol/m^3)	44.135	44.326	44.635	[231]

$n_i^a = f(y_i, P, T)$. The four models selected for this study are shown in Figure 9.1 and include the Langmuir, the BET, the Linear and the Anti-Langmuir models. The equations for each model are provided in the appendices, together with the model parameters. The first two models have been used previously to describe adsorption on shale and coal [67, 276, 138], while the last two have been added here for the sake of generality. The isotherms have been constructed such that the absolute adsorbed amount at P_o (35 MPa) is equal for all adsorption models, namely 5 kg/m^3 for CH_4, as shown in Figure 9.1. For the ESGR process, the mixed-gas adsorption equilibrium is described using the extended Langmuir model formulated for two components (i and k):

$$n_i^a = \frac{n^{max} K_i P y_i}{1 + K_i P y_i + K_k P y_k} \tag{9.19}$$

where K_i and K_k are the pure component Langmuir parameters for component i and k, respectively (values provided in the appendices). We note that to ensure thermodynamic consistency, the molar saturation capacity, n^{max}, is the same for each component in the mixture, meaning that the selectivity of species i relative to species k for any bulk phase composition and pressure is simply the ratio of the Langmuir parameters, K_i/K_k. Equal saturation capacities for both components are reasonably realistic due to the similarity between the collision diameters of CH_4, CO_2 and N_2 [111]. The extended Langmuir model was used in this study for its simplicity, but the approach may be easily adapted to the use of more complex theories, such as RAST. In fact, while these two approaches have been shown to produce similar composition fronts during cyclic adsorption processes, RAST may be needed to improve the agreement between the experimental and modelling results [277].

9.2.2.1 Performance Metrics

The two main parameters that are of interest in an ESGR process are (i) the total recovery of CH_4 and (ii) the total amount of injected gas that remains in the reservoir after abandonment (storage). The Enhanced Recovery factor is defined as the ratio between the total amount of CH_4 produced with enhanced recovery and the amount of CH_4 that would have been produced from primary recovery by

depressurisation to the same pressure (P_{L}), but without any gas injection ($N_{\mathrm{m,PR}}$):

$$R_{\mathrm{m}} = \frac{N^{0}_{\mathrm{m,prod}} + \sum_{q=1}^{Q} N^{q}_{\mathrm{m,prod}}}{N_{\mathrm{m,PR}}} \tag{9.20}$$

The Storage factor is defined as the ratio between the total number of moles of the injected gas left in the reservoir at the end of cycle Q and the cumulative amount of gas injected into the reservoir:

$$S_{\mathrm{g}} = \frac{N^{Q}_{\mathrm{g,t}}}{\sum_{q=1}^{Q} N^{q}_{\mathrm{g,inj}}} \tag{9.21}$$

9.3 Results

The following section is divided into two main parts: (1) *Primary recovery*, where the impact of different adsorption isotherm models is investigated by evaluating the $P/Z - G_{\mathrm{p}}$ curves for a recovery operation driven exclusively by depressurisation; and (2) *Recovery with gas injection*, where the use of two different gases with opposite selectivity relative to CH_4 is assessed, namely CO_2 and N_2; to this end, only the extended Langmuir adsorption isotherm model will be considered, because of its proven general applicability.

9.3.1 Primary Recovery by Depressurisation

9.3.1.1 GIP and Initial Reservoir Pressure

It is highly instructive to first investigate the $P/Z - G_{\mathrm{p}}$ diagram for the case of the Langmuir adsorption isotherm model, as shown in Figure 9.3a for four initial reservoir pressures, P_{o}. Three sets of curves are plotted to represent three contrasting cases, namely: (i) no adsorption ('base case', dashed straight line); (ii) adsorption without a porosity correction ('absolute', light blue); and (iii) adsorption with a porosity correction ('excess', dark blue). The latter is the true cumulative gas production curve for an adsorbing shale reservoir. For each case, the intercept on the x-axis indicates the predicted OGIP of the reservoir. It can be seen that adsorption increases the gas storage capacity and, accordingly, the amount of recoverable gas reserves. The increase correlates positively with initial reservoir pressure, as a result of increased bulk gas density *and* adsorption. Yet, the characteristic shape of the Langmuir isotherm (Figure 9.1) further indicates that the gain in OGIP brought by adsorption relative to the contribution of the dense bulk phase diminishes with increasing P_{o}; for example, at a P_{o} of 5 MPa,

the OGIP is 119% higher than the volumetric reservoir, while at a P_o of 35 MPa, the same difference is reduced to 13%.

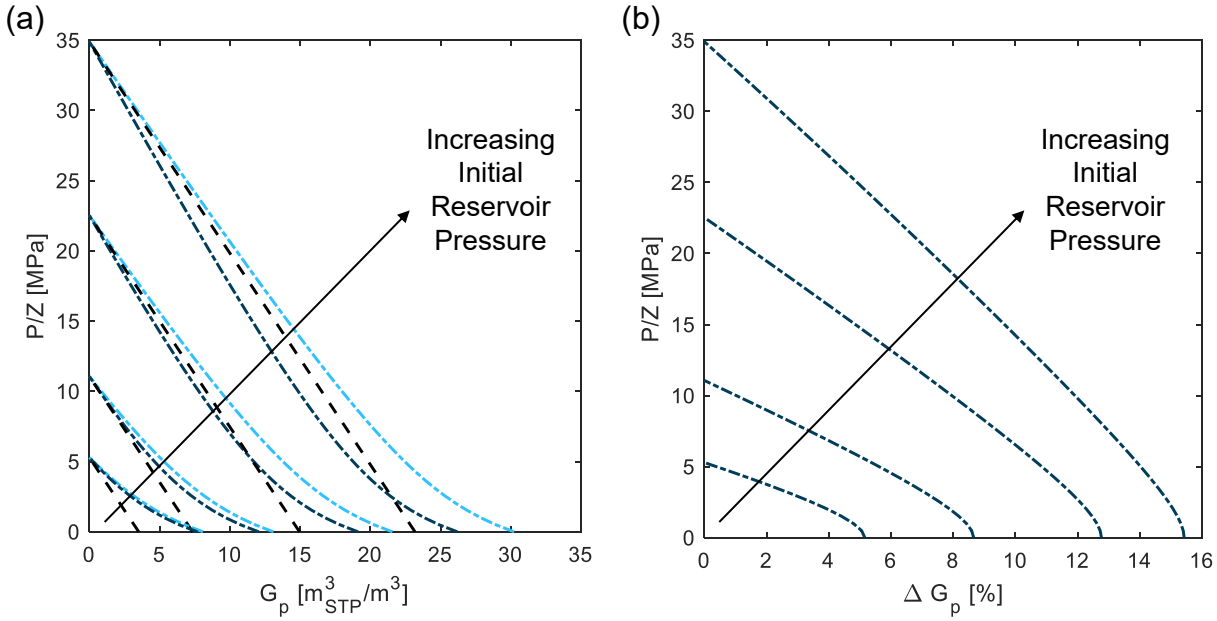

Figure 9.3: (a) CH_4 cumulative gas production (G_p) as a function of P/Z for four initial reservoir pressures ($P_o = 5, 10, 20, 35$ MPa) and three scenarios, namely no adsorption (dashed straight line); adsorption without a porosity correction (light blue); and adsorption with a porosity correction (dark blue). Adsorption is described with a Langmuir isotherm model (parameters given in the appendices). (b) The relative difference, ΔG_p, between the two adsorption scenarios as a function of P/Z for the same initial reservoir pressures as in (a).

For $P_o = 5$ MPa and 10 MPa, the 'absolute' and 'excess' scenarios outline a similar behaviour relative to the base case, while indicating larger recoverable volumes over the entire operating range of pressures. For larger values of P_o, the 'absolute' curve continues to stay on the right-hand side of the trend indicated by the base case (black line). On the contrary, the 'excess' curve follows a path on the left-hand side of the base case, before crossing it, when the pressure is sufficiently low. This behaviour nicely shows the effect of the reduction in pore space due to the presence of the adsorbed phase - the latter decreases the contribution from the decompression of the free gas that drives the initial stages of production for deep reservoirs. As discussed further below, this observation indicates that while adsorption does increase the OGIP, it does not necessarily sustain a larger gas production, and that careful consideration needs to be given to the type of adsorption isotherm and the initial reservoir pressure.

At $P_o = 35$ MPa, both the 'absolute' OGIP (30.2 m^3_{STP}/m^3) and 'excess' OGIP (26.2 m^3_{STP}/m^3) are larger than the OGIP for the 'base case' (23.2 m^3_{STP}/m^3). However, the predicted enhancement is significantly different (30% vs. 13%). Ambrose et al. (2012) demonstrated that the total gas storage capacity decreases between 10–25% when the adsorbed volume is duly considered [263]. Here, we extend this analysis by considering the entire gas production curve - from the initial pressure to any

selected abandonment pressure. This is shown in Figure 9.3b, where the relative difference between the production curves predicted by the two adsorption scenarios ('absolute' and 'excess') is plotted for the four initial reservoir pressures. It can be seen that the overestimation for production starting at $P_o = 5$ MPa is rather limited; the maximum deviation is about 5%. As the initial reservoir pressure rises, this discrepancy increases, and at $P_o = 35$ MPa, the OGIP is overestimated by approximately 15% using the incorrect adsorption framework.

We note that the GIP calculations presented above are based on a fairly large set of parameters, as outlined in Section 9.2.2. While the observed trends are quite general, the relative strength of the overestimation will depend on the specific values of the reservoir porosity and adsorption isotherm parameters. A sensitivity analysis for these parameters is presented in the appendices.

9.3.1.2 GIP and Adsorption Isotherm Model

Cumulative gas production curves obtained using the four different adsorption isotherm models are shown in Figure 9.4a for $P_o = 35$ MPa. For a given value of P/Z, G_p increases in the order Langmuir $<$ Linear $\approx$ BET $<$ Anti-Langmuir, mirroring the order observed for the excess adsorption isotherms (Figure 9.1a). The higher the excess adsorption at a given pressure, the stronger is the reduction in the available pore space for the free gas and, accordingly, in the enhancement of recoverable gas. With the exception of the Langmuir case, the curves obtained for all the isotherm models are on the right-hand side of curve describing the base case, indicating a larger cumulative recovery right from the start of gas production. This behaviour can be traced back to the definition of excess adsorption and is again reflected in the characteristic shape of the excess adsorption isotherm, which may or may not show a maximum. The presence of a maximum (Langmuir case) is an indication that a threshold pressure (or P/Z value) has been reached beyond which the increase in mass stored by adsorption is less than the corresponding increase by simple gas compression. In practical terms, beyond this point the formation of the adsorbed phase reduces the potential for gas storage; in a scenario of primary recovery this translates into less gas being produced compared to a non-adsorbing reservoir with the same porosity. This apparent smaller gas production continues until the pressure is reduced below the threshold value; here, the G_p curve crosses the 'base-case' in Figure 9.4a and the desorbed gas provides the expected enhancement in gas production. This ability to map the characteristic shape of the excess adsorption isotherm to the cumulative gas production curve highlights the importance of accurate adsorption data for the design of a primary recovery operation.

Figure 9.4b shows the relative difference between the G_p obtained from the 'absolute' and 'excess' adsorption scenarios discussed above. The relative difference increases as the reservoir is depressurised, reaching a maximum of approximately 15% at complete reservoir depletion. The different models

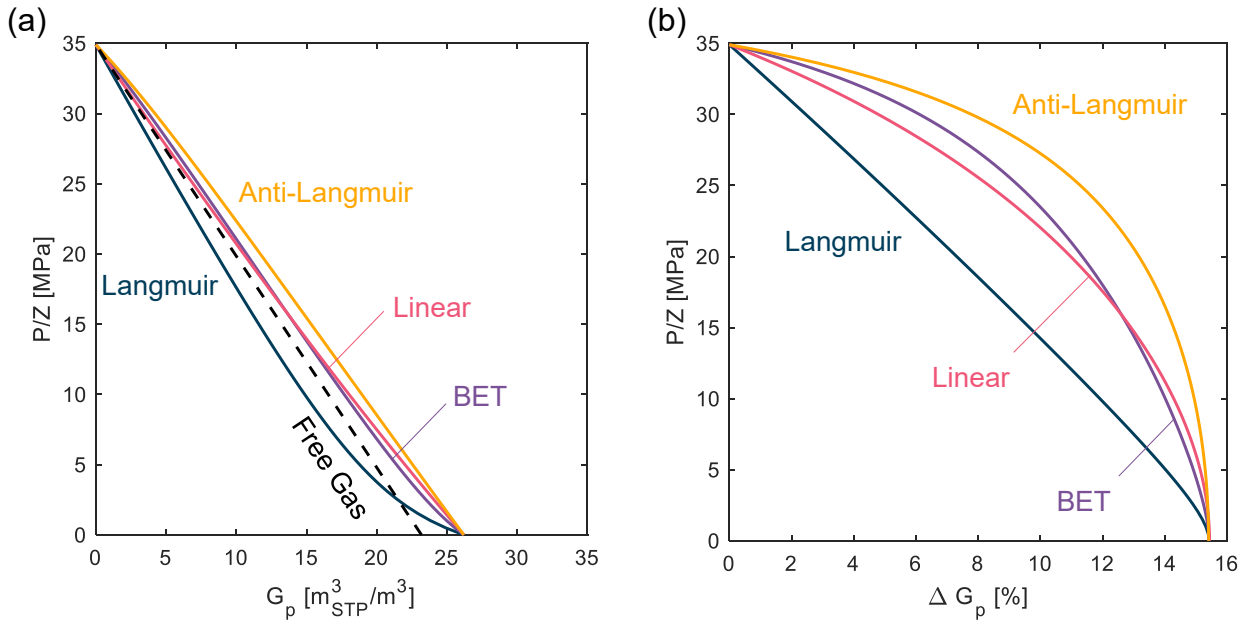

Figure 9.4: (a) CH_4 cumulative gas production (G_p) as a function of P/Z computed using for different adsorption models in the excess formulation and their comparison with the 'base case' (dashed black line, no adsorption). (b) The corresponding relative difference, ΔG_p, between the two adsorption scenarios 'absolute' and 'excess' as a function of P/Z.

approach this maximum at different rates, again reflecting the characteristic shape of each adsorption isotherm. These observations further indicate that at a given production pressure the overestimation brought by the incorrect use of absolute adsorption in GIP calculations depends not only on the extent of adsorption, but also on the shape of the adsorption isotherm.

9.3.2 Recovery with Gas Injection

9.3.2.1 Process Description

The operation of the enhanced recovery process that cycles between the Injection, Soak and Production steps is represented in Figures 9.5a and 9.5b for the case of CO_2 injection and in Figure 9.5c and 9.5d for the case of N_2 injection. Each cycle is depicted by three symbols of the same colour, with the exception of 'Cycle 0' that includes only the transition from the initial state of the reservoir ($y_m^0 = 1$, $P_o = 35$ MPa) to $P_L = 10$ MPa (these points are shown in grey). The transition between each state and cycle (the operating line) is indicated by the black arrows. The reservoir's final state is represented by the yellow point, which is the result of a final Soak after the last Production stage. The competitive absolute adsorption isotherms at various equilibrium compositions (y_m^S or $1-y_m^S$) at the Soak stage are also shown in each plot. These have been obtained from the extended Langmuir adsorption isotherm model. We note that the methane adsorption parameters used for this case study differ from those used in the previous section (see appendices).

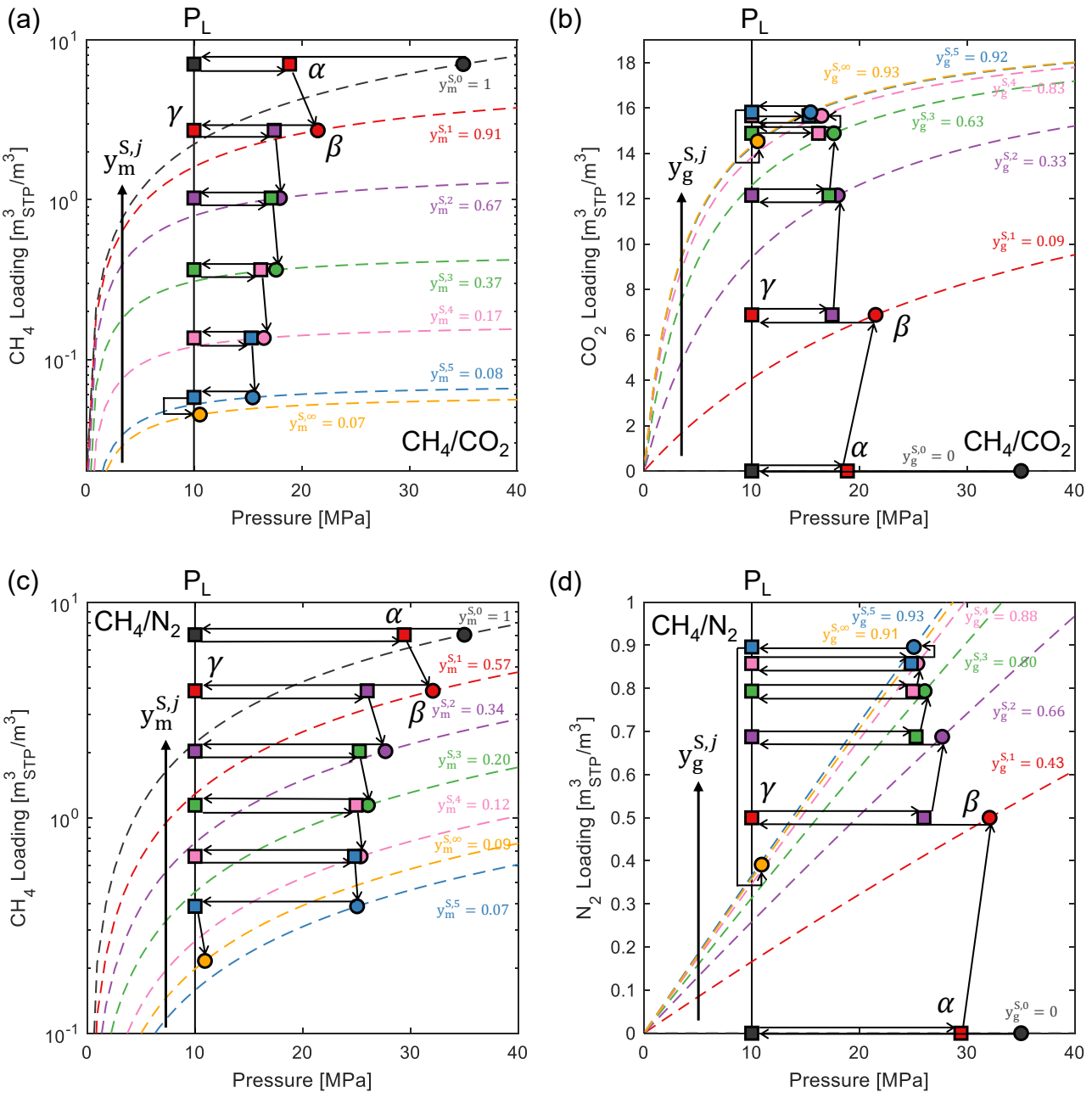

Figure 9.5: Transitions (black arrows) during the cyclic CH_4 recovery with gas injection by either CO_2 (a, b) or N_2 (c, d). The results are plotted as absolute adsorption loadings for each gas and the dashed lines indicate the competitive loadings at the equilibrium composition in the Soak stages ($y_i^{S,q}$). The superscripts '0' and '∞' represent the initial and abandoned reservoir conditions representatively. The symbols α, β and γ represent the Injection, Soak and Production stages, respectively, for the first cycle. P_L refers to the production pressure and each cycle is illustrated by a different colour.

As an example of general validity, the first cycle of the CO_2-ESGR operation is discussed first (red symbols in Figures 9.5a and 9.5b). The reservoir has been depressurised to $P_L = 10$ MPa, followed by the injection of CO_2 (state α), which raises the reservoir pressure to approximately 21 MPa. During the Soak stage (state β), the composition of the bulk gas changes, as a result of the equilibration with the adsorbed phase, reaching a final value $y_m^S = 0.91$. It should be noted that this point lies on the corresponding equilibrium adsorption isotherm (dashed line). The reservoir is then depressurised to $P_L = 10$ MPa (state γ) by producing a gas mixture with composition $y_m = 0.91$. Thereafter, a new cycle starts by re-introducing CO_2 in the reservoir. Through the sequence of cycles, the symbols in Figure 9.5a (CH_4 loading) move downwards, while those in Figure 9.5b (CO_2 loading) move upwards, meaning that the reservoir is being depleted in CH_4 and enriched in CO_2. After five cycles, the bulk gas composition has reached a value of $y_m = 0.08$.

In the case of N_2 injection (Figures 9.5c and 9.5d), the pressure swing is much wider, reaching pressures as high as 32 MPa at the end of the first injection step (state α). The higher N_2 partial pressure leads to an equally strong reduction in the CH_4 loading already after the first Soak stage (state β, 3.9 m^3_{STP}/m^3 vs. 2.7 m^3_{STP}/m^3 with CO_2), albeit with a produced gas that is leaner in CH_4 (state γ, $y_m = 0.57$ vs. $y_m = 0.91$ with CO_2). The lower concentration of CH_4 in the gas phase is the result of the unfavourable adsorption competition, as CH_4 has a stronger affinity for the shale than N_2, while the opposite is true for CO_2/CH_4 mixtures. These observations indicate that partial pressure and competitive adsorption both act towards enhancing gas production, but they do so in complementary ways. The final reservoir pressure after the N_2-ESGR is 11 MPa, similar to the CO_2 injection scenario, but the amount of adsorbed CH_4 remaining in the reservoir is slightly more (0.2 m^3_{STP}/m^3 vs. 0.05 m^3_{STP}/m^3 with CO_2). The reservoir is abandoned with a N_2 loading of approximately 0.4 m^3_{STP}/m^3 ($y_m = 0.09$), as compared to the approximately 15 m^3_{STP}/m^3 of adsorbed CO_2 left in the reservoir after the CO_2-ESGR operation ($y_m = 0.07$).

9.3.2.2 State of the Reservoir

A better understanding of the mechanisms driving the recovery of CH_4 in the two ESGR scenarios is achieved by analysing the evolution of both the FG (y_i) and the AG (z_i) composition. Here, we will additionally consider the partitioning of each gas between the FG and AG, as given by:

$$f_i = \frac{n_i^a}{N_{i,t}} \tag{9.22}$$

for methane and $1 - f_i$ for the injected species (CO_2 or N_2). Figure 9.6 illustrates these different ratios for (a) CO_2-ESGR and (b) N_2-ESGR; in each plot, the lines indicate the variation of these quantities with each Soak stage and the symbols represent the Soak after the last Production stage.

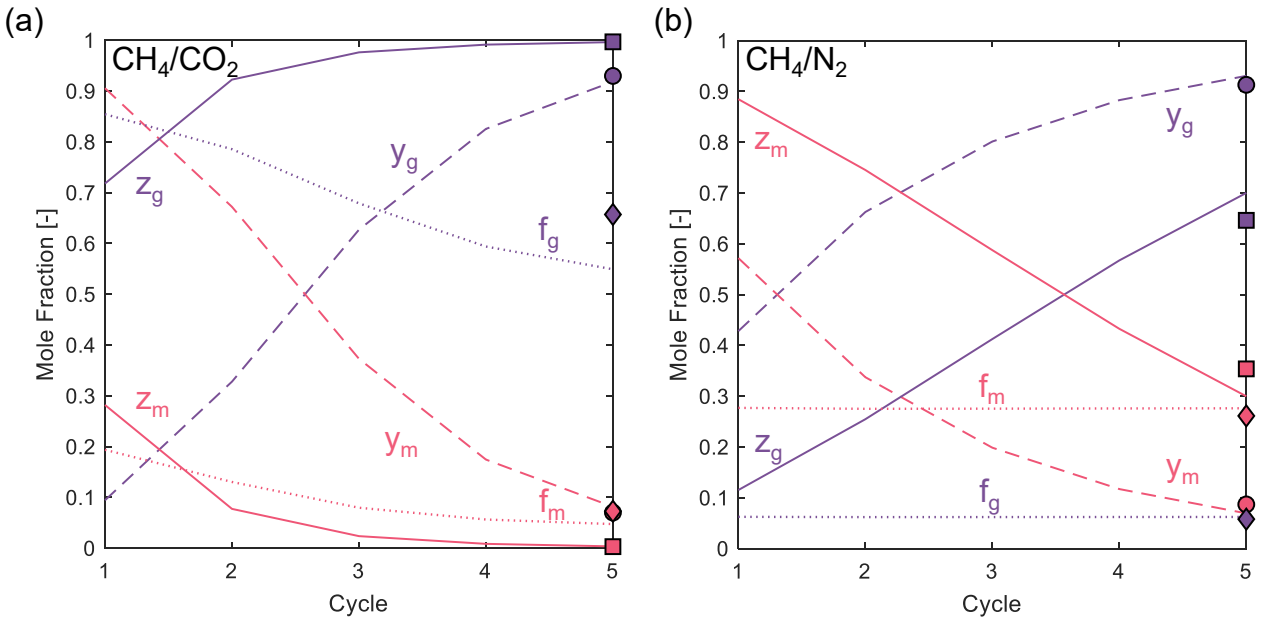

Figure 9.6: Evolution of the composition of both the adsorbed and bulk phase after each soak stage for the (a) CH_4/CO_2 and (b) CH_4/N_2 ESGR scenarios. CH_4 is shown in pink, while the injected gas is shown in purple. Lines indicate the change in mole fractions at each cycle (at the Soak stage), while the symbols indicate the final state of the reservoir (at the final Soak after the last Production stage). Solid lines and squares indicate z_i (adsorbed phase); dashed lines and circles indicate y_i (bulk phase); dotted lines and diamonds indicate f_i (fraction of adsorbed phase).

While they are qualitatively similar, the trends outlined by the two injection schemes show important differences. Across cycles, the fraction f_i of each component is fairly constant (dotted lines), with CH_4 remaining below 30% for both schemes; however, for the injected gas $f_g \approx 55$–$85\% > f_m$ for CO_2-ESGR and $f_g \approx 6\% < f_m$ for N_2-ESGR, highlighting the opposite adsorption selectivity of these two gases relative to CH_4. This ordering applies also after completion of the cyclic operation: the diamond symbols show that 7–26% of the total amount of methane is in the AG phase, whereas 66% and 6% of the total amount of CO_2 and N_2 remains in the AG phase, respectively. In terms of the adsorbed phase composition (solid lines), the AG is dominated by CH_4 in the early N_2-ESGR cycles, with a crossover after Cycle 3; on the contrary, $z_m \approx 0.3$ already at Cycle 1 for CO_2-ESGR and the AG becomes richer in CO_2 at every cycle, reaching a value $z_g \approx 1$ after 5 cycles ($z_g \approx 0.6$ for N_2). As discussed above, this apparent inefficiency of N_2 to extract CH_4 by adsorption is compensated by the stronger reduction in CH_4 partial pressure, relative to the CO_2 injection scenario. This behaviour is confirmed by the trends outlined by the gas phase composition, y_i (dashed lines). In both scenarios, the bulk phase is initially richer in CH_4 ($y_m \approx 0.91$ for CO_2 and $y_m \approx 0.57$ for N_2), with a crossover appearing already after Cycle 1 for N_2-ESGR and only after Cycle 2 for CO_2-ESGR. When the two processes are compared, it can be seen that y_g is always greater with N_2 rather than CO_2.

9.3.2.3 Performance Evaluation

The CO_2-ESGR and N_2-ESGR operations are compared in Figure 9.7 by considering the total volume of CH_4 produced, as well as the volume of gas (CO_2 or N_2) injected and stored in the reservoir, which are evaluated in terms of incremental and cumulative amounts. Both scenarios start with an initial depressurisation from P_o to P_L (Cycle 0), which produces 12.2 m^3_{STP}/m^3 of CH_4. Thereafter, the same amount of gas is introduced in each cycle (8 m^3_{STP}/m^3), for a total of 40 m^3_{STP}/m^3 of gas injected. After five cycles, approximately 26 m^3_{STP}/m^3 of CH_4 have been recovered for both CO_2- and N_2-ESGR. In both cases, the first depressurisation contributes to about 48% of the total recovery and the first two cycles prove to be the most effective in terms of recovery and storage. By the end of Cycle 2, 85% and 87% of the total recovery has been achieved for CO_2- and N_2-ESGR, respectively. The volume of gas stored after five cycles amounts to 22 m^3_{STP}/m^3 (CO_2) and 7 m^3_{STP}/m^3 (N_2); 63% and 71% of this amount is stored by the end of Cycle 2, respectively.

Prior to the start of the ESGR operation, there is only methane in the reservoir and approximately 27% of this mass is found as adsorbed gas. Methane contribution to the GIP reduces to approximately 63% after the first injection, irrespective of the injected gas, and to approximately 3% and 11%, at the end of the operation with CO_2 and N_2, respectively. For CO_2-ESGR, the AG contribution to the GIP increases to an average of 53%, reaching 64% at the end of the operation. The opposite behaviour is observed for N_2-ESGR, whereby the AG contribution to the GIP decreases to an average of 13% during the Soak stages, reaching 8% at the final reservoir pressure. These numbers reflect both the removal of CH_4 from the system as well as the preferential retention of CO_2 in the adsorbed phase. On a volume basis, the AG occupies initially 17% of the total porosity and this value increases to approximately 37% at the final reservoir condition during CO_2-ESGR. On the contrary, when N_2 is used, the fraction of porosity occupied by the AG decreases to 11% after the first cycle and reaches a value of only 1% in the final state. The reservoir is now by and large a 'conventional' reservoir, where most of the gas is found as compressed gas.

9.4 Strategy for Primary Recovery

The sensitivity of the $G_p - P/Z$ curve to the selected adsorption isotherm model provides scope for identifying a suitable strategy for primary recovery. The inverse of the slope of the curves depicted in Figures 9.3a and 9.4a can be interpreted as a 'production rate' - the amount of gas produced within each incremental change in P/Z. While in the absence of adsorption ('base case') this production rate is constant, the non-linearity introduced by the desorption process is such that this rate depends on pressure. It was already anticipated in Section 9.3.1 that the Langmuir isotherm can lead to initial

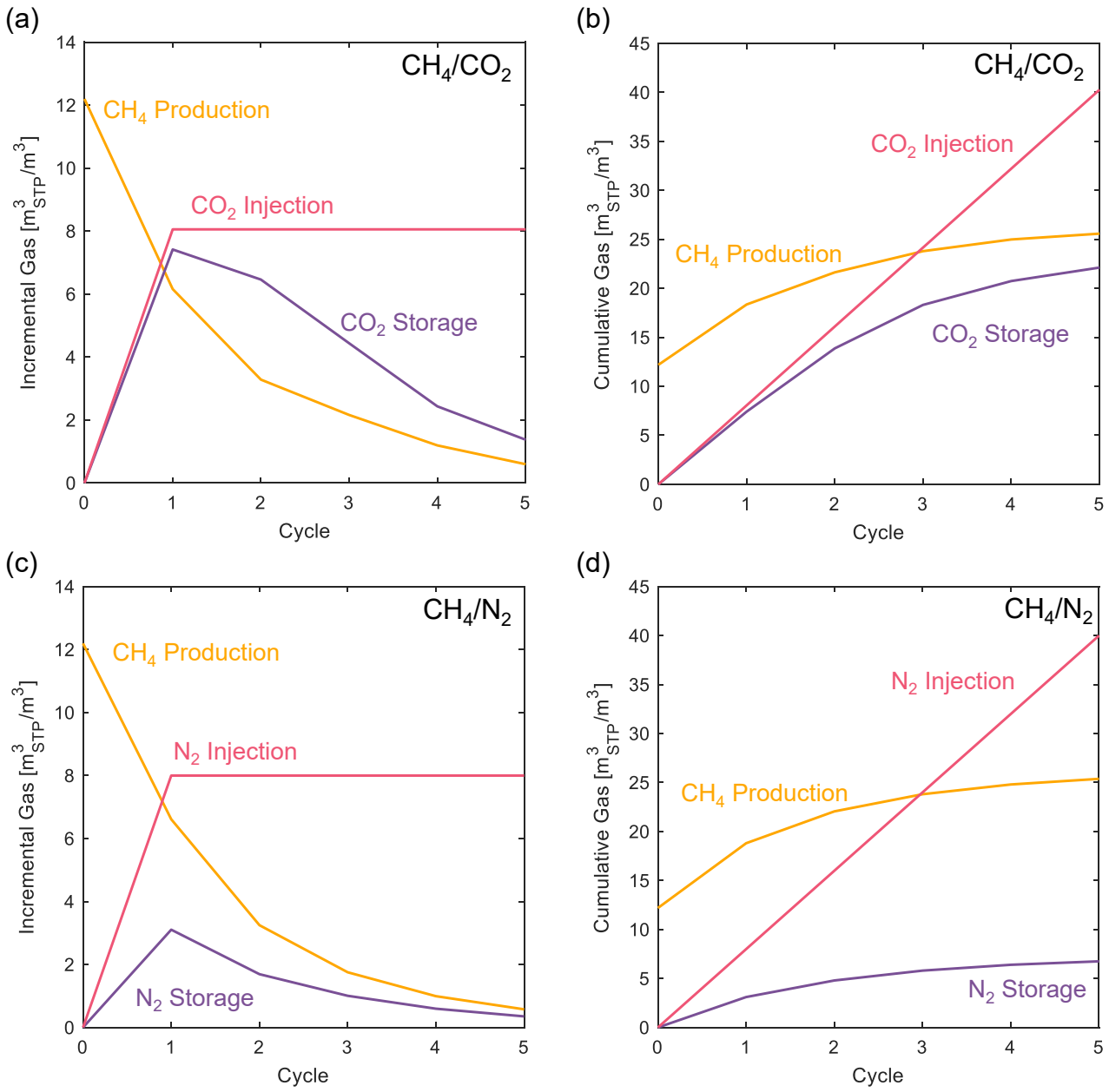

Figure 9.7: Incremental and cumulative volume of gas injected, stored and CH_4 produced for each cycle during the ESGR operation driven by CO_2 (a, b) and N_2 (c, d) injection. 'Cycle 0' refers to the depressurisation of the reservoir from the initial pressure to the production pressure, P_L.

production rates that are lower than those estimated based on total porosity alone. This is typically the case for deep reservoirs (high P_o), which would therefore require fairly low production pressures to observe the desired enhancement brought by the desorbing gas. For two of the cases depicted in Figure 9.3a, the production rates for an adsorbing reservoir are always higher than the volumetric reservoir (P_o = 5 MPa and 10 MPa). At a P_o of 20 MPa or 35 MPa, the same is only true below a production pressure of approximately 11 MPa . These initial considerations have implications in the planning of the primary recovery operation and in the selection of an abandonment pressure.

In general terms, reservoir production continues until declining production rates cause it to be no longer economically viable [278]. In this context, a shale that shows adsorption data following

an Anti-Langmuir isotherm represents the most favourable option, because it has the highest gas production rate right at the start of production (see again Figure 9.4a). Accordingly, a process designed to produce a given amount of gas (G_p) would result in a higher abandonment pressure compared to the value required for an equivalent shale reservoir described with the other adsorption isotherms. For a shale that shows a linear adsorption isotherm, the production rate would increase linearly with the depressurisation of the reservoir. The characteristic shape of the BET adsorption isotherm leads to a production scenario that share similarities with the Anti-Langmuir and Langmuir cases, which enables maintaining a fairly high production rate throughout the entire pressure range. Based on this analysis, to achieve a given value of G_p, the abandonment pressures of the reservoirs would be in the order P(AL) > P(Lin) > P(BET) > P(L). Because of the fairly low abandonment pressure associated with a shale characterised by a Langmuir-type adsorption isotherm, a production strategy that involves the injection of a sweep gas is advisable, as discussed in the next section.

9.5 Strategy for Recovery with Gas Injection

The CO_2 and N_2-ESGR strategies studied in this work can be evaluated on the basis of the performance metrics shown in Table 9.3.

Table 9.3: Performance metrics estimated from the Shortcut Pressure Swing Adsorption Analogue Model using CO_2 and N_2 injection to enhance CH_4 recovery. The Enhanced Recovery (R_m) and Storage (S_g) factors are defined by Eqs. 9.20 and 9.21, respectively.

Parameter	CO_2	N_2
R_m	150%	149%
S_g	54.9%	16.9%
Primary Recovery	65.0%	
Recovery with Gas Injection	97.6%	96.8%

Primary recovery results in extraction of only 65% of the CH_4 in the reservoir, while production using CO_2 or N_2 yields a methane recovery of 97.6% and 96.8%, respectively. The corresponding increase relative to the primary recovery is thus approximately $R_m = 150\%$. As discussed above, for CO_2 this is primarily due to favourable competitive adsorption, while for N_2 the primary mechanism is the strong reduction in CH_4 partial pressure associated with the wider pressure swing. To produce the same volume of CH_4 without any gas injection, the reservoir would have to be depressurised to about 0.5 MPa. This pressure is thus much lower than the production pressure sustained during the ESGR operation ($P_L = 10$ MPa). For the reservoir to have the same final absolute adsorbed amount of CH_4 as the reservoir with CO_2 or N_2 storage, primary recovery would result in depressurisation to below 1 MPa. A key advantage of CO_2-ESGR is the storage of CO_2 and the consequent environmental benefit; approximately half of the injected CO_2 is effectively stored ($S_g = 54.9\%$) and 66% of this

CO_2 is adsorbed. For N_2, S_g = 16.9% and 6% of this amount is adsorbed. Simulation studies reported in the literature indicate similar trends in terms of recovery and storage [279]. Others propose to inject a mixture of the two gases [280], although this potentially lowers the CO_2 storage potential of the shale reservoir. Most notably, the results obtained with our simplified model compare favourably with observations from a field operation [25]. In the latter case, a single CO_2 injection cycle was completed that enabled the increase of hydrocarbon production by 2–3 times (compared to the forecasted production by primary recovery), while storing approximately 60% of the injected CO_2. The field study concluded that larger recovery factors could have been achieved upon increasing the volume of CO_2 injected and its pressure. As shown in this study, one strategy to achieve this goal is to carry out additional Injection (and Soak) cycles.

Figure 9.8 shows the cumulative and incremental changes of performance metrics reported in Table 9.3 (R_m and S_g) as a function of each cycle for both (a) CO_2- and (b) N_2-ESGR. The trends observed for both systems are very similar, with N_2 sustaining a slightly lower level of production at every cycle. It can also be seen that initial depressurisation (Cycle 0) contributes greatly to the total recovery (48% of the total CH_4 recovered using either CO_2 or N_2). The total pressure of the reservoir for CO_2-ESGR oscillates between 10 MPa (the production pressure, P_L) and the pressure after the Injection and Soak stages, which is between 15–21 MPa. For N_2-ESGR, the pressure increase is up to 25–32 MPa with gas injection; as discussed above, the wider pressure swing compensates for the unfavourable competitive adsorption of the N_2/CH_4 system. Accordingly, more CH_4 could be produced by CO_2-ESGR if a higher Injection/Soak pressure could be obtained using a higher volume of CO_2 injected per cycle. As discussed above, CO_2 leads also to significantly larger storage than N_2, the majority of which is already achieved during the first cycle.

The Enhanced Recovery and Storage factors discussed above should be regarded as theoretical maxima, because they are based on complete equilibrium being achieved at the Soak stages. Realistically, this might take a significant amount of time, which might not be economical. We also note that more than half of the CO_2 injected is produced, and there will be some cost associated with its separation from the produced CH_4 before its reinjection into the reservoir. An optimisation strategy that prioritises CO_2 storage and CH_4 recovery, without compromising the purity of the produced stream, is required. Similar considerations apply to N_2-ESGR, but with a heavier burden on the economics of the operation, given that there is no real incentive in storing N_2.

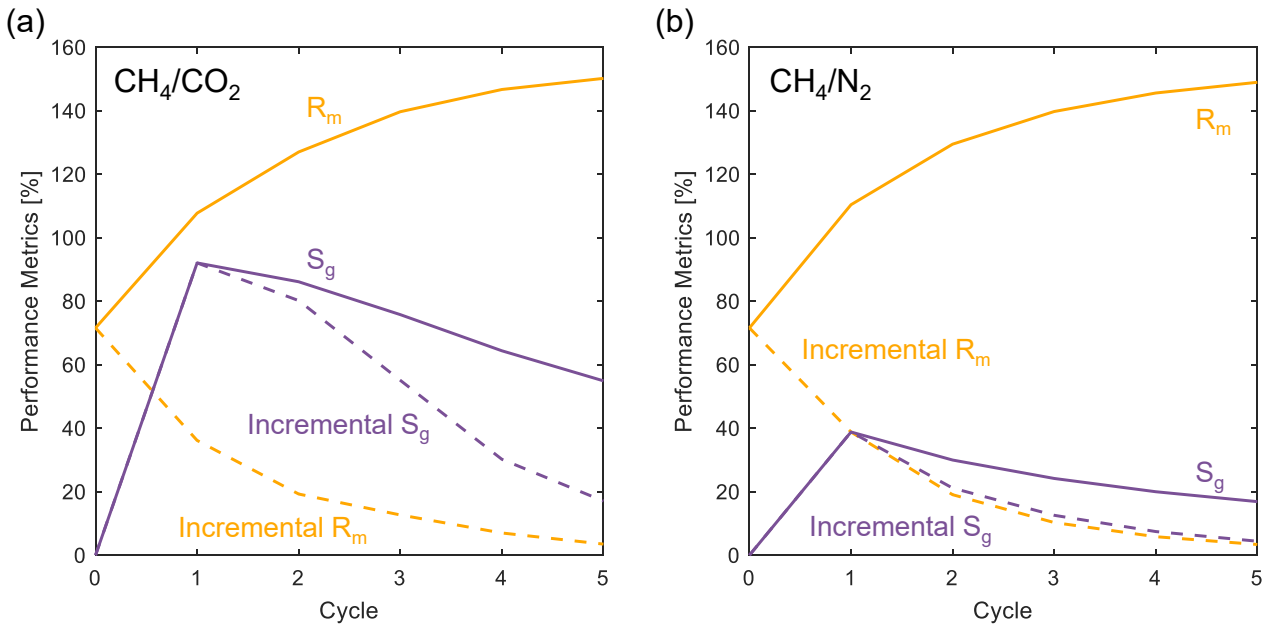

Figure 9.8: The performance metrics as a function of each injection cycle for the (a) CH_4/CO_2 and (b) CH_4/N_2 systems. Both R_m and S_g, which are cumulative quantities, are shown as solid lines and incremental quantities, i.e. metrics that are based solely on each cycle, are shown as dashed lines. 'Cycle 0' refers to the initial depressurisation of the reservoir where there is no gas injection.

9.6 Conclusion

We have analysed shale gas production from primary and secondary recovery with gas injection using material balance calculations that correctly account for the reduction in the available porosity due to gas adsorption. While previous work has shown that the OGIP is overestimated if the adsorbed volume is not duly considered, we have extended here the analysis to the entire gas production curve – from the initial pressure to any selected abandonment pressure. In this endeavour, we have shown that adsorption does not necessarily sustain a larger gas production relative to a non-adsorbing reservoir with the same porosity, and that careful consideration needs to be given to the initial reservoir pressure and the type of adsorption isotherm. The latter can significantly impact the strategy used for primary or recovery with gas injection.

The shortcut Pressure Swing Adsorption analogue model developed in this work provides a practical way to test injection strategies for ESGR. We evaluated CO_2 and N_2 as injection gases and observed that (i) they are both equally successful at enhancing recovery of CH_4 and (ii) they exploit different means to achieve this (competitive adsorption and partial pressure reduction, respectively). In N_2-ESGR, the volume of N_2 stored is less than half of the volume of CO_2 stored. This further indicates that more N_2 is being produced with natural gas, leading to higher separation costs. In CO_2-ESGR, about half of the CO_2 injected is stored in the reservoir, meaning that the operation may be both economically and environmentally attractive. Yet, as CO_2 increases in the system, the benefit

gained by the recovery process might be offset by the costs involved in maintaining the injection of CO_2, as a lot of the CH_4 has already left the system. Various injection strategies could be explored in the future, whereby the injection volume is gradually reduced with each cycle.

The Soak stage represents a key element of the cyclic operation, because it is where adsorption equilibrium is attained. In our model formulation we did not consider the time to reach this equilibrium, although this represents a key aspect of shale gas production. The dynamics of adsorption/desorption and the consequences of not waiting for true equilibrium to be achieved are topics for further study. We envisage that current production strategies that use several lateral wells could be exploited also for ESGR, whereby each well undergoes alternately Injection, Soaking and Production. In this context, the proposed proxy model could be exploited to identify optimum strategies to operate such a multi-well system.

Chapter 10

Conclusions and Future Work

10.1 Research Outcomes and Conclusions

As the production of shale gas continues to grow globally, it has become increasingly important to understand the intrinsic gas storage properties of shales. This need has been reinforced by the possibility of using injected CO_2 to simultaneously improve shale gas recovery and permanently sequester carbon within these deep geological formations. The inherent heterogeneity of shales, which manifests itself in the varying mineralogy, pore structure, and therefore adsorption capacities, within these reservoirs, makes the design of CO_2-ESGR challenging. The supercritical nature of the two relevant fluids, CO_2 and CH_4, presents an additional level of complexity, as reliable adsorption measurements at these conditions are difficult to obtain and interpret. Furthermore, adsorption models suitable for the description of supercritical adsorption data have limited predictive capability since they have been typically based on semi-empirical or simplified approaches (such as the Langmuir model) or more computationally expensive molecular simulations. Given this, one of the main aims of this thesis was to establish and implement a research workflow, shown in Figure 10.1, to evaluate a shale's potential for CO_2-ESGR, such that it could be used for practical applications and guide future research in this area.

The experimental part of the workflow is comprised of: (i) the characterisation of the shale in terms of both mineralogy and pore structure, obtained using geochemical analyses (not carried out as part of this work) and subcritical adsorption measurements with N_2, Ar and CO_2, and (ii) high pressure (0–300 bar) and temperature (up to 80 °C) supercritical adsorption measurements with CO_2 and CH_4 (which addresses the first research objective discussed in Chapter 1). While the former provides various textural properties of the adsorbent, the latter can be used to obtain the Gas-in-Place of the reservoir directly, yields insights about the primary recovery of CH_4, and quantifies the selectivity

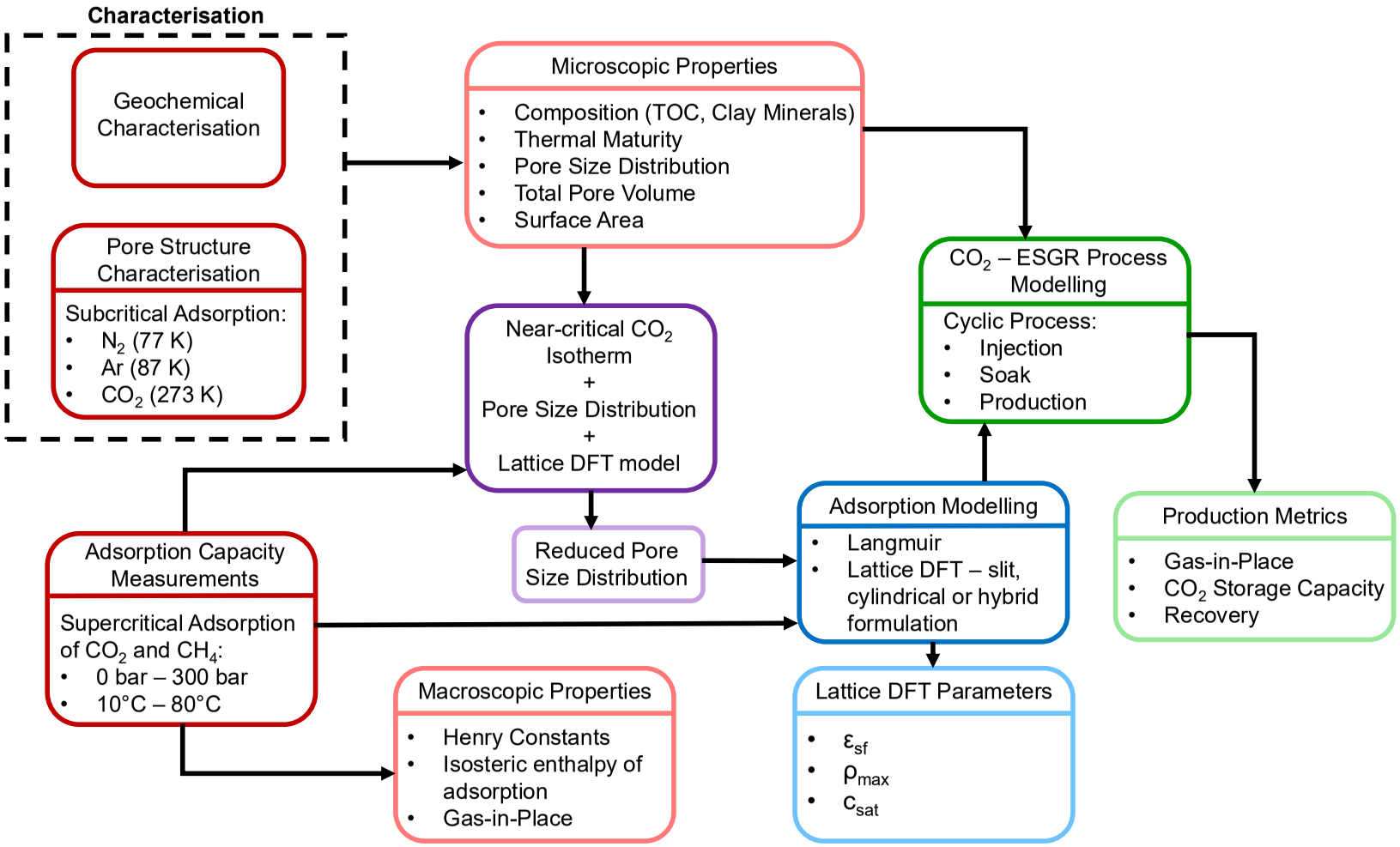

Figure 10.1: Research workflow used as part of this thesis.

for CO_2 over CH_4. The adsorption modelling approaches used in this research were predominantly based on the lattice DFT model, which has been extended to cylindrical pores and hybrid systems encompassing both slit and cylindrical pores (addressing the third research objective of this thesis). The model elucidates the interaction energies between the adsorbent surfaces (carbon or clays) and each fluid (ε_{sf}), the maximum fluid density in the pores (ρ_{max}), and the degree of occupancy of the total pore volume by the adsorbed phase (c_{sat}). The lattice DFT model's predictive capability represents a significant departure from more simplified modelling approaches. The modelled isotherms can then be used within the CO_2-ESGR cyclic process model to obtain the CH_4 recovery and CO_2 storage capacity. In this work, the binary Langmuir model was used to describe competitive adsorption due to its simplicity but, in principle, any model can be integrated within the process model.

In this thesis, samples from three shale plays, namely the Longmaxi, Marcellus, and Bowland shales, were systematically investigated using the workflow described above. The shales vary in terms of their TOC and clay content as well their thermal maturity, and these differences were reflected in the textural characterisation and supercritical adsorption results. The total pore volume was in the range 0.02–0.05 cm^3/g, with all shales being mostly mesoporous (at an average of $\sim$ 54%), with a significant degree of microporosity ($\sim$ 12% on average). The textural properties, including specific surface area, micropore, mesopore, and total pore volume were positively correlated with the organic content of the shale, irrespective of its thermal maturity. The same was also true for the Bowland shales and their clay content, while, conversely, a negative correlation with clay was obtained with the more thermally mature Longmaxi and Marcellus shales. The TOC was also identified as the strongest controlling influence on the supercritical adsorption measurements of both CO_2 and CH_4 on the four shale samples (LG4, ML, B6 and B8) that were selected for further adsorption studies. Linear correlations of temperature, TOC and the total pore volume with the maximum excess adsorbed amount were obtained indicating that these factors can also be used to predict adsorption capacities in a given shale by appropriate extrapolation or interpolation (meeting the second research objective identified in Chapter 1 of this thesis). The supercritical adsorption capacities were in the range $\sim$ 100–400 µmol/g (CO_2) and $\sim$ 30–200 µmol/g (CH_4) at 40 °C, with CO_2 adsorbing more than CH_4 at all temperatures for all shales.

The workflow was also validated on three synthetic adsorbents, mesoporous carbon (MC), microporous activated carbon (AC), and mesoporous zeolite (MZ). The rationale behind these analyses was that the porous carbons can be considered analogues of the TOC in shale and that MZ most closely replicates the pore size distribution of shales, although these model sorbents have a much higher adsorption capacity than shale. A key message from this work is that the supercritical adsorption isotherms also reveal some of the same features as the subcritical adsorption isotherms. The microporous AC showed steep uptakes at lower pressures with almost a linear decrease after the maximum in its

excess isotherms. MC's isotherms had a more gradual uptake at low densities, an excess adsorption isotherm peak that was obtained at a higher bulk density than AC, and a non-linear descent at high pressures. MZ, which includes both micro- and meso-pores, combined both these effects, especially for its supercritical CO_2 isotherms, where the experimental temperature is closer to the critical point, and pore size effects manifest themselves visibly in the isotherm shape. This particular characteristic of the CO_2 isotherms was exploited when the near-critical isotherm (at 35 °C–40 °C) was combined with the lattice DFT model to illuminate the dominant pore sizes that most strongly contribute to adsorption. This reduced discrete pore size distribution was then used in the model to successfully describe the full experimental dataset.

The synthetic adsorbents serve as important benchmarks to understand supercritical adsorption in mesoporous materials. The analysis on the shale measurements was routinely supplemented by the synthetic adsorbents and the results of the same workflow applied to measurements on pure Illite from another study. The primary aim here was to evaluate whether these 'idealised' sorbents could predict some of the adsorption behaviour in shale. This was first tested when the textural properties of these synthetic sorbents were scaled based on either the TOC or the clay content, and compared to the same properties of shale. The results showed that the micro/meso-porous carbons were a better predictor of the properties of shale, supporting the earlier indication of the TOC being such a strong influence on adsorption in shale. Another use of these materials was when their lattice DFT modelled CO_2 and CH_4 supercritical adsorption isotherms were combined based on the composition (clays and TOC) of each shale to create synthetic isotherms. Good agreement was observed between these and the experimental shale measurements at 40 °C, indicating the utility of these model materials as powerful representatives of the major adsorbing components in heterogeneous shales. Finally, the experimental supercritical adsorption isotherms of the shales were modelled without the use of each shale's individual pore size distribution. Instead, the reduced discrete PSD attained from the lattice DFT model and the near-critical CO_2 isotherms of MC, AC and Illite was combined based on the TOC and clay volumetric fractions in each shale and used within the hybrid formulation of the lattice DFT model. An excellent description of the results was obtained using this approach and the clear difference in the adsorption behaviour between a slit and a cylindrical pore was apparent. Collectively, these findings indicate that the use of these 'idealised' adsorbents, which integrate variation in adsorption surface and pore morphology, can be extended to shales beyond this study to even avoid some of the challenging and time-consuming experimental adsorption work associated with shales, once their composition is known.

The final part of the workflow is the process model of the CO_2-ESGR process (the last research objective of this thesis). The model is based on the cyclic injection of CO_2 in a shale reservoir, with each cycle having three stages (Injection, Soak and Production). Excess adsorption was included

within the analysis to quantify accurately the free gas and, by extension, the Gas-in-Place and CO_2 storage capacity. With CO_2 injection, the increase in CH_4 recovery relative to primary extraction was 150% and about 55% of the injected CO_2 was stored within the reservoir over 5 cycles. Both competitive adsorption and CH_4 partial pressure reduction due to gas injection are exploited as part of this process, which was further confirmed by comparison with the injection of N_2. These results demonstrate that CO_2-ESGR is feasible, has significant benefits, and that adsorption plays a dominant role in these reservoirs in both their original condition and their optimal production.

In summary, this thesis has provided new insights into supercritical adsorption of CO_2 and CH_4 at elevated pressures, by focusing on the distinct behaviour in micro- and meso-porous adsorbents. Validating the research workflow on a major class of materials like porous carbons, which have widespread applications, demonstrates the utility of this approach. In the context of shales, four samples were systematically investigated through a full characterisation, high pressure adsorption experiments and modelling. The reliability of these inherently challenging experimental measurements was extended by a methodical experimental procedure involving repeated degassing and multiple Helium measurements. It was recurrently observed that the shale would undergo some change as a result of exposure to supercritical fluids at elevated pressures, whereby some gas was permanently locked within its pores. All experimental data were well described by variations of a new, extended lattice DFT model that depicts adsorption on a pore-by-pore basis. Valuable thermodynamic parameters such as Henry constants and the isosteric heat of adsorption were also ascertained by both the experiments and the model. Finally, the CO_2-ESGR process was modelled through a cyclic injection process. These research achievements are in line with the original thesis objectives set out in Chapter 1.

The extensive workflow presented might lead practitioners in the field to question where to focus their attention most when evaluating a shale play. Although the geochemical characterisation was not carried out as part of this work, it serves as an extremely useful means of understanding and predicting the adsorption behaviour in a shale. Across the analyses, the most accurate predictor was the TOC content. This, and if available, the total pore volume, can lead to a reasonable estimation of the supercritical adsorption capacity of CO_2 and CH_4 on a given shale at reservoir conditions. Although the supercritical adsorption measurements with shale are the most useful in terms of evaluating the economic value of a shale play, they are time-consuming and complicated. In the absence of these measurements, this research has shown that the results from porous carbons and pure clay minerals can be used together with the measured shale mineralogy to predict (synthetic) shale isotherms. These can be easily integrated into a reservoir model and used to both estimate the GIP and design optimal combined CH_4 production and CO_2 storage processes.

10.2 Future Work

The following sections highlight some recommended areas for further research.

10.2.1 Binary Adsorption of CO_2 and CH_4 in Shale

One of the main driving forces behind CO_2-ESGR is the competitive adsorption between CO_2 and CH_4. The binary Langmuir isotherm was used for this purpose in the ESGR model described in Chapter 9. When CO_2 is injected into a shale reservoir, some CH_4 will desorb as some CO_2 adsorbs. The bulk phase will now be made up of both gases, and this will affect the adsorption of both gases on shale. Confirming the selectivity of shale towards CO_2 is one of the most fundamental prerequisites of designing such a process. The measurement of adsorption using mixtures is very difficult [265], which is why there are very few studies [281, 256] that report these measurements on shales. Binary adsorption has been measured using the MSB before [218, 183], so the same methodology could be considered for these measurements with shales too. The sole additional measurement required, which only needs to be performed once, is that of the void volume of the entire system. This can be determined using gas expansion with Helium or Argon, when the adsorbent is not present in the system. A small pressure vessel can be connected to the MSB system such that it can be decoupled easily using an isolation valve. The MSB can be filled with the gas and then the gas can be allowed to expand into the small vessel. The procedure can then be repeated when the small vessel's volume is reduced by a known amount (e.g. by filling it with spherical balls, each with a known volume). By measuring the fluid density before and after the expansion in both cases, the void volume of the MSB system can be determined. The overall process can be repeated several times by evacuating the system and using different initial pressures to reduce the uncertainty on the calculated void volume [282]. Otherwise, the same experimental procedure as for the pure component measurements described in this thesis can be used. Between various feed gas compositions, it is advisable to regenerate the sample and evacuate the system such that the feed composition is known precisely each time and measurement uncertainties do not accumulate. The analysis of the experimental measurements will be more complex in this case, however. The equilibrium gas phase composition can be obtained using a suitable equation of state. Alternatively, calibration curves (with no adsorbent) can be generated, involving density measurements of multiple feed gas compositions at various fixed pressure and temperature points. A Virial equation of state can then be fitted to this data [218]. The challenge with the shale measurements would be to produce enough of a change in the bulk phase composition from the feed, as their level of adsorption is relatively low. This could potentially be achieved by increasing the amount of shale in the MSB, beyond just the sample basket capacity, thereby effectively boosting the amount of adsorption.

The experimental data also need to be described by suitable adsorption models, such that they can be integrated with the CO_2-ESGR process model. The lattice DFT has been previously extended to describe competitive adsorption [150, 283] and could be considered for shales, as well. The concept of the fluid-fluid interaction energy has to be broadened to include interactions between neighbouring CO_2 and CH_4 molecules. The same approach that was used in this thesis could be utilised whereby the slit and cylindrical pores have independent surface interaction energies.

A similar workflow as Figure 10.1 could be developed for these binary gas measurements, that could first be validated with the synthetic adsorbents to ensure reliability of the experimental and modelling approaches. Although the interaction between CO_2 and CH_4 is of primary interest, other fluid pairs could also be investigated such as CH_4–C_2H_6, CO_2–C_2H_6, CH_4–N_2, or ternary mixtures eventually.

10.2.2 Supercritical Adsorption of Ethane

In Section 2.4, it was highlighted that shale gas contains hydrocarbons other than just CH_4, including up to about 1% of C_2H_6. It would be really valuable to replicate the workflow used with CO_2 and CH_4 with ethane, as the latter has a critical point (T_c = 305.3 K [284]) similar to CO_2 and much closer to temperatures encountered in shale reservoirs. This would be interesting even from a purely scientific perspective as the near-critical behaviour observed with CO_2 on mostly micro- and meso-porous materials (such as AC and MC) could also potentially be seen with this hydrocarbon. As these isotherms with CO_2 were used to obtain the principal pore sizes influencing adsorption the most, C_2H_6 isotherms could be used to determine the pore sizes most relevant for adsorption specifically with hydrocarbons. Additionally, there are very few studies that report ethane isotherms on shales at elevated pressures and temperatures [285, 286]. The experimental and modelling approaches described here would require very little modifications to address this significant research gap.

10.2.3 Supercritical Adsorption on Hydrated Shales

At subsurface conditions, shale can be considered 'wet', interacting with hydrocarbons and brines [287]. Analagous to coal, swelling due to interaction with water has been reported on shale [288, 289], and consequently, it is very important to understand the adsorption behaviour in these reservoirs under hydrated conditions. Clay minerals, in particular, can interact strongly with water [290], due to the expansion of their interlayer spacing in the presence of water [291, 292]. This phenomenon is particularly relevant to swelling clay minerals, such as Smectite [292]. Research has shown that CO_2 and CH_4 can access this expanded interlayer spacing of hydrated Smectite [293, 294, 295], yet water also competes with both fluids for adsorption sites [296]. Both these factors suggest that adsorption

capacities under hydrated conditions will differ from shales in their dry state. The effect of water on adsorption in shales has been highlighted by a few studies [297, 298], but measurements at supercritical conditions are lacking. A challenge is that these systems (CH_4-H_2O or CO_2-H_2O) do not necessarily follow Raoult's law, and therefore the equilibrium partial pressure of water could be substantially different from the vapour pressure of pure water at the same temperature.

To investigate the effect of water on gas adsorption in shale at supercritical conditions, the MSB system can be utilised. The primary concern would be to first saturate the shale with water externally, quantify the amount of pre-adsorbed water, and then maintain this level of humidity while still being able to evacuate the system, which may be possible if vacuum was pulled gently and quickly. CO_2 and CH_4 isotherms at various temperatures could then be measured, as normal, but the excess adsorbed amount would now be given by the following equation:

$$n^{\mathrm{ex}} = \frac{\mathrm{MP}_1(\rho_{\mathrm{b}}, T) - \mathrm{MP}_{1,0} + \rho_{\mathrm{b}}(V_0 + V_{\mathrm{w}})}{M_{\mathrm{w}}(m_{\mathrm{s}} + m_{\mathrm{w}})} \tag{10.1}$$

where V_{w} and m_{w} are the volume and the mass of the pre-adsorbed water, respectively (in contrast with Eq. 3.3b, which is the corresponding equation for a dry sample). The sums $V_0 + V_{\mathrm{w}}$ and $m_{\mathrm{s}} + m_{\mathrm{w}}$ would still be obtained via the Helium measurement. At the end of the experiments, the sample could be properly degassed to determine m_{w} explicitly (by comparing the vacuum points before and after). The underlying assumption during all these experiments would be that the amount of pre-adsorbed water does not change with increasing pressure. The lattice DFT model could then be used to describe the data and determine the amount of increased (micro-)pore volume that occurs as a result of hydration of the shale. A study using the experimental and modelling approach described here was recently carried out with pure clay minerals [299]. Extending this work to shales would be extremely valuable.

Extension of the current research to include the three areas described in Sections 10.2.1–10.2.3 would enable the workflow (Figure 10.1) to be adapted to even more realistic shale gas reservoir conditions.

Bibliography

[1] H. Ansari, E. Rietmann, L. Joss, J. P. M. Trusler, G. Maitland, and R. Pini, "A shortcut pressure swing adsorption analogue model to estimate Gas-in-Place and CO2 storage potential of gas shales," *Fuel*, vol. 301, p. 121014, 2021.

[2] International Energy Agency, "Putting CO2 to use," report, International Energy Agency, 2019.

[3] M. Melikoglu, "Shale gas: Analysis of its role in the global energy market," *Renewable and Sustainable Energy Reviews*, vol. 37, pp. 460–468, 2014.

[4] Q. Wang, X. Chen, A. N. Jha, and H. Rogers, "Natural gas from shale formation - The evolution, evidences and challenges of shale gas revolution in United States," *Renewable and Sustainable Energy Reviews*, vol. 30, pp. 1–28, 2014.

[5] J. Cooper, L. Stamford, and A. Azapagic, "Shale gas: A review of the economic, environmental, and social sustainability," *Energy Technology*, vol. 4, no. 7, pp. 772–792, 2016.

[6] R. Pini, "Assessing the adsorption properties of mudrocks for CO2 sequestration," *Energy Procedia*, vol. 63, pp. 5556–5561, 2014.

[7] X. Cui, A. M. M. Bustin, and R. M. Bustin, "Measurements of gas permeability and diffusivity of tight reservoir rocks: different approaches and their applications," *Geofluids*, vol. 9, no. 3, pp. 208–223, 2009.

[8] B. K. Sovacool, "Cornucopia or curse? Reviewing the costs and benefits of shale gas hydraulic fracturing (fracking)," *Renewable and Sustainable Energy Reviews*, vol. 37, pp. 249–264, 2014.

[9] EIA, "Technically recoverable shale oil and shale gas resources: An assessment of 137 shale formations in 41 countries outside the United States," report, U.S. Energy Information Administration, 2013.

[10] R. Sandrea and I. Sandrea, "New well-productivity data provides US shale potential insights," *Oil & Gas Journal*, vol. 112, no. 11, 2014.

[11] R. Pini, G. Storti, and M. Mazzotti, "A model for enhanced coal bed methane recovery aimed at carbon dioxide storage," *Adsorption*, vol. 17, no. 5, pp. 889–900, 2011.

[12] M. Godec, G. Koperna, R. Petrusak, and A. Oudinot, "Potential for enhanced gas recovery and CO2 storage in the Marcellus Shale in the Eastern United States," *International Journal of Coal Geology*, vol. 118, pp. 95–104, 2013.

[13] X. Li and D. Elsworth, "Geomechanics of CO2 enhanced shale gas recovery," *Journal of Natural Gas Science and Engineering*, vol. 26, pp. 1607–1619, 2015.

[14] Z. Tao and A. Clarens, "Estimating the carbon sequestration capacity of shale formations using methane production rates," *Environmental Science & Technology*, vol. 47, no. 19, pp. 11318–11325, 2013.

[15] R. Xu, K. Zeng, C. Zhang, and P. Jiang, "Assessing the feasibility and CO2 storage capacity of CO2 enhanced shale gas recovery using Triple-Porosity reservoir model," *Applied Thermal Engineering*, vol. 115, pp. 1306–1314, 2017.

[16] IPCC, "Climate change 2014: Synthesis report. contribution of working groups I, II and III to the fifth assessment report of the Intergovernmental Panel on Climate Change," report, 2014.

[17] International Energy Agency, "Technology roadmap: Carbon capture and storage 2013," report, International Energy Agency, 2013.

[18] International Energy Agency, "Energy and climate change - world energy outlook special report," report, International Energy Agency, 2015.

[19] A. R. Brandt, G. A. Heath, E. A. Kort, F. O'Sullivan, G. Petron, S. M. Jordaan, P. Tans, J. Wilcox, A. M. Gopstein, D. Arent, S. Wofsy, N. J. Brown, R. Bradley, G. D. Stucky, D. Eardley, and R. Harriss, "Energy and environment. methane leaks from North American natural gas systems," *Science*, vol. 343, no. 6172, pp. 733–5, 2014.

[20] EIA, "How much carbon dioxide is produced when different fuels are burned?," 2016.

[21] N. Hirst, C. S. Khor, and S. Buckle, "Shale gas and climate change," report, Imperial College London, 2013.

[22] EIA, "U.S. energy-related CO2 emissions in early 2012 lowest since 1992," *Today in Energy*, no. 3rd May, 2012.

[23] M. Godec, G. Koperna, R. Petrusak, and A. Oudinot, "Enhanced gas recovery and CO2 storage in gas shales: A summary review of its status and potential," *Energy Procedia*, vol. 63, pp. 5849–5857, 2014.

[24] R. W. J. Edwards, M. A. Celia, K. W. Bandilla, F. Doster, and C. M. Kanno, "A model to estimate carbon dioxide injectivity and storage capacity for geological sequestration in shale gas wells," *Environmental Science & Technology*, vol. 49, no. 15, pp. 9222–9229, 2015.

[25] K. Louk, N. Ripepi, K. Luxbacher, E. Gilliland, X. Tang, C. Keles, C. Schlosser, E. Diminick, S. Keim, J. Amante, and K. Michael, "Monitoring CO2 storage and enhanced gas recovery in unconventional shale reservoirs: Results from the Morgan County, Tennessee injection test," *Journal of Natural Gas Science and Engineering*, vol. 45, pp. 11–25, 2017.

[26] P. Charoensuppanimit, S. A. Mohammad, and K. A. M. Gasem, "Measurements and modeling of gas adsorption on shales," *Energy & Fuels*, vol. 30, no. 3, pp. 2309–2319, 2016.

[27] S. Merey and C. Sinayuc, "Analysis of carbon dioxide sequestration in shale gas reservoirs by using experimental adsorption data and adsorption models," *Journal of Natural Gas Science and Engineering*, vol. 36, Part A, pp. 1087–1105, 2016.

[28] H. Ansari, L. Joss, M. Trusler, G. Maitland, C. Delle Piane, and R. Pini, "Enhanced shale gas recovery: Gas sorption controls on recoverable gas and CO2 storage capacity," in *14th Greenhouse Gas Control Technologies Conference (GHGT-14)*, 2018.

[29] H. Ansari, L. Joss, J. Hwang, J. P. M. Trusler, G. Maitland, and R. Pini, "Supercritical adsorption in micro- and meso-porous carbons and its utilisation for textural characterisation," *Microporous and Mesoporous Materials*, vol. 308, p. 110537, 2020.

[30] T. Zeller Jr., "Does anyone really know how long the shale gas boom will last?," *Forbes*, 9th May 2017 2015.

[31] M. Inman, "Natural gas: The fracking fallacy," *Nature*, vol. 516, no. 7529, pp. 28–30, 2014.

[32] POST, "Unconventional gas," report, Houses of Parliament, 2011.

[33] M. H. Stephenson, "Shale gas in North America and Europe," *Energy Science & Engineering*, vol. 4, no. 1, pp. 4–13, 2016.

[34] J. Speirs, "Shale gas: What do the estimates mean?," 2013.

[35] EIA, "Shale gas production drives world natural gas production growth," *Today in Energy*, 2016.

[36] EIA, "Natural gas explained," 2021.

[37] V. A. Kuuskraa, *Natural Gas Resources, Unconventional*, pp. 257–272. New York: Elsevier, 2004.

[38] B. Law and C. Spencer, "Gas in tight reservoirs - an emerging major source of energy," *United States Geological Survey, Professional Paper; (United States)*, pp. Medium: X; Size: Pages: 233–252, 1993.

[39] P. Cook, V. Beck, D. Brereton, R. Clark, B. Fisher, S. Kentish, J. Toomey, and J. Williams, "Engineering energy: Unconventional gas production," report, Australian Council of Learned Academies, 2013.

[40] D. M. Kargbo, R. G. Wilhelm, and D. J. Campbell, "Natural gas plays in the Marcellus shale: Challenges and potential opportunities," *Environmental Science & Technology*, vol. 44, no. 15, pp. 5679–5684, 2010.

[41] M. K. Fisher, J. R. Heinze, C. D. Harris, B. M. Davidson, C. A. Wright, and K. P. Dunn, "Optimizing horizontal completion techniques in the Barnett shale using microseismic fracture mapping," 2004.

[42] Royal Society and Royal Academy of Engineering, "Shale gas extraction in the UK: a review of hydraulic fracturing," report, 2012.

[43] J. D. Arthur, B. Bohm, and M. Layne, "Hydraulic fracturing considerations for natural gas wells of the Marcellus shale," 2008.

[44] J. D. Arthur, B. K. Bohm, B. J. Coughlin, M. A. Layne, and D. Cornue, "Evaluating the environmental implications of hydraulic fracturing in shale gas reservoirs," 2009.

[45] G. P. Hammond and A. O'Grady, "Indicative energy technology assessment of UK shale gas extraction," *Applied Energy*, vol. 185, Part 2, pp. 1907–1918, 2017.

[46] A. Burnham, J. Han, C. E. Clark, M. Wang, J. B. Dunn, and I. Palou-Rivera, "Life-cycle greenhouse gas emissions of shale gas, natural gas, coal, and petroleum," *Environmental Science & Technology*, vol. 46, no. 2, pp. 619–627, 2012.

[47] L. Whitmarsh, N. Nash, P. Upham, A. Lloyd, J. P. Verdon, and J. M. Kendall, "UK public perceptions of shale gas hydraulic fracturing: The role of audience, message and contextual factors on risk perceptions and policy support," *Applied Energy*, vol. 160, pp. 419–430, 2015.

[48] M. O. Eshkalak, E. W. Al-shalabi, A. Sanaei, U. Aybar, and K. Sepehrnoori, "Enhanced gas recovery by CO2 sequestration versus re-fracturing treatment in unconventional shale gas reservoirs," 2014.

[49] P. M. Jarrell, C. E. Fox, M. H. Stein, and S. L. Webb, *Practical aspects of CO2 flooding*, vol. 22. Society of Petroleum Engineers Richardson, TX, 2002.

[50] B. Nuttall, "Reassessment of CO2 sequestration capacity and enhanced gas recovery potential of middle and upper Devonian Black Shales in the Appalachian Basin, MRCSP Phase II topical report," report, Kentucky Geological Survey, 2010.

[51] E. Fathi and I. Y. Akkutlu, "Multi-component gas transport and adsorption effects during CO2 injection and enhanced shale gas recovery," *International Journal of Coal Geology*, vol. 123, pp. 52–61, 2014.

[52] K. C. Schepers, B. C. Nuttall, A. Y. Oudinot, and R. J. Gonzalez, "Reservoir modeling and simulation of the Devonian gas shale of Eastern Kentucky for enhanced gas recovery and CO2 storage," 2009.

[53] W. Yu, E. W. Al-Shalabi, and K. Sepehrnoori, "A sensitivity study of potential CO2 injection for enhanced gas recovery in Barnett shale reservoirs," 2014.

[54] M. Josh, L. Esteban, C. Delle Piane, J. Sarout, D. N. Dewhurst, and M. B. Clennell, "Laboratory characterisation of shale properties," *Journal of Petroleum Science and Engineering*, vol. 88-89, pp. 107–124, 2012.

[55] G. R. Chalmers, R. M. Bustin, and I. M. Power, "Characterization of gas shale pore systems by porosimetry, pycnometry, surface area, and field emission scanning electron microscopy/transmission electron microscopy image analyses: Examples from the Barnett, Woodford, Haynesville, Marcellus, and Doig units," *AAPG Bulletin*, vol. 96, no. 96, pp. 1099–1119, 2012.

[56] T. Dong, N. B. Harris, K. Ayranci, C. E. Twemlow, and B. R. Nassichuk, "The impact of composition on pore throat size and permeability in high maturity shales: Middle and Upper Devonian Horn River Group, northeastern British Columbia, Canada," *Marine and Petroleum Geology*, vol. 81, pp. 220–236, 2017.

[57] D. B. Shaw and C. E. Weaver, "The mineralogical composition of shales," *Journal of Sedimentary Research*, vol. 35, no. 1, pp. 213–222, 1965.

[58] D. J. K. Ross and R. M. Bustin, "The importance of shale composition and pore structure upon gas storage potential of shale gas reservoirs," *Marine and Petroleum Geology*, vol. 26, no. 6, pp. 916–927, 2009.

[59] C. Wu, J. Tuo, L. Zhang, M. Zhang, J. Li, Y. Liu, and Y. Qian, "Pore characteristics differences between clay-rich and clay-poor shales of the Lower Cambrian Niutitang Formation in the Northern Guizhou area, and insights into shale gas storage mechanisms," *International Journal of Coal Geology*, vol. 178, pp. 13–25, 2017.

[60] M. M. Labani, R. Rezaee, A. Saeedi, and A. A. Hinai, "Evaluation of pore size spectrum of gas shale reservoirs using low pressure nitrogen adsorption, gas expansion and mercury porosimetry: A case study from the Perth and Canning Basins, Western Australia," *Journal of Petroleum Science and Engineering*, vol. 112, pp. 7–16, 2013.

[61] P. Zhang, S. Lu, J. Li, P. Zhang, L. Xie, H. Xue, and J. Zhang, "Multi-component segmentation of X-ray computed tomography (CT) image using multi-Otsu thresholding algorithm and scanning electron microscopy," *Energy Exploration & Exploitation*, vol. 35, no. 3, pp. 281–294, 2017.

[62] Z. Horvath and K. Jackson, "Procedure for the isolation of kerogen from sedimentary rocks," report, Bureau of Mineral Resources, Geology and Geophysics, 1981.

[63] M. Vandenbroucke, "Kerogen: from types to models of chemical structure," *Oil & Gas Science and Technology - Rev. IFP*, vol. 58, no. 2, pp. 243–269, 2003.

[64] K. McCarthy, K. Rojas, M. Niemann, D. Palmowski, K. Peters, and A. Stankiewicz, "Basic petroleum geochemistry for source rock evaluation," *Oilfield Review*, vol. 23, no. 2, pp. 32–43, 2011.

[65] M. M. El Nady and M. M. Hammad, "Organic richness, kerogen types and maturity in the shales of the Dakhla and Duwi formations in Abu Tartur area, Western Desert, Egypt: Implication of RockEval pyrolysis," *Egyptian Journal of Petroleum*, vol. 24, no. 4, pp. 423–428, 2015.

[66] D. Cristancho-Albarracin, I. Y. Akkutlu, L. J. Criscenti, and Y. Wang, "Shale gas storage in kerogen nanopores with surface heterogeneities," *Applied Geochemistry*, vol. 84, pp. 1–10, 2017.

[67] T. Zhang, G. S. Ellis, S. C. Ruppel, K. Milliken, and R. Yang, "Effect of organic-matter type and thermal maturity on methane adsorption in shale-gas systems," *Organic Geochemistry*, vol. 47, pp. 120–131, 2012.

[68] Z. Zhai, X. Wang, X. Jin, L. Sun, J. Li, and D. Cao, "Adsorption and diffusion of shale gas reservoirs in modeled clay minerals at different geological depths," *Energy & Fuels*, vol. 28, no. 12, pp. 7467–7473, 2014.

[69] S. Chen, Y. Han, C. Fu, h. Zhang, Y. Zhu, and Z. Zuo, "Micro and nano-size pores of clay minerals in shale reservoirs: Implication for the accumulation of shale gas," *Sedimentary Geology*, vol. 342, pp. 180–190, 2016.

[70] K. Han, Y. Ju, G. Wang, S. Bao, H. Bu, and B. Neupane, "Shale composition and pore structure variations in the progradation direction: A case study of transitional shales in the Xu-Huai

district, southern North China," *Journal of Natural Gas Science and Engineering*, vol. 36, Part B, pp. 1178–1187, 2016.

[71] T. Zhang, G. S. Ellis, S. C. Ruppel, K. Milliken, M. Lewan, and X. Sun, "Effect of organic matter properties, clay mineral type and thermal maturity on gas adsorption in organic-rich shale systems," 2013.

[72] J. Hwang and R. Pini, "Supercritical CO2 and CH4 uptake by illite-smectite clay minerals," *Environmental Science & Technology*, vol. 53, no. 19, pp. 11588–11596, 2019.

[73] U. Kuila and M. Prasad, "Specific surface area and pore-size distribution in clays and shales," *Geophysical Prospecting*, vol. 61, no. 2, pp. 341–362, 2013.

[74] A. M. M. Bustin, R. M. Bustin, and X. Cui, "Importance of fabric on the production of gas shales," 2008.

[75] A. M. M. Bustin and R. M. Bustin, "Importance of rock properties on the producibility of gas shales," *International Journal of Coal Geology*, vol. 103, pp. 132–147, 2012.

[76] R. Fink, B. M. Krooss, Y. Gensterblum, and A. Amann-Hildenbrand, "Apparent permeability of gas shales - Superposition of fluid-dynamic and poro-elastic effects," *Fuel*, vol. 199, pp. 532–550, 2017.

[77] A. A. Hinai, R. Rezaee, L. Esteban, and M. Labani, "Comparisons of pore size distribution: A case from the Western Australian gas shale formations," *Journal of Unconventional Oil and Gas Resources*, vol. 8, pp. 1–13, 2014.

[78] Y. Tan, Z. Pan, J. Liu, Y. Wu, A. Haque, and L. D. Connell, "Experimental study of permeability and its anisotropy for shale fracture supported with proppant," *Journal of Natural Gas Science and Engineering*, vol. 44, pp. 250–264, 2017.

[79] G. R. L. Chalmers, D. J. K. Ross, and R. M. Bustin, "Geological controls on matrix permeability of Devonian Gas Shales in the Horn River and Liard basins, northeastern British Columbia, Canada," *International Journal of Coal Geology*, vol. 103, pp. 120–131, 2012.

[80] M. Liang, Z. Wang, L. Gao, C. Li, and H. Li, "Evolution of pore structure in gas shale related to structural deformation," *Fuel*, vol. 197, pp. 310–319, 2017.

[81] J. Zeng, W. Jia, P. Peng, C. Guan, C. Zhou, X. Yuan, S. Chen, and C. Yu, "Composition and pore characteristics of black shales from the Ediacaran Lantian Formation in the Yangtze Block, South China," *Marine and Petroleum Geology*, vol. 76, pp. 246–261, 2016.

[82] C. R. Clarkson, N. Solano, R. M. Bustin, A. M. M. Bustin, G. R. L. Chalmers, L. He, Y. B. Melnichenko, A. P. Radliński, and T. P. Blach, "Pore structure characterization of North American shale gas reservoirs using USANS/SANS, gas adsorption, and mercury intrusion," *Fuel*, vol. 103, pp. 606–616, 2013.

[83] J. Rouquerol, D. Avnir, C. Fairbridge, D. Everett, J. Haynes, N. Pernicone, J. Ramsay, K. Sing, and K. Unger, "Recommendations for the characterization of porous solids (Technical Report)," *Pure and Applied Chemistry*, vol. 66, no. 8, pp. 1739–1758, 1994.

[84] C. R. Clarkson and R. M. Bustin, "Variation in micropore capacity and size distribution with composition in bituminous coal of the Western Canadian Sedimentary Basin," *Fuel*, vol. 75, no. 13, pp. 1483–1498, 1996.

[85] R. M. Bustin and C. R. Clarkson, "Geological controls on coalbed methane reservoir capacity and gas content," *International Journal of Coal Geology*, vol. 38, no. 12, pp. 3–26, 1998.

[86] K. Bruner and R. Smosna, "A comparative study of the Mississippian Barnett Shale, Fort Worth basin, and Devonian Marcellus shale, Appalachian basin," report, National Energy Technology Laboratory (NETL), US Department of Energy (USDOE), 2011.

[87] T. Pitakbunkate, P. B. Balbuena, G. J. Moridis, and T. A. Blasingame, "Effect of confinement on pressure/volume/temperature properties of hydrocarbons in shale reservoirs," *SPE Journal*, vol. 21, no. 02, p. 621634, 2016.

[88] M. J. Kaiser, "Louisiana Haynesville shale-1: Characteristics, production potential of Haynesville shale wells described," *Oil & Gas Journal*, vol. 109, no. 49, pp. 68–79, 2011.

[89] M. Zhang, Q. Tang, C. Cao, Z. Lv, T. Zhang, D. Zhang, Z. Li, and L. Du, "Molecular and carbon isotopic variation in 3.5 years shale gas production from Longmaxi Formation in Sichuan Basin, China," *Marine and Petroleum Geology*, 2017.

[90] Z. Feng, D. Liu, S. Huang, W. Wu, D. Dong, W. Peng, and e. Han, "Carbon isotopic composition of shale gas in the Silurian Longmaxi Formation of the Changning area, Sichuan Basin," *Petroleum Exploration and Development*, vol. 43, no. 5, pp. 769–777, 2016.

[91] K. Bullin and P. Krouskop, "Composition variety complicates processing plans for US shale gas," *Oil & Gas Journal*, vol. 107, no. 10, pp. 50–55, 2009.

[92] Z. Qu, J. Sun, J. Shi, Z. Zhan, Y. Zou, and P. Peng, "Characteristics of stable carbon isotopic composition of shale gas," *Journal of Natural Gas Geoscience*, vol. 1, no. 2, pp. 147–155, 2016.

[93] B. A. Haider and K. Aziz, "Impact of capillary pressure and critical property shift due to confinement on hydrocarbon production in shale reservoirs," 2017.

[94] B. Didar and I. Akkutlu, "Pore-size dependence of fluid phase behavior and the impact on shale gas reserves," 2013.

[95] Y. Ma, L. Jin, and A. Jamili, "Modifying van der waals equation of state to consider influence of confinement on phase behavior," 2013.

[96] K. Zhang, M. Wang, Q. Liu, K. Wu, L. Yu, J. Zhang, and S. Chen, "Effects of adsorption and confinement on shale gas production behavior," 2015.

[97] L. Jin, Y. Ma, and A. Jamili, "Investigating the effect of pore proximity on phase behavior and fluid properties in shale formations," 2013.

[98] S. Luo, J. L. Lutkenhaus, and H. Nasrabadi, "Experimental study of confinement effect on hydrocarbon phase behavior in nano-scale porous media using Differential Scanning Calorimetry," 2015.

[99] M. Alfi, H. Nasrabadi, and D. Banerjee, "Experimental investigation of confinement effect on phase behavior of hexane, heptane and octane using lab-on-a-chip technology," *Fluid Phase Equilibria*, vol. 423, pp. 25–33, 2016.

[100] B. R. Didar and I. Y. Akkutlu, "Confinement effects on hydrocarbon mixture phase behavior in organic nanopore," 2015.

[101] R. J. Ambrose, R. C. Hartman, M. Diaz Campos, I. Y. Akkutlu, and C. Sondergeld, "New pore-scale considerations for shale gas in place calculations," 2010.

[102] A. Leahy-Dios, M. Das, A. Agarwal, and R. D. Kaminsky, "Modeling of transport phenomena and multicomponent sorption for shale gas and coalbed methane in an unstructured grid simulator," 2011.

[103] F. Hao, H. Zou, and Y. Lu, "Mechanisms of shale gas storage: Implications for shale gas exploration in China," *AAPG bulletin*, vol. 97, no. 8, pp. 1325–1346, 2013.

[104] L. Ma, K. G. Taylor, P. D. Lee, K. J. Dobson, P. J. Dowey, and L. Courtois, "Novel 3D centimetre-to nano-scale quantification of an organic-rich mudstone: The Carboniferous Bowland Shale, Northern England," *Marine and Petroleum Geology*, vol. 72, pp. 193–205, 2016.

[105] X.-C. Lu, F.-C. Li, and A. T. Watson, "Adsorption measurements in Devonian shales," *Fuel*, vol. 74, no. 4, pp. 599–603, 1995.

[106] S. Montgomery, D. Jarvie, K. Bowker, and R. Pollastro, "Mississippian Barnett Shale, Fort Worth basin, north-central Texas: Gas-shale play with multitrillion cubic foot potential," *AAPG Bulletin*, vol. 89, pp. 155–175, 2005.

[107] C. M. Freeman, G. J. Moridis, D. Ilk, and T. A. Blasingame, "A numerical study of performance for tight gas and shale gas reservoir systems," 2009.

[108] T. F. T. Rexer, M. J. Benham, A. C. Aplin, and K. M. Thomas, "Methane adsorption on shale under simulated geological temperature and pressure conditions," *Energy & Fuels*, vol. 27, no. 6, pp. 3099–3109, 2013.

[109] P. G. Menon, "Adsorption at high pressures," *Chemical Reviews*, vol. 68, no. 3, pp. 277–294, 1968.

[110] F. Rouquerol, J. Rouquerol, K. S. Sing, P. Llewellyn, and G. Maurin, *Adsorption by powders and porous solids: principles, methodology and applications*. Oxford, UK: Academic press, second ed., 2014.

[111] D. M. Ruthven, *Principles of adsorption and adsorption processes*. USA: John Wiley & Sons, 1984.

[112] F. E. Bartell, T. L. Thomas, and Y. Fu, "Thermodynamics of adsorption from solutions. IV. temperature dependence of adsorption," *The Journal of Physical Chemistry*, vol. 55, no. 9, pp. 1456–1462, 1951.

[113] A. L. Myers and P. A. Monson, "Adsorption in porous materials at high pressure: Theory and experiment," *Langmuir*, vol. 18, no. 26, pp. 10261–10273, 2002.

[114] M. Thommes, K. Kaneko, A. V. Neimark, J. P. Olivier, F. Rodriguez-Reinoso, J. Rouquerol, and K. S. W. Sing, "Physisorption of gases, with special reference to the evaluation of surface area and pore size distribution (IUPAC technical report)," *Pure and Applied Chemistry*, vol. 87, no. 9-10, p. 1051, 2015.

[115] T. Horikawa, D. D. Do, and D. Nicholson, "Capillary condensation of adsorbates in porous materials," *Advances in Colloid and Interface Science*, vol. 169, no. 1, pp. 40–58, 2011.

[116] G. Rother, E. G. Krukowski, D. Wallacher, N. Grimm, R. J. Bodnar, and D. R. Cole, "Pore size effects on the sorption of supercritical CO2 in mesoporous CPG-10 silica," *The Journal of Physical Chemistry C*, vol. 116, no. 1, pp. 917–922, 2012.

[117] R. Pini, "Interpretation of net and excess adsorption isotherms in microporous adsorbents," *Microporous and Mesoporous Materials*, vol. 187, pp. 40–52, 2014.

[118] S. Gumma and O. Talu, "Net adsorption: A thermodynamic framework for supercritical gas adsorption and storage in porous solids," *Langmuir*, vol. 26, no. 22, pp. 17013–17023, 2010.

[119] S. Brandani, E. Mangano, and L. Sarkisov, "Net, excess and absolute adsorption and adsorption of helium," *Adsorption*, vol. 22, no. 2, pp. 261–276, 2016.

[120] I. Suzuki, K. Kakimoto, and S. Oki, "Volumetric determination of adsorption of helium over some zeolites with a temperature-compensated, differential tensimeter having symmetrical design," *Review of Scientific Instruments*, vol. 58, no. 7, pp. 1226–1230, 1987.

[121] S. Sircar, "Measurement of gibbsian surface excess," *AIChE Journal*, vol. 47, no. 5, pp. 1169–1176, 2001.

[122] D. D. Do and H. D. Do, "Appropriate volumes for adsorption isotherm studies: The absolute void volume, accessible pore volume and enclosing particle volume," *Journal of Colloid and Interface Science*, vol. 316, no. 2, pp. 317–330, 2007.

[123] M. Gasparik, T. F. T. Rexer, A. C. Aplin, P. Billemont, G. De Weireld, Y. Gensterblum, M. Henry, B. M. Krooss, S. Liu, X. Ma, R. Sakurovs, Z. Song, G. Staib, K. M. Thomas, S. Wang, and T. Zhang, "First international inter-laboratory comparison of high-pressure CH4, CO2 and C2H6 sorption isotherms on carbonaceous shales," *International Journal of Coal Geology*, vol. 132, pp. 131–146, 2014.

[124] P. Chareonsuppanimit, S. A. Mohammad, R. L. Robinson, and K. A. M. Gasem, "High-pressure adsorption of gases on shales: Measurements and modeling," *International Journal of Coal Geology*, vol. 95, pp. 34–46, 2012.

[125] P. Weniger, W. Kalkreuth, A. Busch, and B. M. Krooss, "High-pressure methane and carbon dioxide sorption on coal and shale samples from the Paraná Basin, Brazil," *International Journal of Coal Geology*, vol. 84, no. 3-4, pp. 190–205, 2010.

[126] K. Kaneko, R. F. Cracknell, and D. Nicholson, "Nitrogen adsorption in slit pores at ambient temperatures: Comparison of simulation and experiment," *Langmuir*, vol. 10, no. 12, pp. 4606–4609, 1994.

[127] A. V. Neimark and P. I. Ravikovitch, "Calibration of pore volume in adsorption experiments and theoretical models," *Langmuir*, vol. 13, no. 19, pp. 5148–5160, 1997.

[128] S. Jiang, J. A. Zollweg, and K. E. Gubbins, "High-pressure adsorption of methane and ethane in activated carbon and carbon fibers," *The Journal of Physical Chemistry*, vol. 98, no. 22, pp. 5709–5713, 1994.

[129] B. Yan and X. Yang, "Adsorption prediction for three binary supercritical gas mixtures on activated carbon based on a NDFT/PSD approach," *Chemical Engineering Science*, vol. 60, no. 12, pp. 3267–3277, 2005.

[130] T. X. Nguyen, S. K. Bhatia, and D. Nicholson, "Prediction of high-pressure adsorption equilibrium of supercritical gases using density functional theory," *Langmuir*, vol. 21, no. 7, pp. 3187–3197, 2005.

[131] L. Zhou, Y. Zhou, M. Li, P. Chen, and Y. Wang, "Experimental and modeling study of the adsorption of supercritical methane on a high surface activated carbon," *Langmuir*, vol. 16, no. 14, pp. 5955–5959, 2000.

[132] D. Saha and S. Deng, "Adsorption equilibrium and kinetics of CO2, CH4, N2O, and NH3 on ordered mesoporous carbon," *Journal of Colloid and Interface Science*, vol. 345, no. 2, pp. 402–409, 2010.

[133] M. Meng, Z. Qiu, R. Zhong, Z. Liu, Y. Liu, and P. Chen, "Adsorption characteristics of supercritical CO2/CH4 on different types of coal and a machine learning approach," *Chemical Engineering Journal*, vol. 368, pp. 847–864, 2019.

[134] X. Tang and N. Ripepi, "High pressure supercritical carbon dioxide adsorption in coal: Adsorption model and thermodynamic characteristics," *Journal of CO2 Utilization*, vol. 18, pp. 189–197, 2017.

[135] X. Tang, N. Ripepi, N. P. Stadie, L. Yu, and M. R. Hall, "A dual-site Langmuir equation for accurate estimation of high pressure deep shale gas resources," *Fuel*, vol. 185, pp. 10–17, 2016.

[136] Z. Ye, D. Chen, Z. Pan, G. Zhang, Y. Xia, and X. Ding, "An improved Langmuir model for evaluating methane adsorption capacity in shale under various pressures and temperatures," *Journal of Natural Gas Science and Engineering*, vol. 31, pp. 658–680, 2016.

[137] S. Zhou, D. Zhang, H. Wang, and X. Li, "A modified BET equation to investigate supercritical methane adsorption mechanisms in shale," *Marine and Petroleum Geology*, vol. 105, pp. 284–292, 2019.

[138] W. Yu, K. Sepehrnoori, and T. W. Patzek, "Modeling gas adsorption in Marcellus shale with Langmuir and BET isotherms," *SPE Journal*, vol. 21, no. 2, p. 589600, 2016.

[139] J.-S. Bae and S. K. Bhatia, "High-pressure adsorption of methane and carbon dioxide on coal," *Energy & Fuels*, vol. 20, no. 6, pp. 2599–2607, 2006.

[140] R. Sakurovs, S. Day, S. Weir, and G. Duffy, "Application of a modified Dubinin-Radushkevich equation to adsorption of gases by coals under supercritical conditions," *Energy & Fuels*, vol. 21, no. 2, pp. 992–997, 2007.

[141] Y. Sun, S. Li, R. Sun, S. Yang, and X. Liu, "Modified Dubinin-Astakhov model for the accurate estimation of supercritical methane sorption on shales," *ACS Omega*, vol. 5, no. 26, pp. 16189–16199, 2020.

[142] X. Song, X. Lü, Y. Shen, S. Guo, and Y. Guan, "A modified supercritical Dubinin-Radushkevich model for the accurate estimation of high pressure methane adsorption on shales," *International Journal of Coal Geology*, vol. 193, pp. 1–15, 2018.

[143] M. Meng, R. Zhong, and Z. Wei, "Prediction of methane adsorption in shale: Classical models and machine learning based models," *Fuel*, vol. 278, p. 118358, 2020.

[144] X.-J. Wu, Z.-F. Ning, Z.-L. Cheng, Q. Wang, R.-R. Qi, L. Huang, and W.-T. Zhang, "Simplified local density model for gas adsorption in cylindrical carbon pores," *Applied Surface Science*, vol. 491, pp. 335–349, 2019.

[145] J. E. Fitzgerald, M. Sudibandriyo, Z. Pan, R. L. Robinson, and K. A. M. Gasem, "Modeling the adsorption of pure gases on coals with the SLD model," *Carbon*, vol. 41, no. 12, pp. 2203–2216, 2003.

[146] P. Charoensuppanimit, S. A. Mohammad, R. L. Robinson, and K. A. M. Gasem, "Modeling the temperature dependence of supercritical gas adsorption on activated carbons, coals and shales," *International Journal of Coal Geology*, vol. 138, pp. 113–126, 2015.

[147] P. Bénard and R. Chahine, "Modeling of high-pressure adsorption isotherms above the critical temperature on microporous adsorbents: Application to methane," *Langmuir*, vol. 13, no. 4, pp. 808–813, 1997.

[148] M. Sudibandriyo, S. A. Mohammad, R. L. Robinson, Jr, and K. A. M. Gasem, "Ono-Kondo lattice model for high-pressure adsorption: Pure gases," *Fluid Phase Equilibria*, vol. 299, no. 2, pp. 238–251, 2010.

[149] M. Sudibandriyo, S. A. Mohammad, R. L. Robinson, and K. A. M. Gasem, "Ono-Kondo model for high-pressure mixed-gas adsorption on activated carbons and coals," *Energy & Fuels*, vol. 25, no. 7, pp. 3355–3367, 2011.

[150] S. Ottiger, R. Pini, G. Storti, and M. Mazzotti, "Measuring and modeling the competitive adsorption of CO2, CH4, and n2 on a dry coal," *Langmuir*, vol. 24, no. 17, pp. 9531–9540, 2008.

[151] A. Qajar, H. Daigle, and M. Prodanović, "Methane dual-site adsorption in organic-rich shale-gas and coalbed systems," *International Journal of Coal Geology*, vol. 149, pp. 1–8, 2015.

[152] Y. Kurniawan, S. K. Bhatia, and V. Rudolph, "Simulation of binary mixture adsorption of methane and CO2 at supercritical conditions in carbons," *AIChE Journal*, vol. 52, no. 3, pp. 957–967, 2006.

[153] M. Heuchel, G. M. Davies, E. Buss, and N. A. Seaton, "Adsorption of carbon dioxide and methane and their mixtures on an activated carbon: Simulation and experiment," *Langmuir*, vol. 15, no. 25, pp. 8695–8705, 1999.

[154] G. P. Lithoxoos, A. Labropoulos, L. D. Peristeras, N. Kanellopoulos, J. Samios, and I. G. Economou, "Adsorption of N2, CH4, CO and CO2 gases in single walled carbon nanotubes: A combined experimental and Monte Carlo molecular simulation study," *The Journal of Supercritical Fluids*, vol. 55, no. 2, pp. 510–523, 2010.

[155] B. Zhang, J. Kang, and T. Kang, "Monte Carlo simulations of methane adsorption on kaolinite as a function of pore size," *Journal of Natural Gas Science and Engineering*, vol. 49, pp. 410–416, 2018.

[156] N. Yang, S. Liu, and X. Yang, "Molecular simulation of preferential adsorption of CO2 over CH4 in Na-montmorillonite clay material," *Applied Surface Science*, vol. 356, pp. 1262–1271, 2015.

[157] T. Wang, S. Tian, G. Li, and M. Sheng, "Selective adsorption of supercritical carbon dioxide and methane binary mixture in shale kerogen nanopores," *Journal of Natural Gas Science and Engineering*, vol. 50, pp. 181–188, 2018.

[158] Y. Liu, Y. Zhu, W. Li, J. Xiang, Y. Wang, J. Li, and F. Zeng, "Molecular simulation of methane adsorption in shale based on grand canonical Monte Carlo method and pore size distribution," *Journal of Natural Gas Science and Engineering*, vol. 30, pp. 119–126, 2016.

[159] C. R. Clarkson and B. Haghshenas, "Modeling of supercritical fluid adsorption on organic-rich shales and coal," in *SPE unconventional resources conference-USA*, Society of Petroleum Engineers, 2013.

[160] X. Tang, N. Ripepi, K. Luxbacher, and E. Pitcher, "Adsorption models for methane in shales: Review, comparison, and application," *Energy & Fuels*, vol. 31, no. 10, pp. 10787–10801, 2017.

[161] H. Wang, Z. Qu, Y. Yin, J. Bai, and B. Yu, "Review of molecular simulation method for gas adsorption/desorption and diffusion in shale matrix," *Journal of Thermal Science*, vol. 28, no. 1, pp. 1–16, 2019.

[162] T. Hocker, A. Rajendran, and M. Mazzotti, "Measuring and modeling supercritical adsorption in porous solids. carbon dioxide on 13X zeolite and on silica gel," *Langmuir*, vol. 19, no. 4, pp. 1254–1267, 2003.

[163] M. Mastalerz, L. He, Y. B. Melnichenko, and J. A. Rupp, "Porosity of coal and shale: Insights from gas adsorption and SANS/USANS techniques," *Energy & Fuels*, vol. 26, no. 8, pp. 5109–5120, 2012.

[164] H. Qinglin, S. M. Sundaram, and S. Farooq, "Revisiting transport of gases in the micropores of carbon molecular sieves," *Langmuir*, vol. 19, no. 2, pp. 393–405, 2003.

[165] C. Liang, Z. Li, and S. Dai, "Mesoporous carbon materials: Synthesis and modification," *Angewandte Chemie International Edition*, vol. 47, no. 20, pp. 3696–3717, 2008.

[166] K. A. Cychosz, R. Guillet-Nicolas, J. García-Martínez, and M. Thommes, "Recent advances in the textural characterization of hierarchically structured nanoporous materials," *Chemical Society Reviews*, vol. 46, no. 2, pp. 389–414, 2017.

[167] P. A. Monson, "Understanding adsorption/desorption hysteresis for fluids in mesoporous materials using simple molecular models and classical density functional theory," *Microporous and Mesoporous Materials*, vol. 160, pp. 47–66, 2012.

[168] J. Specovius and G. H. Findenegg, "Study of a fluid/solid interface over a wide density range including the critical region. I. Surface excess of ethylene/graphite," *Berichte der Bunsengesellschaft fr physikalische Chemie*, vol. 84, no. 7, pp. 690–696, 1980.

[169] M. Thommes and G. H. Findenegg, "Pore condensation and critical-point shift of a fluid in Controlled-Pore Glass," *Langmuir*, vol. 10, no. 11, pp. 4270–4277, 1994.

[170] M. Thommes, J. Morell, K. A. Cychosz, and M. Fröba, "Combining nitrogen, argon, and water adsorption for advanced characterization of ordered mesoporous carbons (CMKs) and periodic mesoporous organosilicas (PMOs)," *Langmuir*, vol. 29, no. 48, pp. 14893–14902, 2013.

[171] K. A. Sosin and D. F. Quinn, "Using the high pressure methane isotherm for determination of pore size distribution of carbon adsorbents," *Journal of Porous Materials*, vol. 1, no. 1, pp. 111–119, 1995.

[172] V. Y. Gusev, J. A. O'Brien, and N. A. Seaton, "A self-consistent method for characterization of activated carbons using supercritical adsorption and Grand Canonical Monte Carlo simulations," *Langmuir*, vol. 13, no. 10, pp. 2815–2821, 1997.

[173] T. Suzuki, R. Kobori, and K. Kaneko, "Grand canonical Monte Carlo simulation-assisted pore-width determination of molecular sieve carbons by use of ambient temperature N2 adsorption," *Carbon*, vol. 38, pp. 630–633, 2000.

[174] L. Zhou, S. Bai, W. Su, J. Yang, and Y. Zhou, "Comparative study of the excess versus absolute adsorption of CO2 on superactivated carbon for the near-critical region," *Langmuir*, vol. 19, no. 7, pp. 2683–2690, 2003.

[175] E. A. Ustinov and D. D. Do, "High-pressure adsorption of supercritical gases on activated carbons: An improved approach based on the density functional theory and the Bender equation of state," *Langmuir*, vol. 19, no. 20, pp. 8349–8357, 2003.

[176] Y. Liu and J. Wilcox, "Molecular simulation of CO2 adsorption in micro- and mesoporous carbons with surface heterogeneity," *International Journal of Coal Geology*, vol. 104, pp. 83–95, 2012.

[177] P. Malbrunot, D. Vidal, J. Vermesse, R. Chahine, and T. K. Bose, "Adsorption measurements of argon, neon, krypton, nitrogen, and methane on activated carbon up to 650 MPa," *Langmuir*, vol. 8, no. 2, pp. 577–580, 1992.

[178] J. H. Chen, D. S. H. Wong, C. S. Tan, R. Subramanian, C. T. Lira, and M. Orth, "Adsorption and desorption of carbon dioxide onto and from activated carbon at high pressures," *Industrial & Engineering Chemistry Research*, vol. 36, no. 7, pp. 2808–2815, 1997.

[179] R. Humayun and D. L. Tomasko, "High-resolution adsorption isotherms of supercritical carbon dioxide on activated carbon," *AIChE Journal*, vol. 46, no. 10, pp. 2065–2075, 2000.

[180] A. Herbst and P. Harting, "Thermodynamic description of excess isotherms in high-pressure adsorption of methane, argon and nitrogen," *Adsorption*, vol. 8, no. 2, pp. 111–123, 2002.

[181] M. Sudibandriyo, Z. Pan, J. E. Fitzgerald, R. L. Robinson, and K. A. M. Gasem, "Adsorption of methane, nitrogen, carbon dioxide, and their binary mixtures on dry activated carbon at 318.2 K and pressures up to 13.6 MPa," *Langmuir*, vol. 19, no. 13, pp. 5323–5331, 2003.

[182] R. Pini, S. Ottiger, A. Rajendran, G. Storti, and M. Mazzotti, "Reliable measurement of near-critical adsorption by gravimetric method," *Adsorption*, vol. 12, no. 5, pp. 393–403, 2006.

[183] J. Schell, N. Casas, R. Pini, and M. Mazzotti, "Pure and binary adsorption of CO2, H2, and N2 on activated carbon," *Adsorption*, vol. 18, no. 1, pp. 49–65, 2012.

[184] O. Di Giovanni, W. Dörfler, M. Mazzotti, and M. Morbidelli, "Adsorption of supercritical carbon dioxide on silica," *Langmuir*, vol. 17, no. 14, pp. 4316–4321, 2001.

[185] N. Tatsuda, Y. Goto, N. Setoyama, and Y. Fukushima, "Adsorption of carbon dioxide on mesoporous silicas near the critical temperature," *Adsorption Science & Technology*, vol. 23, no. 9, pp. 763–776, 2005.

[186] M. S. Gruszkiewicz, G. Rother, D. J. Wesolowski, D. R. Cole, and D. Wallacher, "Direct measurements of pore fluid density by vibrating tube densimetry," *Langmuir*, vol. 28, no. 11, pp. 5070–5078, 2012.

[187] D. D. Do and H. D. Do, "Adsorption of supercritical fluids in non-porous and porous carbons: analysis of adsorbed phase volume and density," *Carbon*, vol. 41, no. 9, pp. 1777–1791, 2003.

[188] D. D. Do, *Adsorption Analysis: Equilibria and Kinetics*, vol. 2. Singapore: Imperial College Press, 1998.

[189] H. Sun, J. Yao, Y.-c. Cao, D.-y. Fan, and L. Zhang, "Characterization of gas transport behaviors in shale gas and tight gas reservoirs by digital rock analysis," *International Journal of Heat and Mass Transfer*, vol. 104, pp. 227–239, 2017.

[190] W. Yuan, Z. Pan, X. Li, Y. Yang, C. Zhao, L. D. Connell, S. Li, and J. He, "Experimental study and modelling of methane adsorption and diffusion in shale," *Fuel*, vol. 117, Part A, pp. 509–519, 2014.

[191] S. R. Etminan, F. Javadpour, B. B. Maini, and Z. Chen, "Measurement of gas storage processes in shale and of the molecular diffusion coefficient in kerogen," *International Journal of Coal Geology*, vol. 123, pp. 10–19, 2014.

[192] B. Yang, Y. Kang, L. You, X. Li, and Q. Chen, "Measurement of the surface diffusion coefficient for adsorbed gas in the fine mesopores and micropores of shale organic matter," *Fuel*, vol. 181, pp. 793–804, 2016.

[193] H. Ansari, M. Trusler, G. Maitland, C. Delle Piane, and R. Pini, "The Gas-in-Place and CO2 storage capacity of shale reservoirs at subsurface conditions," in *15th Greenhouse Gas Control Technologies Conference (GHGT-15)*, 2021.

[194] A. D. Ebner and J. A. Ritter, "State-of-the-art adsorption and membrane separation processes for carbon dioxide production from carbon dioxide emitting industries," *Separation Science and Technology*, vol. 44, no. 6, pp. 1273–1421, 2009.

[195] S. Sircar, T. C. Golden, and M. B. Rao, "Activated carbon for gas separation and storage," *Carbon*, vol. 34, no. 1, pp. 1–12, 1996.

[196] J. P. Marco-Lozar, M. Kunowsky, F. Suárez-García, J. D. Carruthers, and A. Linares-Solano, "Activated carbon monoliths for gas storage at room temperature," *Energy & Environmental Science*, vol. 5, no. 12, pp. 9833–9842, 2012.

[197] Z. Wu and D. Zhao, "Ordered mesoporous materials as adsorbents," *Chemical Communications*, vol. 47, no. 12, pp. 3332–3338, 2011.

[198] H. Yi, Y. Li, X. Tang, F. Li, K. Li, Q. Yuan, and X. Sun, "Effect of the adsorbent pore structure on the separation of carbon dioxide and methane gas mixtures," *Journal of Chemical & Engineering Data*, vol. 60, no. 5, pp. 1388–1395, 2015.

[199] C. J. H. Jacobsen, C. Madsen, J. Houzvicka, I. Schmidt, and A. Carlsson, "Mesoporous zeolite single crystals," *Journal of the American Chemical Society*, vol. 122, no. 29, pp. 7116–7117, 2000.

[200] EIA, "U.S. crude oil and natural gas proved reserves, year-end 2018," report, EIA, 2019.

[201] C. Liang, Z. Jiang, C. Zhang, L. Guo, Y. Yang, and J. Li, "The shale characteristics and shale gas exploration prospects of the Lower Silurian Longmaxi shale, Sichuan Basin, South China," *Journal of Natural Gas Science and Engineering*, vol. 21, pp. 636–648, 2014.

[202] R. Yang, S. He, Q. Hu, M. Sun, D. Hu, and J. Yi, "Applying SANS technique to characterize nano-scale pore structure of Longmaxi shale, Sichuan Basin (China)," *Fuel*, vol. 197, pp. 91–99, 2017.

[203] I. J. Andrews, "The Carboniferous Bowland Shale gas study: geology and resource estimation," report, British Geological Survey for Department of Energy and Climate Change, 2013.

[204] A.-L. Fauchille, L. Ma, E. Rutter, M. Chandler, P. D. Lee, and K. G. Taylor, "An enhanced understanding of the Basinal Bowland shale in Lancashire (UK), through microtextural and mineralogical observations," *Marine and Petroleum Geology*, vol. 86, pp. 1374–1390, 2017.

[205] C. Delle Piane, J. Bourdet, M. Josh, M. B. Clennell, W. D. A. Rickard, M. Saunders, N. Sherwood, Z. Li, D. N. Dewhurst, and M. D. Raven, "Organic matter network in post-mature Marcellus Shale: Effects on petrophysical properties," *AAPG Bulletin*, vol. 102, no. 11, pp. 2305–2332, 2018.

[206] C. Delle Piane, H. Ansari, Z. Li, J. Mata, W. Rickard, R. Pini, D. N. Dewhurst, and N. Sherwood, "Influence of maceral type on porosity development in the Wufeng-Longmaxi shale: A combined electron microscopy, neutron scattering and physisorption approach," *Submitted for publication*, 2021.

[207] R. Span and W. Wagner, "A new equation of state for carbon dioxide covering the fluid region from the triplepoint temperature to 1100 K at pressures up to 800 MPa," *Journal of Physical and Chemical Reference Data*, vol. 25, no. 6, pp. 1509–1596, 1996.

[208] U. Setzmann and W. Wagner, "A new equation of state and tables of thermodynamic properties for methane covering the range from the melting line to 625 K at pressures up to 100 MPa," *Journal of Physical and Chemical Reference Data*, vol. 20, no. 6, pp. 1061–1155, 1991.

[209] P. Bertier, K. Schweinar, H. Stanjek, A. Ghanizadeh, C. Clarkson, A. Busch, N. Kampman, D. Prinz, A. Amann-Hildenbrand, B. Krooss, and V. Pipich, "On the use and abuse of N2 physisorption for the characterization of the pore structure of shales," *CMS Workshop Lectures*, vol. 21, pp. 151–161, 2016.

[210] M. Thommes and K. A. Cychosz, "Physical adsorption characterization of nanoporous materials: progress and challenges," *Adsorption*, vol. 20, no. 2, pp. 233–250, 2014.

[211] J. Landers, G. Y. Gor, and A. V. Neimark, "Density functional theory methods for characterization of porous materials," *Colloids and Surfaces A: Physicochemical and Engineering Aspects*, vol. 437, pp. 3–32, 2013.

[212] E. A. Ustinov, D. D. Do, and V. B. Fenelonov, "Pore size distribution analysis of activated carbons: Application of density functional theory using nongraphitized carbon black as a reference system," *Carbon*, vol. 44, no. 4, pp. 653–663, 2006.

[213] A. V. Neimark, Y. Lin, P. I. Ravikovitch, and M. Thommes, "Quenched solid density functional theory and pore size analysis of micro-mesoporous carbons," *Carbon*, vol. 47, no. 7, pp. 1617–1628, 2009.

[214] M. Thommes, *Chapter 15 - Textural Characterization of Zeolites and Ordered Mesoporous Materials by Physical Adsorption*, vol. 168, pp. 495–XIII. Elsevier, 2007.

[215] A. V. Neimark and P. I. Ravikovitch, "Capillary condensation in MMS and pore structure characterization," *Microporous and Mesoporous Materials*, vol. 44-45, pp. 697–707, 2001.

[216] F. Dreisbach and H. W. Lösch, "Magnetic suspension balance for simultaneous measurement of a sample and the density of the measuring fluid," *Journal of Thermal Analysis and Calorimetry*, vol. 62, no. 2, pp. 515–521, 2000.

[217] Rubotherm, "Magnetic suspension balances," report, Rubotherm, 2017.

[218] F. Dreisbach, R. Seif A. H, and H. W. Lösch, "Gravimetric measurement of adsorption equilibria of gas mixture CO/H2 with a magnetic suspension balance," *Chemical Engineering & Technology*, vol. 25, no. 11, pp. 1060–1065, 2002.

[219] E. A. Ustinov, D. D. Do, A. Herbst, R. Staudt, and P. Harting, "Modeling of gas adsorption equilibrium over a wide range of pressure: A thermodynamic approach based on equation of state," *Journal of Colloid and Interface Science*, vol. 250, no. 1, pp. 49–62, 2002.

[220] J. Taylor, *An Introduction to Error Analysis: The Study of Uncertainties in Physical Measurements*. University Science Books, 1997.

[221] R. Pini, S. Ottiger, L. Burlini, G. Storti, and M. Mazzotti, "Role of adsorption and swelling on the dynamics of gas injection in coal," *Journal of Geophysical Research*, vol. 114, no. B4, 2009.

[222] K. Murata, M. El-Merraoui, and K. Kaneko, "A new determination method of absolute adsorption isotherm of supercritical gases under high pressure with a special relevance to density-functional theory study," *The Journal of Chemical Physics*, vol. 114, no. 9, pp. 4196–4205, 2001.

[223] R. Pini, S. Ottiger, L. Burlini, G. Storti, and M. Mazzotti, "Sorption of carbon dioxide, methane and nitrogen in dry coals at high pressure and moderate temperature," *International Journal of Greenhouse Gas Control*, vol. 4, no. 1, pp. 90–101, 2010.

[224] S. Ono and S. Kondo, "Molecular theory of surface tension in liquids," *Structure of Liquids, Encyclopedia of Physics*, vol. 3-10, pp. 134–280, 1960.

[225] G. L. Aranovich and M. D. Donohue, "A new model for lattice systems," *The Journal of Chemical Physics*, vol. 105, no. 16, pp. 7059–7063, 1996.

[226] G. Aranovich and M. Donohue, "Analysis of adsorption isotherms: Lattice theory predictions, classification of isotherms for gas-solid equilibria, and similarities in gas and liquid adsorption behavior," *Journal of Colloid and Interface Science*, vol. 200, no. 2, pp. 273–290, 1998.

[227] J. Hwang, L. Joss, and R. Pini, "Measuring and modelling supercritical adsorption of CO2 and CH4 on montmorillonite source clay," *Microporous and Mesoporous Materials*, vol. 273, pp. 107–121, 2019.

[228] A. Qajar, H. Daigle, and M. Prodanović, "The effects of pore geometry on adsorption equilibrium in shale formations and coal-beds: Lattice density functional theory study," *Fuel*, vol. 163, pp. 205–213, 2016.

[229] G. Sposito, N. T. Skipper, R. Sutton, S. Park, A. K. Soper, and J. A. Greathouse, "Surface geochemistry of the clay minerals," *Proceedings of the National Academy of Sciences*, vol. 96, no. 7, pp. 3358–3364, 1999.

[230] A. L. Myers, *Thermodynamics of adsorption*, pp. 243–253. The Royal Society of Chemistry, 2004.

[231] P. Linstrom and W. Mallard, *NIST Chemistry WebBook, NIST Standard Reference Database Number 69*. Gaithersburg MD, 20899: National Institute of Standards and Technology.

[232] H. Ansari, M. Trusler, G. Maitland, C. Delle Piane, and R. Pini, "Characterisation of the Bowland shale porosity using N2 and CO2 adsorption," in *Sixth EAGE Shale Workshop, Apr 2019*, vol. 2019, pp. 1–5, 2019.

[233] R. Pini, H. Ansari, and J. Hwang, "Measurement and interpretation of unary supercritical gas adsorption isotherms in micro-mesoporous solids," *Adsorption*, vol. 27, pp. 659–671, 2021.

[234] Sigma-Aldrich, "Carbon, mesoporous," 2017.

[235] A. B. Fuertes, G. Marbán, and D. M. Nevskaia, "Adsorption of volatile organic compounds by means of activated carbon fibre-based monoliths," *Carbon*, vol. 41, no. 1, pp. 87–96, 2003.

[236] D. Hulicova-Jurcakova, A. M. Puziy, O. I. Poddubnaya, F. Suárez-García, J. M. D. Tascón, and G. Q. Lu, "Highly stable performance of supercapacitors from phosphorus-enriched carbons," *Journal of the American Chemical Society*, vol. 131, no. 14, pp. 5026–5027, 2009.

[237] T. E. Rufford, G. C. Y. Watson, T. L. Saleman, P. S. Hofman, N. K. Jensen, and E. F. May, "Adsorption equilibria and kinetics of methane + nitrogen mixtures on the activated carbon norit RB3," *Industrial & Engineering Chemistry Research*, vol. 52, no. 39, pp. 14270–14281, 2013.

[238] J.-P. Bellat, I. Bezverkhyy, G. Weber, S. Royer, R. Averlant, J.-M. Giraudon, and J.-F. Lamonier, "Capture of formaldehyde by adsorption on nanoporous materials," *Journal of Hazardous Materials*, vol. 300, pp. 711–717, 2015.

[239] J. C. Groen, L. A. A. Peffer, and J. Pérez-Ramírez, "Pore size determination in modified micro- and mesoporous materials. Pitfalls and limitations in gas adsorption data analysis," *Microporous and Mesoporous Materials*, vol. 60, no. 1, pp. 1–17, 2003.

[240] H. Aljamaan, R. Holmes, V. Vishal, R. Haghpanah, J. Wilcox, and A. R. Kovscek, "CO2 storage and flow capacity measurements on idealized shales from dynamic breakthrough experiments," *Energy & Fuels*, 2017.

[241] J. Moellmer, E. B. Celer, R. Luebke, A. J. Cairns, R. Staudt, M. Eddaoudi, and M. Thommes, "Insights on adsorption characterization of metal-organic frameworks: A benchmark study on the novel soc-MOF," *Microporous and Mesoporous Materials*, vol. 129, no. 3, pp. 345–353, 2010.

[242] E. W. Lemmon, M. L. Huber, and M. O. McLinden, "NIST standard reference database 23: Reference fluid thermodynamic and transport properties-REFPROP, version 10.0," 2018.

[243] X. Yang, R. Kleinrahm, M. O. McLinden, and M. Richter, "Uncertainty analysis of adsorption measurements using commercial gravimetric sorption analyzers with simultaneous density measurement based on a magnetic-suspension balance," *Adsorption*, vol. 26, no. 4, pp. 645–659, 2020.

[244] S. Himeno, T. Komatsu, and S. Fujita, "High-pressure adsorption equilibria of methane and carbon dioxide on several activated carbons," *Journal of Chemical & Engineering Data*, vol. 50, no. 2, pp. 369–376, 2005.

[245] D. M. Ruthven, *Adsorption*, vol. 1 of *Kirk-Othmer Encyclopedia of Chemical Technology*. New York: Wiley-Interscience, 4th ed., 1991.

[246] S. Cavenati, C. A. Grande, and A. E. Rodrigues, "Adsorption equilibrium of methane, carbon dioxide, and nitrogen on zeolite 13X at high pressures," *Journal of Chemical & Engineering Data*, vol. 49, no. 4, pp. 1095–1101, 2004.

[247] J. A. Dunne, M. Rao, S. Sircar, R. J. Gorte, and A. L. Myers, "Calorimetric heats of adsorption and adsorption isotherms. 2. O2, N2, Ar, CO2, CH4, C2H6, and SF6 on NaX, H-ZSM-5, and Na-ZSM-5 zeolites," *Langmuir*, vol. 12, no. 24, pp. 5896–5904, 1996.

[248] S. B̈lumel and G. H. Findenegg, "Critical adsorption of a pure fluid on a graphite substrate," *Physical Review Letters*, vol. 54, no. 5, pp. 447–450, 1985.

[249] L. Ma, A.-L. Fauchille, H. Ansari, M. Chandler, P. Ashby, K. Taylor, R. Pini, and P. D. Lee, "Linking multi-scale 3D microstructure to potential enhanced natural gas recovery and subsurface CO2 storage for Bowland shale, UK," *Energy & Environmental Science*, 2021.

[250] H. Yin, J. Zhou, Y. Jiang, X. Xian, and Q. Liu, "Physical and structural changes in shale associated with supercritical CO2 exposure," *Fuel*, vol. 184, pp. 289–303, 2016.

[251] S. Sanguinito, A. Goodman, M. Tkach, B. Kutchko, J. Culp, S. Natesakhawat, J. Fazio, I. Fukai, and D. Crandall, "Quantifying dry supercritical CO2-induced changes of the Utica Shale," *Fuel*, vol. 226, pp. 54–64, 2018.

[252] J. Zhou, S. Xie, Y. Jiang, X. Xian, Q. Liu, Z. Lu, and Q. Lyu, "Influence of supercritical CO2 exposure on CH4 and CO2 adsorption behaviors of shale: Implications for CO2 sequestration," *Energy & Fuels*, vol. 32, no. 5, pp. 6073–6089, 2018.

[253] B. L. Alemu, P. Aagaard, I. A. Munz, and E. Skurtveit, "Caprock interaction with CO2: A laboratory study of reactivity of shale with supercritical CO2 and brine," *Applied Geochemistry*, vol. 26, no. 12, pp. 1975–1989, 2011.

[254] R. Lahann, M. Mastalerz, J. A. Rupp, and A. Drobniak, "Influence of CO2 on New Albany Shale composition and pore structure," *International Journal of Coal Geology*, vol. 108, pp. 2–9, 2013.

[255] T. F. Rexer, E. J. Mathia, A. C. Aplin, and K. M. Thomas, "High-pressure methane adsorption and characterization of pores in Posidonia shales and isolated kerogens," *Energy & Fuels*, vol. 28, no. 5, pp. 2886–2901, 2014.

[256] S. Duan, M. Gu, X. Du, and X. Xian, "Adsorption equilibrium of CO2 and CH4 and their mixture on Sichuan Basin Shale," *Energy & Fuels*, vol. 30, no. 3, pp. 2248–2256, 2016.

[257] X. Tang, N. Ripepi, N. P. Stadie, and L. Yu, "Thermodynamic analysis of high pressure methane adsorption in Longmaxi shale," *Fuel*, vol. 193, pp. 411–418, 2017.

[258] Z. Jiang, L. Zhao, and D. Zhang, "Study of adsorption behavior in shale reservoirs under high pressure," *Journal of Natural Gas Science and Engineering*, vol. 49, pp. 275–285, 2018.

[259] K. Zeng, P. Jiang, Z. Lun, and R. Xu, "Molecular simulation of carbon dioxide and methane adsorption in shale organic nanopores," *Energy & Fuels*, vol. 33, no. 3, pp. 1785–1796, 2019.

[260] H. Aljamaan, M. Al Ismail, and A. R. Kovscek, "Experimental investigation and Grand Canonical Monte Carlo simulation of gas shale adsorption from the macro to the nano scale," *Journal of Natural Gas Science and Engineering*, 2016.

[261] H. Zhao, T. Wu, and A. Firoozabadi, "High pressure sorption of various hydrocarbons and carbon dioxide in Kimmeridge Blackstone and isolated kerogen," *Fuel*, vol. 224, pp. 412–423, 2018.

[262] S. M. Kang, E. Fathi, R. J. Ambrose, I. Y. Akkutlu, and R. F. Sigal, "Carbon dioxide storage capacity of organic-rich shales," *SPE Journal*, vol. 16, no. 04, 2011.

[263] R. J. Ambrose, R. C. Hartman, M. Diaz-Campos, I. Y. Akkutlu, and C. H. Sondergeld, "Shale gas-in-place calculations part I: New pore-scale considerations," *SPE Journal*, vol. 17, no. 01, pp. 219–229, 2012.

[264] D. Silin and T. J. Kneafsey, "Shale gas: Nanometer-scale observations and well modelling," *Journal of Canadian Petroleum Technology*, vol. 51, no. 06, pp. 464–475, 2012.

[265] K. S. Walton and D. S. Sholl, "Predicting multicomponent adsorption: 50 years of the ideal adsorbed solution theory," *AIChE Journal*, vol. 61, no. 9, pp. 2757–2762, 2015.

[266] V. S. Balashankar, A. K. Rajagopalan, R. de Pauw, A. M. Avila, and A. Rajendran, "Analysis of a batch adsorber analogue for rapid screening of adsorbents for postcombustion CO2 capture," *Industrial & Engineering Chemistry Research*, vol. 58, no. 8, pp. 3314–3328, 2019.

[267] L. P. Dake, *Fundamentals of reservoir engineering*. Elsevier, 1983.

[268] V. Pranesh, "Subsurface CO2 storage estimation in Bakken tight oil and Eagle Ford shale gas condensate reservoirs by retention mechanism," *Fuel*, vol. 215, pp. 580–591, 2018.

[269] T. Wan and Z. Mu, "The use of numerical simulation to investigate the enhanced Eagle Ford shale gas condensate well recovery using cyclic CO2 injection method with nano-pore effect," *Fuel*, vol. 233, pp. 123–132, 2018.

[270] R. Iddphonce, J. Wang, and L. Zhao, "Review of CO2 injection techniques for enhanced shale gas recovery: Prospect and challenges," *Journal of Natural Gas Science and Engineering*, vol. 77, p. 103240, 2020.

[271] J. S. Levine, I. Fukai, D. J. Soeder, G. Bromhal, R. M. Dilmore, G. D. Guthrie, T. Rodosta, S. Sanguinito, S. Frailey, C. Gorecki, W. Peck, and A. L. Goodman, "U.S. DOE NETL methodology for estimating the prospective CO2 storage resource of shales at the national and regional scale," *International Journal of Greenhouse Gas Control*, vol. 51, pp. 81–94, 2016.

[272] S. Moghadam, O. Jeje, and L. Mattar, "Advanced gas material balance in simplified format," *Journal of Canadian Petroleum Technology*, vol. 50, no. 01, pp. 90–98, 2011.

[273] R. H. Williams, D. K. Khatri, R. F. Keese, S. Le Roy-Delage, J. M. Roye, D. L. R. Leach, O. Porcherie, P. Rottler, and J. Rodriguez, "Flexible, Expanding Cement System (FECS) successfully provides zonal isolation across Marcellus shale gas trends," 2011.

[274] EIA, "Review of emerging resources: U.S. gas and shale oil plays," report, EIA, 2011.

[275] M. L. Boyce, T. R. Carr, T. Carr, T. D'Agostino, W. Ambrose, J. Pashin, and N. C. Rosen, *Lithostratigraphy and Petrophysics of the Devonian Marcellus Interval in West Virginia and Southwestern Pennsylvania*, vol. 29, p. 0. SEPM Society for Sedimentary Geology, 2009.

[276] R. Heller and M. Zoback, "Adsorption of methane and carbon dioxide on gas shale and pure mineral samples," *Journal of Unconventional Oil and Gas Resources*, vol. 8, pp. 14–24, 2014.

[277] A. Streb and M. Mazzotti, "Adsorption for efficient low carbon hydrogen production: part 2-Cyclic experiments and model predictions," *Adsorption*, 2021.

[278] A. Satter and G. M. Iqbal, *4 - Reservoir fluid properties*, pp. 81–105. Boston: Gulf Professional Publishing, 2016.

[279] K. Lin, Q. Yuan, Y.-P. Zhao, and C. Cheng, "Which is the most efficient candidate for the recovery of confined methane: Water, carbon dioxide or nitrogen?," *Extreme Mechanics Letters*, vol. 9, pp. 127–138, 2016.

[280] Z. Li and D. Elsworth, "Controls of CO2-N2 gas flood ratios on enhanced shale gas recovery and ultimate CO2 sequestration," *Journal of Petroleum Science and Engineering*, vol. 179, pp. 1037–1045, 2019.

[281] X. Luo, S. Wang, Z. Wang, Z. Jing, M. Lv, Z. Zhai, and T. Han, "Adsorption of methane, carbon dioxide and their binary mixtures on Jurassic shale from the Qaidam Basin in China," *International Journal of Coal Geology*, vol. 150151, pp. 210–223, 2015.

[282] S. Ottiger, R. Pini, G. Storti, and M. Mazzotti, "Competitive adsorption equilibria of CO2 and CH4 on a dry coal," *Adsorption*, vol. 14, no. 4, pp. 539–556, 2008.

[283] R. Pini, S. Ottiger, G. Storti, and M. Mazzotti, "Prediction of competitive adsorption on coal by a lattice DFT model," *Adsorption*, vol. 16, no. 1, pp. 37–46, 2010.

[284] D. G. Friend, H. Ingham, and J. F. Fly, "Thermophysical properties of ethane," *Journal of Physical and Chemical Reference Data*, vol. 20, no. 2, pp. 275–347, 1991.

[285] Y. Wang, T. T. Tsotsis, and K. Jessen, "Competitive sorption of methane/ethane mixtures on shale: Measurements and modeling," *Industrial & Engineering Chemistry Research*, vol. 54, no. 48, pp. 12187–12195, 2015.

[286] D. Dasani, Y. Wang, T. T. Tsotsis, and K. Jessen, "Laboratory-scale investigation of sorption kinetics of methane/ethane mixtures in shale," *Industrial & Engineering Chemistry Research*, vol. 56, no. 36, pp. 9953–9963, 2017.

[287] L. F. Ruppert, R. Sakurovs, T. P. Blach, L. He, Y. B. Melnichenko, D. F. R. Mildner, and L. Alcantar-Lopez, "A USANS/SANS study of the accessibility of pores in the Barnett shale to methane and water," *Energy & Fuels*, vol. 27, no. 2, pp. 772–779, 2013.

[288] M. E. Chenevert, "Shale alteration by water adsorption," *Journal of petroleum technology*, vol. 22, no. 09, pp. 1141–1148, 1970.

[289] Q. Lyu, P. G. Ranjith, X. Long, Y. Kang, and M. Huang, "A review of shale swelling by water adsorption," *Journal of Natural Gas Science and Engineering*, vol. 27, pp. 1421–1431, 2015.

[290] A. A. Sabtan, "Geotechnical properties of expansive clay shale in Tabuk, Saudi Arabia," *Journal of Asian Earth Sciences*, vol. 25, no. 5, pp. 747–757, 2005.

[291] C. Tournassat, A. Neaman, F. Villiéras, D. Bosbach, and L. Charlet, "Nanomorphology of montmorillonite particles: Estimation of the clay edge sorption site density by low-pressure gas adsorption and AFM observations," *American Mineralogist*, vol. 88, no. 11-12, pp. 1989–1995, 2003.

[292] A. Busch, P. Bertier, Y. Gensterblum, G. Rother, C. J. Spiers, M. Zhang, and H. M. Wentinck, "On sorption and swelling of CO2 in clays," *Geomechanics and Geophysics for Geo-Energy and Geo-Resources*, vol. 2, no. 2, pp. 111–130, 2016.

[293] P. Giesting, S. Guggenheim, A. F. Koster van Groos, and A. Busch, "Interaction of carbon dioxide with Na-exchanged montmorillonite at pressures to 640bars: Implications for CO2 sequestration," *International Journal of Greenhouse Gas Control*, vol. 8, pp. 73–81, 2012.

[294] G. Rother, E. S. Ilton, D. Wallacher, T. Hauβ, H. T. Schaef, O. Qafoku, K. M. Rosso, A. R. Felmy, E. G. Krukowski, A. G. Stack, N. Grimm, and R. J. Bodnar, "CO2 sorption to subsingle hydration layer montmorillonite clay studied by excess sorption and neutron diffraction measurements," *Environmental Science & Technology*, vol. 47, no. 1, pp. 205–211, 2013.

[295] G. M. Bowers, J. S. Loring, E. D. Walter, S. D. Burton, M. E. Bowden, D. W. Hoyt, B. Arey, R. K. Larsen, and R. J. Kirkpatrick, "Influence of smectite structure and hydration on supercritical methane binding and dynamics in smectite pores," *The Journal of Physical Chemistry C*, vol. 123, no. 48, pp. 29231–29244, 2019.

[296] Z. Jin and A. Firoozabadi, "Effect of water on methane and carbon dioxide sorption in clay minerals by Monte Carlo simulations," *Fluid Phase Equilibria*, vol. 382, pp. 10–20, 2014.

[297] J. Zou, R. Rezaee, Q. Xie, L. You, K. Liu, and A. Saeedi, "Investigation of moisture effect on methane adsorption capacity of shale samples," *Fuel*, vol. 232, pp. 323–332, 2018.

[298] J. Zhou, Z. Jin, and K. H. Luo, "Effects of moisture contents on shale gas recovery and CO2 sequestration," *Langmuir*, vol. 35, no. 26, pp. 8716–8725, 2019.

[299] J. Hwang and R. Pini, "Enhanced sorption of supercritical CO2 and CH4 in the hydrated interlayer pores of smectite," *Langmuir*, vol. 37, no. 12, pp. 3778–3788, 2021.

[300] J. Bahadur, A. P. Radlinski, Y. B. Melnichenko, M. Mastalerz, and A. Schimmelmann, "Small-angle and ultrasmall-angle neutron scattering (SANS/USANS) study of New Albany shale: A treatise on microporosity," *Energy & Fuels*, vol. 29, no. 2, pp. 567–576, 2015.

[301] H. E. King, A. P. R. Eberle, C. C. Walters, C. E. Kliewer, D. Ertas, and C. Huynh, "Pore architecture and connectivity in gas shale," *Energy & Fuels*, vol. 29, no. 3, pp. 1375–1390, 2015.

[302] S. Hao, W. Chu, Q. Jiang, and X. Yu, "Methane adsorption characteristics on coal surface above critical temperature through DubininAstakhov model and Langmuir model," *Colloids and Surfaces A: Physicochemical and Engineering Aspects*, vol. 444, pp. 104–113, 2014.

Appendix A

Synthetic Adsorbents

Some of the material in this chapter has been published in Ansari et al. (2020) [29] and Pini et al. (2021) [233].

A.1 Experimental Data

A.1.1 Subcritical Adsorption

Figure A.1 shows the results of the subcritical CO_2 adsorption experiments on mesoporous carbon and mesoporous zeolite.

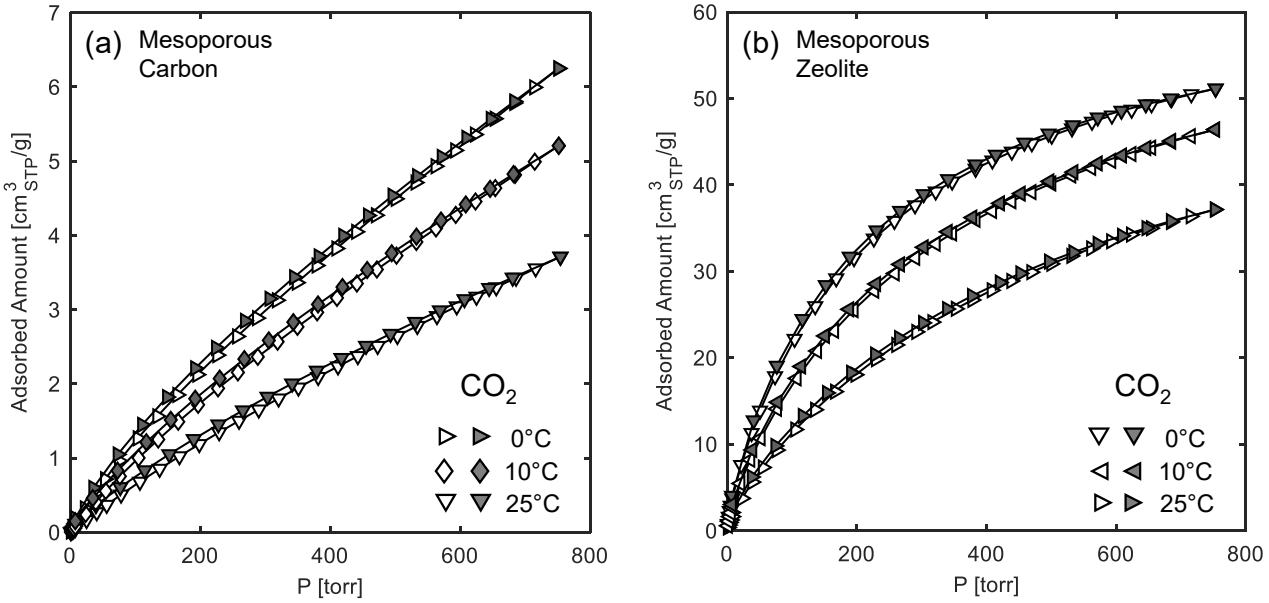

Figure A.1: Subcritical CO_2 adsorption on (a) mesoporous carbon and (b) mesoporous zeolite. STP conditions are defined as 273.15 K and 1 atm. Empty symbols represent points taken in adsorption mode and filled symbols represent points taken in desorption mode.

A.1.2 Supercritical Adsorption

The experimental adsorption results for MC (Tables A.1 and A.2) and MZ (Tables A.3 and A.4) are shown below.

Table A.1: Experimental measurements of supercritical adsorption of CO_2 on mesoporous carbon at various temperatures.

T [°C]	P [bar]	ρ_b [mol/L]		n^{ex} [mmol/g]		n^{net} [mmol/g]	
80	19.8992	0.7151	± 0.0004	0.7046	± 0.0021	0.2811	± 0.0009
	55.0042	2.2406	± 0.0010	1.3338	± 0.0042	0.0066	± 0.0007
	104.0234	5.3193	± 0.0029	1.7112	± 0.0077	-1.4395	± 0.0047
	249.5584	15.5035	± 0.0077	0.6141	± 0.0168	-8.5690	± 0.0233
	193.7926	13.0473	± 0.0065	0.9377	± 0.0146	-6.7905	± 0.0187
	167.1292	11.1530	± 0.0055	1.2070	± 0.0123	-5.3991	± 0.0147
	148.1260	9.4297	± 0.0046	1.4415	± 0.0108	-4.1439	± 0.0114
	132.2334	7.8462	± 0.0054	1.6088	± 0.0112	-3.0386	± 0.0097
	117.1566	6.4336	± 0.0032	1.7039	± 0.0082	-2.1069	± 0.0059
	98.1106	4.8622	± 0.0023	1.6988	± 0.0068	-1.1812	± 0.0035
	77.9450	3.5017	± 0.0017	1.5809	± 0.0056	-0.4933	± 0.0017
	66.8124	2.8596	± 0.0029	1.4746	± 0.0081	-0.2193	± 0.0059
	53.5202	2.1678	± 0.0010	1.3221	± 0.0042	0.0380	± 0.0008
	37.8244	1.4462	± 0.0007	1.0906	± 0.0033	0.2339	± 0.0009
	25.6070	0.9379	± 0.0005	0.8535	± 0.0025	0.2979	± 0.0010
	10.0250	0.3494	± 0.0003	0.4305	± 0.0013	0.2236	± 0.0008
	3.0348	0.1032	± 0.0003	0.1726	± 0.0008	0.1115	± 0.0006
	1.0810	0.0362	± 0.0002	0.0851	± 0.0006	0.0637	± 0.0006
	0.5544	0.0190	± 0.0003	0.0589	± 0.0008	0.0477	± 0.0007
	0.1590	0.0056	± 0.0003	0.0370	± 0.0008	0.0337	± 0.0007
40	250.0764	19.9307	± 0.0091	0.2920	± 0.0206	-11.5134	± 0.0308
	210.2248	19.2248	± 0.0090	0.3639	± 0.0200	-11.0234	± 0.0296
	159.8106	17.9628	± 0.0089	0.5181	± 0.0193	-10.1216	± 0.0274
	119.8824	16.1483	± 0.0099	0.8073	± 0.0196	-8.7577	± 0.0247
	100.0822	14.0217	± 0.0073	1.2734	± 0.0166	-7.0319	± 0.0200
	91.9868	11.5659	± 0.0059	1.9432	± 0.0135	-4.9075	± 0.0135
	89.0430	9.8936	± 0.0054	2.4343	± 0.0131	-3.4259	± 0.0103
	85.0960	7.8377	± 0.0049	2.9389	± 0.0135	-1.7035	± 0.0083
	79.9304	6.2085	± 0.0030	3.0586	± 0.0104	-0.6188	± 0.0025

Table A.1: Experimental measurements of supercritical adsorption of CO_2 on mesoporous carbon at various temperatures.

T [°C]	P [bar]	ρ_b [mol/L]		n^{ex} [mmol/g]		n^{net} [mmol/g]	
	75.0014	5.2142	± 0.0030	2.9689	± 0.0099	-0.1196	± 0.0026
	60.4638	3.4178	± 0.0033	2.5118	± 0.0092	0.4874	± 0.0047
	46.6200	2.3242	± 0.0011	2.0857	± 0.0060	0.7090	± 0.0021
	25.1446	1.0869	± 0.0007	1.4197	± 0.0041	0.7759	± 0.0023
	10.0818	0.4040	± 0.0003	0.7886	± 0.0023	0.5493	± 0.0016
	3.0746	0.1194	± 0.0002	0.3241	± 0.0010	0.2534	± 0.0008
	1.1616	0.0447	± 0.0002	0.1660	± 0.0006	0.1395	± 0.0006
	0.5214	0.0201	± 0.0002	0.1049	± 0.0005	0.0930	± 0.0005
	0.1646	0.0064	± 0.0002	0.0654	± 0.0005	0.0617	± 0.0004
60	250.7544	17.8222	± 0.0082	0.4413	± 0.0185	-10.1151	± 0.0271
	209.8348	16.6997	± 0.0077	0.5759	± 0.0174	-9.3157	± 0.0250
	179.9668	15.5022	± 0.0079	0.7402	± 0.0168	-8.4420	± 0.0228
	160.0196	14.3423	± 0.0096	0.9207	± 0.0190	-7.5746	± 0.0224
	130.0448	11.3110	± 0.0053	1.4741	± 0.0125	-5.2256	± 0.0142
	117.9878	9.3420	± 0.0066	1.8214	± 0.0130	-3.7120	± 0.0114
	108.8550	7.8297	± 0.0036	2.0372	± 0.0098	-2.6005	± 0.0072
	97.9738	6.2467	± 0.0032	2.1451	± 0.0088	-1.5549	± 0.0046
	85.9320	4.8884	± 0.0023	2.1176	± 0.0076	-0.7779	± 0.0025
	69.8708	3.5109	± 0.0018	1.9403	± 0.0065	-0.1392	± 0.0017
	54.0726	2.4629	± 0.0013	1.6941	± 0.0053	0.2353	± 0.0015
	30.2962	1.2256	± 0.0006	1.2201	± 0.0035	0.4941	± 0.0014
	15.0032	0.5704	± 0.0003	0.7768	± 0.0022	0.4390	± 0.0012
	5.0864	0.1867	± 0.0003	0.3513	± 0.0013	0.2407	± 0.0010
	3.0560	0.1116	± 0.0002	0.2447	± 0.0009	0.1786	± 0.0007
	1.1496	0.0421	± 0.0004	0.1335	± 0.0011	0.1085	± 0.0010
	0.5812	0.0210	± 0.0003	0.0960	± 0.0009	0.0835	± 0.0009
	0.1620	0.0060	± 0.0002	0.0653	± 0.0006	0.0618	± 0.0006

Table A.2: Experimental measurements of supercritical adsorption of CH_4 on mesoporous carbon at various temperatures.

T [°C]	P [bar]	ρ_b [mol/L]		n^{ex} [mmol/g]		n^{net} [mmol/g]	
80	0.1600	0.0057	± 0.0010	0.0059	± 0.0028	0.0025	± 0.0026
	0.5140	0.0178	± 0.0009	0.0184	± 0.0024	0.0079	± 0.0022
	1.1142	0.0382	± 0.0010	0.0354	± 0.0026	0.0127	± 0.0024
	5.3180	0.1823	± 0.0009	0.1432	± 0.0024	0.0352	± 0.0022
	10.0170	0.3448	± 0.0009	0.2391	± 0.0024	0.0349	± 0.0021
	20.0350	0.6943	± 0.0009	0.3965	± 0.0026	-0.0148	± 0.0021
	31.9984	1.1194	± 0.0011	0.5359	± 0.0031	-0.1271	± 0.0023
	52.1180	1.8512	± 0.0013	0.6918	± 0.0036	-0.4047	± 0.0026
	69.7984	2.5073	± 0.0018	0.7789	± 0.0050	-0.7062	± 0.0040
	83.9238	3.0380	± 0.0017	0.8238	± 0.0046	-0.9757	± 0.0035
	99.8832	3.6434	± 0.0020	0.8598	± 0.0053	-1.2982	± 0.0045
	115.0092	4.2177	± 0.0022	0.8785	± 0.0055	-1.6197	± 0.0050
	131.4120	4.8403	± 0.0026	0.8892	± 0.0063	-1.9778	± 0.0060
	149.9038	5.5347	± 0.0029	0.8862	± 0.0069	-2.3921	± 0.0071
	175.9026	6.4850	± 0.0032	0.8682	± 0.0075	-2.9730	± 0.0083
	237.7130	8.5804	± 0.0048	0.7914	± 0.0102	-4.2910	± 0.0121
	219.5104	7.9927	± 0.0043	0.8201	± 0.0093	-3.9142	± 0.0109
	189.8750	6.9823	± 0.0035	0.8615	± 0.0080	-3.2742	± 0.0091
40	205.8554	9.1742	± 0.0052	0.9372	± 0.0116	-4.4969	± 0.0132
	191.8912	8.5999	± 0.0046	0.9752	± 0.0104	-4.1187	± 0.0118
	175.7740	7.9087	± 0.0038	1.0092	± 0.0090	-3.6753	± 0.0102
	173.4202	7.8032	± 0.0040	1.0249	± 0.0091	-3.5972	± 0.0100
	159.7100	7.1846	± 0.0038	1.0475	± 0.0089	-3.2081	± 0.0094
	143.3302	6.4250	± 0.0032	1.0807	± 0.0077	-2.7250	± 0.0077
	130.1244	5.7990	± 0.0028	1.0992	± 0.0070	-2.3357	± 0.0066
	115.0608	5.0785	± 0.0026	1.1094	± 0.0068	-1.8987	± 0.0060
	100.0308	4.3622	± 0.0023	1.1065	± 0.0059	-1.4773	± 0.0047
	80.0052	3.4192	± 0.0018	1.0740	± 0.0050	-0.9513	± 0.0034
	63.4740	2.6612	± 0.0015	1.0176	± 0.0044	-0.5587	± 0.0025
	49.9732	2.0606	± 0.0012	0.9437	± 0.0039	-0.2768	± 0.0022
	32.2568	1.2984	± 0.0010	0.7870	± 0.0033	0.0180	± 0.0020
	19.9730	0.7916	± 0.0009	0.6121	± 0.0028	0.1432	± 0.0020

Table A.2: Experimental measurements of supercritical adsorption of CH_4 on mesoporous carbon at various temperatures.

T [°C]	P [bar]	ρ_b [mol/L]		n^{ex} [mmol/g]		n^{net} [mmol/g]	
	10.0632	0.3948	± 0.0008	0.3938	± 0.0024	0.1600	± 0.0020
	4.8850	0.1919	± 0.0008	0.2323	± 0.0022	0.1187	± 0.0020
	1.0850	0.0447	± 0.0008	0.0728	± 0.0021	0.0463	± 0.0020
	0.4980	0.0221	± 0.0008	0.0409	± 0.0022	0.0278	± 0.0021
	0.1530	0.0089	± 0.0008	0.0197	± 0.0021	0.0145	± 0.0020
60	214.7308	8.5847	± 0.0042	0.8726	± 0.0098	-4.2123	± 0.0117
	184.7096	7.4586	± 0.0038	0.9306	± 0.0086	-3.4873	± 0.0097
	160.0428	6.4745	± 0.0035	0.9699	± 0.0082	-2.8651	± 0.0085
	134.7574	5.4297	± 0.0028	0.9947	± 0.0071	-2.2214	± 0.0068
	110.0372	4.3869	± 0.0023	0.9922	± 0.0060	-1.6063	± 0.0051
	87.0470	3.4218	± 0.0018	0.9603	± 0.0048	-1.0665	± 0.0035
	64.7974	2.5032	± 0.0014	0.8893	± 0.0042	-0.5933	± 0.0027
	40.0042	1.5109	± 0.0013	0.7332	± 0.0040	-0.1617	± 0.0029
	20.0888	0.7431	± 0.0009	0.5012	± 0.0027	0.0610	± 0.0021
	10.0200	0.3682	± 0.0012	0.3124	± 0.0032	0.0943	± 0.0028
	5.0106	0.1844	± 0.0008	0.1877	± 0.0022	0.0785	± 0.0020
	1.0470	0.0411	± 0.0010	0.0600	± 0.0026	0.0356	± 0.0024
	0.4990	0.0187	± 0.0008	0.0374	± 0.0023	0.0263	± 0.0021
	0.1520	0.0062	± 0.0008	0.0215	± 0.0021	0.0178	± 0.0020

Table A.3: Experimental measurements of supercritical adsorption of CO_2 on mesoporous zeolite at various temperatures.

T [°C]	P [bar]	ρ_b [mol/L]		n^{ex} [mmol/g]		n^{net} [mmol/g]	
80	20.0796	0.7201	± 0.0053	2.2378	± 0.0091	1.9537	± 0.0070
	54.0860	2.1950	± 0.0054	2.5767	± 0.0106	1.7108	± 0.0074
	120.6860	6.7513	± 0.0059	2.2263	± 0.0182	-0.4372	± 0.0077
	250.7504	15.5447	± 0.0088	0.5950	± 0.0386	-5.5374	± 0.0129
	220.1630	14.3733	± 0.0092	0.8015	± 0.0362	-4.8689	± 0.0125
	189.9572	12.7955	± 0.0089	1.0983	± 0.0336	-3.9496	± 0.0142
	165.0572	10.9821	± 0.0073	1.4562	± 0.0280	-2.8763	± 0.0103
	139.8570	8.6122	± 0.0064	1.9060	± 0.0229	-1.4915	± 0.0100
	120.0214	6.6957	± 0.0059	2.2412	± 0.0184	-0.4003	± 0.0084

Table A.3: Experimental measurements of supercritical adsorption of CO_2 on mesoporous zeolite at various temperatures.

T [°C]	P [bar]	ρ_b [mol/L]		n^{ex} [mmol/g]		n^{net} [mmol/g]	
	100.0192	5.0113	± 0.0055	2.4594	± 0.0152	0.4824	± 0.0083
	80.3062	3.6465	± 0.0052	2.5693	± 0.0121	1.1308	± 0.0069
	60.3872	2.5101	± 0.0052	2.5863	± 0.0108	1.5960	± 0.0073
	48.1760	1.9106	± 0.0050	2.5576	± 0.0098	1.8038	± 0.0070
	30.2154	1.1213	± 0.0049	2.4140	± 0.0090	1.9716	± 0.0069
	15.0176	0.5295	± 0.0049	2.1082	± 0.0085	1.8993	± 0.0066
	5.1360	0.1730	± 0.0049	1.4949	± 0.0083	1.4266	± 0.0065
	2.7558	0.0900	± 0.0050	1.1080	± 0.0088	1.0725	± 0.0070
	1.2144	0.0388	± 0.0049	0.6744	± 0.0083	0.6591	± 0.0065
	0.5424	0.0151	± 0.0050	0.3756	± 0.0094	0.3697	± 0.0078
	0.1460	0.0009	± 0.0049	0.1327	± 0.0083	0.1323	± 0.0065
60	51.4270	2.3084	± 0.0050	2.8205	± 0.0103	1.9098	± 0.0071
	251.2120	17.8521	± 0.0102	0.2893	± 0.0439	-6.7534	± 0.0135
	222.0000	17.0919	± 0.0093	0.4129	± 0.0418	-6.3299	± 0.0126
	201.3884	16.4181	± 0.0078	0.5677	± 0.0395	-5.8810	± 0.0107
	170.1004	15.0021	± 0.0073	0.8359	± 0.0361	-5.0582	± 0.0096
	149.9684	13.6090	± 0.0066	1.1272	± 0.0328	-4.2213	± 0.0090
	137.0332	12.2611	± 0.0067	1.4109	± 0.0301	-3.4097	± 0.0093
	127.1136	10.9097	± 0.0054	1.7105	± 0.0264	-2.5810	± 0.0075
	120.0120	9.7610	± 0.0068	1.9571	± 0.0259	-1.8846	± 0.0114
	111.1738	8.2400	± 0.0040	2.2744	± 0.0198	-0.9717	± 0.0052
	103.0276	6.9641	± 0.0033	2.5030	± 0.0167	-0.2432	± 0.0044
	92.0706	5.5391	± 0.0035	2.6979	± 0.0141	0.5103	± 0.0053
	77.6472	4.1301	± 0.0020	2.8268	± 0.0100	1.1917	± 0.0028
	60.9950	2.8943	± 0.0014	2.8643	± 0.0071	1.7142	± 0.0022
	34.9878	1.4488	± 0.0009	2.7515	± 0.0039	2.1694	± 0.0019
	15.1304	0.5750	± 0.0006	2.4165	± 0.0021	2.1792	± 0.0015
	5.0530	0.1848	± 0.0005	1.8399	± 0.0017	1.7585	± 0.0015
	2.7520	0.0997	± 0.0006	1.4675	± 0.0019	1.4213	± 0.0018
	1.2262	0.0441	± 0.0004	0.9727	± 0.0013	0.9507	± 0.0013
	0.4936	0.0175	± 0.0004	0.5381	± 0.0013	0.5287	± 0.0012
	0.1620	0.0054	± 0.0005	0.2408	± 0.0014	0.2375	± 0.0014

Table A.3: Experimental measurements of supercritical adsorption of CO_2 on mesoporous zeolite at various temperatures.

T [°C]	P [bar]	ρ_b [mol/L]		n^{ex} [mmol/g]		n^{net} [mmol/g]	
40	49.4600	2.5282	± 0.0013	3.1889	± 0.0063	2.1810	± 0.0022
	49.5392	2.5328	± 0.0013	3.1880	± 0.0062	2.1783	± 0.0021
	250.1486	19.9633	± 0.0092	0.0673	± 0.0478	-7.7709	± 0.0120
	219.4772	19.4243	± 0.0090	0.1406	± 0.0464	-7.4863	± 0.0114
	193.0026	18.8770	± 0.0087	0.2312	± 0.0451	-7.1813	± 0.0110
	169.8648	18.2938	± 0.0085	0.3376	± 0.0437	-6.8464	± 0.0108
	129.8798	16.7924	± 0.0080	0.6280	± 0.0406	-5.9679	± 0.0115
	107.9574	15.1887	± 0.0076	0.9755	± 0.0368	-4.9925	± 0.0103
	97.1506	13.4846	± 0.0070	1.3935	± 0.0341	-3.9074	± 0.0131
	92.0954	11.7595	± 0.0089	1.8544	± 0.0328	-2.7715	± 0.0165
	89.1882	10.1388	± 0.0068	2.3195	± 0.0275	-1.6722	± 0.0132
	87.3590	9.0426	± 0.0066	2.6195	± 0.0275	-0.9433	± 0.0169
	84.0186	7.4810	± 0.0061	2.9943	± 0.0204	0.0428	± 0.0092
	79.9638	6.2557	± 0.0048	3.1630	± 0.0167	0.6918	± 0.0072
	71.0726	4.6490	± 0.0032	3.2843	± 0.0142	1.4433	± 0.0088
	60.7324	3.4461	± 0.0019	3.2291	± 0.0087	1.8607	± 0.0032
	35.8902	1.6603	± 0.0009	3.0841	± 0.0043	2.4175	± 0.0018
	21.9868	0.9342	± 0.0007	2.8945	± 0.0027	2.5139	± 0.0016
	5.0566	0.1975	± 0.0005	2.2171	± 0.0015	2.1290	± 0.0013
	1.5284	0.0585	± 0.0005	1.5180	± 0.0015	1.4878	± 0.0014
	0.5012	0.0189	± 0.0006	0.8470	± 0.0018	0.8355	± 0.0017
	0.1572	0.0057	± 0.0005	0.3990	± 0.0015	0.3949	± 0.0014
35	46.7482	2.4286	± 0.0013	3.2757	± 0.0063	2.3065	± 0.0027
	250.5420	20.4555	± 0.0094	0.0010	± 0.0488	-8.0301	± 0.0119
	206.9710	19.7541	± 0.0091	0.1050	± 0.0472	-7.6513	± 0.0117
	172.5366	19.0333	± 0.0090	0.2256	± 0.0457	-7.2483	± 0.0117
	130.1256	17.7731	± 0.0092	0.4592	± 0.0432	-6.5210	± 0.0123
	107.3344	16.6046	± 0.0080	0.6997	± 0.0399	-5.8228	± 0.0104
	91.1258	14.9919	± 0.0155	1.0712	± 0.0498	-4.8200	± 0.0323
	85.1268	13.5842	± 0.0088	1.4489	± 0.0356	-3.8914	± 0.0153
	82.1450	11.6762	± 0.0075	2.0275	± 0.0301	-2.5664	± 0.0120
	81.0462	10.0712	± 0.0284	2.5219	± 0.0684	-1.4443	± 0.0567

Table A.3: Experimental measurements of supercritical adsorption of CO_2 on mesoporous zeolite at various temperatures.

T [°C]	P [bar]	ρ_b [mol/L]		n^{ex} [mmol/g]		n^{net} [mmol/g]	
	79.3282	8.1778	± 0.0056	3.1652	± 0.0212	-0.0607	± 0.0083
	77.9752	7.3181	± 0.0060	3.3298	± 0.0210	0.4407	± 0.0112
	75.0472	6.1492	± 0.0040	3.4370	± 0.0158	1.0063	± 0.0062
	67.9762	4.6375	± 0.0117	3.4461	± 0.0231	1.6089	± 0.0163
	55.8440	3.1829	± 0.0015	3.3460	± 0.0078	2.0803	± 0.0024
	36.1048	1.7238	± 0.0018	3.1754	± 0.0063	2.4834	± 0.0046
	20.1786	0.8695	± 0.0007	2.9434	± 0.0026	2.5879	± 0.0015
	5.0548	0.2019	± 0.0007	2.3114	± 0.0022	2.2210	± 0.0020
	1.2548	0.0497	± 0.0005	1.5028	± 0.0016	1.4761	± 0.0015
	0.5356	0.0215	± 0.0004	0.9780	± 0.0014	0.9649	± 0.0013
	0.1600	0.0063	± 0.0005	0.4773	± 0.0016	0.4725	± 0.0015

Table A.4: Experimental measurements of supercritical adsorption of CH_4 on mesoporous zeolite at various temperatures.

T [°C]	P [bar]	ρ_b [mol/L]		n^{ex} [mmol/g]		n^{net} [mmol/g]	
80	10.3660	0.3564	± 0.0018	1.0256	± 0.0053	0.8885	± 0.0049
	99.1686	3.6170	± 0.0019	1.6581	± 0.0083	0.2663	± 0.0031
	158.3946	5.8554	± 0.0135	1.4637	± 0.0321	-0.7894	± 0.0262
	148.4512	5.4839	± 0.0094	1.5029	± 0.0240	-0.6074	± 0.0188
	128.4426	4.7325	± 0.0115	1.5767	± 0.0326	-0.2444	± 0.0287
	109.8704	4.0220	± 0.0027	1.6333	± 0.0099	0.0856	± 0.0047
	90.1438	3.2739	± 0.0019	1.6757	± 0.0079	0.4159	± 0.0037
	70.9218	2.5500	± 0.0014	1.6885	± 0.0059	0.7072	± 0.0025
	44.8244	1.5849	± 0.0010	1.6239	± 0.0039	1.0140	± 0.0019
	26.1596	0.9104	± 0.0008	1.4482	± 0.0028	1.0979	± 0.0019
	15.0088	0.5176	± 0.0008	1.1995	± 0.0025	1.0003	± 0.0020
	5.0100	0.1716	± 0.0007	0.6698	± 0.0020	0.6038	± 0.0018
	1.2080	0.0415	± 0.0008	0.2133	± 0.0023	0.1973	± 0.0022
	0.4856	0.0168	± 0.0007	0.0875	± 0.0022	0.0810	± 0.0021
	0.1360	0.0049	± 0.0008	0.0198	± 0.0023	0.0179	± 0.0021
60	0.1300	0.0067	± 0.0007	0.0512	± 0.0019	0.0486	± 0.0018
	0.5520	0.0214	± 0.0007	0.1686	± 0.0021	0.1604	± 0.0019

Table A.4: Experimental measurements of supercritical adsorption of CH_4 on mesoporous zeolite at various temperatures.

T [°C]	P [bar]	ρ_b [mol/L]		n^{ex} [mmol/g]		n^{net} [mmol/g]	
	1.6792	0.0625	± 0.0007	0.4229	± 0.0022	0.3989	± 0.0020
	4.9780	0.1823	± 0.0009	0.8819	± 0.0027	0.8118	± 0.0025
	15.4330	0.5684	± 0.0010	1.4447	± 0.0029	1.2259	± 0.0025
	25.1528	0.9370	± 0.0008	1.6431	± 0.0028	1.2825	± 0.0019
	48.0404	1.8286	± 0.0026	1.8140	± 0.0069	1.1103	± 0.0052
	64.4446	2.4888	± 0.0014	1.8389	± 0.0059	0.8812	± 0.0027
	89.6230	3.5308	± 0.0019	1.8053	± 0.0081	0.4466	± 0.0032
	108.8782	4.3415	± 0.0029	1.7409	± 0.0107	0.0703	± 0.0052
	123.8272	4.9716	± 0.0042	1.6787	± 0.0133	-0.2344	± 0.0074
	140.4724	5.6724	± 0.0079	1.6042	± 0.0194	-0.5785	± 0.0132
	148.8726	6.0198	± 0.0061	1.5593	± 0.0178	-0.7571	± 0.0111
	186.2900	7.5268	± 0.0086	1.3608	± 0.0228	-1.5356	± 0.0143
40	1.9508	0.0787	± 0.0006	0.6747	± 0.0019	0.6445	± 0.0018
	5.0492	0.1990	± 0.0006	1.1504	± 0.0019	1.0738	± 0.0017
	15.0786	0.5954	± 0.0007	1.6767	± 0.0024	1.4476	± 0.0019
	34.8078	1.4109	± 0.0010	1.9452	± 0.0038	1.4023	± 0.0023
	55.7362	2.3180	± 0.0019	1.9979	± 0.0063	1.1060	± 0.0036
	75.7146	3.2249	± 0.0016	1.9698	± 0.0073	0.7289	± 0.0026
	96.9278	4.2195	± 0.0020	1.8922	± 0.0094	0.2685	± 0.0029
	112.6604	4.9699	± 0.0036	1.8146	± 0.0124	-0.0978	± 0.0060
	131.7342	5.8843	± 0.0091	1.7053	± 0.0227	-0.5590	± 0.0167
	152.6656	6.8701	± 0.0112	1.5719	± 0.0280	-1.0717	± 0.0212
	167.6186	7.5524	± 0.0088	1.4693	± 0.0252	-1.4369	± 0.0176
	185.8554	8.3559	± 0.0049	1.3510	± 0.0205	-1.8643	± 0.0101
	0.4980	0.0230	± 0.0016	0.2346	± 0.0050	0.2258	± 0.0047
	0.1510	0.0099	± 0.0008	0.0866	± 0.0022	0.0828	± 0.0020

A.2 Lattice DFT modelling

A.2.1 Parameters of the Lattice DFT model for Slit Pores

The fitted parameters obtained upon application of the slit lattice DFT model to supercritical CO_2 and CH_4 adsorption isotherms measured on MC, AC and MZ are summarised in Table A.5.

Table A.5: Parameters of the slit lattice DFT model applied to describe supercritical CO_2 and CH_4 adsorption on mesoporous carbon, activated carbon and mesoporous zeolite, and the obtained values of the objective function per experimental point (Φ/N).

	Mesoporous carbon		Activated carbon		Mesoporous zeolite	
Parameter	CO_2	CH_4	CO_2	CH_4	CO_2	CH_4
	Fitted Parameters					
ε_{sf}/k_B [K]	−739.64	−860.92	−1109	−1042	−1503	−1229
ρ_{max} [mol/L]	22.82	32.57	28.60	28.22	20.46	18.22
	Saturation Factor, c_{sat}					
25 °C	–	–	–	1.33	–	–
35 °C	–	–	–	–	1.20	–
40 °C	1.48	0.59	1.52	1.28	1.18	1.06
55 °C	–	–	1.47	1.26	–	–
60 °C	1.28	0.57	–	–	1.09	1.01
70 °C	–	–	1.43	1.22	–	–
80 °C	1.14	0.54	–	–	1.04	0.95
Φ/N [mmol/g]^2	0.0156	0.00134	0.356	0.0571	0.0563	0.00491

A.2.2 Henry constants from the lattice DFT model

For the van't Hoff equation to apply to the calculated Henry constants from the lattice DFT model, it is evident that $\ln(c_{sat})$ vs. 1/T needs to be linear. Figure A.2 shows that this is the case, and that the integrity of the van't Hoff equation is maintained.

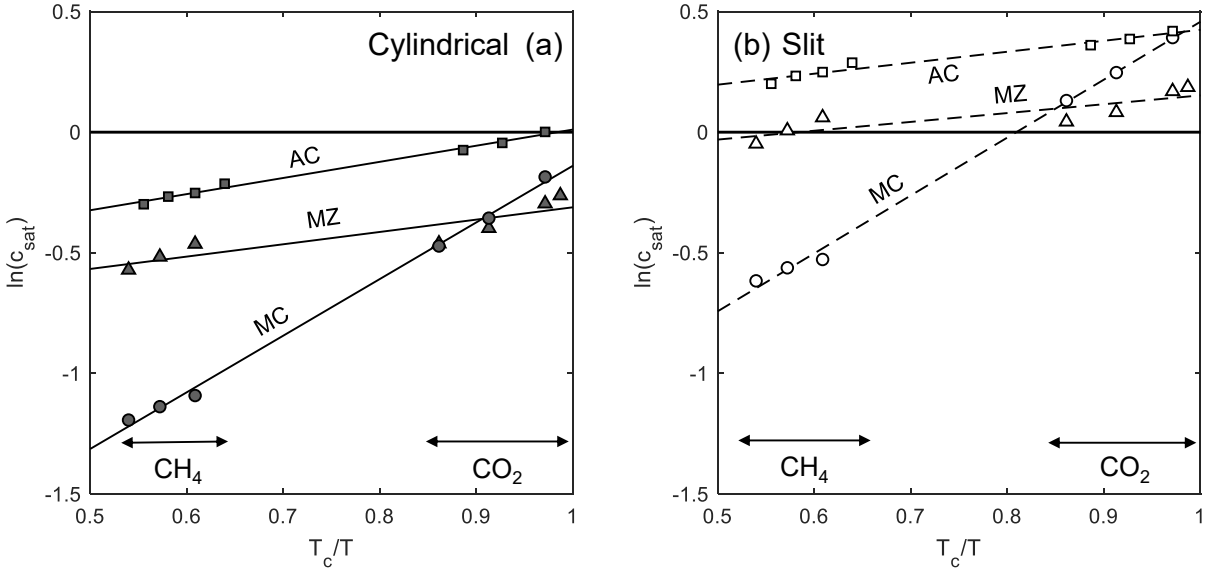

Figure A.2: The pore saturation factor, $\ln(c_{\mathrm{sat}})$, as a function of T_{c}/T for mesoporous carbon (circles), activated carbon (squares) and mesoporous zeolite (triangles) obtained with the lattice DFT model that uses (a) cylindrical and (b) slit pores. Linear fits for both pore geometries and and all materials are also shown.

Appendix B

Shales

B.1 Experimental Data

B.1.1 Subcritical Adsorption

Figure B.1 shows the subcritical CO_2 adsorption isotherms at various temperatures for all four shales.

B.1.2 Supercritical Adsorption

Figure B.2 shows the in-situ bulk fluid density measurements which accompany the net and excess adsorption isotherms for all four shales.

The supercritical adsorption results for LG4 (Tables B.1 and B.2), ML (Tables B.3 and B.4), B6 (Tables B.5 and B.6) and B8 (Tables B.7 and B.8) are shown below.

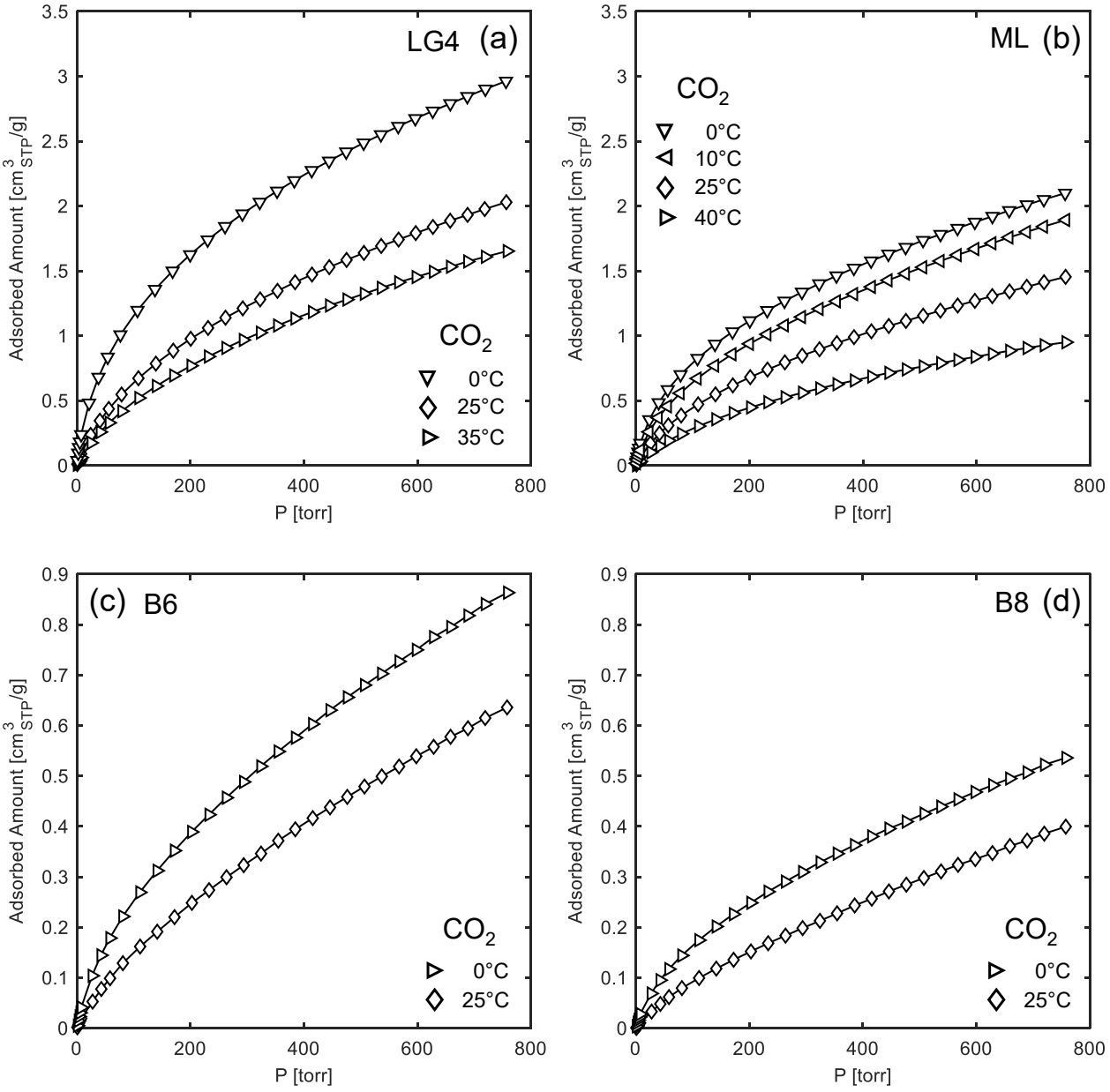

Figure B.1: Subcritical CO_2 adsorption on the (a) LG4, (b) ML, (c) B6, and (d) B8 shales. STP conditions are defined as 273.15 K and 1 atm.

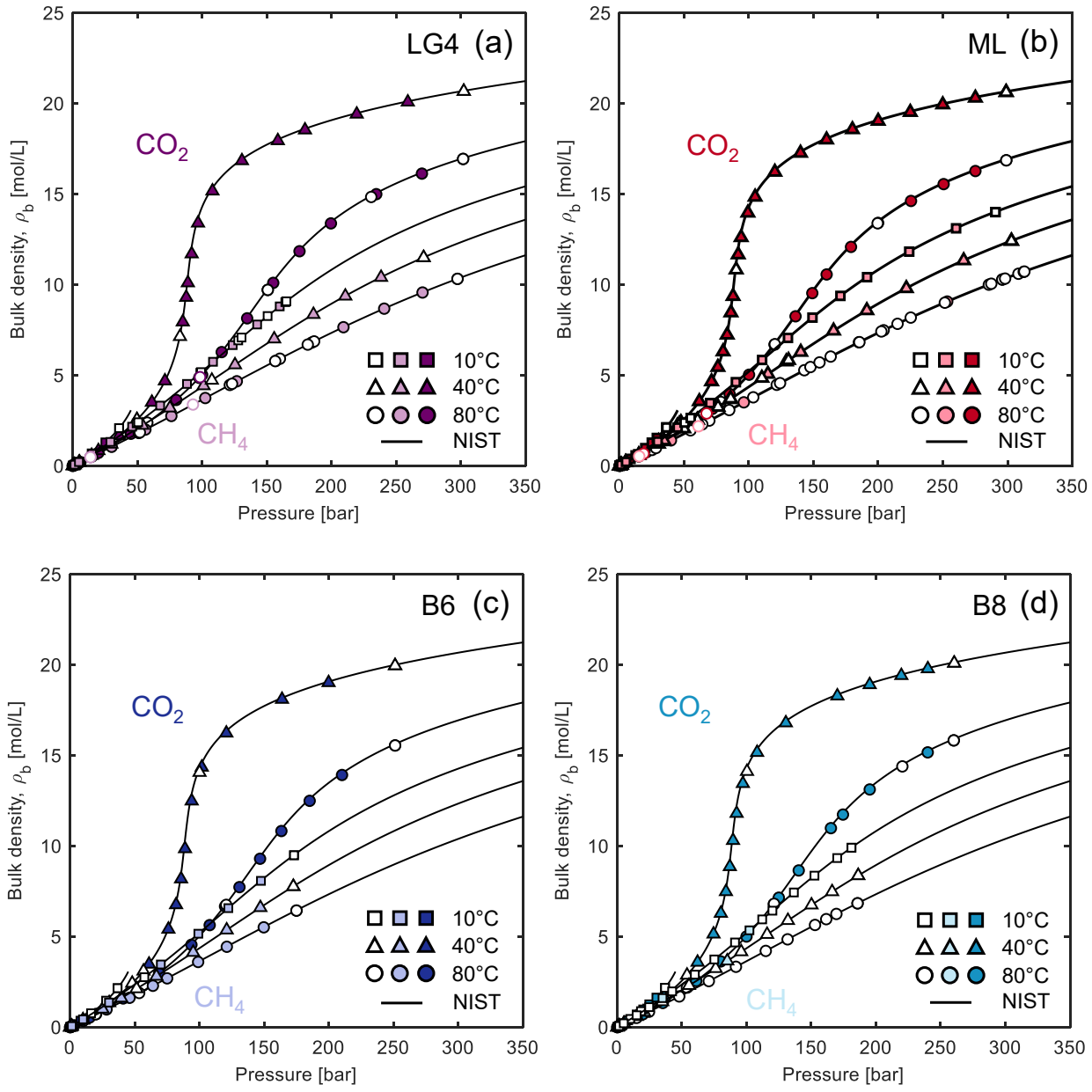

Figure B.2: Bulk density measurements plotted as a function of the measured pressure and their comparison with data reported by NIST (solid lines) [242] for the (a) LG4, (b) ML, (c) B6 and (d) B8 shales. Empty symbols denote data taken in adsorption mode and filled symbols represent data taken in desorption mode. Symbols with a black outline represent data on the powdered sample, while those with a coloured outline, only relevant to the LG4 and ML shales, represent data on the chip sample.

Table B.1: Experimental measurements of supercritical adsorption of CO_2 on the LG4 shale at various temperatures.

T [°C]	P [bar]	ρ_b [mol/L]		n^{ex} [µmol/g]		n^{net} [µmol/g]	
80	301.7818	16.9457	± 0.0088	134.3829	± 15.4563	-6458.3926	± 6.7961
	269.9436	16.1361	± 0.0078	139.8105	± 14.2387	-6138.0117	± 5.9259
	234.6548	15.0015	± 0.0071	156.5957	± 13.1294	-5679.7765	± 5.3740
	199.6192	13.3881	± 0.0093	173.8877	± 15.1180	-5034.8109	± 9.0090
	175.3456	11.8505	± 0.0055	194.6045	± 10.2529	-4415.8889	± 4.0762
	155.0366	10.1043	± 0.0069	218.2446	± 11.0507	-3712.8839	± 6.2321
	134.8770	8.1459	± 0.0038	249.5295	± 7.0491	-2919.6685	± 2.7916
	115.2138	6.2822	± 0.0099	266.6876	± 13.4830	-2177.4356	± 9.5987
	100.0704	5.0277	± 0.0033	275.0772	± 5.6584	-1680.9661	± 3.4966
	80.0638	3.6411	± 0.0023	271.5118	± 3.8439	-1145.0524	± 2.1630
	45.0326	1.7736	± 0.0008	235.7095	± 1.5551	-454.2967	± 0.6498
	19.8122	0.7144	± 0.0004	176.9189	± 0.7139	-101.0206	± 0.3866
	6.0558	0.2095	± 0.0004	107.7305	± 0.6997	26.2062	± 0.6107
	1.5310	0.0524	± 0.0002	54.1960	± 0.2889	33.8007	± 0.2565
	0.5798	0.0199	± 0.0002	33.2520	± 0.3066	25.5080	± 0.2759
	0.1078	0.0039	± 0.0001	17.0732	± 0.2854	15.5658	± 0.2559
	57.7214	2.3873	± 0.0021	250.8807	± 3.3342	-677.8954	± 2.3082
	98.0458	4.8747	± 0.0024	274.7467	± 4.3376	-1621.7765	± 1.8597
	150.8284	9.7169	± 0.0045	226.3964	± 8.5204	-3553.9986	± 3.5708
40	302.2634	20.6777	± 0.0101	135.2689	± 18.3674	-7909.4837	± 7.6863
	259.0412	20.0879	± 0.0092	138.9433	± 17.3080	-7676.3152	± 6.7624
	219.5716	19.4191	± 0.0098	143.5894	± 17.6806	-7411.4787	± 7.9547
	179.5788	18.5452	± 0.0105	151.9009	± 18.2314	-7063.1789	± 9.4146
	158.5956	17.9516	± 0.0092	159.4497	± 16.4350	-6824.6851	± 7.4710
	130.8420	16.8463	± 0.0077	175.5473	± 14.5318	-6378.5692	± 5.7058
	108.0694	15.1734	± 0.0180	196.4186	± 25.8772	-5706.8532	± 18.0999
	96.9286	13.4036	± 0.0230	224.7706	± 33.4271	-4989.9376	± 25.5431
	92.0120	11.7026	± 0.0142	262.7884	± 20.9921	-4290.1501	± 15.1752
	89.0784	10.1042	± 0.0107	305.6196	± 16.4255	-3625.4643	± 11.7610
	87.7888	9.3035	± 0.0056	335.2997	± 9.6272	-3284.2796	± 5.3821
	85.1200	7.9457	± 0.0050	378.9271	± 8.0790	-2712.3775	± 4.1553
	71.3202	4.6893	± 0.0027	393.2396	± 4.5544	-1431.1363	± 2.2588

Table B.1: Experimental measurements of supercritical adsorption of CO_2 on the LG4 shale at various temperatures.

T [°C]	P [bar]	ρ_b [mol/L]		n^{ex} [µmol/g]		n^{net} [µmol/g]	
	61.2470	3.5099	± 0.0118	376.4161	± 15.7493	-989.1255	± 11.9645
	35.8788	1.6627	± 0.0008	317.1352	± 1.4985	-329.7423	± 0.6890
	19.9294	0.8399	± 0.0006	262.5165	± 1.0209	-64.2492	± 0.6715
	4.8356	0.1902	± 0.0002	159.1509	± 0.3291	85.1518	± 0.2638
	1.5182	0.0593	± 0.0002	102.1105	± 0.2899	79.0205	± 0.2567
	0.5148	0.0205	± 0.0002	65.9378	± 0.2899	57.9750	± 0.2579
	0.1820	0.0078	± 0.0001	44.4463	± 0.2854	41.3990	± 0.2559
	49.6800	2.5481	± 0.0012	350.9034	± 2.2185	-640.4605	± 0.9003
	82.9800	7.1406	± 0.0040	389.9681	± 6.7776	-2388.1096	± 3.2085
10	35.9178	2.0849	± 0.0011	470.8430	± 1.9663	-340.2825	± 0.9539
	25.3050	1.2985	± 0.0006	393.8806	± 1.1840	-111.3000	± 0.5447
	14.7112	0.6900	± 0.0004	323.5441	± 0.6783	55.0830	± 0.3738
	5.3578	0.2357	± 0.0002	235.1305	± 0.3536	143.4269	± 0.2698
	1.4606	0.0629	± 0.0002	153.1107	± 0.2905	128.6308	± 0.2568
	0.4760	0.0205	± 0.0001	103.9128	± 0.2859	95.9338	± 0.2560
	0.1290	0.0057	± 0.0001	65.9394	± 0.2854	63.7066	± 0.2559

Table B.2: Experimental measurements of supercritical adsorption of CH_4 on the LG4 shale at various temperatures.

T [°C]	P [bar]	ρ_b [mol/L]		n^{ex} [µmol/g]		n^{net} [µmol/g]	
80	297.4328	10.3228	± 0.0100	137.4395	± 14.9293	-3866.8024	± 11.9390
	270.4150	9.5703	± 0.0075	142.4788	± 11.0377	-3569.8979	± 8.6079
	240.7912	8.6792	± 0.0063	147.6962	± 9.7077	-3218.9952	± 7.6810
	209.3052	7.6542	± 0.0056	155.5013	± 8.8720	-2813.5910	± 7.1605
	184.8136	6.8058	± 0.0049	159.5700	± 8.0321	-2480.4284	± 6.5681
	156.9648	5.7975	± 0.0050	162.8554	± 8.4890	-2086.0055	± 7.1747
	126.8716	4.6702	± 0.0040	164.1443	± 7.0805	-1647.4396	± 6.0735
	102.4996	3.7455	± 0.0038	161.7744	± 6.9823	-1291.1236	± 6.1002
	76.3000	2.7541	± 0.0036	154.5545	± 6.7040	-913.7894	± 5.9299
	56.2246	2.0054	± 0.0035	144.1724	± 6.6558	-633.7138	± 5.9404
	30.1440	1.0529	± 0.0034	117.2748	± 6.5686	-291.1304	± 5.9052
	14.9540	0.5163	± 0.0033	87.4674	± 6.5019	-112.7951	± 5.8555

Table B.2: Experimental measurements of supercritical adsorption of CH_4 on the LG4 shale at various temperatures.

T [°C]	P [bar]	ρ_b [mol/L]		n^{ex} [µmol/g]		n^{net} [µmol/g]	
	4.9440	0.1700	± 0.0034	52.0310	± 6.5886	-13.9141	± 5.9391
	1.4402	0.0499	± 0.0033	28.5301	± 6.4924	9.1788	± 5.8519
	0.5338	0.0191	± 0.0033	20.0575	± 6.4948	12.6428	± 5.8540
	0.1396	0.0057	± 0.0033	15.8064	± 6.4927	13.5787	± 5.8521
	51.9554	1.8486	± 0.0035	140.9521	± 6.6068	-576.1205	± 5.9014
	181.7086	6.6948	± 0.0051	162.5185	± 8.3012	-2434.4217	± 6.7954
	123.2028	4.5314	± 0.0046	166.9194	± 7.9400	-1590.8445	± 6.8011
	156.5666	5.7832	± 0.0049	166.1413	± 8.2101	-2077.1780	± 6.8777
40	271.2620	11.4953	± 0.0120	164.8681	± 17.7911	-4294.2065	± 14.2070
	238.3834	10.4035	± 0.0077	173.8088	± 11.2992	-3861.7653	± 8.7294
	210.7562	9.3703	± 0.0061	182.2112	± 9.3533	-3452.5830	± 7.3204
	186.1294	8.3583	± 0.0054	190.0867	± 8.4974	-3052.1402	± 6.7462
	155.7690	7.0060	± 0.0047	198.9494	± 7.8698	-2518.7202	± 6.4473
	125.4742	5.5781	± 0.0042	205.4276	± 7.2842	-1958.3364	± 6.1426
	101.2248	4.4207	± 0.0039	207.1436	± 7.0134	-1507.6839	± 6.0426
	75.1848	3.1963	± 0.0037	201.8875	± 6.7967	-1037.9690	± 5.9687
	53.9666	2.2381	± 0.0035	191.1069	± 6.6726	-677.0631	± 5.9278
	29.9476	1.1996	± 0.0034	164.3527	± 6.5361	-300.9759	± 5.8680
	14.6810	0.5754	± 0.0034	130.1907	± 6.5156	-93.0141	± 5.8639
	5.3710	0.2075	± 0.0034	89.0102	± 6.5047	8.5129	± 5.8586
	1.5286	0.0587	± 0.0033	54.0925	± 6.4924	31.3387	± 5.8519
	0.4680	0.0173	± 0.0033	36.0815	± 6.4923	29.3540	± 5.8519
	0.1510	0.0051	± 0.0033	28.1891	± 6.4923	26.1941	± 5.8519
10	165.1740	9.0832	± 0.0086	215.0977	± 13.7400	-3316.6233	± 10.2849
	160.0426	8.8027	± 0.0113	217.0443	± 16.8068	-3205.6050	± 12.7339
	142.5904	7.8037	± 0.0087	224.9135	± 13.1303	-2809.3304	± 9.8237
	123.7016	6.6665	± 0.0052	232.1962	± 7.8977	-2359.8507	± 5.2082
	108.4882	5.7449	± 0.0093	237.0784	± 16.4235	-1996.6584	± 13.9971
	88.3720	4.5236	± 0.0025	238.6958	± 4.3639	-1520.1713	± 2.6554
	67.6484	3.3270	± 0.0018	233.4315	± 3.0908	-1060.1868	± 1.8046
	45.9726	2.1624	± 0.0013	218.6101	± 2.2902	-622.1796	± 1.5238
	29.1986	1.3219	± 0.0010	196.0036	± 1.8847	-317.9709	± 1.4585

Table B.2: Experimental measurements of supercritical adsorption of CH_4 on the LG4 shale at various temperatures.

T [°C]	P [bar]	ρ_b [mol/L]		n^{ex} [µmol/g]		n^{net} [µmol/g]	
	14.9680	0.6590	± 0.0009	162.5148	± 1.6357	-93.7004	± 1.3914
	4.8680	0.2112	± 0.0010	111.4481	± 1.8108	29.3167	± 1.6119
	1.4724	0.0647	± 0.0008	71.6959	± 1.5049	46.5443	± 1.3330
	0.5190	0.0241	± 0.0008	49.4056	± 1.5042	40.0182	± 1.3328
	0.1570	0.0089	± 0.0010	35.2200	± 1.7567	31.7650	± 1.5588
	50.7314	2.4089	± 0.0016	226.5396	± 2.9290	-710.0794	± 2.1487
	99.2330	5.1744	± 0.0031	243.0113	± 5.3280	-1768.8937	± 3.4162
	130.5258	7.0849	± 0.0035	236.4682	± 6.1408	-2518.2753	± 3.2474

Table B.3: Experimental measurements of supercritical adsorption of CO_2 on the ML shale at various temperatures.

T [°C]	P [bar]	ρ_b [mol/L]		n^{ex} [µmol/g]		n^{net} [µmol/g]	
80	298.9990	16.8714	± 0.0078	60.8189	± 15.8292	-6200.3889	± 7.1894
	275.1334	16.2784	± 0.0077	66.0315	± 15.6977	-5975.0901	± 7.6886
	250.5972	15.5555	± 0.0072	72.5576	± 14.6140	-5700.2834	± 6.6506
	225.3760	14.6265	± 0.0069	81.0745	± 13.9000	-5346.9891	± 6.4670
	199.9628	13.4142	± 0.0064	92.5991	± 13.0641	-4885.5743	± 6.5297
	179.0162	12.0899	± 0.0056	106.5297	± 11.4626	-4380.1808	± 5.3704
	160.1750	10.5686	± 0.0061	122.8172	± 11.5034	-3799.3388	± 6.6107
	149.1014	9.5375	± 0.0045	137.5697	± 9.2528	-3401.9122	± 4.5741
	136.1438	8.2583	± 0.0049	152.2098	± 9.0768	-2912.5426	± 5.2295
	119.9126	6.6965	± 0.0031	168.3967	± 6.3819	-2316.7685	± 3.0352
	100.2090	5.0332	± 0.0024	178.4240	± 4.8565	-1689.4506	± 2.3768
	85.2102	3.9687	± 0.0019	177.9891	± 3.8483	-1294.8342	± 1.8834
	71.8886	3.1488	± 0.0016	173.4966	± 3.1934	-995.0630	± 1.6708
	55.4014	2.2668	± 0.0011	162.2598	± 2.3416	-678.9632	± 1.3190
	37.1270	1.4210	± 0.0007	141.8075	± 1.5376	-385.5615	± 0.9291
	25.1546	0.9215	± 0.0006	122.6618	± 1.3303	-219.3055	± 0.9934
	14.9592	0.5306	± 0.0004	99.4048	± 0.8958	-97.5120	± 0.7199
	4.9512	0.1702	± 0.0005	60.0324	± 1.0898	-3.1172	± 1.0012
	1.3852	0.0468	± 0.0004	30.9554	± 0.8827	13.5880	± 0.8131
	0.4140	0.0138	± 0.0004	15.7414	± 0.8565	10.6159	± 0.7807

Table B.3: Experimental measurements of supercritical adsorption of CO_2 on the ML shale at various temperatures.

T [°C]	P [bar]	ρ_b [mol/L]		n^{ex} [µmol/g]		n^{net} [µmol/g]	
	0.1518	0.0050	± 0.0004	9.4109	± 0.8504	7.5555	± 0.7800
	78.3344	3.5318	± 0.0017	175.9369	± 3.4533	-1134.7431	± 1.7442
40	298.8934	20.6300	± 0.0095	61.6070	± 19.2785	-7594.4313	± 8.6450
	275.1180	20.3163	± 0.0093	63.5667	± 18.9985	-7476.0718	± 8.5366
	249.9070	19.9479	± 0.0092	65.6466	± 18.6771	-7337.2637	± 8.4169
	224.8108	19.5292	± 0.0090	69.3717	± 18.2729	-7178.1558	± 8.2227
	200.0118	19.0413	± 0.0087	73.4941	± 17.8199	-6992.9842	± 8.0290
	180.1022	18.5755	± 0.0087	77.3470	± 17.6796	-6816.2497	± 8.3002
	160.1194	18.0085	± 0.0084	82.6225	± 16.9267	-6600.5748	± 7.6818
	139.9752	17.2742	± 0.0080	90.4166	± 16.1904	-6320.2676	± 7.3168
	120.1440	16.2265	± 0.0075	103.7273	± 15.2246	-5918.1483	± 6.9165
	104.8902	14.8496	± 0.0068	121.2840	± 13.9608	-5389.5966	± 6.3768
	99.3138	13.9702	± 0.0065	134.2766	± 13.2378	-5050.2570	± 6.1958
	94.0990	12.6172	± 0.0091	153.4524	± 16.5734	-4528.9650	± 11.1396
	91.8218	11.6655	± 0.0069	165.2717	± 13.4354	-4163.9416	± 8.3911
	87.8554	9.3682	± 0.0096	219.0484	± 15.6680	-3257.6163	± 11.1546
	86.2260	8.4621	± 0.0057	245.5776	± 10.6335	-2894.8329	± 7.0065
	83.2952	7.2361	± 0.0044	276.5345	± 8.5101	-2408.8796	± 5.4211
	80.1282	6.3085	± 0.0040	285.4000	± 7.5355	-2055.7507	± 4.7604
	76.1310	5.4501	± 0.0042	282.9144	± 7.2104	-1739.6898	± 4.7263
	71.2392	4.6569	± 0.0033	272.1005	± 5.9961	-1456.1160	± 3.9344
	61.8074	3.5599	± 0.0018	260.4945	± 3.5134	-1060.6414	± 1.7677
	46.2626	2.3077	± 0.0012	235.4242	± 2.3943	-620.9899	± 1.3479
	30.2842	1.3515	± 0.0007	202.5862	± 1.4996	-298.9887	± 0.9310
	14.9980	0.6162	± 0.0004	159.4238	± 0.9125	-69.2437	± 0.6939
	4.8688	0.1908	± 0.0003	107.1069	± 0.7014	36.3153	± 0.6275
	1.4986	0.0578	± 0.0003	69.8860	± 0.6820	48.4406	± 0.6237
	0.4122	0.0158	± 0.0003	44.0787	± 0.7787	38.2033	± 0.7176
	0.1374	0.0053	± 0.0003	30.6525	± 0.6784	28.6966	± 0.6225
	47.5906	2.3990	± 0.0012	237.2690	± 2.3792	-653.0141	± 1.2341
	90.2566	10.8338	± 0.0053	185.8005	± 10.5077	-3834.7657	± 5.0772
10	36.3098	2.1218	± 0.0011	339.4520	± 2.2561	-447.9796	± 1.3189

Table B.3: Experimental measurements of supercritical adsorption of CO_2 on the ML shale at various temperatures.

T [°C]	P [bar]	ρ_b [mol/L]		n^{ex} [µmol/g]		n^{net} [µmol/g]	
	28.9562	1.5407	± 0.0008	290.3620	± 1.6904	-281.4015	± 1.0397
	25.0484	1.2823	± 0.0007	270.6293	± 1.4516	-205.2443	± 0.9231
	20.0228	0.9798	± 0.0006	246.1305	± 1.1646	-117.4754	± 0.7775
	12.5336	0.5790	± 0.0004	208.5677	± 0.8896	-6.3080	± 0.6926
	8.6206	0.3875	± 0.0004	183.9129	± 0.8090	40.1187	± 0.6823
	4.5660	0.2001	± 0.0003	150.6567	± 0.7224	76.3824	± 0.6458
	1.4950	0.0645	± 0.0003	105.9267	± 0.6850	81.9958	± 0.6269
	0.5654	0.0244	± 0.0003	78.4916	± 0.7472	69.4194	± 0.6860
	0.1438	0.0064	± 0.0003	52.1814	± 0.6784	49.7886	± 0.6225

Table B.4: Experimental measurements of supercritical adsorption of CH_4 on the ML shale at various temperatures.

T [°C]	P [bar]	ρ_b [mol/L]		n^{ex} [µmol/g]		n^{net} [µmol/g]	
80	295.9362	10.2859	± 0.0056	95.3679	± 9.7425	-3722.1324	± 5.7023
	253.3488	9.0716	± 0.0050	101.4946	± 9.1076	-3265.3273	± 5.8060
	185.1216	6.8228	± 0.0037	111.9144	± 6.7842	-2420.2830	± 4.3370
	96.1756	3.5077	± 0.0018	113.2390	± 3.3815	-1188.6064	± 2.1413
	39.8612	1.4077	± 0.0010	91.6291	± 2.0816	-430.8185	± 1.6781
	15.1360	0.5250	± 0.0008	66.1650	± 1.8202	-128.6659	± 1.6421
	4.9430	0.1715	± 0.0007	42.8015	± 1.6685	-20.8343	± 1.5291
	2.9932	0.1044	± 0.0011	36.6585	± 2.8192	-2.0892	± 2.6414
	1.3010	0.0469	± 0.0008	29.0160	± 1.9216	11.6039	± 1.7746
	0.3940	0.0157	± 0.0008	22.7070	± 1.8513	16.8747	± 1.6970
	0.1260	0.0065	± 0.0008	21.0916	± 1.8807	18.6845	± 1.7285
40	302.9900	12.4147	± 0.0066	113.8076	± 11.8099	-4493.7901	± 7.0653
	266.0886	11.3353	± 0.0057	121.8390	± 10.3424	-4085.1428	± 5.9493
	221.7636	9.7991	± 0.0047	131.1420	± 8.6116	-3505.6945	± 4.7378
	191.2380	8.5809	± 0.0041	138.9636	± 7.4142	-3045.7524	± 3.9537
	165.5204	7.4567	± 0.0036	144.4093	± 6.5299	-2623.0634	± 3.5626
	140.1700	6.2834	± 0.0030	149.4393	± 5.4658	-2182.5827	± 2.9550
	114.7704	5.0721	± 0.0024	151.8791	± 4.4538	-1730.5779	± 2.4373
	85.3186	3.6719	± 0.0018	149.3964	± 3.3064	-1213.3807	± 1.9042

Table B.4: Experimental measurements of supercritical adsorption of CH_4 on the ML shale at various temperatures.

T [°C]	P [bar]	ρ_b [mol/L]		n^{ex} [µmol/g]		n^{net} [µmol/g]	
	60.1034	2.5151	± 0.0014	142.4107	± 2.7842	-791.0450	± 1.9803
	34.4534	1.3967	± 0.0009	125.8339	± 1.7011	-392.5204	± 1.2731
	14.9682	0.5908	± 0.0006	98.7980	± 1.3331	-120.4544	± 1.1585
	4.8144	0.1898	± 0.0006	70.4654	± 1.2486	0.0323	± 1.1348
	1.3480	0.0556	± 0.0006	51.0492	± 1.2394	30.4240	± 1.1323
	0.3870	0.0185	± 0.0006	41.0139	± 1.2386	34.1423	± 1.1321
	0.1608	0.0100	± 0.0006	37.4650	± 1.2956	33.7535	± 1.1864
	60.4292	2.5299	± 0.0013	141.6733	± 2.4948	-797.2647	± 1.5891
	86.0366	3.7075	± 0.0018	149.5289	± 3.3401	-1226.4823	± 1.9215
	130.7064	5.8340	± 0.0028	150.8795	± 5.1620	-2014.3384	± 2.8509
10	290.6294	14.0077	± 0.0075	130.6054	± 13.2517	-5068.2187	± 7.8336
	260.2270	13.1118	± 0.0066	136.0441	± 12.3299	-4730.2430	± 7.4650
	223.9968	11.8268	± 0.0060	145.4949	± 10.8241	-4243.9109	± 6.2130
	191.4170	10.4175	± 0.0054	158.3460	± 9.6735	-3707.9972	± 5.6187
	170.8238	9.3831	± 0.0046	166.3769	± 8.3180	-3316.0520	± 4.5878
	149.2220	8.1854	± 0.0039	175.4220	± 7.2093	-2862.5107	± 4.0082
	130.2800	7.0637	± 0.0034	179.6048	± 6.1725	-2442.0072	± 3.3700
	110.3192	5.8466	± 0.0030	185.5272	± 5.3657	-1984.3777	± 3.0999
	90.0190	4.6200	± 0.0022	185.4545	± 4.0911	-1529.1911	± 2.2706
	70.1574	3.4678	± 0.0017	182.9237	± 3.1730	-1104.1183	± 1.8614
	45.0700	2.1172	± 0.0013	172.1575	± 2.5875	-613.6135	± 1.9545
	29.6216	1.3439	± 0.0008	157.2246	± 1.6712	-341.5650	± 1.2631
	14.5848	0.6431	± 0.0006	132.7746	± 1.3499	-105.8941	± 1.1634
	5.1090	0.2237	± 0.0006	102.1942	± 1.2525	19.1846	± 1.1359
	1.3030	0.0598	± 0.0006	75.7877	± 1.2395	53.6037	± 1.1323
	0.5256	0.0268	± 0.0006	65.1791	± 1.2887	55.2324	± 1.1597
	0.1406	0.0103	± 0.0006	56.1732	± 1.2385	52.3663	± 1.1321
	55.1216	2.6414	± 0.0013	177.2999	± 2.5307	-803.0369	± 1.5805

Table B.5: Experimental measurements of supercritical adsorption of CO_2 on the B6 shale at various temperatures.

T [°C]	P [bar]	ρ_b [mol/L]		n^{ex} [µmol/g]		n^{net} [µmol/g]	
80	251.2572	15.5589	± 0.0071	19.0779	± 9.6442	-5824.8885	± 2.2784
	210.2328	13.9270	± 0.0065	30.4245	± 8.6928	-5200.5784	± 2.1687
	185.2312	12.5011	± 0.0058	40.1185	± 7.7677	-4655.3355	± 1.8889
	163.3804	10.8331	± 0.0050	51.6251	± 6.8336	-4017.3135	± 1.9684
	146.8982	9.3036	± 0.0048	62.4141	± 5.9915	-3432.0570	± 1.6755
	130.9748	7.7355	± 0.0039	74.5619	± 5.0268	-2830.9275	± 1.6518
	119.8294	6.6746	± 0.0032	80.8886	± 4.2620	-2426.1236	± 1.2984
	107.9622	5.6387	± 0.0026	85.4204	± 3.5788	-2032.4961	± 1.0828
	93.8392	4.5534	± 0.0022	88.7090	± 2.8829	-1621.5680	± 0.8126
	68.9128	2.9747	± 0.0015	87.1580	± 1.9646	-1030.1546	± 0.7080
	41.0762	1.5900	± 0.0008	76.4653	± 1.1109	-520.7516	± 0.5172
	15.1492	0.5372	± 0.0005	54.5845	± 0.7568	-147.1989	± 0.6286
	3.1122	0.1064	± 0.0003	29.4909	± 0.4714	-10.4762	± 0.4253
	1.0400	0.0354	± 0.0002	19.6944	± 0.3334	6.4085	± 0.3002
	0.5088	0.0172	± 0.0002	16.4221	± 0.2998	9.9513	± 0.2714
	0.1584	0.0053	± 0.0004	13.4081	± 0.6219	11.4011	± 0.5710
	19.9560	0.7185	± 0.0004	58.0550	± 0.5421	-211.8164	± 0.3040
	56.3922	2.3118	± 0.0011	81.2839	± 1.4883	-787.0289	± 0.4780
40	48.0890	2.4275	± 0.0011	116.0918	± 1.5262	-795.6934	± 0.4210
	56.8274	3.0984	0.0015	122.6207	± 1.9489	-1041.1610	± 0.5309
	100.1308	14.0705	± 0.0067	55.5667	± 8.8431	-5229.3424	± 2.3251
	251.2354	19.9614	± 0.0092	13.7822	± 12.3631	-7483.7812	± 2.8870
	199.8552	19.0250	± 0.0088	17.8186	± 11.8104	-7128.0224	± 2.7848
	163.8722	18.1031	± 0.0084	22.9117	± 11.2730	-6776.6682	± 2.7559
	120.8420	16.2398	± 0.0075	36.3170	± 10.1537	-6063.3781	± 2.6889
	101.8622	14.3566	± 0.0070	51.7505	± 9.1346	-5340.6110	± 2.5560
	94.0582	12.4903	± 0.0059	69.2203	± 7.8781	-4622.1532	± 2.2082
	88.9046	9.8546	± 0.0058	93.9804	± 6.6868	-3607.4343	± 2.1055
	85.8584	8.1892	± 0.0073	117.4477	± 7.6701	-2958.4336	± 4.4621
	82.0040	6.7628	± 0.0040	131.4190	± 4.7099	-2408.6904	± 1.8203
	76.0718	5.4117	± 0.0027	136.6618	± 3.4838	-1895.9765	± 1.0436
	61.0838	3.4813	± 0.0020	129.0218	± 2.5235	-1178.5529	± 1.1922

Table B.5: Experimental measurements of supercritical adsorption of CO_2 on the B6 shale at various temperatures.

T [°C]	P [bar]	ρ_b [mol/L]		n^{ex} [µmol/g]		n^{net} [µmol/g]	
	30.3156	1.3515	± 0.0006	103.2948	± 0.8754	-404.3171	± 0.3044
	10.0980	0.4048	± 0.0003	73.3245	± 0.3600	-78.7153	± 0.2420
	1.0418	0.0401	± 0.0002	35.9376	± 0.3518	20.8834	± 0.3219
	0.6174	0.0237	± 0.0002	30.4813	± 0.2584	21.5771	± 0.2348
	0.1398	0.0053	± 0.0002	22.6846	± 0.2580	20.6815	± 0.2348
10	16.2726	0.7728	± 0.0004	112.8610	± 0.5461	-177.4125	± 0.2607
	27.9118	1.4692	± 0.0007	139.9578	± 0.9563	-411.8776	± 0.3389
	36.7726	2.1575	± 0.0011	167.2705	± 1.4028	-643.0753	± 0.4678
	8.0878	0.3626	± 0.0002	92.1463	± 0.3420	-44.0334	± 0.2405
	1.0190	0.0442	± 0.0002	50.9720	± 0.2595	34.3843	± 0.2349
	0.5024	0.0220	± 0.0002	41.9914	± 0.2584	33.7406	± 0.2348
	0.1474	0.0068	± 0.0002	31.5258	± 0.2707	28.9555	± 0.2377

Table B.6: Experimental measurements of supercritical adsorption of CH_4 on the B6 shale at various temperatures.

T [°C]	P [bar]	ρ_b [mol/L]		n^{ex} [µmol/g]		n^{net} [µmol/g]	
80	175.0352	6.4398	± 0.0031	26.8181	± 4.1761	-2391.5866	± 1.3078
	149.7644	5.5158	± 0.0028	29.3645	± 3.7320	-2042.0240	± 1.4803
	121.2020	4.4433	± 0.0022	32.6151	± 2.9369	-1636.0153	± 1.0530
	99.0406	3.6030	± 0.0017	32.8966	± 2.3949	-1320.1563	± 0.9004
	75.0766	2.6992	± 0.0015	31.8615	± 2.0156	-981.7935	± 1.0690
	64.0824	2.2894	± 0.0014	31.1786	± 1.9362	-828.5986	± 1.2319
	46.0506	1.6263	± 0.0010	29.0712	± 1.3788	-581.6863	± 0.8889
	28.2682	0.9842	± 0.0008	24.4688	± 1.2168	-345.1338	± 0.9666
	10.2890	0.3533	± 0.0007	15.4631	± 0.9923	-117.2016	± 0.8887
	1.8262	0.0515	± 0.0008	8.2976	± 1.3393	-11.0377	± 1.2412
	0.5170	0.0182	± 0.0005	6.8141	± 0.7736	-0.0316	± 0.6971
	0.1344	0.0053	± 0.0006	6.2054	± 0.8017	4.1989	± 0.7134
40	172.6220	7.7673	± 0.0037	38.9927	± 4.9925	-2877.9452	± 1.4495
	147.1520	6.6034	± 0.0031	42.8701	± 4.2059	-2436.9740	± 1.1785
	121.1098	5.3686	± 0.0025	46.0708	± 3.4527	-1970.0371	± 1.0431
	95.2070	4.1325	± 0.0020	47.5042	± 2.7088	-1504.4062	± 0.9460

Table B.6: Experimental measurements of supercritical adsorption of CH_4 on the B6 shale at various temperatures.

T [°C]	P [bar]	ρ_b [mol/L]		n^{ex} [µmol/g]		n^{net} [µmol/g]	
	66.8120	2.8123	± 0.0014	46.5308	± 1.9201	-1009.5932	± 0.8046
	39.6004	1.6106	± 0.0009	41.5507	± 1.2757	-563.2946	± 0.7457
	25.1312	1.0012	± 0.0007	35.9769	± 1.0011	-339.9993	± 0.7231
	9.9938	0.3906	± 0.0006	25.9553	± 0.8038	-120.7119	± 0.6976
	1.4780	0.0583	± 0.0005	14.5174	± 0.7666	-7.3717	± 0.6954
	0.5148	0.0210	± 0.0007	12.3382	± 1.0655	4.4624	± 0.9712
	0.1312	0.0064	± 0.0005	11.1919	± 0.7685	8.7992	± 0.6959
10	173.1258	9.4954	± 0.0046	47.2656	± 6.3121	-3518.6176	± 2.3399
	147.5660	8.0810	± 0.0039	54.2988	± 5.1828	-2980.4321	± 1.4214
	122.3854	6.5749	± 0.0032	59.1396	± 4.2845	-2409.9853	± 1.3676
	99.1976	5.1622	± 0.0025	62.3705	± 3.3339	-1876.2460	± 1.0326
	70.2128	3.4649	± 0.0017	63.6964	± 2.3536	-1237.5203	± 0.9489
	30.1174	1.3648	± 0.0008	53.1041	± 1.1561	-459.4317	± 0.7349
	10.0330	0.4364	± 0.0006	38.4599	± 0.8129	-125.4073	± 0.6981
	1.4048	0.0607	± 0.0005	22.6812	± 0.7667	-0.1306	± 0.6954
	0.5022	0.0222	± 0.0005	19.0045	± 0.7659	10.6781	± 0.6953
	0.1180	0.0059	± 0.0005	16.8194	± 0.7658	14.6091	± 0.6953

Table B.7: Experimental measurements of supercritical adsorption of CO_2 on the B8 shale at various temperatures.

T [°C]	P [bar]	ρ_b [mol/L]		n^{ex} [µmol/g]		n^{net} [µmol/g]	
80	260.1346	15.8375	± 0.0073	38.1507	± 10.4934	-5843.1802	± 4.0488
	240.0124	15.1758	± 0.0071	42.4598	± 10.0997	-5593.1556	± 3.9465
	195.1972	13.1282	± 0.0061	45.0150	± 8.7120	-4830.1840	± 3.3922
	174.5098	11.7418	± 0.0057	46.2546	± 8.1497	-4314.1160	± 3.6381
	165.1876	10.9926	± 0.0051	49.0231	± 7.3101	-4033.1179	± 2.8731
	140.3148	8.6570	± 0.0045	54.7215	± 6.1707	-3160.0813	± 2.7509
	124.9204	7.1533	± 0.0034	59.7085	± 4.8511	-2596.6973	± 1.9868
	99.9576	5.0086	± 0.0027	63.0118	± 3.7576	-1796.9592	± 1.9363
	80.0152	3.6338	± 0.0024	61.6241	± 3.1303	-1287.7964	± 1.8246
	61.1296	2.5570	± 0.0015	58.4163	± 2.1560	-891.1391	± 1.3414
	35.2812	1.3401	± 0.0008	49.0547	± 1.1507	-448.5807	± 0.7247

Table B.7: Experimental measurements of supercritical adsorption of CO_2 on the B8 shale at various temperatures.

T [°C]	P [bar]	ρ_b [mol/L]		n^{ex} [µmol/g]		n^{net} [µmol/g]	
	19.7932	0.7128	± 0.0007	40.5211	± 1.0184	-224.1784	± 0.8090
	5.0758	0.1751	± 0.0006	25.3400	± 0.8151	-39.6803	± 0.7013
	1.8036	0.0619	± 0.0005	18.8844	± 0.7597	-4.0913	± 0.6618
	0.4890	0.0170	± 0.0005	14.3937	± 0.7934	8.0735	± 0.6926
	0.1354	0.0050	± 0.0005	12.5593	± 0.7679	10.7104	± 0.6710
	53.9138	2.1922	± 0.0012	54.6085	± 1.6894	-759.4835	± 0.9288
	121.2414	6.8153	± 0.0032	59.4949	± 4.5849	-2471.3841	± 1.8726
40	54.0076	2.8742	± 0.0022	80.2937	± 3.1666	-987.0486	± 2.2839
	100.3530	14.1227	± 0.0066	59.8518	± 9.5756	-5184.6710	± 4.0393
	260.4718	20.1003	± 0.0092	52.7220	± 13.2702	-7411.6307	± 5.0631
	240.0964	19.7897	± 0.0093	52.3238	± 13.3368	-7296.6517	± 5.4634
	219.6282	19.4164	± 0.0090	52.2174	± 12.8888	-7158.1307	± 4.9737
	195.1536	18.9136	± 0.0092	52.0932	± 13.0321	-6971.5681	± 5.6209
	170.1728	18.2904	± 0.0088	52.8456	± 12.3514	-6739.3767	± 4.9465
	130.3578	16.8046	± 0.0078	55.3817	± 11.2320	-6185.0887	± 4.4698
	108.1500	15.1709	± 0.0083	56.6912	± 11.7980	-5577.0791	± 6.5445
	97.1472	13.4545	± 0.0068	61.8488	± 9.3185	-4934.5370	± 3.9233
	92.3304	11.8072	± 0.0136	71.1850	± 15.4216	-4313.4531	± 10.1689
	89.5590	10.3103	± 0.0055	95.9899	± 7.4870	-3732.7731	± 3.4891
	87.0806	8.8677	± 0.0045	103.4930	± 6.1674	-3189.5546	± 2.6282
	84.0734	7.4862	± 0.0075	108.1373	± 8.9664	-2671.8843	± 5.9786
	80.1372	6.2906	± 0.0039	110.1888	± 5.1778	-2225.8538	± 2.8757
	74.4836	5.1439	± 0.0033	103.3152	± 4.2912	-1806.8811	± 2.3907
	62.1454	3.5882	± 0.0027	87.2438	± 3.2840	-1245.2505	± 1.9174
	36.2532	1.6830	± 0.0009	70.4602	± 1.3522	-554.5237	± 0.7864
	20.1294	0.8496	± 0.0006	58.1508	± 0.9187	-257.3697	± 0.6692
	5.0408	0.1991	± 0.0005	39.0250	± 0.7482	-34.8954	± 0.6419
	1.5758	0.0624	± 0.0005	28.7553	± 0.7342	5.5940	± 0.6362
	0.4608	0.0193	± 0.0005	22.2277	± 0.7331	15.0758	± 0.6360
	0.1314	0.0066	± 0.0005	18.7063	± 0.7429	16.2540	± 0.6424
10	10.0902	0.4586	± 0.0005	61.3423	± 0.7873	-108.9791	± 0.6438
	18.3920	0.8881	± 0.0007	74.5337	± 1.0798	-255.2596	± 0.8174

Table B.7: Experimental measurements of supercritical adsorption of CO_2 on the B8 shale at various temperatures.

T [°C]	P [bar]	ρ_b [mol/L]		n^{ex} [µmol/g]		n^{net} [µmol/g]	
	36.9942	2.1778	± 0.0011	109.1299	± 1.6251	-699.5933	± 0.8501
	30.3338	1.6377	± 0.0009	93.0547	± 1.3376	-515.1036	± 0.7842
	24.8050	1.2666	± 0.0008	84.4677	± 1.1192	-385.8754	± 0.7167
	20.1038	0.9847	± 0.0007	77.3464	± 0.9771	-288.3105	± 0.6806
	15.0484	0.7083	± 0.0006	70.1946	± 0.8709	-192.8340	± 0.6633
	8.5070	0.3827	± 0.0005	59.5062	± 0.7696	-82.6295	± 0.6407
	4.4806	0.1969	± 0.0005	50.1137	± 0.8013	-23.0177	± 0.6917
	1.4688	0.0642	± 0.0005	38.4172	± 0.7303	14.5945	± 0.6346
	0.5236	0.0236	± 0.0005	30.6384	± 0.7824	21.8852	± 0.6779
	0.1360	0.0069	± 0.0005	24.0545	± 0.7716	21.5016	± 0.6734

Table B.8: Experimental measurements of supercritical adsorption of CH_4 on the B8 shale at various temperatures.

T [°C]	P [bar]	ρ_b [mol/L]		n^{ex} [µmol/g]		n^{net} [µmol/g]	
80	0.1450	0.0058	± 0.0009	2.7576	± 1.2205	0.6120	± 1.0347
	0.5684	0.0204	± 0.0008	2.8347	± 1.1408	-4.7014	± 0.9936
	1.3260	0.0462	± 0.0007	3.7272	± 0.9613	-13.3744	± 0.8124
	5.0782	0.1744	± 0.0007	5.5633	± 0.9210	-58.9640	± 0.7793
	15.0384	0.5192	± 0.0007	9.4235	± 1.0153	-182.6468	± 0.8498
	24.6482	0.8574	± 0.0009	12.4540	± 1.4393	-304.7073	± 1.1961
	47.9954	1.7010	± 0.0010	16.6085	± 1.4912	-612.6300	± 0.9495
	70.8412	2.5478	± 0.0014	19.1697	± 1.9680	-923.3193	± 1.0743
	91.8018	3.3377	± 0.0020	21.6605	± 2.9379	-1213.0560	± 1.8571
	114.8522	4.2130	± 0.0022	22.3041	± 3.1108	-1536.2114	± 1.5239
	131.7162	4.8525	± 0.0024	21.7744	± 3.4496	-1773.2988	± 1.5994
	152.9104	5.6465	± 0.0027	22.2307	± 3.8693	-2066.5815	± 1.6543
	161.5688	5.9663	± 0.0032	21.4386	± 4.3731	-2185.6577	± 2.0840
	169.4154	6.2540	± 0.0033	22.2925	± 4.6186	-2291.2183	± 2.2491
	185.7956	6.8406	± 0.0034	21.6472	± 4.7612	-2508.8781	± 2.0436
40	0.2020	0.0092	± 0.0006	8.1095	± 0.8290	4.7166	± 0.7221
	0.5114	0.0209	± 0.0006	8.5399	± 0.8381	0.8030	± 0.7310
	1.7920	0.0701	± 0.0006	10.4717	± 0.8303	-15.4766	± 0.7223

Table B.8: Experimental measurements of supercritical adsorption of CH_4 on the B8 shale at various temperatures.

T [°C]	P [bar]	ρ_b [mol/L]		n^{ex} [µmol/g]		n^{net} [µmol/g]	
	5.4460	0.2121	± 0.0006	13.7232	± 0.8824	-64.7242	± 0.7411
	15.0638	0.5922	± 0.0006	18.6752	± 0.9170	-200.4004	± 0.7370
	34.8298	1.4092	± 0.0009	25.2109	± 1.3023	-496.1016	± 0.8366
	55.5082	2.3054	± 0.0012	29.5725	± 1.7527	-823.2442	± 0.9322
	76.1164	3.2405	± 0.0017	31.7111	± 2.3691	-1167.0478	± 1.1676
	95.8574	4.1663	± 0.0020	33.0234	± 2.9160	-1508.1897	± 1.3081
	115.8900	5.1238	± 0.0031	33.6525	± 4.1398	-1861.7787	± 2.2602
	131.9666	5.8919	± 0.0034	33.3949	± 4.5816	-2146.1677	± 2.3766
	150.1812	6.7485	± 0.0032	33.4381	± 4.5496	-2463.0320	± 1.8308
	166.1220	7.4808	± 0.0036	33.2981	± 5.1420	-2734.0597	± 2.1731
	186.2740	8.3691	± 0.0045	32.1014	± 6.1391	-3063.8538	± 2.8745
10	0.1440	0.0072	± 0.0006	13.5129	± 0.8401	10.8493	± 0.7318
	0.6008	0.0267	± 0.0006	14.8205	± 0.8403	4.9380	± 0.7318
	1.5280	0.0661	± 0.0006	16.6234	± 0.8301	-7.8451	± 0.7223
	5.0680	0.2188	± 0.0006	21.0189	± 0.8415	-59.9123	± 0.7242
	15.0472	0.6613	± 0.0006	27.9086	± 0.9374	-216.7242	± 0.7406
	24.7602	1.1102	± 0.0008	32.4831	± 1.1077	-378.2083	± 0.7730
	42.4798	1.9800	± 0.0012	38.3100	± 1.7168	-694.1509	± 1.0957
	60.0402	2.9034	± 0.0015	41.6834	± 2.1148	-1032.3651	± 1.0481
	75.0866	3.7427	± 0.0018	43.6470	± 2.6419	-1340.8722	± 1.2103
	91.0874	4.6800	± 0.0024	44.8847	± 3.4055	-1686.3799	± 1.6467
	112.0968	5.9524	± 0.0031	47.1550	± 4.4681	-2154.7833	± 2.3524
	119.9884	6.4342	± 0.0037	45.3420	± 4.9733	-2334.8523	± 2.5291
	136.5752	7.4396	± 0.0037	47.0121	± 5.1549	-2705.0937	± 2.1593
	152.4838	8.3673	± 0.0042	45.0348	± 6.0571	-3050.2546	± 2.9274
	170.0592	9.3392	± 0.0050	44.7357	± 6.8335	-3410.0778	± 3.2155
	181.0710	9.9097	± 0.0058	44.3603	± 7.7149	-3621.5276	± 3.9387

B.1.2.1 Shale Chips

Figures B.3 and B.4 show the supercritical adsorption experiments with the LG4 shale in chip form at 80 °C and two different pressures with CH_4 and CO_2 respectively. Figures B.5 and B.6 show the same MSB experiments with the ML shale chip. Both chips were approximately 2 cm in width. Excess adsorption and the bulk density were calculated at 30 seconds intervals from the first point until ∼150 minutes, and then after every 5 minutes.

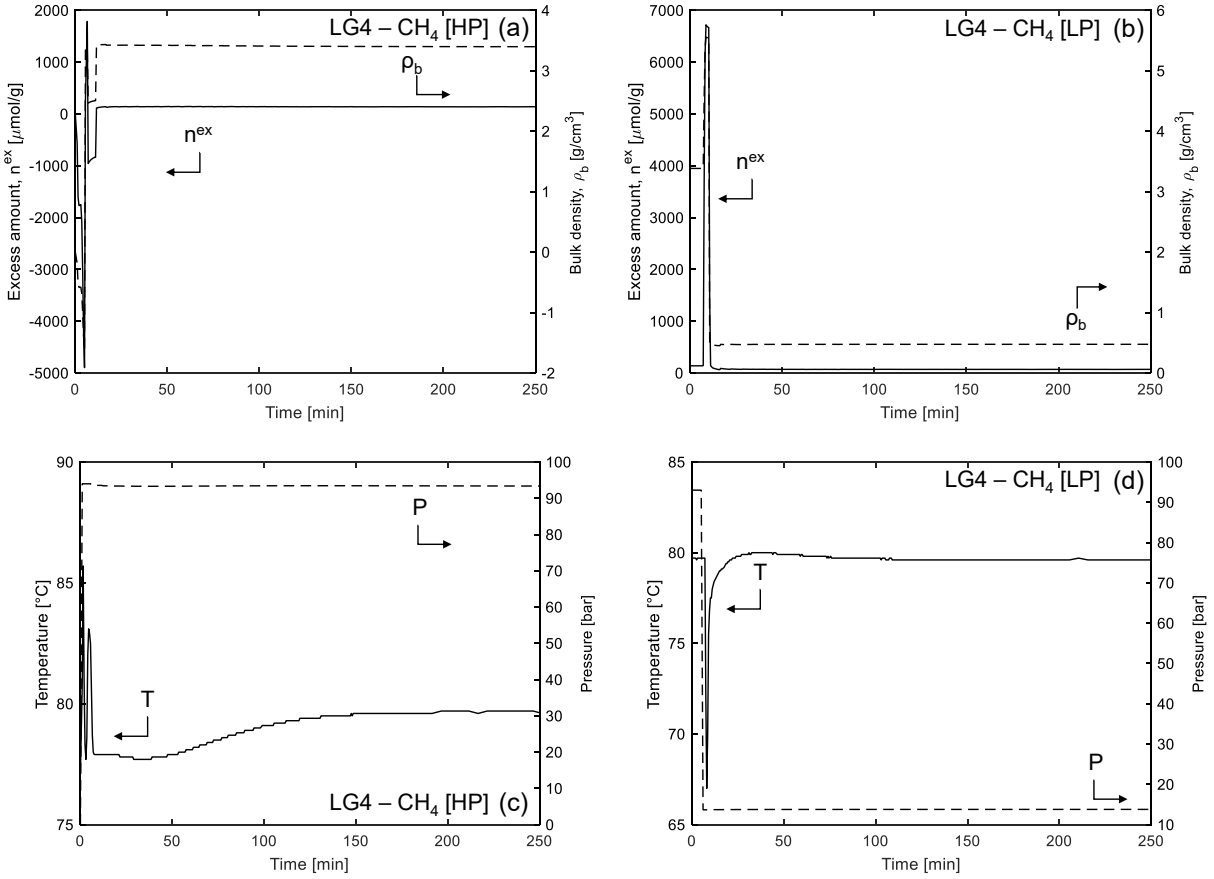

Figure B.3: Results of (a, c) injection (HP = 93.0 bar) and (b, d) blowdown (LP = 13.8 bar) of the MSB with the LG4 chip at 80 °C with CH_4. The figures (a) and (b) shows the progression of the excess adsorbed amount and the bulk density and figures (c) and (d) show the variation in the measured temperature and pressure as a function of time.

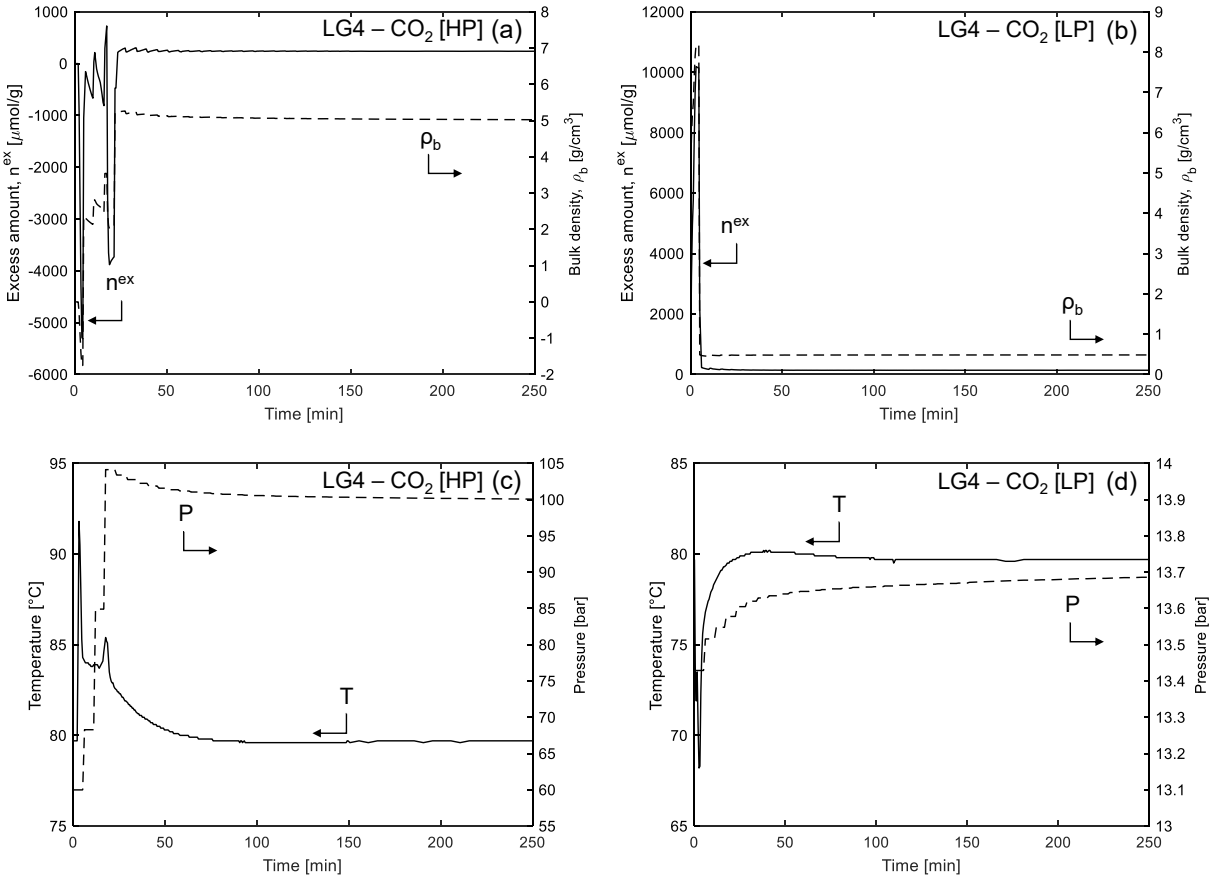

Figure B.4: Results of (a, c) injection (HP = 98.5 bar) and (b, d) blowdown (LP = 13.8 bar) of the MSB with the LG4 chip at 80 °C with CO_2. The figures (a) and (b) shows the progression of the excess adsorbed amount and the bulk density and figures (c) and (d) show the variation in the measured temperature and pressure as a function of time.

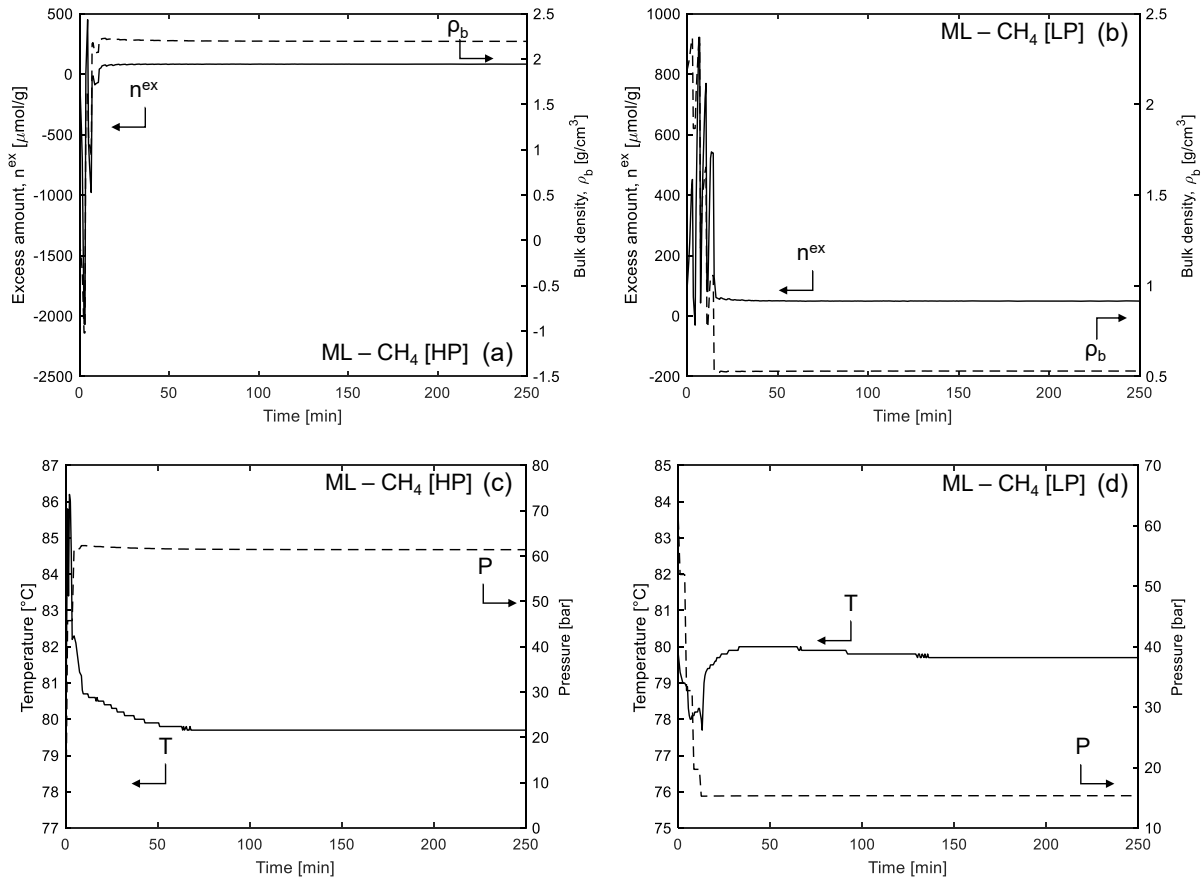

Figure B.5: Results of (a, c) injection (HP = 61.2 bar) and (b, d) blowdown (LP = 15.4 bar) of the MSB with the ML chip at 80 °C with CH_4. The figures (a) and (b) shows the progression of the excess adsorbed amount and the bulk density and figures (c) and (d) show the variation in the measured temperature and pressure as a function of time.

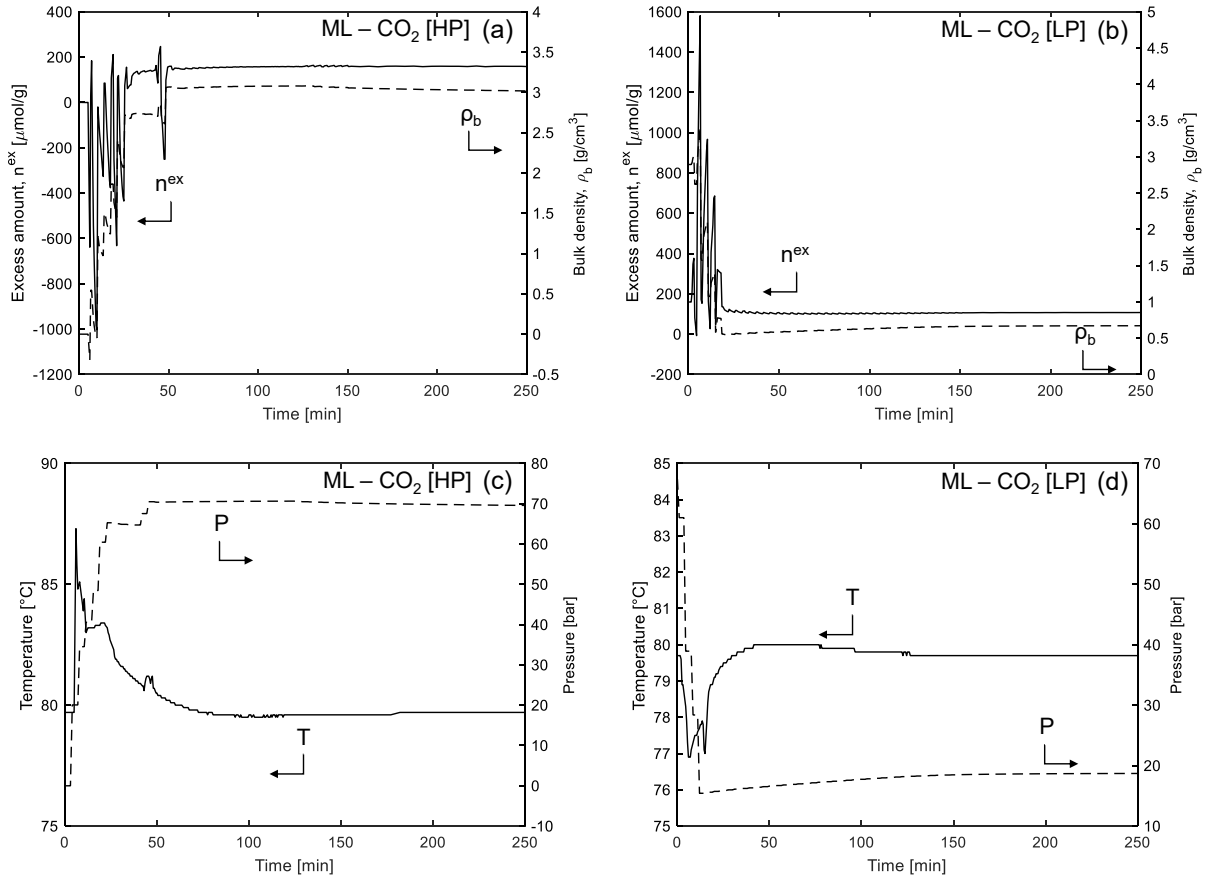

Figure B.6: Results of (a, c) injection (HP = 67.4 bar) and (b, d) blowdown (LP = 18.7 bar) of the MSB with the ML chip at 80 °C with CO_2. The figures (a) and (b) shows the progression of the excess adsorbed amount and the bulk density and figures (c) and (d) show the variation in the measured temperature and pressure as a function of time.

B.2 Lattice DFT modelling

B.2.1 Volumetric Fractions

The volumetric fractions of the TOC and clay content in each shale, for use in the lattice DFT model, were calculated using Eq. B.1.

$$x_i(\text{vol\%}) = \frac{x_i(\text{wt\%})/\rho_{\text{e},i}}{\sum_i x_i(\text{wt\%})/\rho_{\text{e},i}} \tag{B.1}$$

where $\rho_{\text{e},i}$ is the mineral density (in g/cm^3) of component i in each shale and x_i is the fraction of each element in the shale. The mineral densities were obtained from Bahudar et al. (2015) and King et al. (2015) [300, 301]. Once the volumetric fractions of the TOC and clay minerals (the two adsorbing components in shale) were calculated, the normalised TOC fraction in each shale was obtained using Eq. B.2.

$$\text{Normalised TOC (vol\%)} = \frac{\text{TOC (vol\%)}}{\text{TOC (vol\%)} + \text{Clay (vol\%)}} \tag{B.2}$$

B.2.2 Parameters of the Lattice DFT model

The parameters of the lattice DFT model for the single surface system are tabulated in Tables B.9 (slit pores), B.10 (cylindrical pores) and B.11 (hybrid - slit and cylindrical pores). The parameters for the dual site lattice DFT model are tabulated in Tables B.12 (slit/slit) and B.13 (cylindrical/cylindrical).

Table B.9: Parameters of the single surface lattice DFT model for slit pores applied to the description of experimental excess adsorption isotherms measured on the three shales. The value of the objective function, Eq. 4.20 (normalised by the number of experimental points, E) is also given.

	LG4		ML		B6	
Parameter	CO_2	CH_4	CO_2	CH_4	CO_2	CH_4
	Fitted Parameters					
$\varepsilon_{\text{sf}}/k_{\text{B}}$ [K]	−1158.89	−1046.02	−1071.69	−1145.61	−1468.87	−984.37
ρ_{max} [mol/L]	31.30		26.87		22.11	
	Saturation Factor, c_{sat}					
10 °C	–	0.79	–	0.87	–	0.77
40 °C	0.96	0.73	0.96	0.74	1.21	0.60
80 °C	0.80	0.63	0.72	0.60	0.86	0.45
Φ/E [mmol/g]^2	0.000398		0.000351		0.0000702	

Table B.10: Parameters of the single surface lattice DFT model for cylindrical pores applied to the description of experimental excess adsorption isotherms measured on the three shales. The value of the objective function, Eq. 4.20 (normalised by the number of experimental points, E) is also given.

	LG4		ML		B6	
Parameter	CO_2	CH_4	CO_2	CH_4	CO_2	CH_4
	Fitted Parameters					
ε_{sf}/k_B [K]	−764.84	−702.55	−688.50	−793.92	−861.19	−758.35
$\overline{\varepsilon}_{sf}/k_B$ [K]	−1209.95	−1111.41	−1119.11	−1290.45	−1399.80	−1232.64
ρ_{max} [mol/L]	31.68		27.30		22.54	
	Saturation Factor, c_{sat}					
10 °C	–	0.51	–	0.55	–	0.47
40 °C	0.65	0.47	0.67	0.47	0.82	0.36
80 °C	0.53	0.40	0.48	0.38	0.58	0.27
Φ/E [mmol/g]^2	0.000299		0.000305		0.0000679	

Table B.11: Parameters of the single surface hybrid lattice DFT model applied to the description of experimental excess adsorption isotherms measured on the three shales. The value of the objective function, Eq. 4.20 (normalised by the number of experimental points, E) is also given.

	LG4		ML		B6	
Parameter	CO_2	CH_4	CO_2	CH_4	CO_2	CH_4
	Fitted Parameters					
ε_{sf}/k_B [K]	−994.11	−897.71	−972.66	−1057.87	−1228.03	−1000.17
$\overline{\varepsilon}_{sf}/k_B$ [K]	−1313.32	−1185.97	−1284.99	−1397.56	−1622.36	−1321.33
ρ_{max} [mol/L]	31.41		27.12		22.32	
	Saturation Factor, c_{sat}					
10 °C	–	0.61	–	0.70	–	0.60
40 °C	0.76	0.56	0.79	0.59	0.99	0.46
80 °C	0.62	0.49	0.59	0.48	0.71	0.34
Φ/E [mmol/g]^2	0.000267		0.000270		0.0000571	

Table B.12: Parameters of the hybrid slit/slit lattice DFT model applied to the description of experimental excess adsorption isotherms measured on the three shales. The value of the objective function, Eq. 4.20 (normalised by the number of experimental points, E) is also given.

	LG4		ML		B6	
Parameter	CO_2	CH_4	CO_2	CH_4	CO_2	CH_4
	Fitted Parameters					
$\varepsilon_{sf,slit,1}/k_B$ [K]	−1600.33	−1372.66	−1389.09	−1494.05	−851.54	−711.42
$\varepsilon_{sf,slit,2}/k_B$ [K]	−737.64	−531.91	−617.35	−493.64	−2232.21	−2217.76
ρ_{max} [mol/L]	30.92		26.65		21.53	
	Saturation Factor, c_{sat}					
10 °C	–	0.89	–	0.96	–	0.84
40 °C	1.00	0.83	1.00	0.82	1.31	0.66
80 °C	0.84	0.72	0.76	0.65	0.98	0.50
Φ/E [mmol/g]^2	0.000186		0.000198		0.0000136	

Table B.13: Parameters of the hybrid cylindrical/cylindrical lattice DFT model applied to the description of experimental excess adsorption isotherms measured on the three shales. The value of the objective function, Eq. 4.20 (normalised by the number of experimental points, E) is also given.

	LG4		ML		B6	
Parameter	CO_2	CH_4	CO_2	CH_4	CO_2	CH_4
	Fitted Parameters					
$\varepsilon_{sf,cyl,1}/k_B$ [K]	−929.94	−851.67	−800.69	−921.24	−941.46	−913.21
$\overline{\varepsilon}_{sf,1}/k_B$ [K]	−1632.83	−1495.42	−1405.89	−1617.57	−1653.07	−1603.47
$\varepsilon_{sf,cyl,2}/k_B$ [K]	−439.52	−376.99	−326.78	−350.29	−358.35	−384.56
$\overline{\varepsilon}_{sf,2}/k_B$ [K]	−580.65	−498.05	−431.71	−462.77	−473.41	−508.04
ρ_{max} [mol/L]	30.75		26.75		21.90	
	Saturation Factor, c_{sat}					
10 °C	–	0.60	–	0.64	–	0.53
40 °C	0.73	0.56	0.75	0.55	0.94	0.42
80 °C	0.60	0.48	0.56	0.44	0.70	0.31
Φ/E [mmol/g]^2	0.0000877		0.000145		0.0000282	

Appendix C

ESGR Model

The material in this chapter is published in Ansari et al. (2021) [1].

C.1 Adsorption Models

C.1.1 Primary Recovery

The following section describes the adsorption models considered in the primary recovery analysis.

1. Linear

$$m_{\mathrm{a,\ H}} = K_{\mathrm{H}} P \tag{C.1}$$

where K_{H} is the linearity constant.

2. Langmuir

$$m_{\mathrm{a,\ L}} = m_{\mathrm{L}}^{\mathrm{max}} \frac{K_{\mathrm{L}} P}{1 + K_{\mathrm{L}} P} \tag{C.2}$$

where $m_{\mathrm{L}}^{\mathrm{max}}$ is the saturation capacity and K_{L} is the Langmuir constant. The Langmuir model is able to model Type I adsorption isotherms in the classification by IUPAC [114].

3. Anti-Langmuir

$$m_{\mathrm{a,\ AL}} = m_{\mathrm{AL}}^{\mathrm{max}} \frac{K_{\mathrm{AL}} P}{1 - K_{\mathrm{AL}} P} \tag{C.3}$$

Type III isotherms can often be described by an Anti-Langmuir model.

4. BET

$$m_{\mathrm{a,\ B}} = m^{\mathrm{mono}} \frac{K_{\mathrm{B}} P}{\Big[P_{\mathrm{S}} - P\Big]\Big[1 + \Big(K_{\mathrm{B}} - 1\Big)\Big(P/P_{\mathrm{S}}\Big)\Big]} \tag{C.4}$$

where m^{mono} represents the monolayer coverage, P_{S} is the saturation pressure and the constant K_{B} relates the heat of adsorption between the first layer and adjacent layers. In the context of supercritical adsorption, a pseudosaturation pressure is more appropriate. In this work, this is given by the extrapolation of Antoine's equation [302, 138], shown below. The BET Model usually describes Type II adsorption behaviour

The pseudosaturation pressure (P_{S}) for the BET adsorption model was found by fitting the Antoine equation (below) to the vapour-liquid saturation data from NIST [231]. Excel SOLVER was used for the fitting.

$$\ln(P) = A - \frac{B}{C+T} \tag{C.5}$$

where T is in K and P has units of MPa. Figure C.1 shows the results of the fitting. The parameters were found to be A = 7.661, B = 1278 and C = 17.55. P_{S} is then 52.7 MPa at the reservoir temperature (328.15 K).

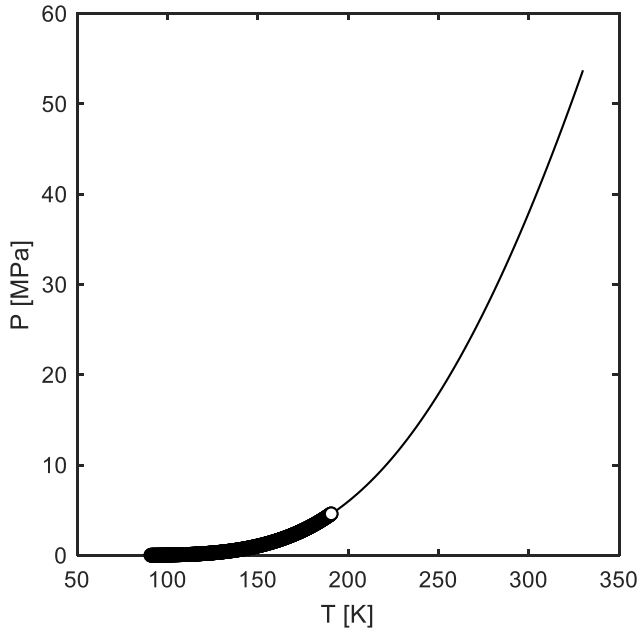

Figure C.1: Vapour-liquid equilibria for methane from NIST [231] shown by the points. Solid line is the fitting based on the Antoine Equation.

With the exception of the linear adsorption model, the remaining adsorption isotherm models have at least one additional degree of freedom when constraining the maximum adsorbed amount at the reservoir pressure. The choice of these parameters was guided by the objective of having four significantly different curves. The following heuristics were applied. The saturation capacity in the Langmuir model, $m_{\text{L}}^{\max}$, was chosen to be approximately 110% of the adsorbed amount at 35 MPa,

and 50% of this value was considered to the be the equivalent for the Anti-Langmuir model ($m_{\mathrm{AL}}^{\mathrm{max}}$). For the BET model, K_{B} was considered to be the product of P_{s} and K_{L}. Based on this, all remaining unknown parameters can be found and Table C.1 summarises these.

Table C.1: Parameters of the adsorption isotherm models used in the primary recovery analysis.

Parameter	CH_4
Linear	
K_{H} (kg/m^{3}MPa)	0.129
Langmuir	
$m_{\mathrm{L}}^{\mathrm{max}}$ (kg/m^3)	5.5
K_{L} (1/MPa)	0.286
Anti-Langmuir	
$m_{\mathrm{AL}}^{\mathrm{max}}$ (kg/m^3)	2.25
K_{AL} (1/MPa)	0.0192
BET	
m^{mono} (kg/m^3)	1.73
K_{B} (-)	15.1
P_{s} (MPa)	52.7

The CH_4 adsorption isotherms used in the primary recovery analysis can be found in Figure 9.1.

C.1.2 Recovery with Gas Injection

The Langmuir isotherm parameters for the recovery with gas injection analysis are shown in Table C.2 and the corresponding isotherms are shown in Figure C.2. The absolute adsorbed amount for the gases at P_{o} is defined as 5 kg/m^3 (CH_4), 35 kg/m^3 (CO_2) and 1.67 kg/m^3 (N_2).

Table C.2: Parameters of the adsorption isotherm models used for the recovery with gas injection analysis.

Parameter	CH_4	CO_2	N_2
Langmuir			
$m_{\mathrm{L}}^{\mathrm{max}}$ (kg/m^3)	38.5	38.5	38.5
K_{L} (1/MPa)	0.00426	0.286	0.00130

C.2 Primary Recovery - Sensitivity Analysis

To ascertain the effect of key model parameters, we have conducted a sensitivity analysis. We use the primary recovery case as our basis, and the most realistic adsorption isotherm, the Langmuir model to demonstrate the analysis. Four parameters have been considered, namely the porosity (ϕ), the adsorbed phase density (ρ_{a}), and the Langmuir parameters (the saturation capacity, $m_{\mathrm{L}}^{\mathrm{max}}$, and the

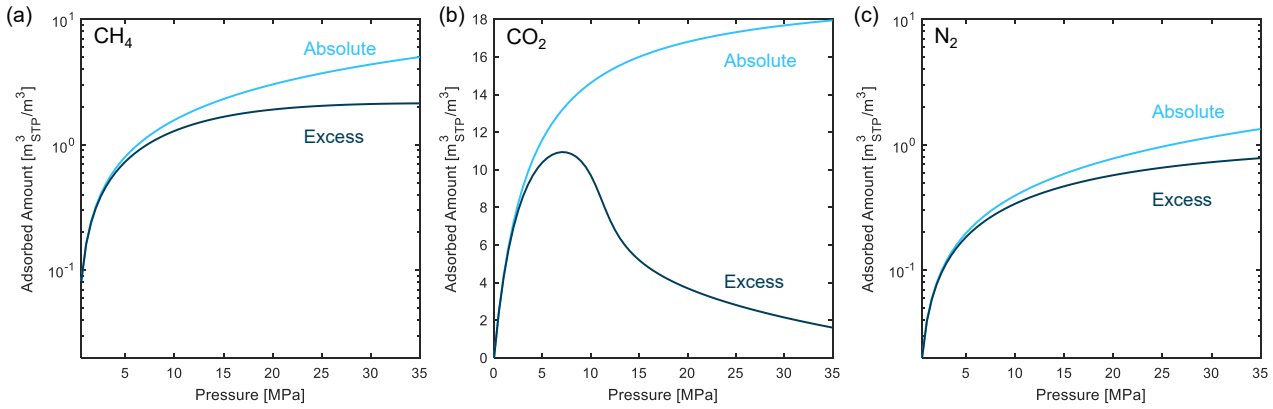

Figure C.2: (a) CH_4, (b) CO_2 and (c) N_2 absolute and excess adsorption isotherms used in the recovery with gas injection analysis.

Langmuir constant, K_L). In each analysis, just one parameter has been changed, while the others remain at their original values. Table C.3 shows the range of values considered for the sensitivity analysis.

Table C.3: Model parameters for the sensitivity analysis. * denotes the base values.

Parameter	Values				
Reservoir Porosity (%)	4	6	8*	12	16
Adsorbed Gas Density - CH_4 (mol/m^3)	8936.8	15639.4	22342.0*	29044.6	35747.2
Saturation Capacity (kg/m^3)	2.0	3.5	5.5*	8.0	11.0
Langmuir Constant (1/MPa)	0.100	0.200	0.286*	0.450	0.600

C.2.1 The Effect of the Reservoir Porosity

Figure C.3 shows the effect of varying the reservoir porosity on the cumulative production of methane. Changing the porosity of the reservoir affects the amount of free gas in the system but does not influence the adsorbed amount (absolute or excess). This observation is only true if the porosity accessible by the adsorbed phase remains unchanged. This is reflected in Figure C.3a. From Figure C.3b, it is clear that increasing the porosity increases the free gas, resulting in a higher OGIP, but the point of intersection between the G_p curve and the volumetric reservoir line, in terms of P/Z remains constant. This is due to the fact that the isotherms are the same between all five cases. This is also true for the production rate, where the rate becomes more negative with higher porosities, as the G_p is significantly higher. In general, higher porosities leads to higher G_p, OGIP and production rates, as a higher pore volume is available for the gas.

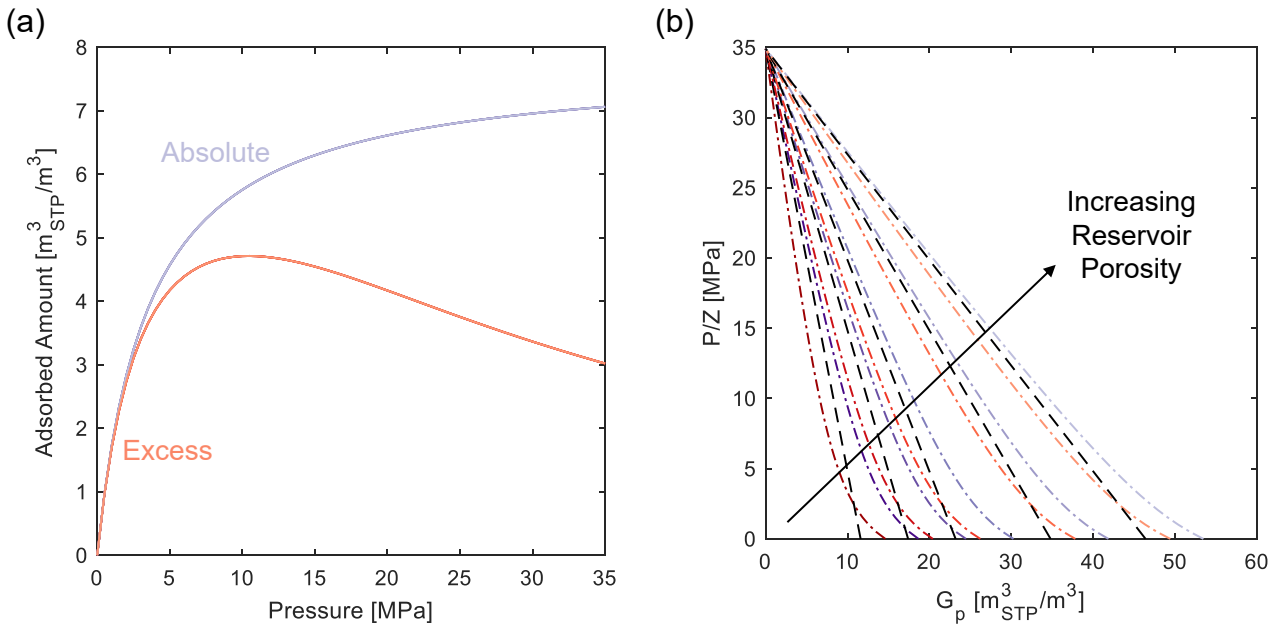

Figure C.3: CH_4 (a) absolute and excess adsorption isotherms and (b) G_p for various porosities (ϕ=4, 5, 8, 12, 16 %) for three scenarios, namely no adsorption (dashed black lines); adsorption without porosity correction (purple); and adsorption with porosity correction (orange).

C.2.2 The Effect of the Adsorbed Phase Density

The adsorbed phase density only affects excess adsorption, as seen in Figure C.4. At low pressure (< 2 MPa), all adsorption isotherms are indistinguishable; the impact of the adsorbed phase density becomes significant only at higher pressures. The lower the ρ_a, the lower the excess adsorbed amount at the same pressure, causing the excess amount to go even negative for the lowest case considered. The cumulative gas produced and OGIP both increase with ρ_a. The isotherm maximum shifts to higher pressures, which causes the crossing of the production rate with the volumetric reservoir line, to be at higher P/Z for higher adsorbed phase densities (Figure C.4c). Lower adsorbed phase densities result in lower absolute gas production rates, which then become indistinguishable as the reservoir approaches very low pressures.

This particular analysis highlights the importance of using excess adsorption directly when working with GIP, as the adsorbed phase density has a significant impact. Furthermore, one needs to make an assumption of this density, such as the liquid density assumption in our base case, as it cannot be directly measured.

C.2.3 The Effect of the Langmuir Model Parameters

The Langmuir isotherm parameters also have an effect on the cumulative production of methane. The adsorbed amount increases in proportion with the increase in the saturation capacity, m_L^{max}, i.e. the

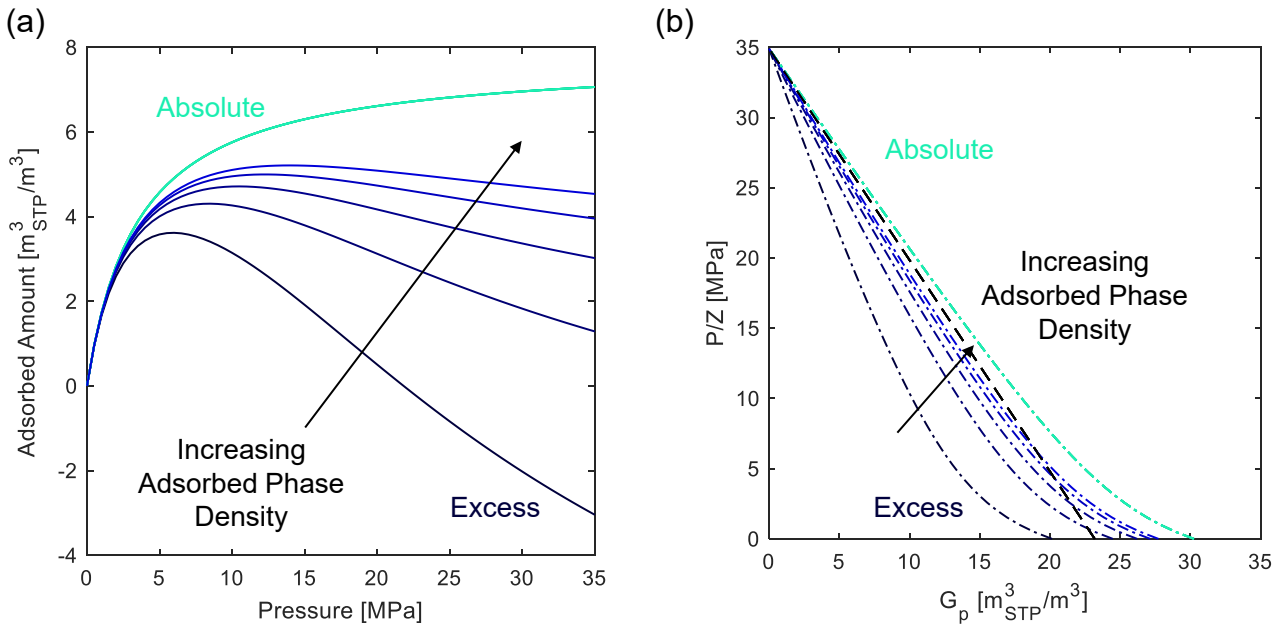

Figure C.4: CH_4 (a) absolute and excess adsorption isotherms and (b) G_p for various adsorbed-phase densities ($\rho_a = 8936.8, 15639.4, 22342.0, 29044.6, 35747.2$ mol/m^3) for three scenarios, namely no adsorption (dashed black line); adsorption without porosity correction (light blue); and adsorption with porosity correction (dark blue).

maximum of the excess adsorption isotherm stays at the same P/Z value, as shown in Figure C.5a. Consequently, the absolute cumulative gas produced also increases linearly with m_L^{max}. On the other hand, Figure C.5b illustrates that the cumulative gas produced using the excess adsorption framework decreases linearly with the saturation capacity until about 2.6 MPa, where all the excess cumulative gas produced curves intersect the free gas cumulative gas produced curve. After that point, going higher in P/Z values, G_p follows the same trend as the absolute adsorption case, i.e. the higher the m_L^{max}, the higher the G_p and the OGIP. Similarly, the production rates for the absolute framework grow linearly with saturation capacity. The excess framework shows similar trends as for G_p; initially, the higher the saturation capacity, the lower the production rate, but as the curves intersect the volumetric reservoir case, the trend flips, causing the rate to be higher for higher m_L^{max}.

As K_L increases, the initial slope of the isotherms increases, and, indeed, adsorption rises (Figure C.6a). The excess adsorption maximum shifts to lower P/Z. The effect of the increase in the Langmuir constant decreases with higher K_L values. Figure C.6b shows that the G_p using the absolute framework moves closer to the volumetric reservoir when increasing the Langmuir constant. The reverse is true for the excess adsorption framework. The intersection of the excess cumulative gas produced curve and the volumetric reservoir line occurs at lower P/Z values as K_L increases, which is true for the production rate as well. The production rate is higher with higher Langmuir constants in the low pressure range, after which, at higher pressures, the opposite is the case.

As the saturation capacity of all adsorption isotherms is constant in this case, the isotherms would

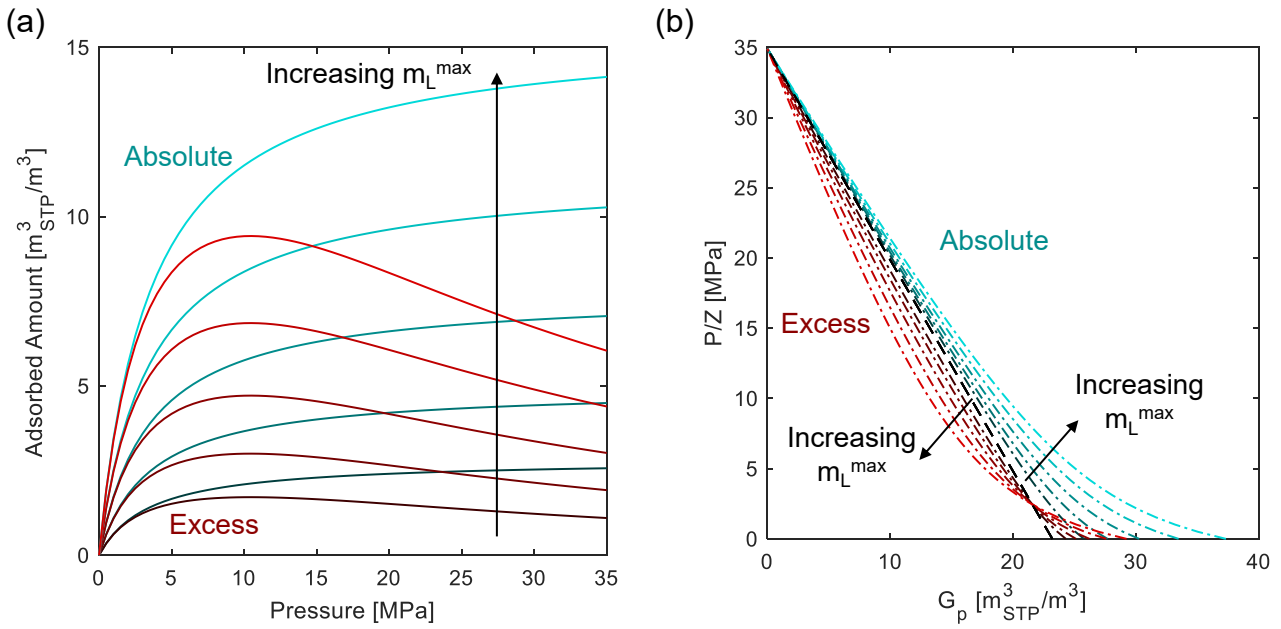

Figure C.5: CH_4 (a) absolute and excess adsorption isotherms and (b) G_p for various m_L^{max} (2.0, 3.5, 5.5, 8.0, 11.0 kg/m^3) for three scenarios, namely no adsorption (dashed black line); adsorption without porosity correction (blue); and adsorption with porosity correction (red).

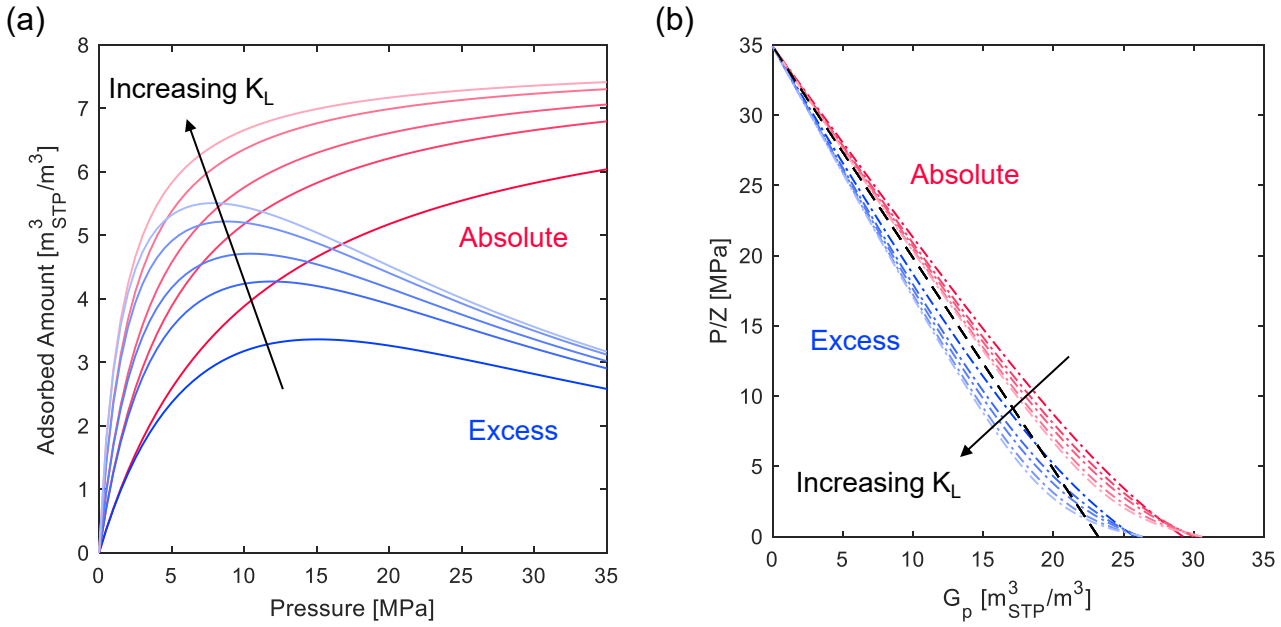

Figure C.6: CH_4 (a) absolute and excess adsorption isotherms and (b) G_p for various K_L (0.100, 0.200, 0.286, 0.450, 0.600 1/MPa) for for three scenarios, namely no adsorption (dashed black line); adsorption without porosity correction (pink); and adsorption with porosity correction (blue).

coalesce at a certain pressure. Interestingly, once the saturation capacity is reached, changes in the pressure do not affect the adsorbed amount, and the reservoir then acts in a similar way to a volumetric reservoir, as observed in Figure C.6. The change in adsorption behaviour leads to an especially higher slope of the adsorption isotherm for higher K_L values in the pressure range of up to 5 MPa, while smaller K_L values lead to a more distributed desorption of the gas.

C.3 Recovery with Gas Injection - Excess Loading

Figure C.7 show the operating regions of the CH_4/CO_2 and CH_4/N_2 systems in terms of the excess adsorption isotherms.

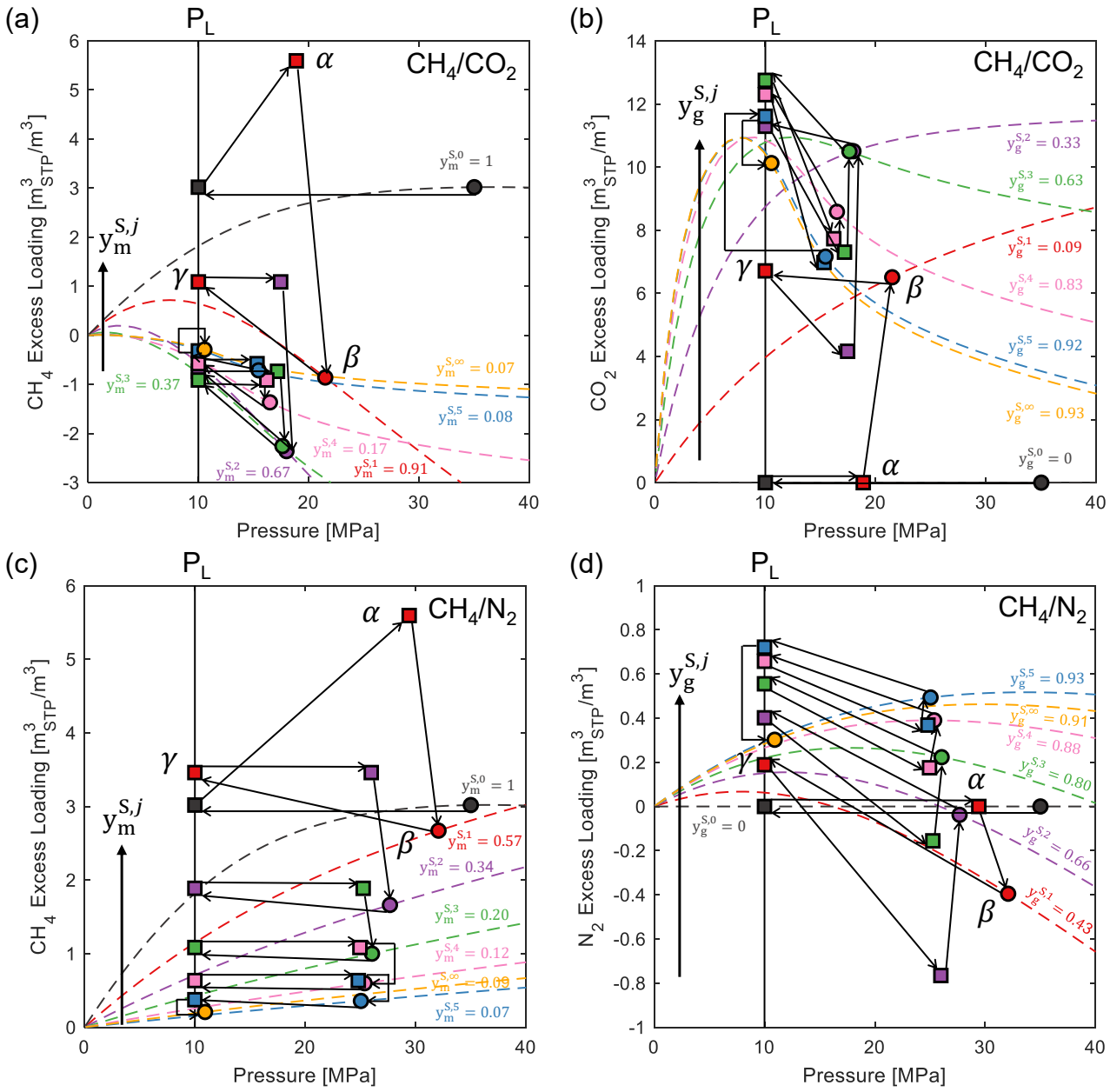

Figure C.7: Transitions (black arrows) during the cyclic CH_4 recovery with gas injection by either CO_2 (a, b) or N_2 (c, d). The results are plotted as excess adsorption loadings for each gas and the dashed lines indicate the competitive loadings at the equilibrium composition in the Soak stages ($y_i^{S,j}$). The superscripts '0' and '∞' represent the initial and abandoned reservoir conditions representatively. The symbols α, β and γ represent the Injection, Soak and Production stages, respectively, for the first cycle. P_L refers to the production pressure and each cycle is illustrated by a different colour.